Développement d'imagerie THz de champs de teneur en eau et de température en vue de la caractérisation thermique et massique de coefficients de diffusions

Mohamed Bensalem

université de BORDEAUX

THÈSE PRÉSENTÉE

POUR OBTENIR LE GRADE DE

DOCTEUR DE

L'UNIVERSITÉ DE BORDEAUX

ÉCOLE DOCTORALE DES SCIENCES PHYSIQUES ET DE L'INGÉNIEUR (ED SPI)

SPÉCIALITÉ : MÉCANIQUE

PAR **Mohamed BENSALEM**

DEVELOPPEMENT D'IMAGERIE *THz* DE CHAMPS DE TENEUR EN EAU ET DE TEMPERATURE EN VUE DE LA CARACTERISATION THERMIQUE ET MASSIQUE DE COEFFICIENTS DE DIFFUSIONS

DEVELOPMENT OF CONTACTLESS *THz* IMAGING OF WATER CONTENT AND TEMPERATURE FIELDS FOR THE PURPOSE OF THERMAL AND MASS CHARACTERIZATION OF DIFFUSION COEFFICIENTS

Direction de thèse : Christophe PRADERE
Encadrement : Alain SOMMIER
Jean-Christophe MINDEGUIA

Soutenue le : 08/10/2018

Membres du jury :

M. DUBOIS Frédéric	Professeur des Universités, GC2D, Limoges	Rapporteur
M. WATTRISSE Bertrand	Professeur des Universités, LMGC, Montpellier	Rapporteur
Mme. CHEVALLIER Sylvie	Ingénieur de recherche CNRS, GEPEA, Saint-Nazaire	Examinateur
M. GRIL Joseph	Directeur de recherche CNRS, LMGC, Montpellier	Examinateur
M. MOUNAIX Patrick	Directeur de recherche CNRS, IMS, Bordeaux	Président du jury
M. MINDEGUIA Jean-Christophe	Maitre de conférences, I2M, Bordeaux	Co-encadrant
M. SOMMIER Alain	Ingénieur de Recherche CNRS, I2M, Bordeaux	Co-encadrant
M. PRADERE Christophe	Chargé de Recherche CNRS, I2M, Bordeaux	Directeur

Abstract:

The investigation of water transport during drying processes represents a serious challenge for the wood-based material industry. In particular, the movement of water in glued products (such as cross-laminated timber or glue-laminated timber) can induce severe mechanical strains along the glued interfaces. Consequently, drying can lead to the spread of cracks within the material, voiding the use of the material for construction. The process of water movement in wood is complex and must be validated by measurements of water content fields in samples.

Accordingly, the aim of this study is to develop an experimental device that is able to measure the water content field in small wood samples during a drying (or wetting) process. The conventional techniques for humidity transport monitoring during drying or the imbibition process only allow access to global information, such as the global mass diffusion coefficient and the global water content losses or gains with time (sorption curves).

The goal is to show the efficiency of the *THz* technique as a low-cost and contactless technique that can be implemented in the industry for studying drying processes that couple heat and mass transfer. Due to the different sensitivities and time characteristics of each phenomenon, a separate study of heat and mass transfer is carried out. Two experimental benchmarks based on different detector technologies are developed for the contactless estimation of temperature and water content. A high-acquisition *THz* facility, based on infrared coupled with a *TTC* (*THz*-to-thermal converter), is used for the new application as a contactless measurement of the transient temperature of insulating materials opaque in the visible or IR range (*PVC*, *PMMA*, *PTFE* and wood). Moreover, a monodetector-based technique is employed for the contactless estimation of the water content at the local scale within homogeneous and heterogeneous samples (blotting paper and maritime pine).

Finally, these *THz* techniques permit estimations of the optical property of insulating materials and the hydric diffusion coefficient of hygroscopic materials. This demonstration shows the capability of *THz* methods to be used at different space and time scales. However, due to the wavelength, the technique does not reveal submillimeter details, such as wood growth rings. Moreover, the particularity of transient thermal measurements (contactless estimation of temperature part) is the large amount of information provided. Therefore, it is necessary to process the obtained images before estimating the desired parameter by an inverse method.

Keywords:

Water content, transient heat transfer, *THz*, *TTC*, infrared camera, image processing, inverse method, optical properties, diffusion coefficient, hydric transfer.

Résumé:

L'étude du transport de l'eau pendant les processus de séchage représente un défi majeur pour l'industrie des matériaux à base de bois. En particulier, le mouvement de l'eau dans les produits collés (tels que le bois lamellé-croisé ou le bois lamellé-collé) peut induire de fortes contraintes mécaniques au niveau des interfaces assemblées. Par conséquent, le séchage peut entraîner la propagation de fissures dans le matériau qui vont être préjudiciables pour la construction. La simulation du mouvement de l'eau dans le bois est complexe et doit être validée en utilisant des mesures de champs de teneur en eau sur des échantillons.

Dans ce contexte, le but de cette étude est de développer un dispositif expérimental capable de mesurer le champ de teneur en eau sur de petits échantillons de bois pendant un processus de séchage (ou d'humidification). Les techniques classiques de mesure de teneur en eau pendant le séchage ou le processus d'imbibition permettent uniquement d'accéder à des informations globales, telles que le coefficient de diffusion massique global et les pertes ou les gains globaux de teneur en eau au cours de temps (courbes de sorption).

Dans ce travail, l'objectif est de montrer l'efficacité de la technique *THz* en tant que technique peu coûteuse, non intrusive pour l'étude des transferts de chaleur et de masse dans ces processus de séchage. Pour cela, la séparation de l'étude de transfert de chaleur et de masse due à la sensibilité différente et à la caractéristique temporelle de chaque phénomène est réalisée. Deux bancs d'essai basés sur différentes technologies de détecteurs sont développés pour l'estimation sans contact de la température et de la teneur en eau. Un premier banc d'essai de *THz* à acquisition rapide a consisté à coupler une caméra infrarouge avec un « Tera Thermal Convertisseur (*TTC*) » pour la mesure sans contact de la température transitoire de matériaux isolants opaques dans le visible ou IR (*PVC*, *PMMA*, *PTFE* et bois). Par ailleurs des mesures de teneur en eau sans contact, réalisées sur un banc point par point pour caractériser des matériaux homogènes ou hétérogènes (papier buvard et pin maritime).

En définitive, la technique *THz* a permis d'estimer respectivement la propriété optique des matériaux isolants et le coefficient de diffusion hydrique des matériaux hygroscopiques. Ceci démontre la capacité d'utilisation des techniques *THz* à différentes échelles d'espace et de temps. Cependant, en raison de la longueur d'onde, la technique ne permet pas de révéler des détails submillimétriques tels que les cernes du bois. De plus, la particularité de la mesure thermique transitoire est la grande quantité d'informations enregistrées Par conséquent, il est nécessaire de traiter les images obtenues avant d'estimer le paramètre indiqué par méthode inverse.

Mots clés:

Teneur en eau, transfert de chaleur transitoire, *THz*, *TTC*, caméra infrarouge, traitement d'images, méthode inverse, propriétés optiques, coefficient de diffusion, transfert hydrique.

Unité de recherche

I2M, UMR CNRS 5295, Esplanade des arts et Métiers 33405 Talence

REMERCIEMENTS

Tout d'abord, j'aimerais remercier l'ensemble des membres du jury :

M. DUBOIS Frédéric, Professeur, Université de Limoges, et M. WATTRISSE Bertrand, Professeur, Université de Montpellier, qui ont accepté d'être les rapporteurs de cette thèse et de juger mon travail. Je les remercie également pour les discussions, questions et remarques sur la thèse.

Mme CHEVALLIER Sylvie, Ingénieur de recherche, CNRS GEPEA, Saint-Nazaire, et M. GRIL Joseph, Directeur de recherche, CNRS LMGC, Montpellier pour avoir accepté de participer au jury et avoir examiné mon travail.

Enfin je remercie M. MOUNAIX Patrick, Directeur de recherche, CNRS IMS, Talence pour avoir accepté de présider le jury de thèse ainsi que pour ses questions et remarques intéressantes et constructives sur le THz.

J'aimerais aussi remercier les personnes qui ont contribué à ce travail:

Christophe Pradère, Chargé de Recherche au CNRS I2M et directeur de ma thèse. Merci Christophe pour ton encadrement et ta rigueur qui ont permis d'obtenir une thèse de qualité bien que je me sois parfois un peu dispersé, « Désolé !!, je suis toujours curieux de tes méthodes astucieuses ».

Alain Sommier, Ingénieur de Recherche au CNRS I2M et encadrant de la thèse. Merci pour ta disponibilité, ta patience, ton aide aux manips et la bonne humeur durant la thèse. Tes blagues gardaient le sourire sur le visage de tout le monde dans la salle de manip. « Merci son Alain !!»

Jean-Christophe Mindeguia, Maitre de conférences à l'université de Bordeaux et encadrant de la thèse, pour m'avoir soutenu, m'avoir encouragé et avoir été patient avec moi pendant 3 ans. De plus, j'aimerais te remercier pour ta vision de spécialiste du bois.

Jean-Christophe Batsale, Professeur aux Arts et Métiers, Directeur de l'institut I2M. Je te remercie « papa JC » pour l'aspect de thermicien et d'inverseur que tu m'as transmis. Je te remercie pour les minutes de discussion que tu trouvais pour moi malgré tes responsabilités et tes conseils pour le Momo « doctorant » et le Momo « futur chercheur ». Tu es mon exemple de la réussite dans la vie.

Jean-Luc Battaglia, Professeur à l'Université de Bordeaux, que j'aimerais remercier pour les shorts discussions scientifiques pendant le déjeuner qui m'ont certainement aidé à améliorer mon bagage scientifique.

J'aimerais remercier mes parents qui m'ont toujours soutenu au cours de mes études et sans qui je ne serais jamais arrivé jusqu'ici. De plus, j'aimerais remercier mon frère Khaled, mes sœurs Noura et Kheira. Je vous remercie de tout cœur.

Je remercie madame Marina SEREBRYAKOVA « ma deuxième maman » pour son soutien et ses conseils. Je n'oublie pas sa fille Masha « la plus belle fille que j'ai rencontrée sur cette terre».

J’aimerais également remercier les différentes personnes que j’ai rencontrées au cours de ces trois années :

Ludovic GAVERINA, mon collègue, que j’ai rencontré au laboratoire lorsqu’il était doctorant à l’institut I2M. Merci « Lulo », tu m’as appris pas mal des bêtises, après ton départ, tu nous manquais.

Sara Kirchner, post doctorante au CNRS, avec qui j’ai eu de nombreuses conversations fructueuses. Je te remercie infiniment pour tes conseils pendant la rédaction, la présentation et toutes autres aides, « merci maman !!».

Valentin Tramu, stagiaire à l’institut I2M, avec qui j’ai également eu de nombreuses conversations. Je te souhaite une bonne continuation, vas-y il ne te reste qu’un an pour être ingénieur. Ça va passer vite surtout avec Alain.

Moncef « le Monce », un doctorant à l’Université de Bordeaux, que j’ai rencontré pendant ma dernière année. C’est à toi maintenant !! Bon courage notre spectroscopiste.

‘Le musclé’ Bastien Gavory, doctorant à l’Université de Bordeaux, que j’ai rencontré au laboratoire.

Sebastien Narinsamy, stagiaire à l’institut I2M, avec qui aussi j’ai eu de nombreuses conversations.

Cynthia Besson, notre collègue que j’ai rencontrée quand elle était stagiaire chez nous. Bonne continuation à THERMOCONCEPT.

Marta Romano, Responsable secteur Aquitaine d’Epsilon, merci pour tes efforts à collaborer avec nous et merci pour le sourire qui ne quittait pas ton visage lors de chacune de tes visites au laboratoire. « Bon courage avec Tao ».

Je remercie également les différentes personnes que j’ai rencontrées à l’institut I2M et au département TREFLE :

Bauka, Sagyn, Tolganay, Mira, Mary and Marat, mes très chers amis kazakh à qui je souhaite une bonne continuation dans cette vie « ммм.... вижня ! ».

Miguel, Marita, Marie, Alex, Charlottte, Yibao, Jose, Vincent, Audrey, Yannick, son Yannick, Cécile, Muriel «notre Mumu », Gérard, Alain, Fouzia, Ludovic.

Je remercie mes amis qui m’ont soutenu jusqu’au dernier jour de soutenance : Taki « bon courage à Reims », Abdelhak « Courage pour ta soutenance bientôt », Nacer « Bon courage en Argentine », Tawfik « Tu finiras aussi bientôt ta thèse, bon courage », Hamza « l’aventurier », Nabil « notre curieux scientifique », Momo « le courageux libanais » et Khalifa « mon récent mais vrai ami ».

C’est une page qui se tourne dans ma vie, mais une nouvelle arrive…

TABLE OF CONTENTS

NOMENCLATURE

f	Acquisition frequency	Hz
IT	Integration time	μs
x, y, z	Space dimensions	m
ρ	Density	$kg.m^{-3}$
C_p	Specific heat	$J.kg^{-1}.K^{-1}$
k	Thermal conductivity	$W.m^{-1}.K^{-1}$
e	Thickness	m
H	Convection coefficient	$W.m^{-2}.K^{-1}$
Bi	Biot number	(-)
T_{ini}	Initial temperature	K
T_{fin}	Final temperature	K
t	Time	s
$\Delta x, \Delta y, \Delta z, \Delta t$	Discretization steps of dimensions x, y, and z and time	m, s
A	Raw signal	DL
$S_{1,2,3,4}$	Signal calculated at quarter of period	DL
N_{ppp}	Number of points per period	(-)
U	Space base in *SVD*	(-)
S	Singular values matrix	(-)
V	Time base in *SVD*	(-)
S^*	Truncated singular value matrix	(-)
r	Singular values	(-)
r^*	Truncated singular values	(-)

I	Transmitted signal	*DL* or *V*
I_0	Emitted signal	*DL* or *V*
μ	Absorption coefficient of solid	m^{-1}
λ	Wavelength	*m*
κ	Thermotransmittance coefficient	$K^{-1}.m^{-1}$
Γ	Thermotransmittance	(-)
l_s	Solid thickness	*m*
R^2	Correlation coefficient	(-)
T_{mes}	Temperature measured by a thermocouple	*K*
T_{moy}	Mean temperature of a field	*K*
μ_s	Absorption coefficient of a solid	m^{-1}
μ_w	Absorption coefficient of water	m^{-1}
W	Mass water content	*kg* of water/*kg* of dry wood
l_w	Water thickness	*m*
$A(x,y,\lambda)$	Absorbance of the sample	(-)
m_s	Mass solid	*kg of solid*
m	Global mass of multiphase material	*kg*
Y	Absorption coefficient of the multiphase material	m^{-1}
RH	Relative humidity	%
T	Temperature	*K*
D	Diffusion coefficient	$m^2.s^{-1}$

ABBREVIATIONS

THz	Terahertz
SVD	Singular value decomposition
ROI	Region of interest
PVC	Polyvinyl chloride
PMMA	Poly(methyl methacrylate)
PTFE	Polytetrafluoroethylene
POM	Polyoxymethylene

GENERAL INTRODUCTION

1 Terahertz (THz) techniques - General and local context

Terahertz (*THz*) radiation consists of nonionizing electromagnetic waves located between the infrared (*IR*) and microwave regions (30-3000 μm). *THz* radiation is characterized by its safety because of its nonionizing properties due to the low photon energy, low cost and ease of use. *THz* radiation can penetrate insulating materials (for a few centimeters) but is reflected by metals and absorbed by water. This makes *THz* technology an optimal choice for several applications, such as security scanning, biological imaging, medical sciences and nondestructive testing (*NDT*). The optical properties of materials show a different spectral dependency in this wavelength range in comparison to their behavior in the *IR* range. Figure 1 shows the *THz* region in the spectral range.

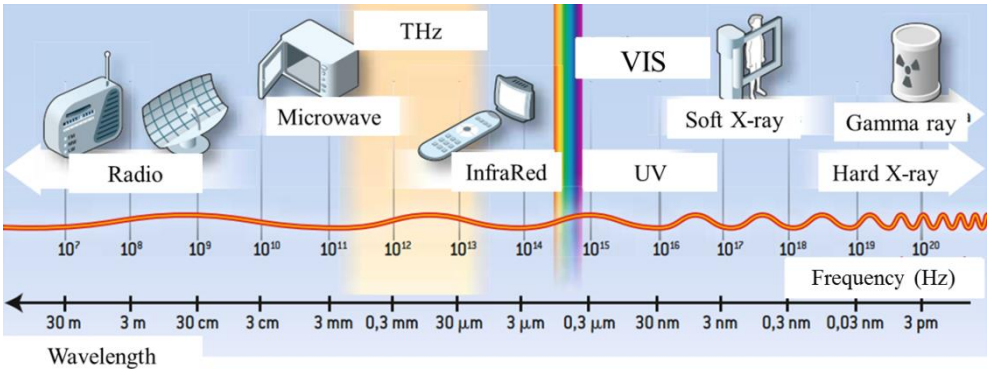

Figure 1: Terahertz region position in the frequency range with several applications.

THz radiation, classically called the "far *IR*" or "*THz* gap", has not been an intensively studied research field because of the established potential of the IR domain. However, due to the transmission limitation of different wavelength domains to several materials and/or their high cost, *THz* has attracted a great deal of interest over the last three decades as an alternative or a complement to other radiation techniques. Recently, *THz* sources appeared from two different frequency ranges. The electronic engineers preferred to generate *THz* radiation sources from low-frequency sources (microwaves). On the other hand, opticians preferred to use photonics technologies from high-frequency sources (*IR*). Moreover, the development of materials research and lasers allowed the development of high-power *THz* sources. In addition, the advances in *THz* sources were accompanied by the development of detection systems and optics components, which make the *THz* technology an active research field. Moreover, *THz* technology has become attractive to not only researchers but also industrials, as this technology is increasingly being inserted into different industry applications.

Three main ways of generating *THz* radiation exist: ***THz quantum cascade lasers*** [1], ***optical THz generation*** [2] and ***solid-state electronic devices*** [3].

THz quantum cascade lasers emit *THz* radiation through electron relaxation between the subbands of quantum wells.

Optical *THz* generation can be carried out in nonlinear media, such as GaAs, GaSe, and ZnTe, or generated via electron acceleration. In nonlinear media, the incident waves undergo a nonlinear frequency conversion. The nonlinear conversion process can be carried out using optical rectification or difference frequency generation. Optical rectification is performed by a femtosecond-laser excitation that can generate *THz* pulses in nonlinear media. However, the difference frequency generation method can generate continuous-wave (*CW) THz* via two *CW* optical beams in nonlinear media.

On the other hand, *THz* radiation can be generated through electron acceleration using photoconductive antennas excited by laser beams, which generates photocarriers. The generated photocarriers are then accelerated by a *DC* bias field between the two electrodes of the antenna, producing a photocurrent. The photocurrent is proportional to the laser beam intensity in time; thereby, *THz* pulses can be generated by femtosecond laser pulses, and *CW THz* radiation can be produced by mixing two laser beams with different frequencies [4]. Moreover, the air plasmas represent an important medium in which electrons are accelerated to generate *THz* radiation.

Finally, solid-state electronic devices produce *THz* radiation near or below 1 *THz,* such as tunneling diodes that use a slot antenna to couple the third harmonic of the fundamental 342 *GHz* oscillation.

In parallel, *THz* detection systems can be based on the ***electro-optic sampling technique***, ***photoconductive antennas*** or the ***thermal-absorption-based method***. The electro-optic sampling technique represents a time-domain *THz* detection method allowing ultrawideband spectrum detection due to its time-domain detection characteristic [4]. It uses materials such as *ZnTe* crystals. The photoconductive antenna can be used for time-domain *THz* detection. Finally, the thermal-absorption-based method uses germanium and indium antimonide bolometers. Comparing with time-domain *THz* detection, bolometers lack frequency spectrum detection. Thus, the interferometer method is often used to extract the spectral information from the bolometer detection. Thermal detectors can be based on Golay cells, utilizing the induced thermal expansion of a gas, or pyroelectric devices, relying on spontaneous polarization changes [4].

In addition, as a consequence of the development of *THz* sources and detectors, *THz* optics is an important field. Due to the high losses of optical components used in other frequency ranges, some polymer and semiconductor materials, such as Teflon and silicon, show a high transmission in the *THz* region. Therefore, lenses for the *THz* range are often made of those materials. Moreover, metallic meshes can be used as *THz* bandpass filters. However, recently, metamaterials have shown unusual electromagnetic properties, making them a potential candidate to play an important role in *THz* optical components.

For thermal specialists, a simple way to generate *THz* waves is using electronic sources (Gunn diodes). In addition, pyroelectric detectors are low-cost detectors allowing a preliminary validation of first tests aiming to check physical phenomenon such as mass diffusion within materials. Moreover, the knowledge of heat transfer and materials characterization in the *IR* domain within the *TIFC*[1] team accumulated over several years leads us to consider the development of a thermal bolometer allowing an IR imager to detect *THz* waves.

For a decade, the *TIFC* team (part of the *TREFLE*[2] department in the *I2M*[3] Institute of Bordeaux) has developed techniques and methods of characterization of heterogeneous materials. The main works have been conducted to develop new methods for thermophysical property measurements and nondestructive testing. Figure 2 shows an estimation of the thermal properties of four samples in the *IR* by the flying spot technique using the parabola method, as conducted by the *TIFC* team.

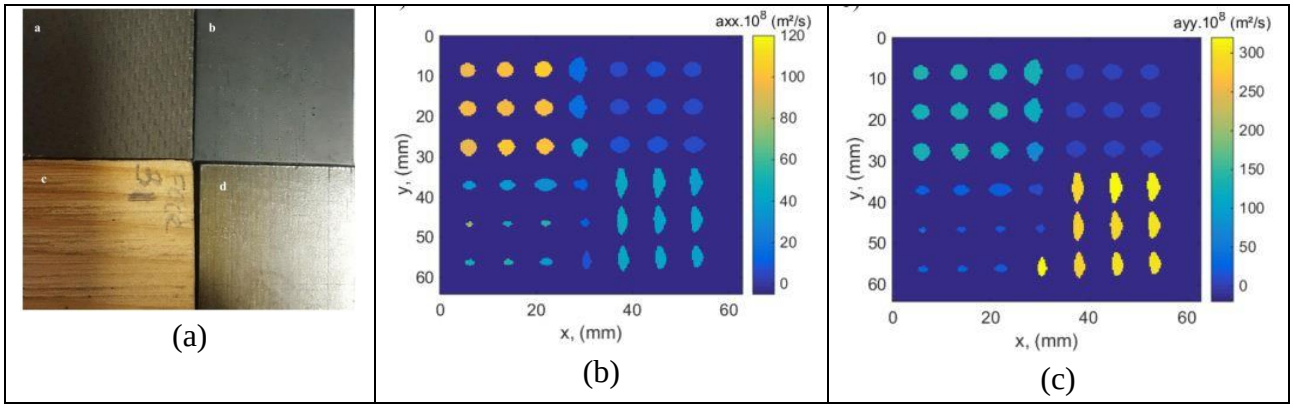

Figure 2: Estimation of the in-plane thermal properties via the parabolic method following different grids of laser sources: (a) different types of materials: ((a) braided carbon / epoxy composite fiber, (b) Plexiglas, (c) maritime pine and (d) carbon / epoxy composite), (b) the estimate according to x, (c) and the estimate according to y [5].

During the last few years, the team has expanded its domain of study from infrared to millimeter wavelengths. The bolometer (also called tera-to-thermal conversion, or *TTC*) was designed based on the thermal response of a carbon sheet exposed to a *THz* excitation. The developed bolometer allowed the visualization of objects for different applications, such as quality inspection, as illustrated in Figure 3.

[1] Thermal Imaging Fields and Characterization
[2] Transfert Fluide Énergétique
[3] Institut de Mécanique et Ingénierie

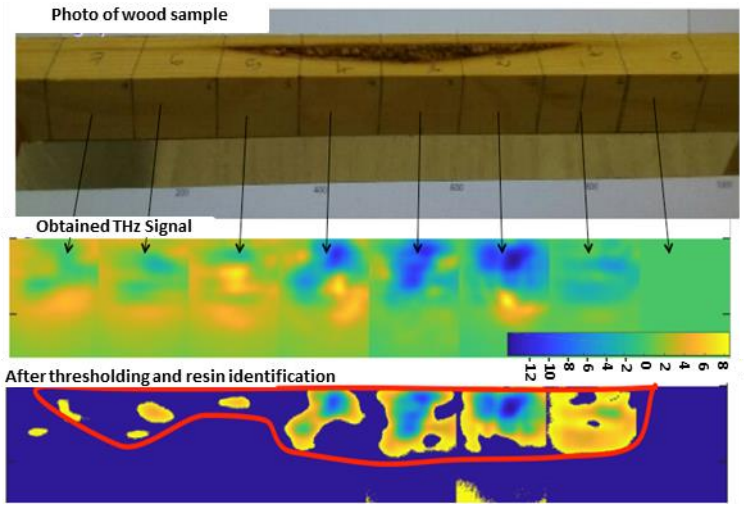

Figure 3: *THz* application in the quality inspection of wood aims to detect resin pockets using *TTC*.

2 The issue of wood drying

Drying is an operation that consists of reducing the degree of humidity in wood by eliminating part of the water it contains. Wood is commonly dried for the following reasons:

- to use the material with humidity levels in hygroscopic equilibrium with its service environment (freshly cut wood can have an average humidity of more than 80 % and must be brought back to a value close to 11 % to realize indoor furniture, for example)

- to obtain relatively stable products

- to reduce the risk of deterioration and disorders caused by the attack of fungi and other parasites

The drying of wood is generally done by convection. This technique is based on two coupled principles: energy supply and the evacuation of moisture (mainly by the vapor phase). Conventional (artificial) dryers are hot air-conditioned, i.e., the dryers regulate both the humidity (by steam injection, for example) and the temperature (by heating coils, for example) of the drying cell (see Figure 4).

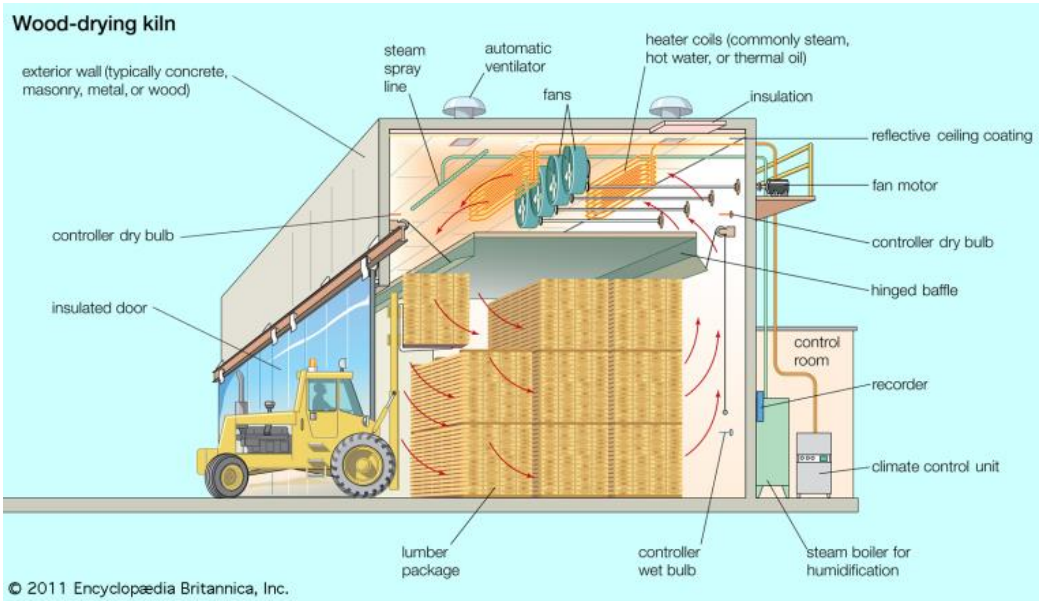

Figure 4: Schematic view of a conventional wood dryer (also called a "kiln" in the industry).

To prevent wood damage during drying (see the next paragraph), industrialists have developed specific humidity/temperature cycles in the dryer. For simplification, the relative humidity in the dryer is generally high (up to 90 %) at the beginning of the process to homogenize the water content of the freshly cut wood. Then, the humidity is slowly decreased while the air is heated (up to 80 °*C*) in order to accelerate the departure of moisture from the wood. Finally, a slow cooling phase at constant humidity is applied to prevent damages induced by thermal shock. From a scientific point of view, the artificial drying of wood can then be seen as a coupled heat and mass transfer problem, where wood is exposed to a variable hygro-thermal environment.

The drying process leads to the movement of humidity within the material, which can induce nonuniformity of the temperature and/or water content distribution. The hygro-thermal state of wood has an impact on its mechanical behavior since the material generally expands when its water content increases, while it shrinks when its water content decreases (at the fibers' saturation point, i.e., approximately 30 %). Moreover, wood has a natural anisotropic mechanical behavior, resulting in differential hygro-mechanical behaviors depending on the fibers' orientation (longitudinal, radial or tangential). This coupled anisotropic thermo-hygro-mechanical behavior can lead to the spread of cracks and delamination, mainly at the glued interfaces of industrial products such as glue-laminated timber (*GLT*) or cross-laminated timber (*CLT*), especially when these products are fabricated by "green gluing" (gluing of wood lamella before drying). Thereby, the resulting product quality can be useless for construction.

To optimize the drying process (the limitation of damage, obtaining homogeneous batches of wood, energy optimization of the drying, etc.), hygro-mechanical models for wood are developed [6], with the main purpose of predicting, and therefore limiting, the various mechanical damages that can be induced by drying. Obviously, the development of these models must be accompanied

by experimental measurements, often made at the scale of wood samples. Water data (global and/or local water content) and mechanical data (displacements or deformations, measured punctually or in the form of full fields) can be used to validate these theoretical models.

In this context, the *GCE*[4] department of *I2M* developed contactless measurements of mechanical stresses and strains during the drying of glued wood elements. These measurements were carried out in parallel to the development of an anisotropic hygro-mechanical model [7]. For that, the team used a digital image correlation technique (*DIC*) used also by [8], and allowing a nondestructive measurement of strains in different zones of wood samples during drying. Figure 5 shows the technique.

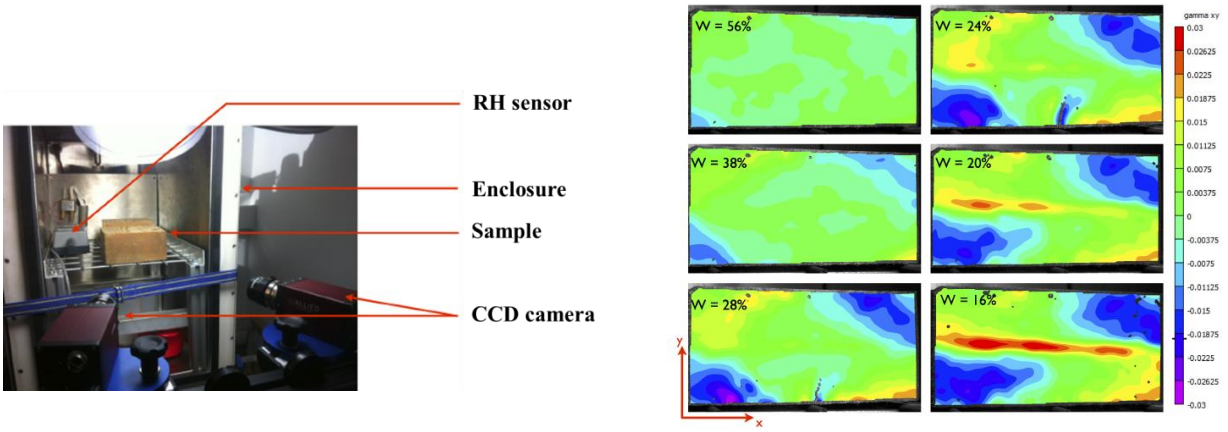

(a) (b)

Figure 5: On the left, the experimental setup for displacement measurement by *DIC* in the *GCE* department. On the right, an example of a contactless measurement of the shear strain of a sample at different times of drying (*W* is water content of the sample) [7].

During these drying experiments, the water content field in the wood samples was not measured. Only the global mass of the sample was measured at different drying times. This lack of information can be explained by the absence of a contactless, simple, safe and cheap technique for water content field measurement. As a consequence, it was not easy to validate the diffusion part of the developed model.

In this context, a common project between the *TREFLE* and *GCE* departments of *I2M* was established. The starting point of the project relied on a common scientific objective based on the study of a process (drying), where heat and mass transfers take place.

[4] Génie Civil et Environnemental

3 Scientific reasoning for the study

The main aim of this work is thus to show the feasibility of a *THz* technique to monitor the water content of hygroscopic materials, such as wood. The main challenge is to develop a robust system of *THz* imaging for the contactless estimation of both temperature and water content in other homogeneous or heterogeneous material, in addition to wood, under a transient heat and/or mass regime. Such a system may have several outcomes, such as the improvement of theoretical knowledge of drying, the validation of numerical models, inverse methods for determining coefficients of thermal and/or hydric diffusion, the implantation of sensors on an industrial scale.

A unique feature of our study lies in the fact that the two types of transfer (heat and mass) are separately treated. This distinctive study can be justified by (i) the very different spectral sensitivities of temperature and water content to *THz* radiation (Γ) and (ii) the very different characteristic times of heat and mass diffusion (t_c).

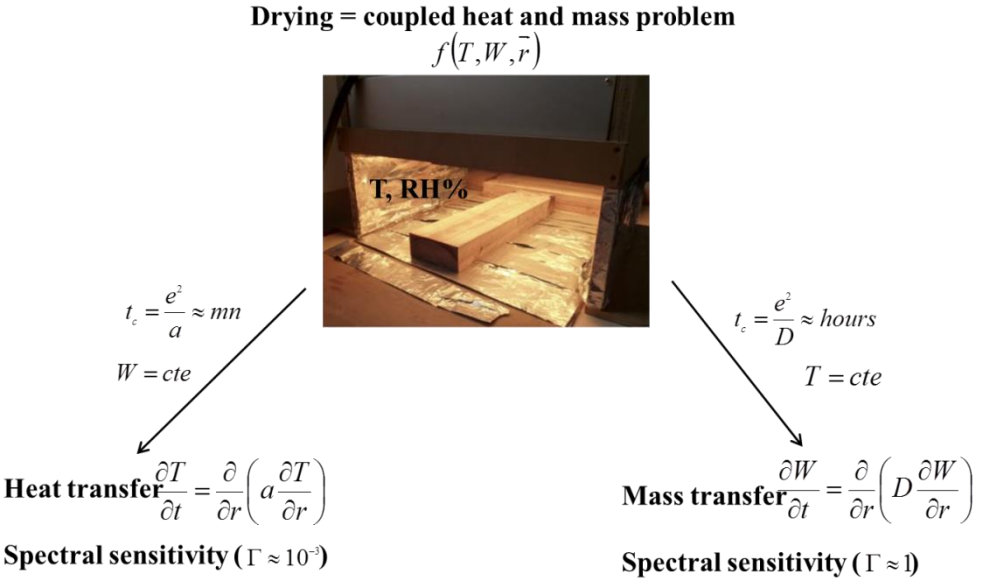

Figure 6: Coupled problem in the drying process (heat and mass transfer).

Another unique point of the study is to deal with the problem of mass transfer by a thermal analogy. In other words, classical thermal diffusion models will be used to deal with mass diffusion. We specify that mass transfer by capillarity (the movement of the free water in wood, i.e., significantly above the saturation point of the fibers) will not be treated.

The distinguishing of the 2 modes of transfer led us to carry out separate and independent experimental studies, with the following main objectives:

- To develop an experimental *THz* setup and acquisition method allowing the determination of the water content dependency of *THz* and then to propose ***a contactless measurement of the water content field of a sample***, including under a transient regime.
- To develop an experimental *THz* setup and acquisition method allowing the determination of the temperature dependency of *THz radiation* and then to propose ***a contactless measurement of the temperature field of a sample***, including under a transient regime.
- ***To estimate diffusion coefficients*** based on an image processing method coupled with an ordinary least-square-based inverse method.

4 Organization of the manuscript

This dissertation is divided into four independent chapters.

The first chapter resumes the discussion of techniques used for the contactless estimation of the water content within wood. The need to develop a low-cost scanning system able to inline scan the product with an acceptable resolution during drying process is highlighted. First, the water transfer within a hygroscopic material is presented. Then, some theoretical methods of resolving Fick equations are explained. Thereafter, state-of-the-art methods are used for the contactless measurement of water content and their experimental limits is performed. This section evaluates the used experimental and theoretical methods to measure the water content. In addition, an exploration of using *THz* radiation in several applications is detailed. In this section, it is shown that the *THz* technique is mainly used to monitor the water content in food and plant industry applications.

The second chapter presents the instrumentation used for the contactless quantitative measurements of water content. The developed experimental techniques lead to obtaining a sensitive scan system depending on the studied phenomenon (heat or mass transfer). The setups are mainly based on a monodetector or *2D* detector (images). The use of an infrared monodetector with focalizing optics leads to a so-called “point-by-point” system, which is more suitable for mapping a steady water content field. The monodetector is used to validate the calibration between the *THz* signal and the hydric state of wood samples. It should be indicated that this system shows efficiency in inertial applications, such as inspection quality or nondestructive testing (*NDT*), due to the sensitivity of the waves to density. The *2D* detector couples an infrared camera with a bolometer, allowing for a rapid visualization of the thermal or water content field. This system shows sensitivity to water content in the situation of hydric excitation, which allows for the *2D* monitoring of mass diffusion within hygroscopic materials. Moreover, this system also shows sensitivity to temperature, which makes it suitable for the contactless measurement of a transient temperature field of an insulating thin material’s surface.

In the third chapter, it is proposed to revise the acquisition and processing methods to extract the amplitude in lock-in mode-based experimentations. For that purpose, an efficiency study of the bolometer and the involved phenomena during scanning (the numerical modeling of the

setup) is proposed. This study allows for understanding the obtained signal and justifies the resort to image processing to extract the workable information incoming from the source, independent of the environment.

The last chapter presents the first obtained results using the developed setups and processing methods. First, a calibration study showing the link between *THz* absorption and the water content of two kinds of hygroscopic materials (blotting paper and soft wood) is detailed. A model allowing the mapping of the water content is proposed and validated. The second part is devoted to the first results obtained using a hydric excitation on blotting paper and softwood samples. The capability of *THz* waves to monitor the transient hydric regime and thereby to estimate the diffusion coefficient of hygroscopic materials is detailed. The estimation of diffusion coefficients is performed using the Gauss-Markov method to minimize the space-time image with the theoretical solution in Fourier space or as a numerical solution obtained using the finite differences method in the situation of drying and hydric excitation. Finally, the last part of chapter 4 (independent of the other parts) deals with heat transfer within insulating materials, including softwood samples. A developed model based on a lumped body allows for the estimation of the optical properties of materials and thereby a contactless estimation of the transient temperature field.

CHAPTER I: STATE OF THE ART

In this chapter, a comprehensive overview of key state-of-the-art techniques for exploring water content inside wood materials will be presented as well as the problem of the industrial drying of wood and the damage it can cause to products. The objective is to highlight, from this panel of methods, the role and interest in developing contactless and nonionizing imaging methods and the associated inverse processing to characterize such phenomena. These approaches, which are once again complementary, are made possible in particular by the development of terahertz imaging camera techniques allied to the high potential offered by *THz* Gunn diodes.

Though many "conventional" ionizing methods (*X-ray*, *MRI, etc.*) allow for the measurement of water content fields, they are not easy to use because of the associated risks.

In this chapter, as a first step, we recall the theoretical framework of mass transfer within porous materials, as well as some numerical models of diffusion. Since one of the main objectives of the thesis is to design an experimental device for the contactless measurement of water content fields, a state of the art is carried out on the various experimental methods used to date. Finally, we present the different fields of application of terahertz (*THz*) techniques and conclude on their possible use in our research ambitions. The classical methods will be presented and detailed. In addition, a brief description of the theoretical and experimental limits will be made for each method. Moreover, even if *THz* is currently widely used in the field of nondestructive testing and medical applications, it will be shown that very few authors use and develop inverse processing methods devoted to the heat and mass characterization of such water content diffusion and transport. This chapter will make it possible to make an assessment of the various measurement techniques to understand their complementarity. Finally, this chapter will allow us to move towards new experimental approaches and inverse methods.

1 Context of the work

As said in the general introduction, in the timber industry, the conditioning of wood at a precise water content is crucial for product quality. Thermal and hydric phenomena can happen at global and local scales, which affects the structure of hygroscopic materials through swelling or shrinkage. On the other hand, the natural heterogeneous structure and singularities within wood (knots, resin pockets, etc.) can affect the thermal and hydric fields.

Recently, bonding methods allowed the use of wood for structural functions as long-span beams, slabs or walls. Products such as *GLT* (glue-laminated timber) or, more recently, *CLT* (cross-laminated timber) [9] are increasingly used in the construction field.

Classically, before gluing, the wood elements to be connected are dried separately at a water content between 8 and 16 %. The drying can induce cracks in and deformations of the wood pieces, leading to an edging and planing of each element (lamella). Thereafter, the lamellae are glued, and the final product can be planed again. Therefore, this classical fabrication process can induce a loss of material during the edging and planing of elements. Recent adhesives are now effective to glue green wood [10], i.e., wet wood elements (above the fiber saturation point (*FSP)*, i.e., a water content higher than 30 %). This technique, the "green" gluing of wood, consists of gluing the different wet elements (in the green state) and then drying the glued structure and finally edging it. Green gluing provides less material loss, a gain of time and a drying process requiring lower energy. The difference between the two processes is shown in Figure 1-1.

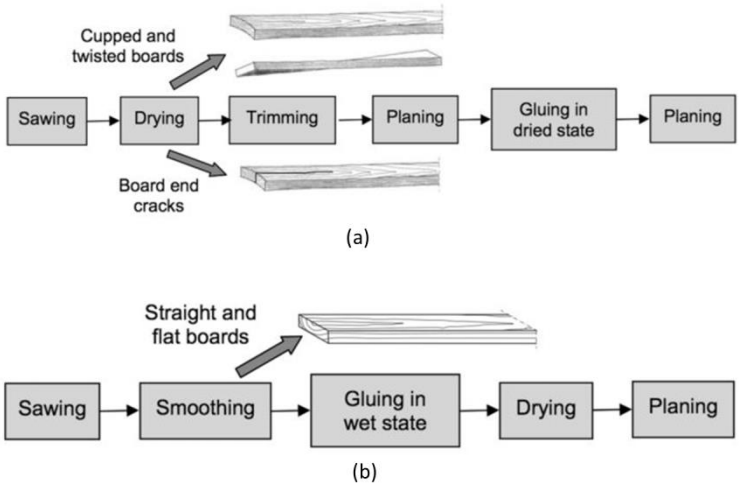

Figure 1-1: (a) Dry gluing process and (b) green gluing process [9].

All wood gluing techniques require strict control of the drying process of bonded wood pieces (lamellae). The drying process is indeed a serious challenge for the wood-based material industry. During drying, thermal and hydric transfers occur and can induce nonuniformities in the temperature and water content distribution. Therefore, the heterogeneity of drying will induce a

change in the structure of the hygroscopic materials in such a way that the wet areas are swelling while the dry areas are shrinking. The different mechanical behaviors (swelling/shrinkage) lead to the appearance and spread of cracks and delamination mainly at the gluing interface, limiting the potential use of the final product for construction. Figure 1-2 shows an example of interface delamination.

Figure 1-2: Detachment of the adhesive interface [7].

Optimizing the drying process in order to limit the damage of glued elements can rely on hygro-mechanical numerical simulations. Coupling the water movement within the material simulation with the induced mechanical behavior (thanks to the swelling and shrinkage anisotropic coefficients) can provide information about the stress field and the potential damage zones. The simulation of water movement in wood is complex and must be validated by the measurement of the water content distribution in samples [11]. In the literature, many models describing mechanical behavior during drying have been developed, but few hygro-mechanical models have been checked experimentally [12].

In [7], Clouet identified the main parameters influencing the hygro-mechanical stresses induced by the drying process. He studied the hygro-mechanical behavior of glued wood lamella by measuring the displacement and strain fields during drying by a digital image correlation (*DIC*) technique. Moreover, he developed a numerical model based on finite elements to simulate the hygro-mechanical behavior of glued wood lamella during drying. However, the absence of a water content distribution measurement of the samples while drying did not allow complete validation of the numerical model, especially the mass transfer part. The need for an experimental device for the contactless measurement of water fields is clearly underlined here.

2 Water transfer in wood

2.1 Water content in hygroscopic materials (wood)

Hygroscopic materials are materials that can attract molecules of water from the air through absorption or adsorption. Hygroscopy can lead to changes in the volume and physical and mechanical properties of a material. The water in wood can exist in one of three forms: the water of constitution, bound water or free water [7]. (i): The water of constitution represents the water that is part of the composition of microfibers in the solid matrix. (ii): Bound water consists of water molecules adsorbed on the hydrophilic part of cell walls (for wood, the cellulose and hemicellulose of cell walls (OH)). (iii): Free water is the water that exists as a liquid or vapor in the cell cavities. Porosity and permeability have strong influences on the quantity of free water. It is worth noting that only the last two kinds of water are generally considered as existing water in wood.

The water content (*WC*), or moisture content (*MC*), represents the total amount of water in wood, and it is defined as the weight of the water in its different forms (vapor or liquid) within the wood divided by the weight of the dry wood (solid matrix). This ratio can be greater than 1, which means that the weight of water within wood is greater than the weight of the dry wood, such as in a living tree. The value can be multiplied by 100 to obtain the water content percentage (equation 1-1).

$$W = \frac{M_w}{M_s} = \frac{M_t - M_s}{M_s} \times 100 \tag{1-1}$$

where M represents the mass in (*kg*) and the indices w, s and t indicate water, solid and total, respectively.

2.2 Sorption isotherms and water capacity

When a dry hygroscopic material is stored at constant relative humidity (*RH*) and temperature, its water content increases and reaches a constant value. At this hygroscopic equilibrium, the water content is called the equilibrium water content (*EWC*). Equilibrium occurs when the ratio between the partial vapor pressure within the material and the pressure of the environment tends to 1. The relative humidity of the environment influences the *EWC* in a way that the higher the *RH* is, the higher the *EWC*. For dry wood, the water molecules in the air are adsorbed on the fiber walls in different layers (bound water). Once the adsorption layers of the fibers are saturated, the water molecules move freely within the pores and voids. At this stage, the fiber saturation point (*FSP*) is reached. The *FSP* is defined as the point where all the free water has been lost within wood or all adsorption layers are saturated. The *FSP* of main wood species is often measured at $W \approx 30$ % [7].

During drying, the material first loses its free water through the vessels and lumens until the *FSP*. Below the *FSP*, adsorbed (bound) water begins to desorb due to the breaking of bonds between water and the hydrophilic groups of wood. Desorption first occurs at the last adsorption layer, where the water-water bond is weaker, and then layer by layer until the layer adsorbed to the cell walls. At this final stage, the water content is $W = 0$ %. The condition of $W = 0$ % is known as oven-dry because an oven is typically required to completely drive out all the water content.

The water content depends on the relative humidity of the environment, the temperature and the material itself. For a given material and at a constant temperature, the relation linking the water content and the relative humidity is called a "sorption isotherm". Figure 1-3 shows the general shape of isotherms.

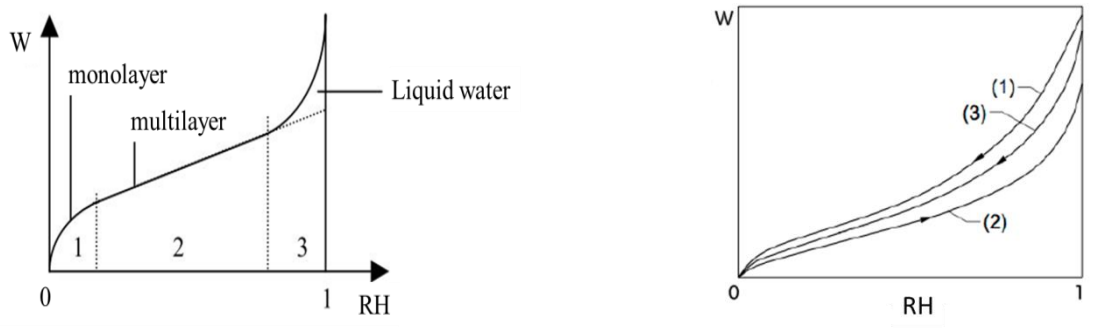

(a) (b)

Figure 1-3: (a) Zones of sorption isotherms, (b) different wood sorption isotherms [7].

Naturally, wood is exposed to hydric conditions that can be drying or humidifying, which respectively induce the desorption and sorption of water. It has been shown that the adsorption and desorption curves of water molecules within a hygroscopic material at the same temperature are not the same. According to [7], the adsorption/desorption cycle shows hysteresis, but the desorption curve remains above the sorption curve. At a given *RH*, the *EWC* ratio between the desorption cure and sorption curve is generally situated between 0.75 and 0.85 [13].

In the literature, there are many sorption models representing the water content as a function of temperature and relative humidity. Table I-1 in appendix I shows some models from the literature, such as GAB's model, Harking's model and Henderson's model [14]. In this study, the Henderson model shows the best fit of the experimental data relative to the other models. The model is given by equation (1-2) as follows:

$$RH = 1 - \exp\left(-A(T + B).W^{C}\right) \tag{1-2}$$

where *RH* is the relative humidity, *T* is temperature in (*K*), *W* is the water content in (*kg* of water / *kg* of dry material) and *A*, *B* and *C* are the coefficients to determine.

2.3 Water diffusion

In a common drying process, wood is placed in a variable temperature and *RH* environment. Drying is therefore based on the coupled phenomenon of heat and mass transfers. In the rest of the study, we will consider that drying is essentially controlled by variations in the external *RH*, i.e., the external temperature will not change. We will also consider that the main mechanism for transporting water in wood is vapor diffusion. The conditioning of dry samples within a wet environment provides for the adsorption of vapor molecules on cell walls. Once the adsorption layers are saturated, the water content reaches equilibrium, and the mass exchange between the sample and environment is then equal. This condition allows for neglecting the capillary transport.

Diffusion is defined as the transport phenomenon of water within porous materials from wet zones to dry zones. In other words, the term can be defined as the movement of water under the effect of a water content gradient [7]. The mass diffusion of water is based on Fick's laws, which are flux and mass conservation equations. In the Fick equations, the variable representative of the water can be the water content, the volume or mass concentration, or the partial vapor pressure. The relation between the water content gradient and the flux is given by the following equation:

$$\vec{q} = -\overline{\overline{D}}.\vec{\nabla}W \tag{1-3}$$

where $\vec{q}$ is the mass flux density in ($kg_{water}.m^{-2}.s^{-1}$), D is the diffusion coefficient tensor in ($kg_{dry}.m^{-1}.s^{-1}$) and W is the mass water content gradient in ($kg_{water}.kg_{dry}^{-1}$). In an elementary volume, the conservation of mass supposes that the sum of incoming and outgoing mass fluxes is equal to the amount of substance variation in volume V (if there is no generation of mass). The flux balance is then given as follows:

$$-\int_V \vec{q}.\vec{n}.ds = -\frac{dm}{dt} \tag{1-4}$$

Substituting (1-3) into (1-4) gives:

$$D\int_V \vec{\nabla}W.\vec{n}.ds = -\frac{dm}{dt} \tag{1-5}$$

The passage between the surface integral and the volume integral is given by the theorem of Green-Ostrogradski as follows:

$$\int_V \vec{q}.\vec{n}.ds = \int_V div\vec{q}.dV \tag{1-6}$$

where the scalar operator *div* is given by $div = \frac{\partial}{\partial x} + \frac{\partial}{\partial y} + \frac{\partial}{\partial z}$. On the other hand, the mass water content can be written as follows:

$$m = \int_V \rho_s . W . dV \tag{1-7}$$

where ρ_s is the density of the dry material. Moreover, substitution of equations (1-6) and (1-7) into equation (1-5) gives:

$$\int_V div\vec{q} . dV = -\frac{d}{dt}\int_V \rho_s . W . dV \tag{1-8}$$

Substitution of equation (1-3) into equation (1-8) and derivation in terms of volume gives:

$$\frac{dW}{dt} = div\left(\overline{\overline{D}}_w \vec{\nabla} W\right) \tag{1-9}$$

where *Dw* is the diffusion coefficient and $\overline{\overline{D}}_w = \frac{\overline{\overline{D}}}{\rho_s}$ in ($m^2.s^{-1}$). Equations (1-3) and (1-9) represent the first and second Fick laws that are analogous to Fourier's law in the conduction mode of heat transfer and Ohm's law in electricity. The driving forces in the Ohm and Fourier equations are the electrical potential and temperature, respectively, while in the Fick equation, the driving parameter can be the water content (*W)* in ($kg_{water}.kg^{-1}_{dry}$), the water concentration or volume water content (*c)* in ($kg.m^{-3}$) or the partial vapor pressure (P_v) in (*Pa*). The passage from one driving force to another in the isothermal case induces a change in the diffusion coefficient (D_w, D_c or D_{pv}). The vapor partial pressure can be written as a function of the saturation pressure and the relative humidity as follows:

$$RH = \frac{p_v}{p_{sat}} \tag{1-10}$$

where P_v is the vapor partial pressure in (*Pa*) and P_{sat} is the saturation pressure, which is a function of temperature, in (*Pa*).

The diffusion coefficient depends on the temperature, which means that it would be easier to vary the relative humidity (*RH*) at a constant or less variable temperature. Otherwise, if the temperature of the system is considerably variable, the resolution of the coupled heat and mass transfer equation based on the mass conservation, momentum and energy equations is unavoidable. Moreover, the solution of the mass transfer equation can be complicated depending

on the initial and boundary conditions. The water transport within hygroscopic materials can be "non-Fickian", mainly when the water content gradient becomes low [15].

The diffusion coefficient D is a coefficient that depends on concentration (water content) according to [16], and it can be given by:

$$D = D_0 e^{\alpha W} \tag{1-11}$$

where D_0 is the diffusion coefficient at the initial water content and α is a constant describing the moisture dependency.

Moreover, the diffusion coefficient is not the same along different directions for anisotropic materials such as wood. In the literature, this coefficient is given for different wood species for different directions, as shown in the Table 1-1.

Species	Direction	D ($m^2.s^{-1}$)
Douglas	Longitudinal	$3.27\ 10^{-9}$
Pine	Radial/Tangential	$2.11\ 10^{-11}$
Epecia	Radial/Tangential	$1.5\ 10^{-8}$

Table 1-1: Values of diffusion coefficients for different species and different directions [7].

In this study, we will consider that the diffusion coefficient is isotropic and does not depend on either the temperature or the water content.

2.4 Analytical models of mass transfer

As mentioned above, the solution to equation (1-9) depends on the configuration of the setup (a finite, semifinite or infinite medium), the excitation type (Dirac, Echelon, etc.) and the boundary and initial conditions (null, constant or moving). Cranck [17] detailed several solutions for different configurations of mass transfer.

2.4.1 Method of separation of variables

Considering a one-dimensional diffusion problem with an isotropic diffusion coefficient leads to the following equation:

$$\frac{\partial W}{\partial t} = D\frac{\partial^2 W}{\partial x^2} \tag{1-12}$$

The separation of variables supposes that the water content is a multiplication of two separable time and space functions as follows:

$$W(x,t) = X(x).T(t) \tag{1-13}$$

$$\begin{aligned} \frac{\partial W}{\partial t} &= X(x).\frac{\partial T(t)}{\partial t} \\ \frac{\partial W}{\partial x} &= T(t).\frac{\partial X(x)}{\partial x} \\ \frac{\partial^2 W}{\partial x^2} &= T(t).\frac{\partial^2 X(x)}{\partial x^2} \end{aligned} \tag{1-14}$$

Substitution of (1-14) into (1-12) gives:

$$\frac{1}{T}\frac{\partial T}{\partial t} = \frac{D}{X}\frac{\partial^2 X}{\partial x^2} \tag{1-15}$$

Since the right-hand side depends only on x and the left-hand side depends only on t, both sides are equal to some negative constant; thus:

$$\begin{cases} \dfrac{1}{T}\dfrac{\partial T}{\partial t} = -\lambda^2 \\ \dfrac{D}{X}\dfrac{\partial^2 X}{\partial x^2} = -\lambda^2 \end{cases} \tag{1-16}$$

Therefore, the general solution to equation (1-16) is given as follows:

$$W(x,t) = Ae^{-\lambda^2 Dt}\left(B.\sin(\lambda.x) + C.\cos(\lambda.x)\right) \tag{1-17}$$

For a finite domain, the initial and boundary conditions can be given as follows:

$$\begin{cases} t = 0, \quad \forall x, \quad W = W_0 \\ t > 0, \quad x = 0, x = l, \quad W = 0 \end{cases} \tag{1-18}$$

Equation (1-18) leads to the exact solution of (1-12) as follows:

$$W(x,t) = \sum_{n=1}^{\infty} A_n \sin(\lambda_n.x) e^{-\lambda^2 Dt}, \quad \lambda_n = \frac{n\pi}{l} \tag{1-19}$$

Equation (1-19) represents the solution to the equation for a finite medium with an initial water content of nonnull.

2.4.2 Semi-infinite medium

The configuration of a semi-infinite medium supposes the following initial and boundary conditions:

$$\begin{cases} t = 0, \quad \forall x, \quad W = 0 \\ t > 0, \quad x = 0, \quad W = W_0 \end{cases} \tag{1-20}$$

The resolution of equation (1-12) with semi-infinite boundary conditions leads to the use of the Laplace transform to remove the time variable. The Laplace transform is a mathematical tool aimed at resolving differential equations in several physical problems, such as heat transfer and mass transfer. The Laplace transform is defined as follows:

$$\phi(p) = \int_0^{\infty} f(t) e^{-pt} dt \tag{1-21}$$

where $\phi(p)$ is the function in Laplace space and $f(t)$ is the function in time domain. The applications of Laplace transforms to equation (1-11) gives:

$$\int_0^{\infty} \frac{\partial W}{\partial t} e^{-pt} dt = D \int_0^{\infty} \frac{\partial^2 W}{\partial x^2} e^{-pt} dt \tag{1-22}$$

The left-hand side of the equation can be calculated by integral by parts, while the right-hand side directly gives the relation between the Laplace transform of the space-derived function and the function itself in the Laplace domain. Thereby, equation (1-22) can be written in the Laplace domain as follows:

$$p\phi(p) = D\frac{\partial^2\phi(p)}{\partial x^2} \tag{1-23}$$

The Laplace transform allows for reducing the partial differential equation to an ordinary differential equation. The Laplace transform is also applied to the boundary conditions equation represented by equation (1-20); thus:

$$\forall p, \quad x = 0, \quad \phi(p) = \frac{W_1}{p} \tag{1-24}$$

The inverse Laplace transform table in [17, 18] allows for obtaining the solution in time domain and satisfying equation (1-12); thus:

$$W = W_1\left(1 - erf\left(\frac{x}{2\sqrt{Dt}}\right)\right) \tag{1-25}$$

Therefore, equation (1-25) represents the exact solution of equation (1-12), satisfying the initial and boundary conditions. The change in boundary conditions (equation 1-20) obtained by fixing a nonnull initial plant water content induces a change to the solution as follows:

$$\frac{W - W_1}{W_0 - W_1} = erf\left(\frac{x}{2\sqrt{Dt}}\right) \tag{1-26}$$

where W_0 is the initial water content and W_1 is the water content at $x = 0$. The special case of equation (1-26) obtained by making the initial water content $W_0 = 0$, provides the solution represented in equation (1-25).

Moreover, once the water content has been calculated, the incoming flux at each instant for the case of zero water content, $W_l\big|_{x=0} = 0$, can be estimated as follows:

$$\varphi(t) = D\frac{\partial W}{\partial x}\bigg|_{x=0} = W_0\sqrt{\frac{D}{\pi}}\frac{1}{\sqrt{t}} \tag{1-27}$$

However, at time t, the diffusion into the material can be estimated by integrating equation (1-27) over time; thus:

$$\zeta = \int_0^t \phi(u)du = 2W_1\sqrt{\frac{D}{\pi}}\sqrt{t} \tag{1-28}$$

Equation (1-28) represents the amount of diffusion through a semi-infinite and initially dry (zero water content) medium during time *t*. Many other cases of time-dependent water content at the boundary are detailed in [17].

2.4.3 Semi-infinite medium with vapor flux at the boundary

This configuration can be found when a vapor flux passes over the surface of a porous medium. The water content flux will be incoming or outgoing depending on the difference in water content (or partial vapor pressure) between the sample surface and the external environment. Similar to heat transfer on surfaces based on Newton's law, the rate of exchange can be supposed as proportional to the difference between the water contents of the air and sample surface. Thereby:

$$-D\left.\frac{\partial W}{\partial x}\right|_{x=0} = H_h\left(W_{eq} - W_s\right) \tag{1-29}$$

where H_h is the hydric convection coefficient in ($m.s^{-1}$), W_{eq} is the water content at the equilibrium of exchange, and W_s in ($kg.kg^{-1}$) is the water content at the surface of the material in ($kg.kg^{-1}$). The water content equation satisfying this configuration is given in [17] as follows:

$$\frac{W - W_0}{W_{eq} - W_0} = 1 - erf\left(\frac{x}{2\sqrt{Dt}}\right) - e^{\left(\frac{H_h}{D}x + \left(\frac{H_h}{D}\right)^2 Dt\right)}\left(1 - erf\left(\frac{x}{2\sqrt{Dt}} + \frac{H_h}{D}\sqrt{Dt}\right)\right) \tag{1-30}$$

Equation (1-30) takes into account the effect of convection exchange on the diffusion process through several coupled terms. The total amount of diffusion can be calculated as follows:

$$\zeta = D\int_0^t \left.\frac{\partial W}{\partial x}\right|_{x=0} du = \frac{D\left(W_{eq} - W_0\right)}{H_h}\left[e^{\left(\frac{H_h}{D}\right)^2 Dt}\left(1 - erf\left(\frac{H_h}{D}\sqrt{Dt}\right)\right) - 1 + \frac{2}{\sqrt{\pi}}\frac{H_h}{D}\sqrt{Dt}\right] \tag{1-31}$$

ζ is the total amount of diffusion during time *t* given in ($m.s^{-1}kg_{water}.kg_{dry}^{-1}$). Figure 1-4 shows equation (1-30) as a function of the parameter $\frac{x}{2\sqrt{Dt}}$ for different values of $\frac{H_h}{D}\sqrt{Dt}$ for a semi-infinite medium.

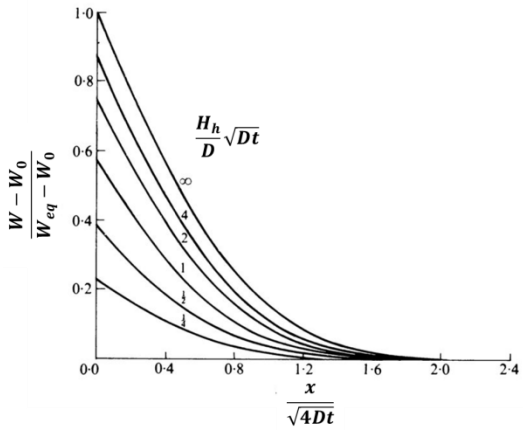

Figure 1-4: Normalized water content for the evaporation boundary condition in a semi-infinite medium [17]

There are many other configurations detailed in [17] covering diffusion in a finite, semi-infinite or infinite medium; constant or moving boundary conditions; zero or initial conditions; constant or concentration-dependent diffusion; Fickian or Non-Fickian behavior; with or without chemical reaction, etc.

2.4.4 Numerical models of mass transfer with the finite difference solution (explicit scheme)

Analytical methods for diffusion problems are mostly developed for simple geometries and/or quite simple initial and boundary conditions. In practice, satisfying realistic boundary conditions represents a technical issue. Moreover, the complexity of transfer phenomena, such as the nonlinearity of a diffusion coefficient or non-Fickian behavior, does not allow the use of analytical models. In that case, numerical methods that can be performed using a space and time grid discretization are used. Numerical methods have become increasingly more effective, particularly in the singularity zones of the phenomenon. Due to the presence of high-performance computers, numerical methods have been widely developed in terms of resolution, schemes, stability, consistence and convergence of solution. Currently, numerical methods can be used not only to validate experiments but also to predict the behavior of a physical phenomenon during experiments or estimate parameters by inverse methods such as the minimization of experimental data with numerical simulations.

The second Fick law, represented by equation (1-12), can be numerically solved using different methods such as finite element or finite difference. The central finite difference method with the explicit scheme is used in section 2 in chapter 4. The Taylor series of the time and space bases gives:

$$W_{i,j+1} = W_{i,j} + \delta t\left(\frac{\partial W}{\partial t}\right)_{i,j} + 0\left(\delta t\right)$$

$$W_{i+1,j} = W_{i,j} + \delta x\left(\frac{\partial W}{\partial x}\right)_{i,j} + \frac{1}{2}\left(\delta x\right)^2\left(\frac{\partial^2 W}{\partial x^2}\right) + 0\left(\delta x^2\right) \tag{1-32}$$

$$W_{i-1,j} = W_{i,j} - \delta x\left(\frac{\partial W}{\partial x}\right)_{i,j} + \frac{1}{2}\left(\delta x\right)^2\left(\frac{\partial^2 W}{\partial x^2}\right) + 0\left(\delta x^2\right)$$

Therefore, equation (1-12) can be represented numerically with a space-time grid by replacing (1-32) in (1-12) and neglecting the error terms in time and space bases as follows:

$$\frac{W_{i,j+1} - W_{i,j}}{\partial t} = D\frac{W_{i+1,j} - 2W_{i,j} + W_{i-1,j}}{\delta x^2} \tag{1-33}$$

The discretized equation (1-33) is mapped in a space-time grid, where the columns represent the time steps (t) and the rows represent the space steps (x). The error due to minimization between the theoretical solution or experimental data and the numerical calculation tends to zero with the increase in time steps. The calculation of the present-instant water content value can be calculated from equation (1-33) as follows:

$$W_{i,j+1} = W_{i,j} + \frac{D\partial t}{\delta x^2}\left(W_{i+1,j} - 2W_{i,j} + W_{i-1,j}\right) \tag{1-34}$$

The dimensionless number $\frac{D\partial t}{\delta x^2}$ is a parameter that represents the ratio between the physical and numerical diffusivities, $\frac{D}{\left(\frac{\delta x^2}{\partial t}\right)}$. The scheme is consistent if the numerical diffusivity is larger than the physical one in order to be able to numerically follow the phenomenon. The condition means that this ratio has to be smaller than unity. A parametric study of this coefficient is shown in [17].

3 Existing water content measurement techniques

Understanding the transfer phenomena of one or more fluid phases in wood needs the use of techniques that allow the space-time monitoring of the saturation profiles at the local scale. The conventional techniques of monitoring humidity movement during the drying or imbibition process only allow access to global information such as the global mass diffusion coefficient and the global water content loses or gains with time (sorption curves). Such conventional techniques do not permit visualization of the geometric and structure effect on humidity movement inside a porous medium (anisotropy and the alternation of rings), such as timber.

Several nondestructive techniques have been used in the literature to evaluate heat and mass transport within porous materials, such as wood. These methods can aim for qualitative applications, such as the detection of defects in wood, or quantitative applications that focus on heat and mass transfers within the material, which will enhance, for example, wood processing or plaster boosting [16]. Nondestructive techniques can provide local scans using a monodetector, partial scans using a line detector or full-field scans using a camera. Images or *2D* signals representing the state of a material (complete or defective, dry or wet) can be obtained by a raster scan or snapshot, depending on the detector used. Imaging techniques using a line detector or a matrix of detectors (cameras, for example) allow for obtaining a continuous monitoring of phenomena in a transient case.

In the literature, several techniques have been used in the context of nondestructive testing or water content monitoring. These techniques can be classified as nuclear radiation methods (such as neutron imaging) or electromagnetic radiation methods (such as *X*-rays, gamma-rays, infrared waves, and terahertz waves). Noninvasive techniques can also be classified by the danger that they can represent to the operators depending on the wavelength range. The waves can be ionizing radiation, such as gamma-rays or *X*-rays, or nonionizing radiation, such as infrared or *THz* radiation. The existing techniques are classified according to [16] depending on the use of mechanical, sonic, chemical or radiative methods. The different techniques are summarized in Figure 1-5.

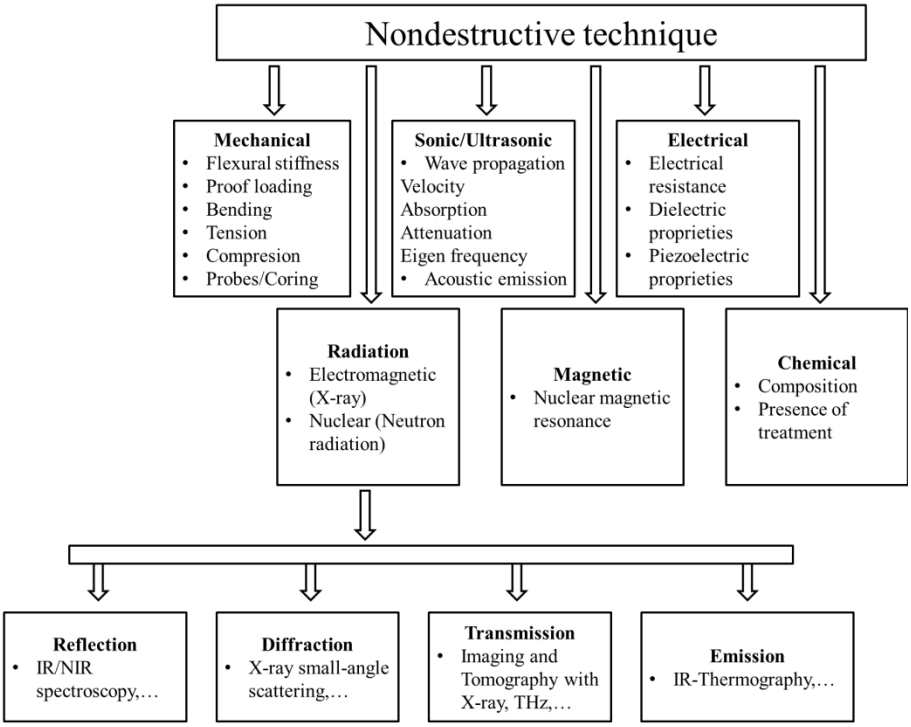

Figure 1-5: Classification of *NDT* methods for wood along with the testing methods [16].

Due to the opacity feature of water in its different forms (vapor or liquid) to noninvasive techniques, the employed radiative and magnetic techniques permit detection of the liquid within porous media because of the signal attenuation when crossing the water. The use of such imaging technique implies modeling the material as a biphasic material composed of a dry solid layer and an effective water layer (further detailed in section 4). In the next paragraphs, the most used techniques for water content monitoring are briefly presented.

3.1 *X*-Ray techniques

X-ray or Röngten radiation [9] consists of electromagnetic waves with wavelengths ranging from 10^{-3} *nm* to 10 *nm*, corresponding to frequencies in the range of 3.10^{16} *Hz* to 3.10^{19} *Hz* and to energies ranging from 100 *eV* to 100 *keV*. *X*-rays are situated between UV rays and gamma rays. *X*-ray radiation can be deemed hard *X*-rays or soft *X*-rays, depending on the photon energy (5 to 10 *keV* for hard *X*-rays). Due to its penetrating ability, hard *X*-rays are widely used in medical radiography, airport security and material characterization. Soft *X*-rays, which can be absorbed by a water layer of 1 μm, are used for monitoring the water content in porous and biomass materials.

Such an *X*-ray technique was used in [19] to visualize the effect of heterogeneous porosity on the diffusivity of vapor inside rock slabs. The authors estimated the relative concentration from the grayscale data as follows:

$$\frac{C}{C_0} = \frac{\ln(I)_{i,j} - \ln(I_d)_{i,j}}{\ln(I_s)_{i,j} - \ln(I_d)_{i,j}} \tag{1-35}$$

where C is the concentration, C_0 is the inlet tracer concentration, I is the transmitted light intensity of a pixel located at coordinates i, j, and I_s is the transmitted light intensity at the same point for the fully saturated tracer condition (C/C_0=1). On the other hand, the porosity field at each pixel is taken into account, and it is determined as follows:

$$\phi_{i,j} = \frac{\ln(I_s)_{i,j} - \ln(I_d)_{i,j}}{E\left(\ln(I_s)_{i,j} - \ln(I_d)_{i,j}\right)} \bar{\phi} \frac{z_{i,j}}{z_{avg}} \tag{1-36}$$

$E(\ln(I_s)_{i,j}\text{-}\ln(I_s)_{i,j})$ is the average difference between the saturated tracer and tracerless images, $\bar{\phi}$ is the bulk porosity of the rock slab measured by gravimetric means, z_{avg} is the average thickness of the rock slab, and $z_{i,j}$ is the rock slab at each pixel estimated from measurements. Thereafter, the normalized cumulative mass is compared to the analytical model corresponding to the same boundary conditions given in [19] as follows:

$$\frac{M_t}{M_\infty} = 1 - \sum_{n=0}^{\infty} \frac{8}{(2n+1)^2 \pi^2} \exp\left[\frac{-D(2n+1)^2 \pi^2 t}{4l^2}\right] \tag{1-37}$$

M_t is the cumulative mass of tracer diffused into the porous medium at time t, $\underline{M_\infty}$ is the same quantity at $t = \infty$, D is the diffusion coefficient, l is the slab length, and n the iteration step.

The diffusion coefficient can be calculated through the following relation [19]:

$$D = \frac{0.196 l^2}{t_{0.5}} \tag{1-38}$$

where $t_{0.5}$ is the time at which $\frac{M_t}{M_\infty}$ = 0.5. The error caused by the truncation is reported to be approximately 0.001 %

The microfocus *X*-ray technique allows for the instant and accurate determination of the two-dimensional transient water content uptake in porous materials, such as brick and ceramic, unlike methods such as γ-ray and nuclear magnetic resonance techniques [20]. The authors used the microfocus *X*-ray projection to obtain a quantitative water content map at a given instant. The water content measured at time steps starting from the dry state is quantified as follows:

$$W = -\frac{\rho_w}{\mu_w.e}\left(\ln\left(I_{wet}\right) - \ln\left(I_{dry}\right)\right) \quad (1\text{-}39)$$

where W is the water content ($kg.m^{-3}$), I_{wet} and I_{dry} are the transmitted X-ray intensities of wet and dry states, ρ_w is the density of liquid water ($kg.m^{-3}$), and μ_w is attenuation coefficient (m^{-1}).

Moreover, X-ray computed tomography has been used in [21] to verify the linear relationship between the computed tomography number and the density, thereby, forecasting heartwood and sapwood densities. The same relationship has been proven for the computed tomography number and water content.

X-rays have been used in [22] to determine the influence of the microstructure of wood and the direction of the grain on the pattern and rate of the water content distribution. The images showed an uptake of liquid water content through the longitudinal direction that is twice the amount of water absorbed in the radial direction. The amount in the tangential direction is 50 % higher than that in the radial direction. In the longitudinal direction, the water content is absorbed preferentially by the latewood, which can be explained by the smaller diameter of the tracheid and the presence of pits along the latewood. In the tangential direction, the distribution of water is more uniform but slower. The uptake is slowest in the radial direction due to the latewood ring positions, which play the role of barriers. Figure 1-6 shows the uptake of liquid water in the three directions of wood.

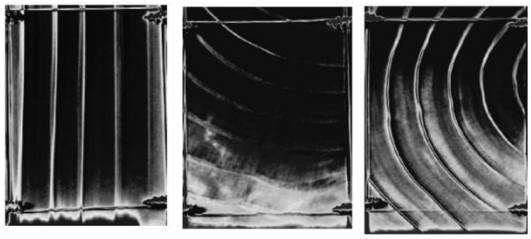

Figure 1-6: Uptake of water in the longitudinal, radial and tangential directions of wood spruce using the X-ray technique [22].

The liquid water sorption in the longitudinal direction of wood using a computed tomography X-ray technique was also studied in [23], and the effects of the vertical position in the tree, the growing site (dry or wet) and the type of tree have been investigated. It has been shown that the heartwood of spruce absorbs less water than the sapwood. In the same context, the measurements of liquid water and water vapor uptakes in wood were carried out using this technique to verify the multiscale approach [13].

3.2 Magnetic resonance imaging (*MRI*)

Magnetic resonance imaging (*MRI*) is an imaging technique used in medical applications. *MRI* uses strong magnetic fields, electric-field gradients and radio waves to generate images of organs in the body. This technique does not involve ionizing radiation and thus represents a safe imaging method. *MRI* is considered a medical application of the nuclear magnetic resonance (*NMR*) technique. The *NMR* principle can be applied as an imaging technique or in other techniques, such as *NMR* spectroscopy. *NMR* is a phenomenon in which nuclei in a magnetic field absorb and re-emit electromagnetic radiation. Its frequency range is similar to that of the very high frequency (*VHF*) and ultrahigh frequency (*UHF*), mostly from 60 *MHz* to 1000 *MHz*. The *NMR* technique was applied in [24] to record the water-content spatial distribution along the different directions of wood. The numerical simulations based on a multi-Fickian model showed to be in agreement with the experiments conducted on a Norway spruce sample. Figure 1-7 shows the experimental and numerical results given in [24].

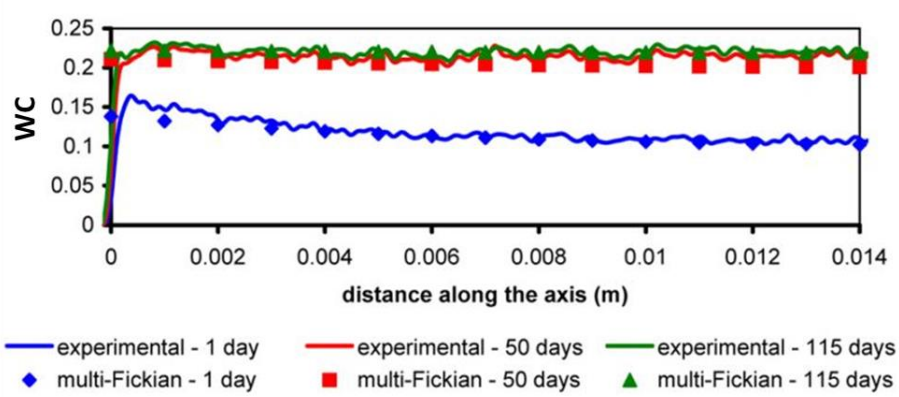

Figure 1-7: Experimental and numerical *WC* values (tangential uncoated case) along the axis of the specimen and starting from the surface in contact with air obtained using *MRI*, with wetting at an *RH* from 65 % to 94 % [24].

The authors in [25] reported the first use of *NMR* to monitor the dynamics of the water content distribution in several porous inorganic materials. This method was shown to be effective for the measurement of the water content profile, which allows the determination of water diffusivity within building materials, such as bricks or mortar [26].

As mentioned above, *MRI* does not expose the body to any radiation, but discomfort associated with *MRI* scans can occur. Compared with computed tomography (*CT*) scans, *MRI* scans are typically louder, take a longer time and usually need the subject to enter a narrow, confining tube. For research applications, the presence of metallic inclusions is not allowed in the *MRI* technique.

Moreover, the *MRI* technique or proton magnetic resonance (^{1}H *MRI*) has been used to visualize the spatial change in the moisture content of wood [27]. The authors used this method to

investigate the interaction between indoor air and Scots pine in the context of building comfort. The method showed a capability to provide accurate information about the wood/water interaction below the *FSP*. An *MRI* technique called single-point ramped imaging with T enhancement (*SPRITE*) was shown to be effective in measuring water concentration at low moisture contents, as compared to conventional two-dimensional spin-echo *MRI* methods, and allowed for the obtaining of high-quality images [28]. Moreover, the *MRI* technique showed the capability to measure the water transport at the interface and to analyze the wood adhesive and wood coating.

The conical-SPRITE *MRI* technique [29] combined with the decay of magnetization due to diffusion in the internal field (*DDIF*) has been shown to be an effective tool to investigate the pore geometry, distribution and connectivity of sandstone and to measure the water-filled pore size distribution in partially saturated porous media [30].

3.3 Gamma-ray technique (γ-ray)

Gamma-rays represent radiation with wavelengths less than 10 pm (10^{-11} *m*), which is less than the diameter of an atom and therefore is situated at a frequency range above 10 exahertz (10^{19} *Hz*). The energy of these waves is typically high, above 100 *keV*. This radiation commonly has an energy of a few hundred *keV* but is almost always less than 10 *MeV*.

The gamma-ray technique is considered to be among the first noninvasive methods used in measurement of water content in porous materials. Gamma waves are ionizing waves and require high precaution during experiments due to the danger that they represent to operators. Due to the advantage of this method being independent of the temperature gradient within a material, the author in [31] has utilized the gamma-ray-attenuation method to check the homogeneity of samples and to measure the water content. The attenuation of mono-energetic gamma radiation for a fixed source-detector distance is given as follows:

$$\ln(I) = \ln(I_0) - (\mu\rho x)_c - (\mu\rho x)_w - (\mu\rho x)_g - (\mu\rho x)_a \tag{1-40}$$

where I and I_0 are the intensities with and without the absorbing material, μ is the mass absorption coefficient ($cm^2.g^{-1}$), ρ is the density of the material ($g.cm^{-3}$) and x is the thickness of material (*cm*); the indices *c*, *w*, *g* and *a* represent concrete, water, glue and acryl. The intensity variations can be calculated by:

$$\psi = \frac{\ln(I_0) - \ln(I)}{\mu.x.\rho} \tag{1-41}$$

where ψ is the water content ($cm^3.cm\text{-}^3$). The gamma-ray technique showed a capability for determining the water content distribution with good accuracy.

The gamma-ray method was used in [32] to determine the distribution profile of water content in a glass fiber block being dried. The Beer-Lambert-based linear behavior between the absorbance and crossed distance and between the absorption coefficient and mass attenuation coefficient is verified. Furthermore, the gamma-ray estimation of the ratio of the densities of two samples prepared from sand is in agreement gravimetric measurements. However, at very low water contents, this method may not be suitable. The author in [33] investigated the use of gamma rays to measure the density and water content of soil. The density of soil is written as a function of the measured intensity as follows:

$$\rho_s = \frac{1}{\left(\mu_s + \mu_w.W_{ad}\right)x_s}\ln\left(\frac{I_{ec}}{I_{ds}}\right) \tag{1-42}$$

where ρ_s is the density of soil ($kg.m^{-3}$), μ is the absorption coefficient (m^{-1}), W is the water content ($kg.kg^{-1}$), x is the distance (m) and I is the beam intensity. The indices s, w, ad, ec and ds represent respectively the solid, water content, air-dry, empty soil container and dry soil. Therefore, obtaining the bulk density required knowledge of the attenuation coefficients of the solid and water content in dry air. Equation (1-42) shows that the variation in density can be indicated only by the magnitude of $\ln\left(\frac{I_{ec}}{I_{ds}}\right)$, as $\frac{1}{\left(\mu_s + \mu_w.W_{ad}\right)x_s}$ is constant. The water content within a moist soil is determined by the gamma-ray method as follows:

$$W - W_{ad} = \frac{1}{\mu_w \rho_s x_s}\ln\left(\frac{I_{ds}}{I_{ms}}\right) \tag{1-43}$$

where W and W_{ad} are the water contents in moist soil and dry-air soil and I_{ds} and I_{ms} are the intensities of dry soil and moist soil. A similar indication can be given by equation (1-43), allowing an estimation of the water content by the magnitude of $\ln\left(\frac{I_{ds}}{I_{ms}}\right)$, as $\frac{1}{\mu_w \rho_s x_s}$ is constant.

3.4 Scanning electron microscopy (*SEM*)

Scanning electron microscopy (*SEM*) consists of scanning a sample by focusing an electron beam at the surface. The electrons interact with the sample atoms producing information about the sample surface and composition. *SEM* can achieve a resolution better than 1 nanometer and is able to scan specimens under different environmental conditions, such as samples in vacuum or wet samples, by a raster-scan pattern.

SEM was used in [34] to document the movement of a viscous liquid in vacuum-impregnated pine and spruce. The microscope allowed for the observation of the liquid flow being enabled through disrupted pinoid pit membranes in pine sapwood. It has been shown that the heartwood is

less permeable due to the deposits of high-molecular-weight substances on the cell wall. However, for spruce, the thick ray cells with small pits highly reduce the permeability.

3.5 Neutron imaging technique (*NI*)

Recently, researchers used neutron imaging (*NI*), which is an advanced technique based on the neutron attenuation properties of the imaged object. This technique can be used in some applications where the object is invisible or hardly visible to *X*-rays. As mentioned above (section 3.1), *X*-rays are attenuated by the density of a sample, but *NI* does not appear to depend on density. Some light materials can absorb neutrons (boron), while others can scatter neutrons (hydrogen) or be crossed by neutrons (metals).

NI was shown to be effective for monitoring water movement during drying. The high sensitivity of neutrons to hydrogen atoms makes this technique suitable for the accurate determination of the water content in wood. The liquid water transport in softwood was visualized using *NI* in [35].

The results showed that liquid water uptake is more significant in latewood than it is in earlywood in the longitudinal direction. This observation is explained by the size of the cell lumens of the tracheid. In tangential and radial directions, the uptake is less than that that in the longitudinal direction. In the tangential direction, the preferential pathway of the water content is initially the latewood, and then, the content undergoes a redistribution to earlywood due to the inclined growth rings. However, along the radial direction, the growth rings behave like barriers and slow the uptake. In [35], the authors measured a significant uptake rate of water content in initially moist samples relative to that of the initially dry sample. The model, based on the Beer-Lambert law, allows expression of the water content in a volume basis ($kg.m^{-3}$) as follows:

$$W(t) = -\frac{\rho_w}{z.\mu_w} \ln\left(\frac{I(t)}{I(t_{initial})}\right) \tag{1-44}$$

where W is the water content ($kg.m^{-3}$), ρ is the density of water ($kg.m^{-3}$), z is the thickness of the sample, μ is the absorption coefficient and the index w is the effective water layer (m). The method was validated by calculating the difference between the measured and *NI*-calculated water contents, was found to be approximately 6 %. The distribution of the water content in a fir sample along different directions obtained using the *NI* technique is shown in Figure 1-8.

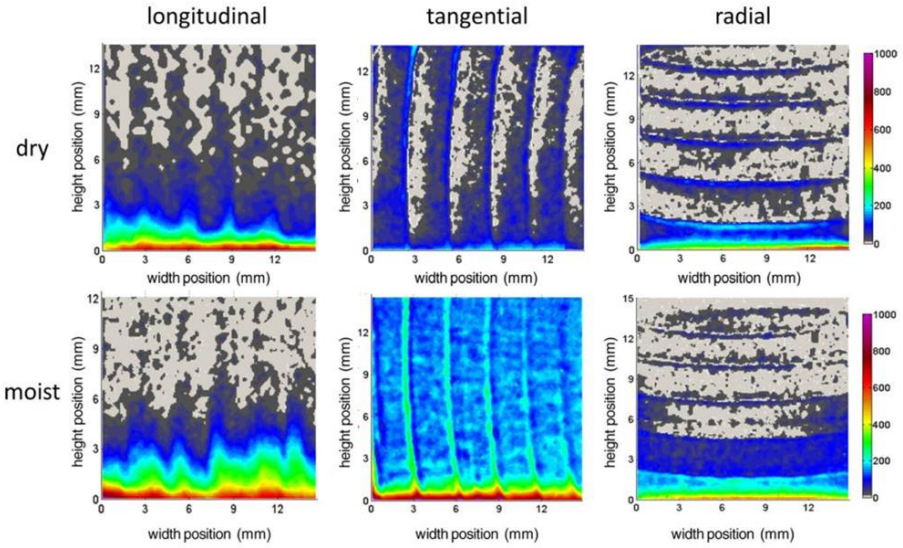

Figure 1-8: The distribution of water content in a fir sample along the L-direction, T-direction and R-direction at *t = 60 min*, *t = 43 min* and *t = 145 min*, respectively [35].

In the same context, *NI* showed a capability for monitoring the water content gradient during steep drying [36]. The wet wood samples were insulated and then heated on the side (bottom) through a metallic foil. Finally, the *NI* images were taken, and the temperature at different heights from the heat source was measured. The water content rate along the longitudinal direction increased faster than that in the radial and tangential directions due to the higher permeability to water vapor through the lumens and vessels. This result confirms the results found in the precedent work mentioned above, but for the situation of drying. In the paper [36], the authors showed the contribution of the high temperature on the displacement of the water content front. The vapor flow rate is given by the following expression:

$$g_v = -\left(D.P_{v,sat}\left(T\right)\right)\nabla\phi - \left(D\phi\frac{\partial P_{v,sat}\left(T\right)}{\partial T}\right)\nabla T \tag{1-45}$$

where g_v is the vapor flow rate ($m^2.s^{-1}$), D is the vapor diffusion coefficient ($m^2.s^{-1}$), ϕ is the relative humidity, and T is the temperature (K). The *NI* showed that below the 100 °*C*, the water content accumulates then decreases with the increase in temperature, which allows visualization of the moving water content front. This behavior was used in [37] to check a thermo-hygro-mechanical model for wood. The use of a poro-mechanical model coupled with the mesoscale features of growth rings allowed for the validation of *NI* as a measurement tool for water content.

A similar study was conducted in [38] to visualize the migration of water content in gypsum plaster with and without fibers by the *NI* technique. The formation of an accumulated water content zone ahead of the advancing front was discussed.

3.6 Summary of existing techniques

In summary, the use of existing techniques can be, on the one hand, dangerous, such as *X*-rays and gamma-rays, or on the other, very expensive, such as *NI*. Moreover, some of these techniques seem to be too difficult to be implemented in industry (production line), such as *MRI*, *NMR* and *SEM*. The monitoring of product quality is crucial, especially for important porous products, such as wood. This requires special precautions in terms of monitoring the manufacturing and transformation processes. Table 1-2 summarizes the mentioned techniques with their main characteristics.

Technique	*X*-ray	Gamma-ray	*MRI*	*SEM*	*NI*
Principle	Electromagnetic radiation	Electromagnetic radiation	Nuclear radiation	-	Nuclear radiation
Hazard	Ionizing (3.10^{16} -3.10^{19}) *Hz*	Ionizing ($>10^{19}$) *Hz*	No radiation (60-1000) *MHz*	-	-
Cost	Expensive	Expensive	Expensive	Expensive	Very expensive
Industry implementation	Rarely implemented in industry but not online	Research applications	Rarely implemented in industry	Rarely implemented in industry but not online	Research applications
Others	• Long exposure time • Limited examination of small samples • Low sensitivity to hydrogen (water)	• Independent of temperature within sample	• Sample not exposed to radiation • No metallic inclusions • Confining and opaque space • Common equipment	• Visualization and no control or monitoring • Common equipment • Sample preparation	• High sensitivity to hydrogen • Passage through metals • Few specialized facilities available

Table 1-2: Comparison between existing techniques for water monitoring

To remedy the metrology deficiencies, a method for the local-scale monitoring of water content within a porous medium using a benign, low-cost and implementable technique is indispensable. The terahertz (*THz*) technique has been carried out in this study. Terahertz technology represents a technique that combines low cost, safety, and ease of implementation in industry with multifunctionality (*NDT*, the monitoring of water content, security, control of quality, etc.). It allows the online mapping of the humidity spread within porous media with an

acceptable resolution. The next section briefly shows the use of this technique in different applications, as reported in the literature.

4 Exploration of terahertz (*THz*) techniques

THz radiation comprises electromagnetic nonionizing waves located between the infrared and microwaves (30–3000 μm). *THz* radiation is characterized by its ease of use, relatively low cost and safety because of its nonionizing wavelength scale. The *THz* source can be a Gunn diode made from microwaves or from a femtosecond laser, as in terahertz time-domain spectroscopy (*THz-TDS*). *THz* radiation can penetrate insulating materials (for a few centimeters) but is reflected by metals and absorbed by water. These properties make *THz* technology an effective tool for security applications. The several applications of reflection- and transmission-mode *THz* include security, medical applications, the paper industry, the polymer industry, the wood and *WPC* industry, food quality (i.e., dried food, wheat grain, damaged fruit, and metallic contamination in food products), packaging quality, breeding and plants and art preservation [39, 40 and 41] and are briefly presented in the next paragraphs.

4.1 Security applications

The transmittance of *THz* radiation through most nonmetallic and nonpolar media enables *THz* techniques to detect metallic objects concealed inside cardboard packages, clothes, shoes and bags. *THz* technology has shown a capability to detect explosives, chemical weapons, flammables and drugs through the signatures of these materials in the terahertz wavelength range [42, 43]. Figure 1-9 shows the absorption coefficient spectra of several prohibited materials that can be used as fingerprints or references to detect such materials.

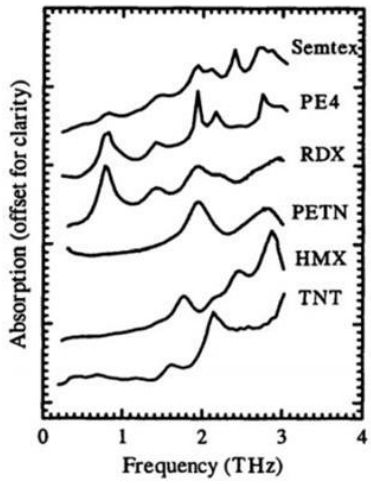

Figure 1-9: Absorption coefficient spectra of Semtex, *PE4*, *RDX*, *PETN*, *HMX*, and *TNT* at *THz* frequencies [42].

4.2 Nondestructive Testing (*NDT*)

THz wave imaging has been used for nondestructive testing (*NDT*) in several industrial settings, such as the aerospace and aeronautics composite material inspection [44] and petroleum industries. *THz* imaging based on reflection images is used to examine the external tank of the space shuttle, which is insulated by sprayed foam. On the other hand, the method allows not only the identification of delamination and water intrusion in composite materials but also the detection of corrosion on insulated pipes subjected to severe atmospheric conditions [43]. This technique allows economic preventive maintenance of pipelines in the petroleum industry. In this context, *THz-TDS* was tested as a tool for the nondestructive testing for some materials used in the aerospace industry [45]. The technique showed a capability to detect defects due to the sensitivity of the phase shift and time delay to the thickness.

4.3 Medical applications

In medical applications, *THz* radiation is used to image skin cancer and thermal damage to skin. The difference in hydration levels between normal and cancerous cells, between normal and thermally damaged cells [46] and between dry and hydrated corneas [47] can be identified through the image contrast. In this domain, the *THz* reflective mode is used rather than the transmission mode due to the high sensitivity of reflectivity to the hydration. It should be indicated that there are trade-offs in maximizing the reflectance gradient at low frequency, minimizing the scattering at low frequency and increasing the spatial resolution at high frequency [39].

4.4 Applications in the paper industry

In the paper industry, the drying process has a strong impact on the final paper quality [48]. It has been shown that both the *THz-TDS* amplitude and phase allow accurate quantification of the water content in paper. The water content influences the mechanical properties of paper (swelling and shrinkage), and thereby, it should be homogeneous to avoid all kinds of tearing (wet zones) and breaking (dry zones). The combination of fibers and absorbed water can be considered an effective medium due to the size of cellulose fibers being smaller than the *THz* wavelength. The *THz* measurement uses a linear combination of attenuation coefficients for dry paper and water to model the effective medium. The measurement of *THz* attenuation and phase and the complex permittivity of the wet paper in combination with an effective medium model leads to the identification of the water content in paper.

4.5 Applications in the polymer and polymer-wood-composite (*PWC*) industries

THz-TDS has been used to measure the elasticity of polymers during their fabrication. The *THz* method proved to be an effective tool in the detection of the glass transition temperature in amorphous and semicrystalline polymers using the refractive index function of temperature at the *THz* wavelength range [40]. The change in refractive index is related to the change in density.

Moreover, the *THz* method showed a capability of revealing delamination, inclusions and wide junctions.

The manufacturing of *PWC* needs to be studied in terms of the hydroscopic nature of polymers [39], as the composite can be widely affected by the water content. As the water content affects the polymer, inducing swelling and plasticization, the integrity of the composite structure can be weakened or rather damaged. Therefore, effective medium models of polymer or *PWC* have to take into account the geometric change.

The effective permittivity of polymer composites include the permittivity of the solid polymer, the permittivity of air (voids and lumens), and the permittivity of bound/free water. As polymers are not easily compressible, the measurement of only the solid phase is quite difficult. An effective medium model can consider that the porous material is the host (solid and air phase). Therefore, the optical effective refractive index of dry polymer can be calculated as a function of the volume fraction of empty space.

$$n(t) = 1 + \frac{(n(t_0) - 1)e(t_0)}{X(t)e(t)} \tag{1-46}$$

where n is the refractive index, e is the thickness, t_0 is the initial instant when the material is dry, t is a given instant when the water is absorbed by polymer, and X is the volume fraction of empty space.

A second approach considers that only the solid phase is the host material embedded with air. The calculation of the permittivity of the solid phase can be performed by estimating the volume fraction of air in the dry material. In this case, the refractive index of the wet material can be calculated using the *THz* measurement data [39] as follows:

$$T(\nu) = \frac{\left(\frac{4n}{(n+1)^2}\right) e^{i\frac{2n\pi\nu e}{c}}}{1 - \left(\frac{n-1}{n+1}\right)^2 e^{i\frac{4n\pi\nu e}{c}}} \tag{1-47}$$

where c is the speed of light, ν is the *THz* frequency, e is the thickness of the effective medium material, and n is the effective complex refractive index, which can be given by several effective medium models, such as the Maxwell-Garnett (*MG*) model:

$$\frac{\varepsilon_{eff} - \varepsilon_h}{\varepsilon_{eff} + 2\varepsilon_h} = X_p \frac{\varepsilon_p - \varepsilon_h}{\varepsilon_p + 2\varepsilon_h} \tag{1-48}$$

the Bruggeman (*BG*) model:

$$\begin{cases} \varepsilon_{eff} = \dfrac{1}{4}\left(a + \sqrt{a^2 + 8\varepsilon_h \varepsilon_p}\right) \\ a = \left(3X_h - 1\right)\varepsilon_h + \left(3X_p - 1\right)\varepsilon_p \end{cases} \tag{1-49}$$

or the Landau-Lifshitz-Looyenga (*LLL*) model:

$$\sqrt[3]{\varepsilon_{eff}} = X_h \sqrt[3]{\varepsilon_h} + X_p \sqrt[3]{\varepsilon_p} \tag{1-50}$$

where ε is the permittivity; the indices *h*, *p* and eff indicate host, particle and effective; and *X* is the volume fraction, with $X_p+X_h = 1$. On the other hand, the effective dielectric properties such as the absorption can be calculated by the linear mixture model as follows:

$$\alpha_{eff}\left(\nu\right) = X_h \alpha_h\left(\nu\right) + X_p \alpha_p\left(\nu\right) \tag{1-51}$$

where α is the absorption coefficient. This linear relation, based on the Beer-Lambert law, is often used in *THz* monitoring techniques.

Once the refractive index is calculated by the *THz* attenuation, as shown in equation (1-47), the volume fraction of water can be obtained using equations (1-46) and (1-49). The water content increases the real refractive index and the absorption coefficient of the polymer, which makes *THz* an effective probe for measuring the water content within hygroscopic plastics [38].

THz radiation has been applied to composite materials, where the sorption of water into polyamide and wood-plastic composites (*WPC*) was shown using *THz* time-domain spectroscopy [49]. The authors proved a linear correlation between the refractive index and the absorption coefficient with water gravimetric measurements using an effective permittivity based on the *LLL* model. It was shown that *THz-TDS* is able to distinguish between the bound water (water content below the *FSP*) and the free water (water content above the *FSP*). Since the vibration of bound water molecules is different from the vibration of free water molecules, the dielectric parameters are not the same. Thereby, the refractive index and absorption coefficient are predicted to be lower for bound water, as shown in Figure 1-10.

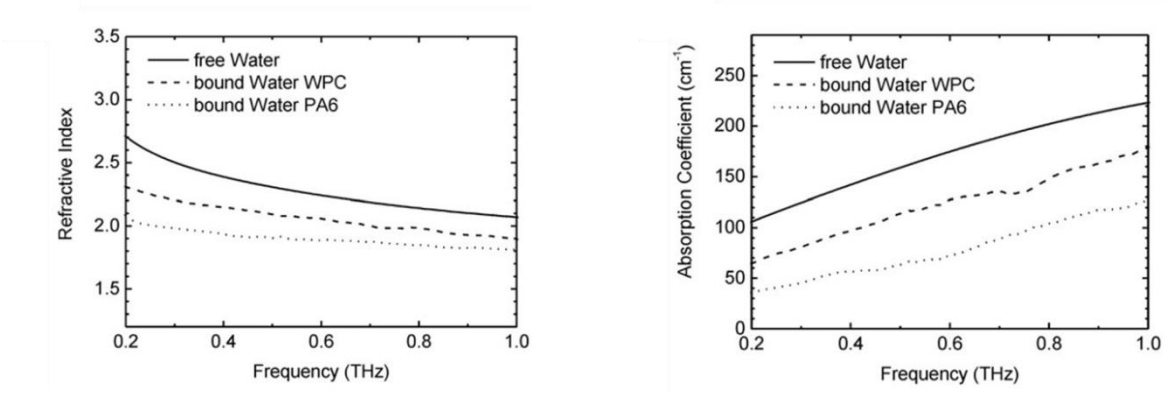

(a) (b)

Figure 1-10: Dielectric properties of free and bound water for *WPC* and *PA6*, (a) refractive index, (b) absorption coefficient [49].

Thereafter, the measured permittivity of a wet sample can be employed to determine its volumetric water content (equations 1-49 and 1-50). *THz-TDS* has also been used to investigate the dielectric parameters (refractive index and absorption coefficient) of several building materials such as wood, brick, plastic, and glass in a frequency range between 0.1 and 1 *THz* [50].

4.6 Applications in agriculture

In agriculture, more attention has been paid to efficient irrigation strategies for economic plants to counteract desertification and water shortages. In this context, *THz* radiation has been used to monitor the water content in coffee leaves [51, 52], celery leaves and cotton [53], tobacco leaves [39], and biomass [54], as well as to monitor the quality of breed [40]. This approach could be useful in evaluating the wetting state, which provides information about the critical stress of leaves, to optimize the irrigation system. In the same context, the authors in [51] employed the dielectric properties of leaves (refractive index and absorption coefficient) based on an effective medium theory model (Landau-Lifshitz-Looyenga) to determine the water content. Contrary to uncompressible polymers, the leaves can be dried out and crushed, which allows for the calculation of the volume fraction of water content.

In [51], the authors showed good agreement between the predicted and measured real refractive index using the *LLL* model. The absorbance and volumetric water content also present the same agreement but with taking into account the scattering. The results are shown in Figure 1-11.

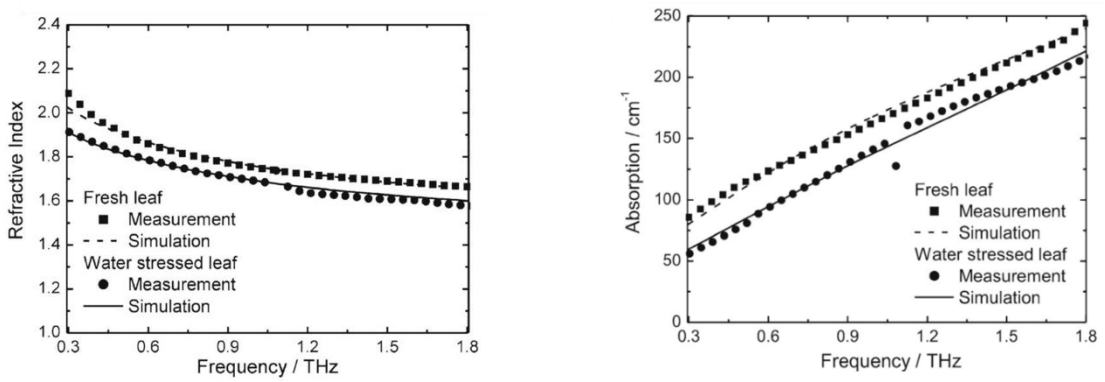

(a) (b)

Figure 1-11: (a) Refractive indices and (b) absorption coefficients of fresh and drought-stressed leaf (measurements: square and circle, line: simulation) [51].

The *THz-TDS* technique has been coupled with an iterative algorithm to calculate the volume water content in leaf tissue [55]. The transmittance was experimentally obtained by *THz* time-domain spectroscopy and was minimized with the theoretical transmittance based on the *LLL* model of the dielectric function (equation 1-50) and scattering coefficient [56]. *THz-TDS* was used in [57] to study the water content absorbed by cork for wine industry applications. The authors used a model based on equations (1-49) and equation (1-51) to determine the dielectric properties of the material in combination with the *THz* experiments on cork cells. [57] measured the diffusion of wine into a cork stopper by analyzing the influence of the cork structure on the migration of chemicals from the cork/wine interface.

THz-TDS reflection mode was shown to be a suitable tool for measuring the water status of a plant, such as grapevines, in real time [58]. The results are in agreement with that of traditional methods of water content measurement such as soil moisture sensors and *TDV* measurement with a dendrometer. Figure 1-12 shows the agreement between the classical method of measuring the water content in soil and the *THz-TDS* reflection method for wine grapes.

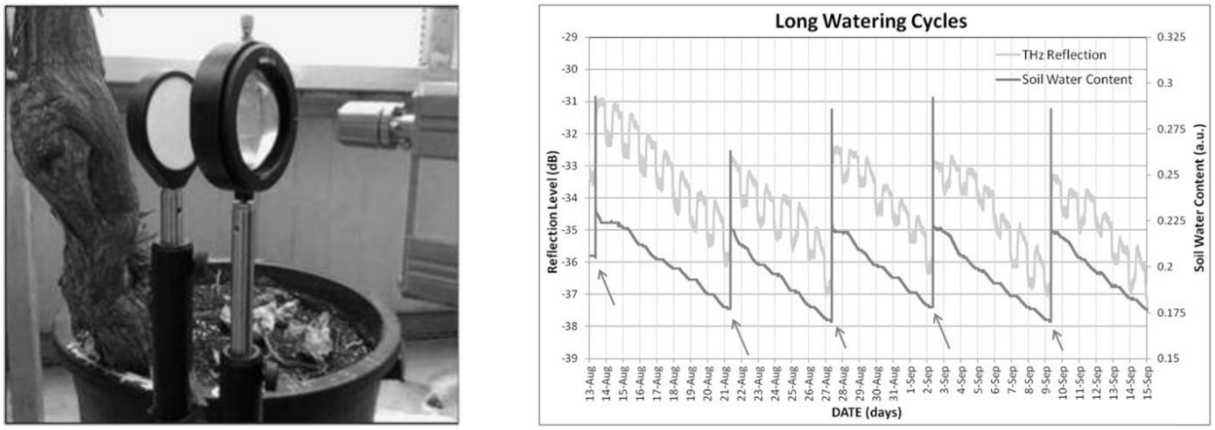

(a) (b)

Figure 1-12: (a) *THz* reflection measurement setup. (b) The evolution of soil water content and trunk *THz* reflection versus watering cycles; The arrows indicate irrigations [58].

4.7 Applications in food industry

The *THz* technique is also used to optimize food drying since the water content affects the texture, taste, bacterial growth, crispness and mechanical strength of food. A study has been conducted in [59] aiming to quantitatively measure the water content in food wafers used in the confectionary food industry. IA linear behavior between the normalized peak-to-peak amplitude of the time domain and the water content measured by a gravimetric method is noticed.

In the same context, *THz-TDS* has been applied to verify the feasibility of evaluating pecan quality through the detection of insects [60]. As the pecan (nutmeat, shell, and inner separator) is transparent in the *THz* region (0.2 – 2 *THz*), living insects are predicted to be absorptive due to their high water content. Therefore, identifying product contamination by insects feeding on the interior nutmeat was proven (Figure 12-a).

The authors in [61] used *THz-TDS* to measure the transmission of dry and wet crushed wheat (powdered) at different water contents (12 %, 14 % and 18 %). Wheat grain is usually stored at 8 - 10 % moisture content to avoid germination. Wheats are typically milled at a water content of 16.5 % by a miller via wetting the outer part of the wheat grain. A linear decrease in the *THz* signal has been remarked against the increase in water content.

The *THz* reflection mode has been used to study the damage in fruits such as tomatoes. Damage occurs when the pressure of the environment is larger than the inside pressure, which induces the filling of water into the damaged area. The reflectivity was shown to be reduced in the damaged area, which can be attributed to the high absorbance of water at this wavelength range. Figure 1-13 shows the attenuation of the *THz* signal as a function of the product humidity level.

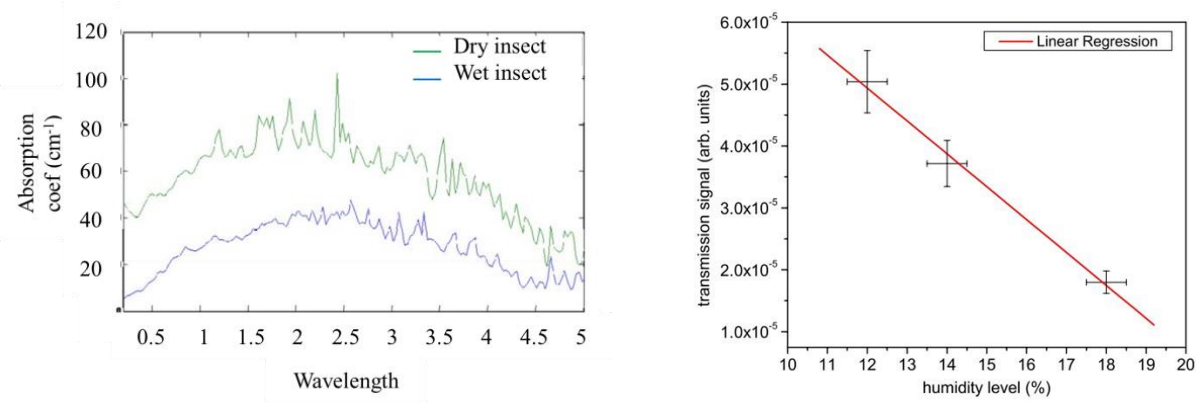

(a) (b)

Figure 1-13: (a) Spectroscopy of insects in the *THz* range [60]. (b) The transmission of wheat grain at different water contents [61].

In the food industry, contrary to techniques such as ultrasonic or *X*-ray, the *THz-TDS* scan showed a capability to detect not only metallic but also nonmetallic contamination (such as stone, plastic and glass) in food products, such as chocolate [40]. As the refractive indices of the stone and glass particles are higher than those of chocolate, the line scan showed double pulses. In [62], the authors indicated that *THz-TDS* showed no identifiable change in the shape of the pulse since the nuts have a similar refractive index to that of the chocolate. Figure 1-14 shows the different *THz-TDS* pulse scans for normal and contaminated chocolate.

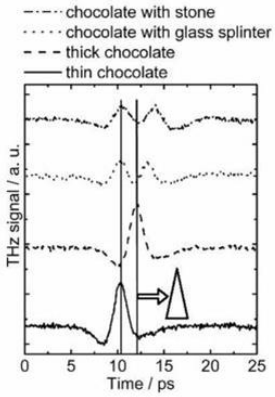

Figure 1-14: Line scans of chocolate of different thicknesses, and chocolate contaminated with stones and glass shards [62].

However, in [40], the authors indicated that using *THz* imaging based on the phase delay can clearly reveal the difference between chocolate and nuts.

The application of *THz* technology in the food industry showed that this technique can be implemented in online food production with a low cost, compact size and good signal-to-noise ratio.

4.8 Painting and art preservation

THz tomography based on reflection has been used to obtain a two-dimensional map of the painting thickness distribution for single-layer and multilayer paint films. The *THz* "paint meter" was shown to be a powerful tool for the quality control of paint films during the in-process monitoring of car body painting [63]. A linear relationship between the time delay (the time between two pulses representing the air/paint and paint/substrate boundaries) and the optical thickness was verified, which allows for the thickness determination of paint with well-known optical characteristics, as given by equation (1-52):

$$\Delta T = \frac{2n_g}{c} d \tag{1-52}$$

where ΔT is the time delay in (ps or s), n_g is the constant group refractive index, and d is the thickness of the paint film in (μm). The linear behavior is shown in Figure 1-15.

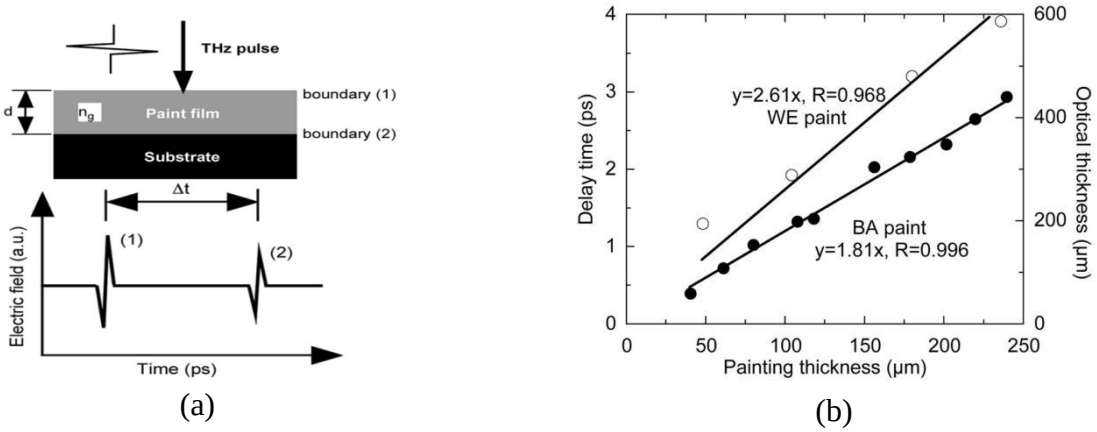

Figure 1-15: (a) *THz* paintmeter, a single-layer paint film and the temporal waveform of the *THz* pulse echo. (b) The optical thickness as a function of the paint film thickness for quick-drying black acryl (*BA*) and white enamel (*WE*) [63].

The *THz* method has also been used to monitor the drying of paint since paint shrinks due to the evaporation of solvent with time, which makes the two peaks (Figure 1-15-a) closer and higher in terms of amplitude. Thus, this method can indicate the thickness of the paint film. *THz-TDS* tomography in reflectance mode was used in [64] to obtain the internal structure (thickness and depth) of materials in a noninvasive way. In [65], the authors used transmission and reflection *THz-TDS* images as a tool to detect hidden defective areas in wooden-artworks (Russian painting icon), as shown in Figure 1-16.

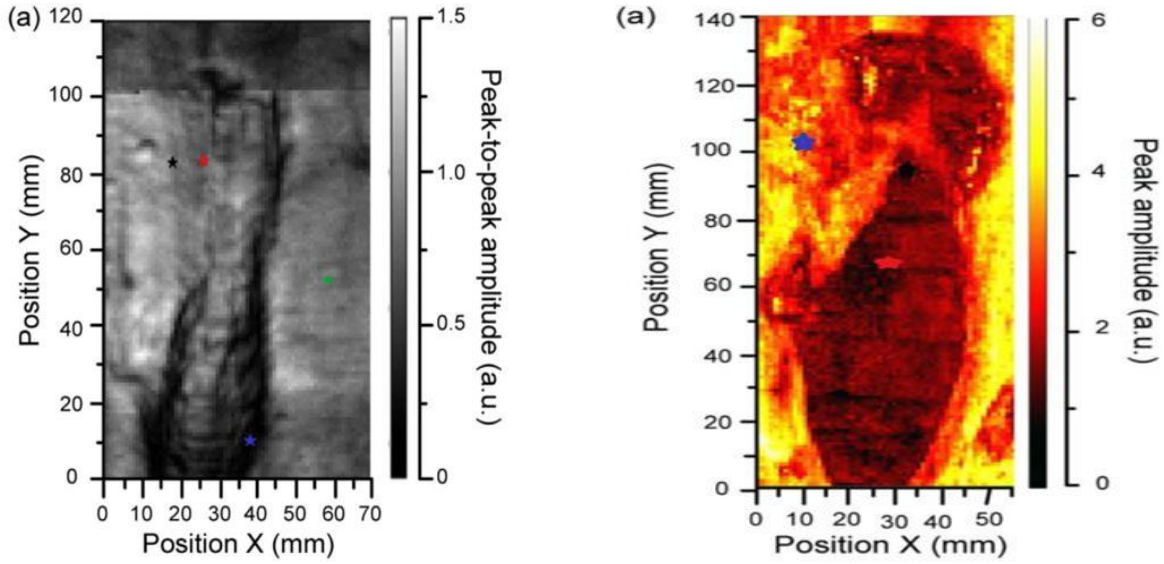

(a) (b)

Figure 1-16: (a) Terahertz transmission image of a defective area. (b) Terahertz reflection image of a defective area [65].

4.9 Applications in the timber industry

In the timber industry, the *THz* has also been implemented as a nondestructive technique aiming to detect fissures and cracks and for quality inspection, such as spotting resin pockets and knots, or as detailed in the previous part, for mapping the water content distribution and monitoring the drying process. It has been shown in this context that the *THz* absorbance is linear with the thickness of dry wood. Moreover, the absorbance is a linear with the water content and with the absorption coefficients of water and dry wood [66].

Indeed, it has been shown that it is possible to map wood density using *THz-TDS* imaging [67]. A sample of 1.7 *mm* thick beech wood was investigated over a range of frequencies between 0.7 *THz* and 1.2 *THz*. Due to the structure differences between earlywood (containing lumens and thin cell walls) and latewood (thick cell walls), their densities are different. The absorption coefficient is a linear function of density, where the slope represents the mass absorption coefficient. Figure 1-17 shows the agreement between the measured *THz* absorption and the local wood density obtained by the gravimetric-volumetric method.

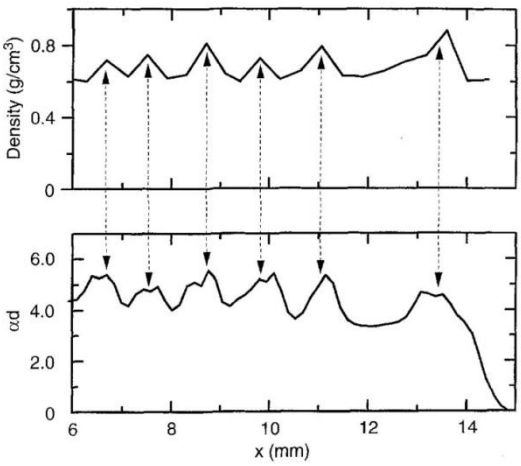

Figure 1-17: Density profile (upper part) obtained by the gravimetric-volumetric technique and the *THz* absorption profile (lower part) of a beech sample [67].

Moreover, a linear *THz* detector allows for the scanning of a sample at a speed of 15 *m/s*. The sensor size is 256 pixels x 1 pixel with an acquisition rate ranging from 100 to 5000 lines / s. Figure 1-18 shows an example of the *NDT* of maritime pine scanned with this TeraFAST scanner, revealing the efficiency in detecting the knot and resin pocket within the sample.

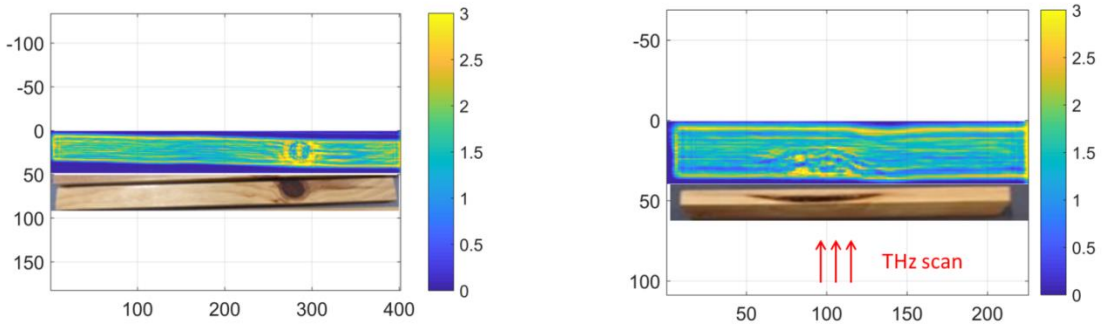

(a) (b)

Figure 1-18: *THz* absorbance images by TeraFAST with photographs of the scanned wood sample, (a) detecting a knot and (b) detecting a resin pocket.

5 Potential applications of *THz* for thermal measurements

As mentioned above, the far-infrared *THz* radiation wavelength range is characterized by nonionizing properties due to the low photon energies. Therefore, it is easy to use this probe in different research applications and industry. The relatively low cost of *THz* radiation makes it the appropriate choice for contactless measurement applications. Waves in this spectral range are absorbed by water, which makes *THz* radiation an effective tool for hydric transfer studies. Few studies have focused on the potential of *THz* contactless temperature measurements in insulating materials. However, the contactless temperature measurement of insulating materials deserves further interest (chapter 4). This type of measurement involves verifying the relationship between the *THz* transmittance of a material and its temperature.

Noncontact methods based on infrared imaging have recently been developed for temperature measurements [68]. For instance, nondestructive techniques, such as infrared thermography, can measure full-field temperature without contacting the sample. This infrared imaging technique has been employed to determine the thermal transmittance of certain solids [68]. In the aforementioned study, the authors used infrared and spectroscopy imaging for the contactless measurement of the absolute temperature of semitransparent materials. The authors used a multispectral middle-wavelength infrared imaging technique in transmission mode to explore the thermotransmittance of solids over this wave range.

Measurements have been performed on three semitransparent solids (a sapphire substrate, potassium bromide (KBr) and a doped silicon wafer) at different wavelengths under different sustained temperatures (21 °*C*, 80 °*C* and 140 °*C*). This technique allows for the thermotransmittance coefficient to be estimated in all images. The method has been shown to be efficient for the contactless temperature measurements of materials semitransparent to the infrared. Figure 1-19 shows the linear relationship between the absorbance and temperature obtained for sapphire.

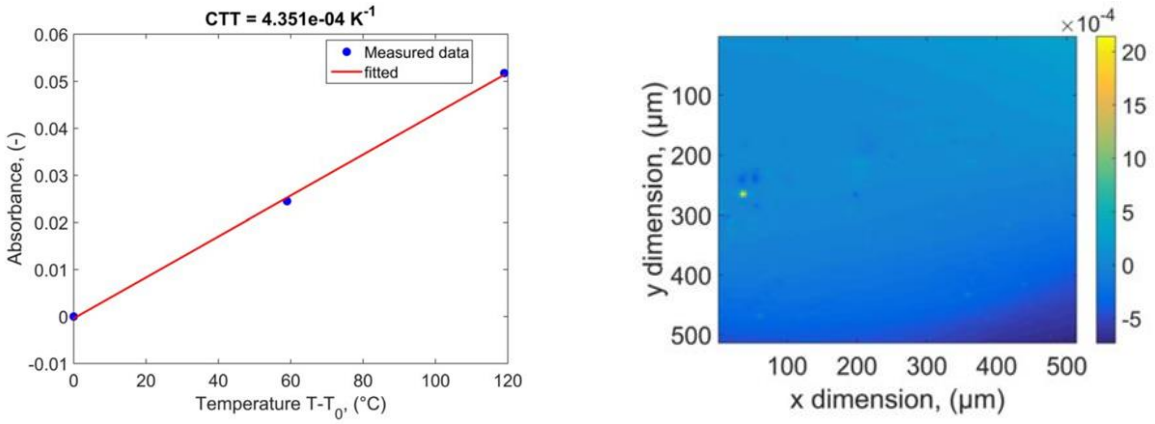

(a) (b)

Figure 1-19: (a) Sapphire absorbance at a wavelength of 3.4 μm function of temperature of central pixel with linear fit to estimate the coefficient of thermotransmittance, (b) coefficient of thermotransmittance map averaged over all wavelengths [68].

Recently, *THz 2D* imaging and *3D* tomography of semiconductors and insulating materials have been demonstrated [69]. C. Pradere et al used the synchronous detection of modulated millimeter-waves coupled with a pyroelectric *THz* monosensor to estimate the thermoreflectance coefficients of metal and semiconductor materials (bulk aluminum, copper and silicon). Lock-in detection has been used to improve the signal-to-noise ratio and to remove the artifacts of temperature variation and proper emission of the sample. Due to reflectivity of *THz* waves by metals, the reflection mode has been investigated. The temperature of the samples was increased by using a heater.

The reflected signal was recorded using the monodetector simultaneously with the recording of the temperature by a thermocouple. The technique allowed for the estimation of the thermoreflectance at transient temperature. Over this wavelength range, the estimated coefficients are approximately 100 times higher than the values captured over the visible range. Thereafter, the transient contactless temperature measurements were estimated based on the identified coefficient. The technique was shown to be an effective tool for noncontact local temperature measurement of metals and semiconductors. However, the lack of a raster pattern results in a point-by-point scan that is slow and does not allow full-field scanning at high frequency.

In [70], C. Poulin et al investigated the thermal dependence of transmitted *THz* beams at steady state for the case of a semitransparent material (*POM* polymer) subjected to a thermal gradient. The absorption coefficient sensitivity to the temperature was determined by coupling *THz* images with a *3D* temperature distribution based on infrared temperature images and a *3D* temperature function. The model used takes into account the convection and radiation at the boundaries and a parabola profile along the third direction that is thought to be symmetric with respect to z=0 in the middle of the thickness, as indicated by equation (1-53).

$$T(x,y,z) = a - b\left(z^2 - \left(\frac{e}{2}\right)^2 \right) \tag{1-53}$$

where T is the temperature (K); e is the thickness (m); x, y and z are the different directions; and a and b are coefficients to be determined by the following boundary conditions:

$$\begin{aligned} T\left(x,y,z=e/2\right)\Big|_{IRcam} &= a \\ \left.\frac{\partial T\left(x,y,z\right)}{\partial z}\right|_{z=e/2} &= h_{air}\left(a - T_\infty\right) + \varepsilon\sigma\left(a^4 - T_\infty{}^4\right) \end{aligned} \tag{1-54}$$

where h_{air} is the convection coefficient ($W.K^{-1}$), σ is the Stefan-Boltzmann constant given as 5.67 10^{-8} $W.m^{-2}.K^{-4}$, ε is the emissivity of the surface and T_∞ is the temperature of air (K). The coefficients a and b were estimated using numerical simulation with a temperature field provided by an infrared camera. On the other hand, the absorption coefficient is written as a linear function of temperature, as described by equation (1-55).

$$\mu(T) = \alpha + \beta\left(T - T_0\right) \tag{1-55}$$

where μ is the absorption coefficient and α and β are the coefficients to estimate. Thus, the Beer-Lambert law can be given as follows:

$$I = I_0\left(1 - n\left(T(x,y,z=e/2)\right)\right)^2 e^{-\int_{-e/2}^{e/2}\left[\alpha+\beta\left(a-b\left(z^2-\left(\frac{e}{2}\right)^2\right)-T_0\right)\right]dz} \tag{1-56}$$

where n is the refractive index that is assumed to be equal to the reflection index and constant. Applying the linear least squares algorithm to equation (1-56), the coefficients α and β can be estimated. Figure 1-20 shows the absorption coefficient as a function of temperature.

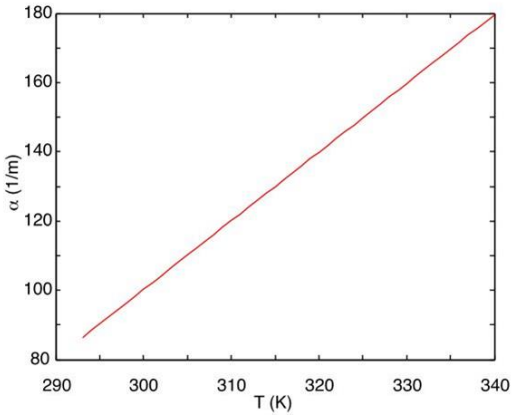

Figure 1-20: Absorption coefficient as a function of temperature [70].

Studies of the *THz* thermal-dependence in the literature are rare and mostly conducted at steady state or at local positions. Tomography methods, including *THz* tomography, require more attention regarding the contactless measurements of transient temperature fields. Such a technique could be a key to obtaining a contactless measurement of *3D* transient temperatures.

The *THz-TDS* tomography of an arbitrarily shaped sample using an automat arm has been carried out in [71]. The arm has been used to hold the emitter-receiver *THz* system and follows the shape of a curved sample in such a way that the incident beam stays perpendicular to the sample, which remains in the focal plane. A *THz* computed tomography based on heterodyne detection has been presented [72]. The authors reimaged the *3D* object in terms of absorbance (a pencil and a defective plastic sheet). The inverse Radon function was used to reconstruct the *3D* field via the images taken at different angles. Terahertz computed tomography (*THz-CT*) showed efficiency in detecting the defects, which makes it an appropriate tool for *NDT* and *3D* temperature contactless measurements.

6 Conclusion

As a summary of this state of the art, it should be indicated that the phenomenon of humidity transport in porous materials is complex and depends on different parameters. During drying, the heat gradient leads to a change in the vapor pressure, which changes the relative humidity and thereby the water content (sorption curves). The diffusion of water within hygroscopic materials depends on the permeability and the hydric state of the structure. Nonhomogeneous drying leads to the nonhomogeneous transport of the water content, which leads to wet and dry zones. Therefore, different mechanical stresses can be generated. There are many theoretical solutions to the mass transfer equation, allowing for characterizing diffusion with different boundary conditions. However, such approaches need to be confronted with the measured water content fields.

Finally, the literature overview shows the importance of developing cameras capable of fast contactless water content and temperature measurements by using the *THz* band. Moreover, while the heat and mass modelization is well documented, the characterization, particularly new tools (setup + associated inverse processing methods), needs to be developed.

CHAPTER II: EXPERIMENTAL SETUP

With the state of the art described in chapter 1, it has been possible to show the different methods that exist in the literature. As shown, the main obstacle is finding a nonionizing measurement device capable of realizing contactless measurements of the water content field and the temperature in wood. Starting from this proposal, it is therefore necessary to develop an experimental tool capable of grouping these different points.

In this chapter, part of the work consists of developing two testbenches: one devoted to *NDT* and a steady-state point-by-point scanning system and the second based on a quantum bolometric *THz* camera. In the first part, the complete point-by-point setup will be described as well as the limitations and advantages.

Then, in order to measure or monitor transient phenomena (such as heat and mass transfers), an imaging setup based on a patented *THz*-to-*IR focal plane array* sensor has been developed. This *THz* scanner is composed of five components: (i), a modulated ***THz Gunn diode***, (ii) an optical system (iii), a ***bolometer or THz-to-thermal converter (TTC)***, and (iv), an ***infrared camera*** that can be considered as the *quantic FPA sensor*. Finally, some raw images are presented.

A final important point is the development of a new “fluidic exciter”. In fact, by using the thermal analogy, the main goal here is to be able to realize a “fluidic laser” to impose point-like, line or homogeneous excitations at the surface of the sample. Moreover, another idea is to control the intensity and the temporal shape of such an excitation.

The experimental setup developed in this work is more like an instrument than a simple testbench. Behind the word “instrument” lies a measuring device and methods of treatment. This device allows a resolutely multiscale (spatial and temporal) approach through a macroscopic scanner system (on the order of m), which allows for the analysis of large structures.

Finally, in general, the characterization of heat and mass fields requires the development of stable and robust methods that require a great deal of control over the measurement error, and especially, the quantification. To do this, it becomes essential to be able to automate the acquisition systems in order to be placed under repeatable optimal operating conditions, which allow a statistical study of the systematic error of the measurement chain. For all these reasons, this part highlights the importance of this work, which, although often undervalued, provides important knowledge on the complete control of the sophisticated measuring device developed in this work.

1 General considerations concerning the setup

In the first chapter, different contactless methods used for heat or mass transfer measurement were presented. We are convinced that the terahertz technique can show an advantage in terms of ease of use, low cost and safety. Therefore, it seemed promising to develop an efficient setup capable of the contactless monitoring of mass and heat transfers.

When working with radiation, one can use transmission, reflection or a coupled mode. Generally, the operating mode is chosen as a function of the studied materials and their transmittance in the *THz* wavelength range. For example, in the case of metals and some composites, the reflection mode would be the best choice. As the materials chosen for this study are semitransparent (blotting paper, wood and *PVC*), the reflected signal is low. We therefore decided to work with the transmission mode, as shown in Figure 2-1.

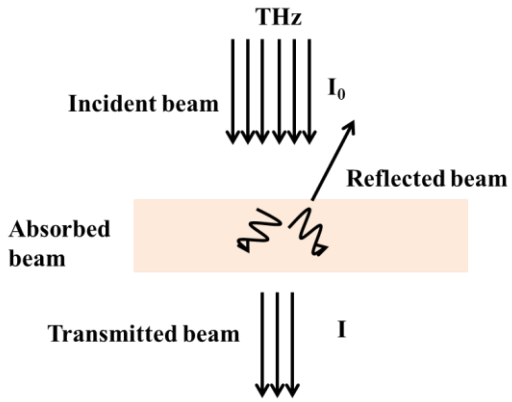

Figure 2-1: Reflected, absorbed and transmitted beams.

The simplified setup scheme of the transmission mode we worked with is shown in Figure 2-2. Two kinds of detectors are used. The first configuration, based on a simple monodetector (a technique we call “point by point”) giving directly workable images, is presented. This configuration is well suited for study at steady state, due to the long time an entire scan of a sample takes. In the second configuration, an imaging system (an infrared camera coupled with a bolometer) is used as the detector. In that configuration, the obtained images have to be processed with specific methods that are detailed in chapter 3. Thanks to the high acquisition frequency of the camera, this system is well suited to study transient thermal and hydric transfers. Both configurations are detailed in the first parts of this chapter.

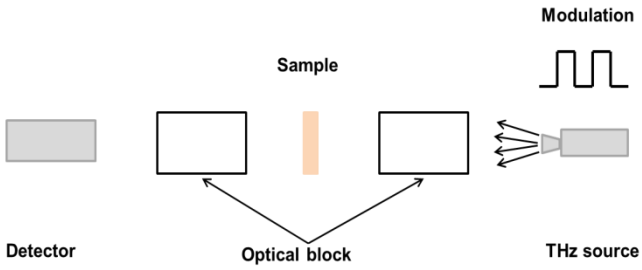

Figure 2-2: General scheme of the transmission-based setup.

2 First configuration: *THz* measurement setup based on an infrared pyrometer

Similar to infrared detectors, *THz* detectors are based on an optical device that detects *THz* waves through the conversion of the absorbed energy to an electric signal (bolometer). We use a punctual pyrometer (monodetector) working in a range extending from the infrared to millimeter waves that allows a scanning region of (1 *px* x 1 *px*).

Since scanning using the monodetector is performed point by point (pixel by pixel) and the time of each pixel scan is approximately 2 to 10 s, a complete scan of a region of interest containing hundreds of pixels can take up to one hour. Thus, the use of the monodetector to study transient transfers would not be the right choice. Monodetectors with a long response time are often designed for nondestructive testing (*NDT*) or the study of quite stationary phenomena.

In our study, the experimental testbed for the study of a steady-state hydric state (water content measurements) consists of (i) a ***THz Gunn diode*** emitter as the source, (ii) an ***infrared monodetector*** as the detector, and (iii) a ***shutter*** to eliminate the continuous component and four plano-convex lenses made of polytetrafluoroethylene (*PTFE*), to focus the beam, first, on the focal plane situated in the middle of the sample, and then, on the detector. Figure 2-3 shows a photograph and the scheme of this "point-by-point" *THz* measurement testbed.

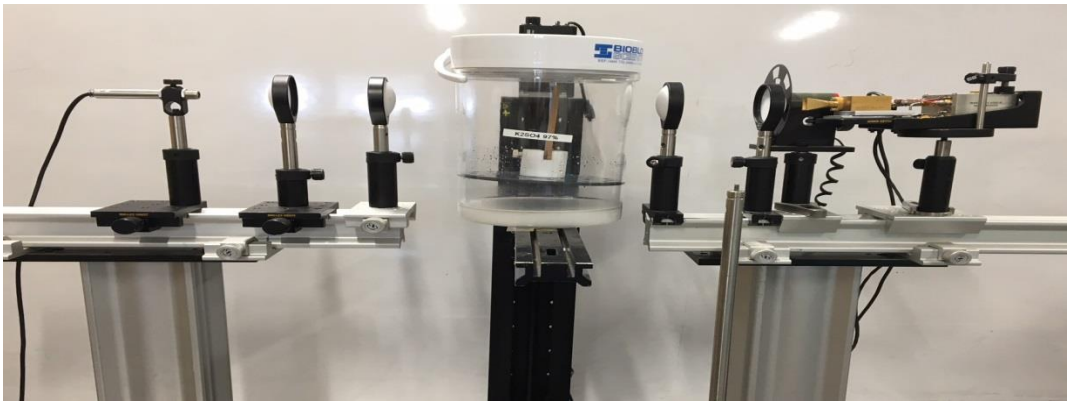

(a)

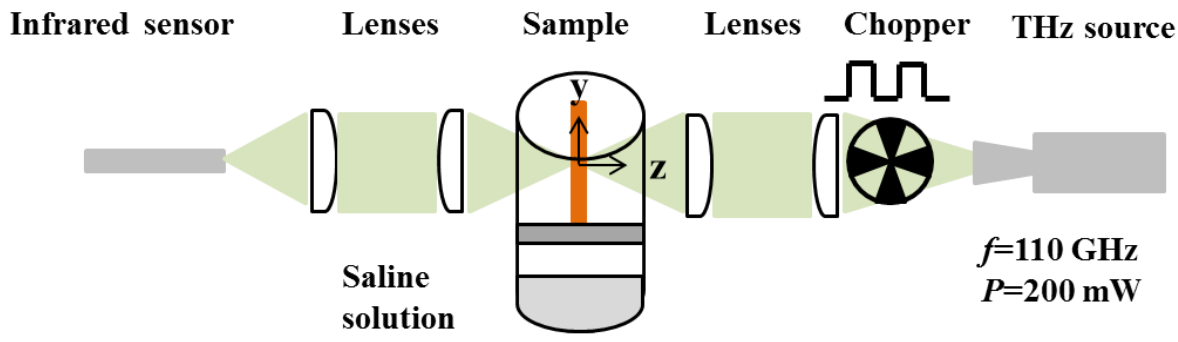

(b)

Figure 2-3: Global scheme of the monodetector-based setup.

2.1 *THz* source

The *THz* source is a Gunn diode (Virginia diodes, Inc. Charlottesville, VA 22902, USA) with a power of 200 mW and a frequency of 110 GHz, equivalent to a wavelength of 2.73 mm. Figure 2-4 shows the *THz* source used in the experiments.

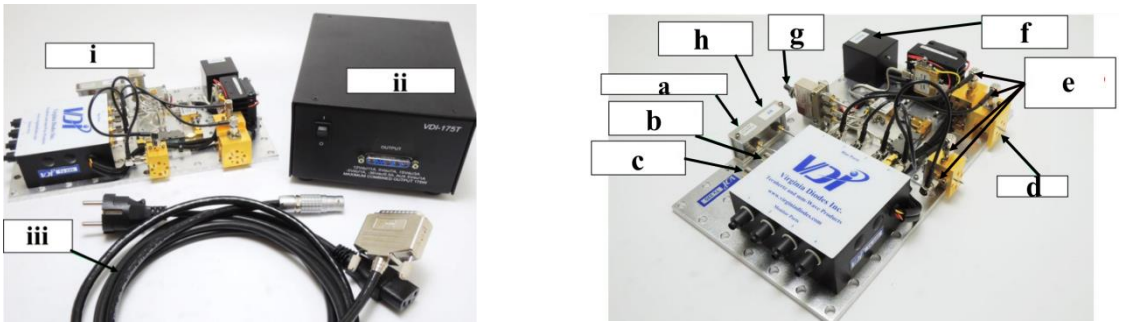

(a) (b)

Figure 2-4: (a) Photograph of the source component. (b) A photograph of the Tx 220 in the 100 GHz configuration: (a) frequency monitor, (b) *TTL* modulation input, (c) user-controlled attenuation, (d) *RF* output, (e) *ESD* sensitive devise, (f) power box connection, (g) source switch and (h) external RF input.

The source includes one 110 *GHz* modular transmitter configured for 200 *mW*. It consists of a power box and power cables. The power of the source is presented as a function of frequency (tunability) and is given in the data sheet from the manufacturer.

2.2 Optical blocks

The optical system in this testbed is composed of four 50 *mm* diameter lenses made of *PTFE* (THORLABS) with a focal distance of 60 *mm*. It is worth noting that the lenses used here are quite inexpensive (tens of euros). Two lenses are positioned between the source and the sample to focus the incoming *THz* beam on a focal plan situated in the middle of the sample thickness (divergence-collimation-convergence). Two other lenses are placed behind the sample to recover the transmitted beam and focus it on the detector aperture. The dimensions and focal distance are given by the provider, THORLAB, and are shown in Table II-2. The detected radiation is transferred into an electrical signal modulated at 15 *Hz*. The modulation is performed through a shutter linked to a lock-in device.

2.3 Monodetector

The used infrared pyrometer (Optris *CS LT*) is a tool intended to measure the temperature in small and narrow environments. It allows contactless measurement of the proper emission of a sample. The working temperature range is between -40 °*C* and 1030 °*C*, and cooling is not required at temperatures up to 80 °*C*. This kind of pyrometer can work for multiple employments of infrared measurement points between 8 μm and 14 μm with emissivity: 0.95 . Again, this kind of pyrometer is quite inexpensive (approximately 100 euros). The used pyrometer is shown in Figure 2-5.

Figure 2-5: Photograph of the used pyrometer (Optris CS TL infrared thermometer).

2.4 Lock-in amplifier

For the conducted experiments, a 5 *V* dual-tracking laboratory DC power supply (GPC 3030D) is used. This power supply has three linear DC power outputs, from 195 *W* to 375 *W*. Figure 2-6 shows the used power supply.

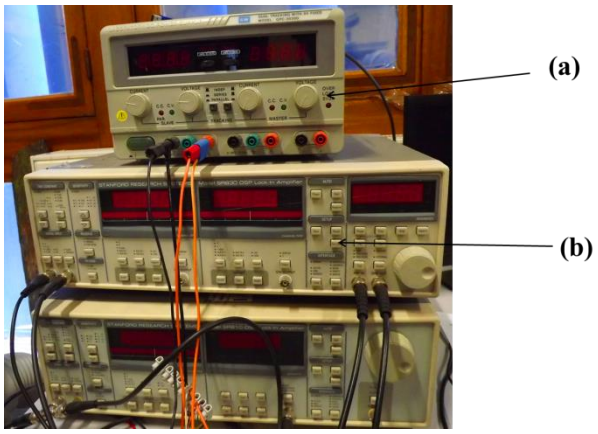

Figure 2-6: GPC 3030D power supply and (b) SR830 DSP lock-in amplifier.

The amplifier used in this study is an SR830 DSP lock-in amplifier aiming to amplify the signal in a way that the signal-to-noise ratio is high. Some specifications of this device are shown in appendix II. Due to the noise from fluctuations in the ambient temperature and the proper emission of the sample, the measurement of the *THz* signal can be affected. The measured signal represents the signal accompanied by the proper emission and environmental noise (background). Therefore, deleting the continuous part through modulation is necessary. For that, a shutter linked to the lock-in devise is used to obtain the information coming from the *THz* source independent of that from the environment. The modulation performed in this part of the study is 15 *Hz*. The modulation of the signal is shown in Figure 2-7.

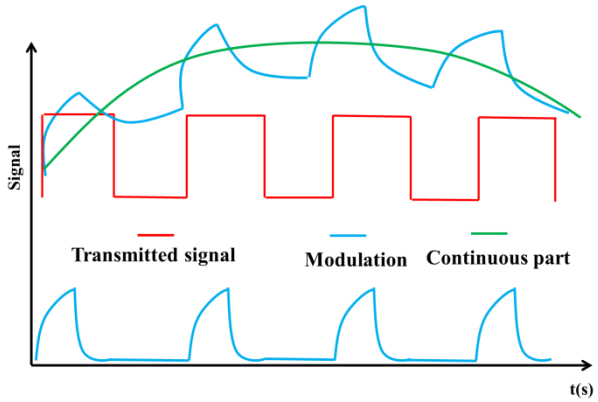

Figure 2-7: Modulation of the *THz* signal and deletion of the baseline (continuous part).

2.5 X-Y scanning

A remote-controlled sample holder (Zaber rail T-LST0500B) moved by a stepper-motor allowing displacement of the sample in the plane perpendicular to the *THz* beam is used. The technical characteristics of the sample holder rail are shown in Table II-3. The stepper control is performed using a National Instrument **GPIB-USB-HS** card interfaced with a homemade LabVIEW application. On the other hand, the *THz* source and the detector are fixed. In this way, the region of interest in the sample is scanned "point by point" in a raster pattern by movement of the sample holder in the x-y plane (perpendicular to the *THz* beam). The region of interest dimensions, the spatial resolution (mm / px) and the stability criterion of each measurement can be fixed by the LabVIEW program. For example, an ROI of 30 x 20 *px* takes approximately 40 *min*.

On the other hand, the beam size is a function of the wavelength, which means that at the used wavelength (~2.7 *mm*), the beam size is approximately 3 mm. Therefore, a displacement step of 1 *px* (1 *mm*) provides submillimeter information, which leads to an image that does not represent an effective *THz* image (contains useless detail). Therefore, the sample should be displaced by a spatial step equal to the beam size. Figure 2-8 shows the resolution of the pixels and the *THz* beam.

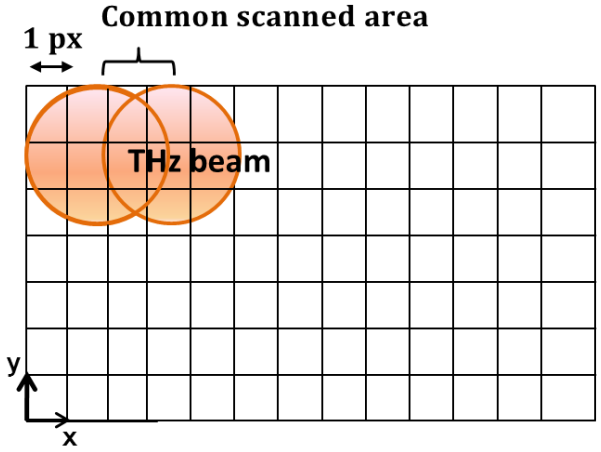

Figure 2-8: *THz* beam size (3 *mm*) displaced by a 1 pixel spatial step.

It is necessary to indicate that the attenuation of the *THz* beam in each pixel is a function of the temperature, water content, density and thickness of the studied sample. When studying the mass (water) diffusion at the ambient temperature of the lab and for a given thickness of sample, the *THz* signal is almost only sensitive to the sample water content. However, the *THz* signal is more sensitive to temperature in the case of the sample experiencing a high temperature gradient. Finally, if the temperature and hydric state of the studied sample are similar to those of the environment, the *THz* signal is more sensitive to the density and thickness of the sample, and thereby, the application can be suitable for a nondestructive testing (*NDT*).

As an illustration, Figure 2-9 shows a building insulation sample that is semitransparent to *THz* waves and its "point-by-point" image obtained with a pixel resolution of 3 *mm* / *px*. The scanning of the whole sample (300 *mm* x 250 *mm*) takes approximately 8 *h*.

Figure 2-9 shows that for *NDT* applications, the *THz* method can be a low-cost efficient technique to reveal the defects and inclusions within materials. Moreover, *THz* imaging is also capable of revealing the heterogeneity of a material.

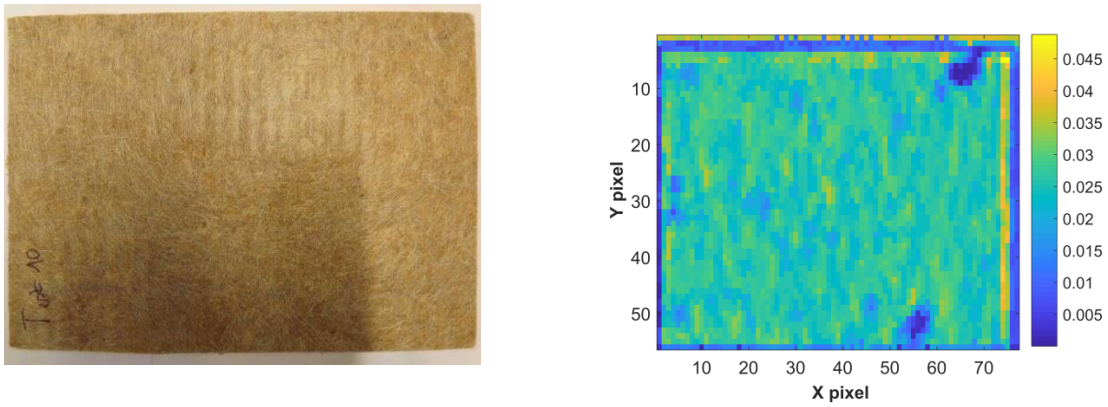

(a) (b)

Figure 2-9: (a) Visible photo of a foam insulating material containing invisible inclusions. (b) A *THz* image obtained by scanning the sample using the monodetector.

2.6 Advantages and limits

The setup based on the monodetector is an efficient tool for nondestructive testing and quality inspection or for the analysis of the thermal and/or hydric steady state of semitransparent materials. In addition, as mentioned above, the scanning time is slow and takes long time (2 *s*-10 *s*) for each pixel. This means that the main limitation of this testbed is the monitoring of fast phenomena, especially heat transfers, where the characteristic time is a hundred times less than that of the hydric transfers. To increase the performance of such detectors in terms of scanning time and/or spatial resolution, some improvements in the detectability and resolution can be carried out. The proposed improvements are presented in appendix III.

3 Second configuration: *THz* measurement setup based on a *2D* detector

To measure or monitor transient phenomena, such as heat or mass diffusion into samples, a test setup based on a *2D* detector has been developed. Due to the short response time of a detector matrix (256 *px* x 320 *px*, for example), monitoring of a thermal or hydric transfer within insulating materials can be performed. A *2D* detector can be an optical detector (*THz* camera); in our case, we use a thermal detector (an infrared camera coupled with a bolometer - *THz*-to-thermal IR converter, a so-called "*TTC*") [73].

The *THz* testbed that aims to carry out contactless measurements of the temperature and/or water consists of: (i) a ***THz Gunn diode***, (ii) an optical system, (iii) an ***infrared camera*** that can be considered as the *2D* detector, (iv) a ***bolometer or THz-to-thermal converter (TTC)*** and (v) a ***modulator***. These elements are shown in Figure 2-10:

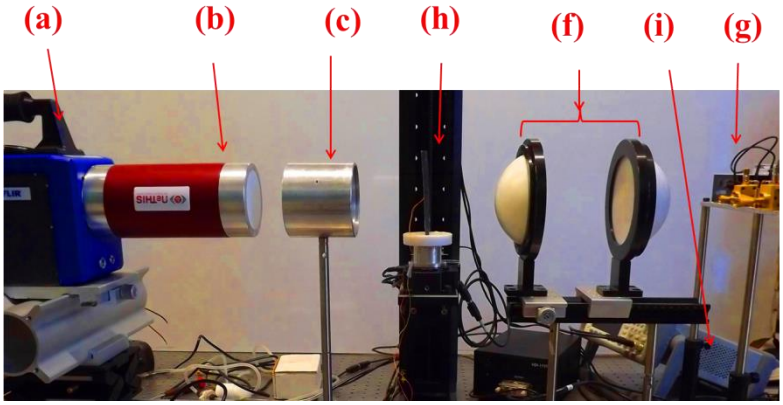

(a)

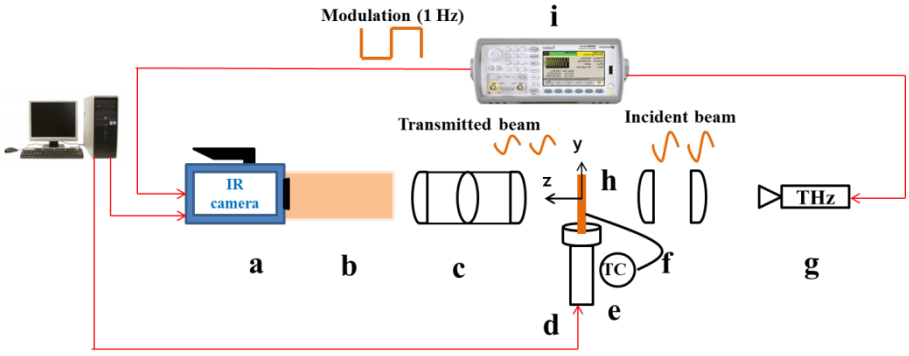

(b)

Figure 2-10: Photo and scheme of the experimental setup: (a) IR camera, (b) *TTC*, (c) focus, (d) sample holder, (e) thermocouple, (f) lenses, (g) *THz* source, (h) sample and (i) modulator.

The *THz* Gunn diode is the same as the source presented in the previous section. However, the optical system in this experiment consists of a beam expander composed of two 110-mm-diameter plano-convex lenses made of *PTFE* (*THORLABS*) with a focal distance of 100 mm ((f) in Figure 2-10) and objective (c) composed of three Teflon lenses designed by Alphanov. The objective situated between the sample and the detector aims to image the sample on the *TTC*, according to different magnifications. It is important to notice that a near-field

configuration is also available by putting the *THz* nose of the camera directly behind the sample. This mode is interesting for thin samples.

However, expanding the beam can provide several optical deviations such as beam deformation, inhomogeneity due optical misalignment or the diffraction phenomenon. This led us to develop image processing methods to extract the necessary information pixel by pixel (see chapter 3).

Moreover, the thermal deviations linked to the use of a thermal detector can be avoided through modulation of the signal. The modulation of the *THz* beam coupled with image processing allows the thermal and optical deviations to be decreased. Thus, the interaction between the *THz* beam and the sample can be visualized.

3.1 Camera characteristics

The camera used in this study (FLIR SC7000) is a mid-wave indium antimonide (InSb) quantum detector-based infrared camera with a spectral band of $3.5\ \mu m$ - $5.15\ \mu m$ and acquisition frequencies up to $1\ kHz$. The detector's matrix size is $256\ px$ x $320\ px$ with a minimum spatial resolution of $25\ \mu m\ /\ px$. This camera can achieve a frame rate (acquisition frequency) of up to 800 images $/\ s$ in snapshot mode. Snapshot mode is when the matrix detectors work concurrently.

The integration time represents the exposure time of the infrared camera to the thermal radiation. It represents an important parameter of the imaging technique due to its influence on the image quality. Indeed, a short integration time induces erratic measurements, and it amplifies the signal noise. However, a long integration time misses the following of variations in the observed phenomenon. Therefore, the setting of the integration time is performed according to the level of the signal-to-noise ratio (*SNR*), i.e., the higher the signal-to-noise ratio, the shorter the integration time is. This requires finding a compromise that allows a high *SNR* without losing information. However, the integration time has to be adjusted as a function of the frequency rate due to the inverse proportionality between these two parameters. In practice, the integration time is variable from $3\ \mu s$ to $2\ s$, but a parametric study of the sensitivity allows obtaining an integration time of IT = $1200\ \mu s$. The integration time is also adjustable through a smart external triggering feature that allows synchronization of the images with excitation, for example. The used infrared camera is shown in Figure 2-11.

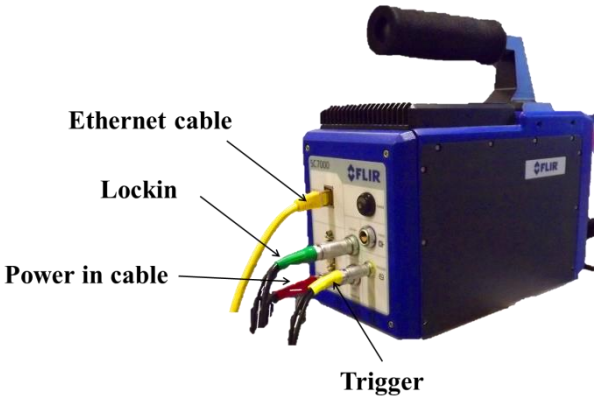

Figure 2-11: Infrared camera (SC7000).

The SC7000 infrared camera works at temperatures ranging from -20 °*C* to 55 °*C* and has a noise equivalent temperature difference (*NETD*) of less than 25 *mK* at 25 °*C*. The *NETD* represents the necessary incident signal for *SNR* = 1. This parameter depends on the sensitivity (*mK*.*DL*) and noise (*DL*) of the detector and is measured in (*mK*). Due to this high detectability, the quantum detectors are cooled to 77 *K* through an integrated Stirling cooler. The technical characteristics are summarized in Table II-4.

3.2 Measurement noise

Figure 2-12 shows a stationary thermal scene (a keyboard) imaged by the FLIR SC7000 infrared camera. When the IR camera records a stationary thermal scene (passive thermography), such as the image shown in Figure 2-12-a, the intensity distribution of each image in time represents a Gaussian distribution (Figure 2-12-b). However, the measurement noise can be found by the difference between the intensity of each pixel and the mean value of intensity in time. The intensity of a given pixel is shown in Figure 2-12-c.

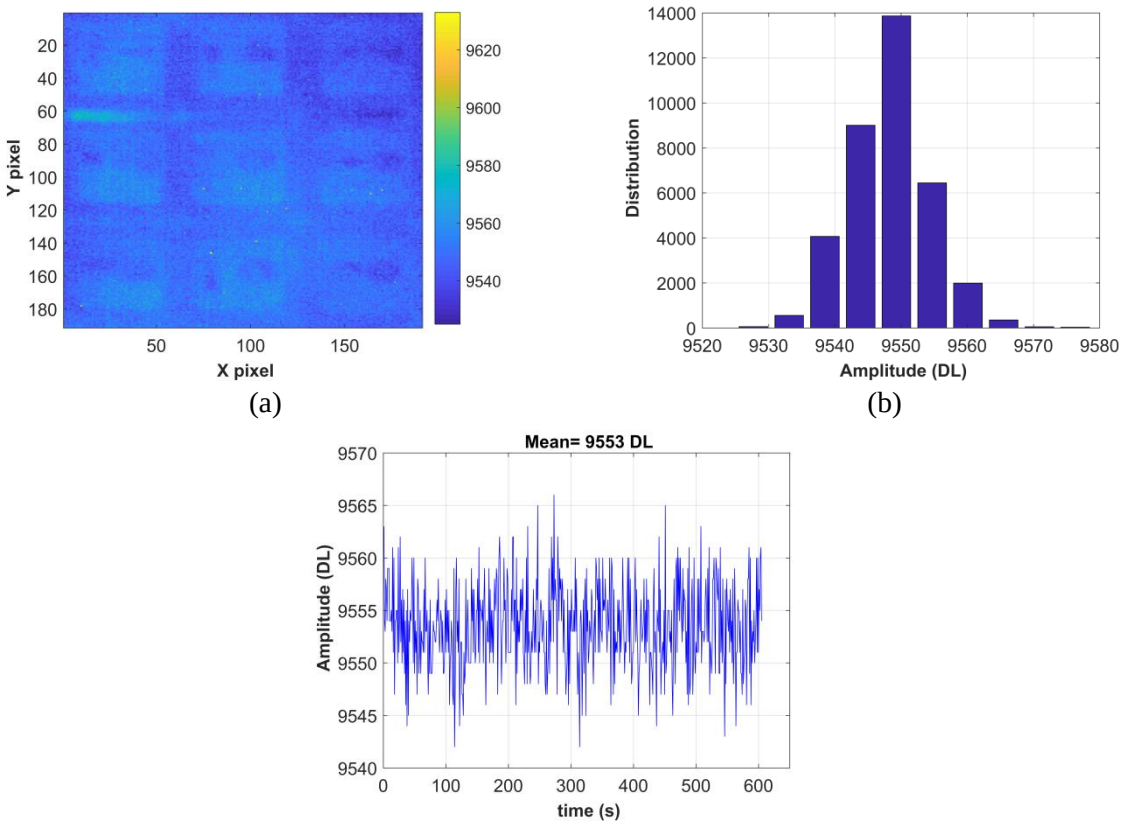

(a) (b) (c)

Figure 2-12: (a) Image of a keyboard taken by the SC7000 FLIR infrared camera, (b) a histogram of the image at ambient temperature and (c) time evolution of the noise of the central pixel.

Moreover, chromatic aberration phenomena are often present during imaging of an object. The chromatic aberrations are optic aberrations, also called chromatic distortion. They result from the failure of a lens to focus all colors to the same plane. This phenomenon occurs because the lenses have different refractive indices at different light wavelengths. Chromatic aberrations affect the visible as well as the infrared domains [74]. For this reason, it is often chosen to work with a half or quarter image (for example, 128 *px* x 160 *px*, instead of 256 *px* x 320 *px*). Moreover, a region of interest (ROI) can be chosen. These subimages are generally chosen to be in the center of the full image.

In thermal images, as in visible ones, defective pixels (also called “dead pixels”) can appear, which decrease the image quality. The dead pixels can be corrected by processing methods [75-77]. The correction of such pixels first needs a means of their detection using algorithms of thresholding, and is followed by replacing them by the neighbors. Another important image processing that allows the cleaning of images is the deleting of environment noise such as that observed in an image at ambient temperature (offset).

3.3 *THz*-to-thermal converter (*TTC*)

The infrared camera coupled with the *TTC* is a tool that allows detection of *THz* waves and is equivalent to a *THz* camera based on photothermal conversion. The *TTC* has been developed in [73], and it makes use of the advantages of an infrared camera (high acquisition

and full-field scanning). Indeed, the *2D* detector represents an advantage over the *THz* monodetector in terms of the monitoring of fast phenomena. For example, if the field scanned with a monodetector is 30 *px* x 30 *px* pixels and the scan of each pixel lasts 1 *s*, the detector will scan the last pixel after 900 *s*. However, the IR or *THz* camera can scan the full field at an acquisition rate of 1 *kHz*. This feature gives to the *THz* camera or (IR camera + *TTC*) an advantage over the monodetector in studying fast transient phenomena, such as cooling by natural convection (see chapter 4).

Herein, the proposed *TTC* consists of the absorption of the incident *THz* radiation by a carbon sheet, which increases its temperature. Then, the temperature increase is detected by an infrared camera. Figure 2-13 shows a picture and a scheme of the interior of the *TTC*.

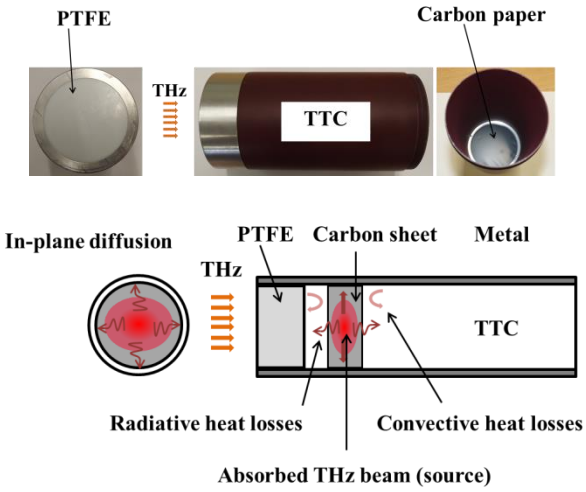

Figure 2-13: (a) Picture of the *TTC*. (b) Crossview of the *TTC*.

As shown in Figure 2-13, the *TTC* mainly relies on a thin homogeneous carbon sheet (thickness 15 μm). The diffusivity of this material is approximately 4.16 10^{-7} m^2/s. In this case, as the thickness is smaller than the wavelength, we can consider that the heat power source is constant along the thickness of the carbon sheet and that the diffusion mainly occurs in the plane perpendicular to the *THz* beam. Therefore, the integration time of the camera and the excitation frequency have to be set as a function of the thermal diffusion time characteristic of carbon. The integration time of the *THz* excitation should not be higher than the characteristic diffusion time of the carbon sheet. This feature prevents in-plane diffusion and allows for confining the *THz* source power to the region of interest. On the other hand, synchronization of the excitation and the acquisition frequencies allows the imaging of the excitation and response phases of the *TTC* in the time.

The parameters of synchronization (film duration, interfilm duration and the duty cycle of excitation) used in our study are given in Figure 2-14Figure 2-15. Thereby, the obtained images represent the response of the *TTC* convoluted with the sample behavior during the heat transfer. Therefore, monitoring of the phenomenon itself requires the subtraction of the continuous component (i.e., the *TTC's* own transient response). The experimental methods developed for the *TTC* are detailed in chapter 3.

3.4 Acquisition synchronization

A two-channel wave-form generator (Agilent 33500B Series) is used to synchronize the *THz* source ignition (channel 1) and the *THz camera* acquisition (channel 2) [73]. The synchronization process is sketched in Figure 2-14:

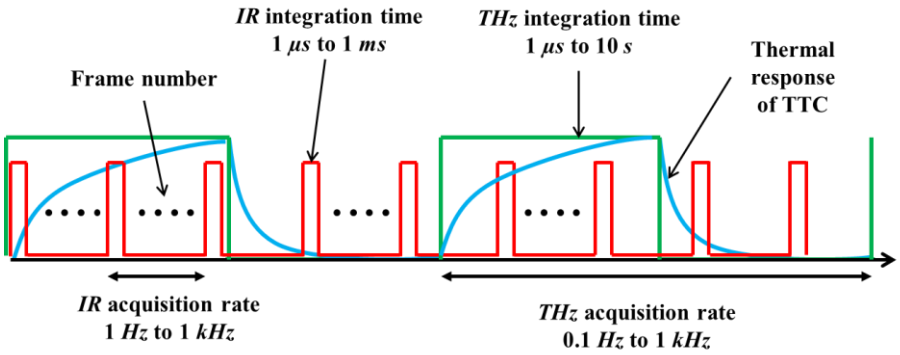

Figure 2-14: Synchronization of the source excitation frequency to the acquisition frequency of the camera.

The first channel contains a square signal, and it represents the *ON*/*OFF* phase of the *THz* source, while the square signal of the second channel triggers the camera. The generator also allows the modulation of the power of the *THz* beam to limit thermal diffusion in the *TTC* x-y. As shown in Figure 2-14, a modulation frequency ranging from 0.1 *Hz* to 1 *kHz* is synchronized with the acquisition frequency ranging from 1 *Hz* to 1 *kHz*. Thus, the *IR* camera records at a high acquisition rate (the red peaks in Figure 2-14) during both on and off phases of the source. The modulation can be carried out through the appropriate duty cycle. A duty cycle represents the ratio between the duration of excitation over a period and the duration of the period. Indeed, a duty cycle greater than 50 % will not allow for sufficient relaxation of the *TTC* (the response will be chopped off).

The duty cycle (*DC*) is an important factor in synchronization due to its effect on the *TTC* thermal response. A *DC* of 10 % means an excitation of the *TTC* during 10 % of a period, and then the *TTC* response relaxes during 90 % of the period, which leads to the blurring of images and decreases the contrast within images because of in-plane diffusion. However, a *DC* of 90 % does not allow for sufficient relaxation of the *TTC*, which decreases the *SNR*. However, the influence of the *DC* on the *THz* signal is limited relative to the influence of the modulation frequency value. To show this behavior, a sample was imaged over time under environmental conditions for three *DC*s with an integration time (*IT*) of 1400 μs, a frequency acquisition (f_{acq}) of 200 *Hz*, a filming duration of 1 *s*, an interfilming duration of 2 *s* and a pixel size of 250 μm. The signal of a chosen pixel in these images is shown in Figure 2-15 as a function of time for *DC*s of 10 %, 50 % and 90 %.

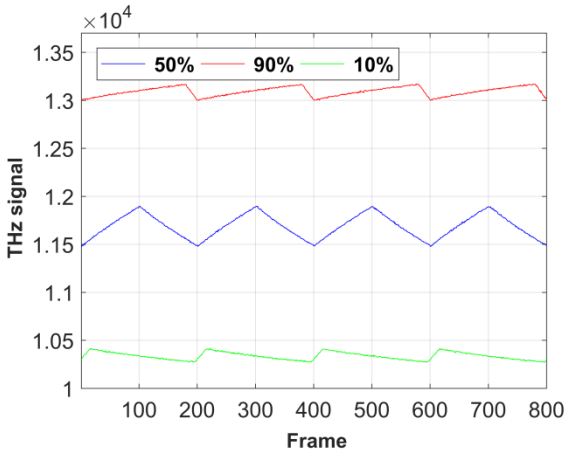

Figure 2-15: Influence of the duty cycle on the *THz* signal.

3.5 Illustration of raw measured images

Given the complete acquisition methods presented in the previous sections, some experimentation has been performed with two types of materials: wood and homogeneous plastics. In all cases, the modulation frequency of the *THz* diode was equal to 1 *Hz* with a duty cycle of 50 % and at the maximum power of the source. The acquisition frequency of the camera was equal to 200 *Hz* with an *IT* of 1400 μs and an *IR* magnification corresponding to 250 μm per *pixel*.

For each sample, a measurement of the beam alone was initially made and then that of the sample itself. Two configurations were established, one corresponding to the near field and the second by using the *ALPHANOV THz* objective lenses.

It is important to note that the presented images are those that come from the live measurements with the camera software without any processing. With practice, we have developed our homemade software, which realizes the lock-in detection in real time. This procedure is discussed in detail in chapter 3. In Figure 2-16, we can clearly observe the entire problem coming from the raw images linked with the *TTC*. In fact, we can distinguish the sample shape and its transparency or reflectivity, but many artifacts are already present in the images.

Another raw example based on semitransparent sample such as wood and *PVC* are presented in Figure 2-17.

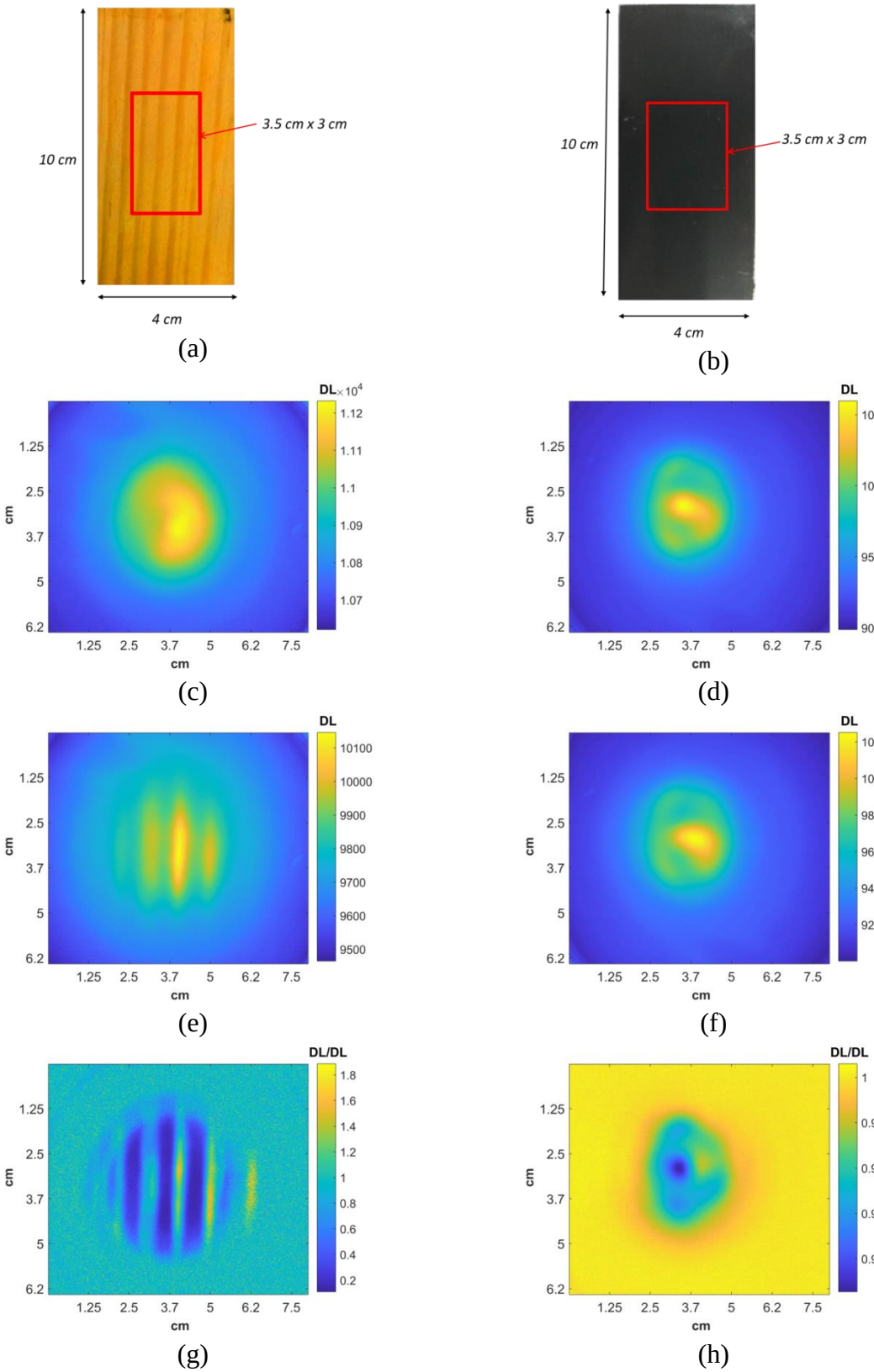

Figure 2-16: (a) Photograph of wood, (b) a photograph of *PVC*, (c) a raw *THz* image of the incident beam (I_0), (d) a raw *THz* image of the incident beam (I_0), (e) a raw *THz* image of wood, (f) a raw *THz* image of *PVC*, (g) an image of the transmittance of wood and (h) an image of the transmittance of *PVC*.

Again, the same artifacts are observed, reinforcing the absolute need for preprocessing.

4 Hydric regulation and excitation

To accomplish the experiments, the use of conditioning, exciting and measuring samples at a given temperature or water content is necessary. For that, an oven, thermocouples, *RH* sensors, an electronic balance and *THz*-semitransparent conditioning containers are used. Moreover, a device is designed aiming to excite dry samples by vapor at a given *RH*.

4.1 Hydric conditioning materials

To load a hygroscopic material at a given hydric state, first, it should be dried until its mass stabilizes at a mass called the solid mass. Usually, an oven is used to dry samples such as wood, and the mass is checked periodically using an electronic balance. The oven (SAPRATIN) is an enclosure used to dry samples at a temperature of 105 °*C*. The heat is generated by the Joule effect and then homogenized through an interior fan. Once the mass of the dry samples is stabilized (at the given criterion of mass variation), the samples are placed within plastic vacuum containers at a fixed relative humidity. The containers (BIOBLOCK SCIENTIFIC) are semitransparent to *THz* beams; therefore, it is possible to scan the sample inside the container. The containers contain different saturated saline solutions and are equipped with a manual pump, leading to a progressive equilibrium between the container environment and the sample. The different saline solutions generating different *RH* levels are prepared by dissolving salt in distilled water. Figure 2-17 shows the oven and containers used.

(a) (b)

Figure 2-17: (a) SAPRATIN oven used for drying samples. (b) Containers (BIOBLOCK) used for conditioning the samples.

The saline solutions correspond the required relative humidity are obtained by dissolving salts with distilled water in different containers. Thereafter, the solution is kept inside the container to stabilize the relative humidity. The *RH* corresponding to each salt is given in the Table 2-1.

Salts	LiCl	KF	K_2CO_3	$CuCl_2$	NaCl	KCl	K_2SO_4
RH (%)	11	31	43	64	75	83	97

Table 2-1: Salts used to obtain saline solutions and the corresponding relative humidity values.

The used electronic balance (METTLER Toledo PG1003-S) allows monitoring the global mass of samples placed inside the conditioning containers. Its accuracy is 0.001 g, and its maximum weight is 1010 g, where the repeatability is 0.0015 g and the linearity is 0.003 g. The balance is equipped with an automatic setting function (*FACT)*, which allows control of the weigh through an external LabVIEW program. Moreover, a programmable contactless sensor is used (Tinytag plus 2, characteristics in Table II-5) allowing the monitoring of the temperature and *RH* within the containers, even during the *THz* scans. Therefore, the sorption curves representing the equilibrium water content (*EWC)* as a function of the relative humidity (*RH)* can be plotted.

In addition, a *K*-type contact thermocouple is used to measure the temperature decrease of the sample surface during the heat transfer experiments (chapter 4).

4.2 Spectral cell for liquid calibration

To assess the *THz* absorption of liquid water, a spacer (Omni-cell) dedicated to analyze liquids at different thicknesses is used. As shown in Figure 2-18-b, the spacer consists of two transparent plastic lamina, and between them, the liquid flows through two filling ports. The thickness of the liquid between the lamina is controlled by a sealed spacer made of polydimethylsiloxane (PDMS) that has different thicknesses ranging from 50 μm to 500 μm. Therefore, the *THz* signal transmitted through the different layers of water will lead to an estimation of the absorption coefficient. Figure 2-18Figure 2-18 represents a cell filled with liquid water of controlled thickness.

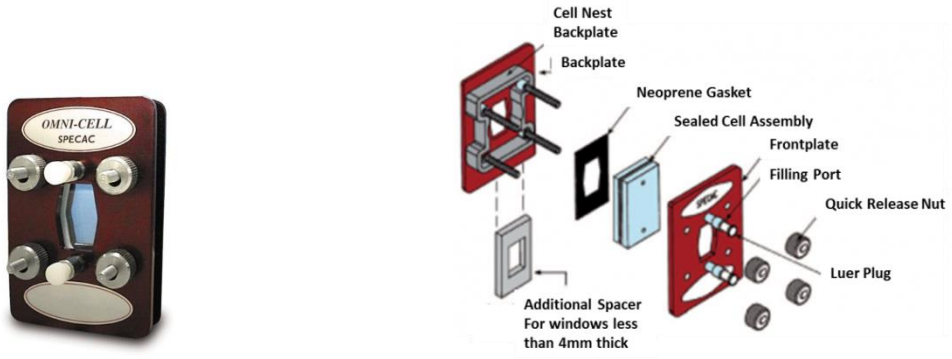

(a) (b)

Figure 2-18: Setup of the water cell with controllable thickness (Omni-cell liquid transmission cell, Specac).

4.3 Hydric excitation device

Taking inspiration from the thermal excitation methods commonly used to measure the thermal diffusion parameters of materials (for example, the flash method, [78, 79]), a "hydric excitation" device has been developed. Its main objective is to fix the hydric conditions (by means of circulating air with a known relative humidity and flow rate) of a defined boundary of a sample while ensuring that there are no hydric exchanges at the other frontiers of the sample. This kind of device should allow us to induce the transfer of moisture within samples that are initially in a homogeneous hydric state. Ideally, this device, coupled to the *THz* measurement, should allow us to estimate the mass diffusion properties of the studied sample.

The hydric excitation to the sample can have a Dirac, Heaviside or periodic form. Since the heat and mass transfers have analogous equations and likely similar boundary conditions, the analytical solutions found for heat transfer can be used to study mass transfer. However, it is important to note that since the characteristic time of mass transfer is longer than that of heat transfer, the hydric excitation duration should be longer. For example, a Dirac form can last several minutes in mass transfer. We could imagine exciting the material with a hydric spot or multispot (hydric laser) and then applying the inverse methods used in heat transfer to reveal the mass diffusion coefficient. This approach will be discussed further in the perspectives of this dissertation.

In the developed hydric excitation device, the sample is placed between two semitransparent plastic enclosures. A rubber stripe is placed on three of the sample edges in order to avoid hydric exchanges. The only side of the sample that is not sealed is exposed to an air flow induced by an aquarium pump (*EHEIM* air pump 100, with a maximum flow rate of 100 *l / h* and a pressure of 200 *mbar*; see Table II-7). The relative humidity of the air is chosen thanks to the saline solution placed in the air circuit and is controlled during the experiments by an *RH* sensor. The hydric excitation device is shown in Figure 2-19.

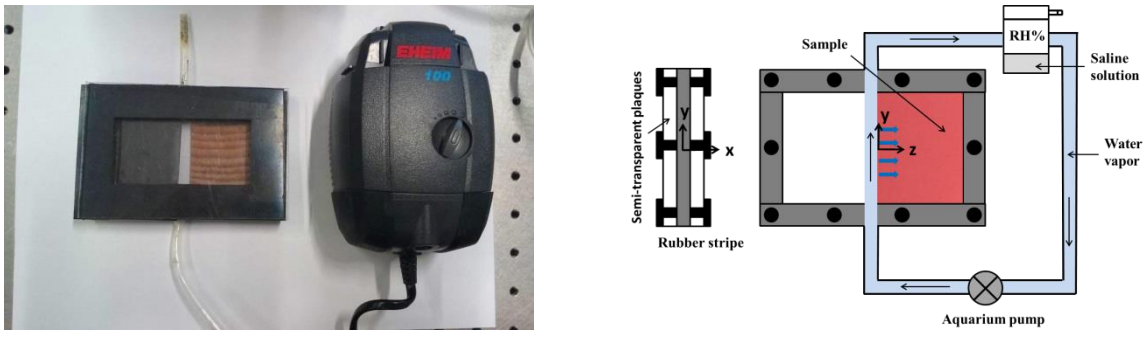

(a) (b)

Figure 2-19: Principle of the hydric excitation device. (a) An aquarium pump next to an enclosure that contains a wood sample insulated by a rubber strip, and (b) the complete scheme of the excitation device.

Based on the axis system presented in Figure 2-19, we assume that the water transfer starts at $z = 0$ and mainly progresses towards the z axis of the sample. Moreover, due to the small thickness of the sample compared to the in-plane dimensions, we assume that the hydric field

is constant along the x axis, for a given *z*. The homogeneity of the hydric exchange along the *y* axis will be presented in chapter 4.

5 Conclusion

In this chapter, we focused on the development of an instrument capable of realizing *THz* imaging in transmission mode based on a *THz*-to-*IR* camera imaging system associated with a scanning motorized stage and a *THz* Gunn diode. The aim was to focus on the development of a versatile experimental tool for characterizing heat and mass transfers by the contactless measurements of water content. To this end, the major idea is to combine a sample scanner system, an *IR* camera and a THz-to-thermal converter into a single device able to transform a simple IR camera to a broadband *GHz* to *THz* one. To avoid external artifacts and deviations, a special lock-in technique was developed by the synchronization of the incident *THz* beam and the acquisition of the camera. To realize that goal, a particular *THz* integration time was created.

With all these developments, we are able to monitor a sample area of 5 *cm* x 5 *cm* with an acquisition frequency of 1 *Hz* and an *SNR* of approximately 1000. This acquisition frequency is currently limited by the power density of the *THz* Gunn diode.

In addition, this *THz* camera is connected to a sample scanner with an extreme flexibility (in terms of geometry) and with a high speed of movement. Indeed, the speed of displacement is proportional to the angular velocity of the motors. The latter can be extremely fast, on the order of 130 *Hz* (or displacements per second) over the entire range of angular positions, and can reach a displacement every 400 μs for a reduced area. The sample scanner is coupled to translation plates to study heterogeneous materials (or systems) of sizes from millimeters up to a meter.

Thus, in view of the very large number of possibilities offered by the system, one of the major contributions of the rest of this work lies in the development of robust acquisition and characterization methods.

Chapter III: Description of the quantum bolometric *THz* camera, acquisition, capability and efficiency

While the previous chapter was focused on the experimental setup design, this chapter presents (i) a complete modelization of the thermal conversion of the *TTC* and then (ii) a benchmark of four numerical lock-in methods (four images algorithm, synchronous detection, Fourier analysis and ordinary least squares). With the best method, (iii) a gallery of some example of images are presented, followed by (iv) a complete simulation of the acquisition chain for the case of tomography of a homogeneous semitransparent sample and for the case of thermotransmittance of a homogeneous sample submitted to a heat pulse thermal response.

It should be remembered that the method developed in this work is easy to implement and that it is based on a linear baseline subtraction associated with a four images algorithm and a singular value decomposition to retrieve the best-quality *THz* imaging. This procedure is implemented directly on the acquisition software because the raw images measured by the camera are not workable, as explained in this chapter.

1 *TTC* modeling, sensitivity and limits

As shown in Figure 3-1, the complete setup corresponds to a sum of transfer functions linked to each step of the measurement method.

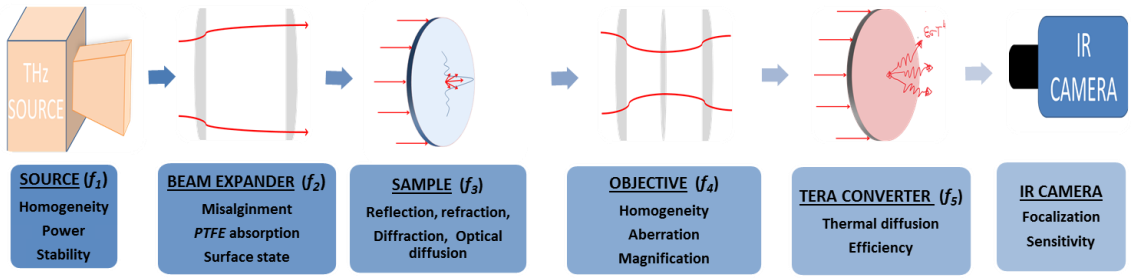

Figure 3-1: Scheme of the complete measurement chain.

As mentioned in the conclusion of chapter 2, the measured images are not immediately workable due to many issues that we are going to analyze in this part. It is important to underline that all the problems coming from geometrical optics or optical interactions between the sample and the electromagnetic wave are neglected in this study.

Figure 3-1 shows that the *THz* beam is emitted with the first transfer function f_1 corresponding to the manufacturer's specificities, beam divergence, beam homogeneity, beam polarization, etc. Then, a second transfer function (f_2) related to the geometrical optic drawbacks corresponds to the beam expander design with two plano-convex Teflon lenses. This crucial part for measurement quality (i.e., the homogeneity of the raw and expanded beam) is far from being optimized in our setup. In fact, this homemade beam expander is not perfectly designed; moreover, due to the important divergence of the reference beam, as well as the misalignment of the lenses and their absorption of the *THz* (*PTFE*), optical artifacts could appear causing beam deformation and achromatism. The major consequence is that the reference beam is not homogeneous, causing the nonuniform detectivity of our camera system. The third transfer function (f_3) is the heart of the thesis problem and represents the physical interaction between the *THz* wave and the phenomena occurring inside the sample. In this work, the phenomena we have considered are (i) Beer-Lambert attenuation to realize *THz* imaging or tomography and (ii) heat and mass transfers inside the sample. The final challenge of this work is to detect variations in the incident beam linked with the physical properties. It is worth mentioning that these dependencies exhibit quite different orders of magnitude, as illustrated in the Figure 3-2.

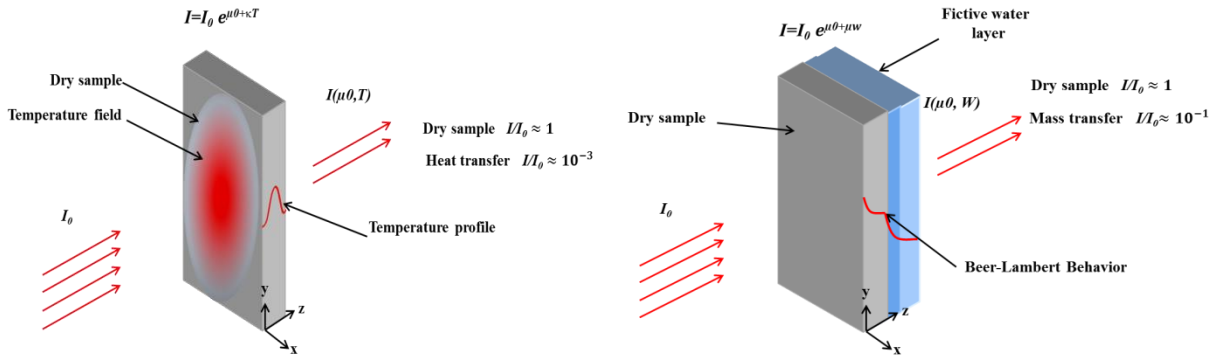

(a) (b)

Figure 3-2: Order of magnitude of the attenuation function depending on the observed physical phenomenon: (a) thermotransmittance during heat transfer and (b) Beer-Lambert during mass transfer.

Again, although several optical problems are possible (such as diffusion, diffraction and reflection, depending on the sample characteristic size, roughness, and heterogeneity), they are not taken into account here. Moreover, additional electromagnetic artifacts that influence the *THz* beam crossing the sample can be pointed out. In the case of the near-field configuration (sample near the *TTC*), the proper emission of the sample shows an influence on the *TTC* response.

In the far-field configuration, a fourth transfer function (f_4) appears with the same drawback as that of the beam expansion transfer function, with problems linked to geometrical optics, magnification, sharpness of the focalization, etc.

If we do not consider the *IR* camera drawback (well known in the literature), the last transfer function (f_5) corresponds to the *THz*-to-*IR* conversion by using the thin carbon sheet. The heat transfer of the thermal conversion, the characteristic time and the thermophysical properties (i.e., the transient thermal response) affect the images detected by the *IR* camera. Finally, the *IR* camera detects the temperature increases of the *TTC*.

Improving the obtained images thus requires an understanding of the transfer functions mentioned previously. The transfer function of the source (f_1) depends on internal performance of the source and its modulation. Moreover, experimental calibration aims to align the beam expander and objective to minimize the optical diffraction and beam deformation, and thereby, transfer functions f_2 and f_4 are neglected. However, beam deformation and diffraction are always present and correspond to the curved surface of lenses and the beam-material interaction in lenses. The electromagnetic artifacts are neglected, and the sample proper emission effects are avoided by conducting experiments in far-field configuration.

Therefore, transfer function f_5, representing the TTC response, will be detailed in section 1. Comprehension of the TTC response is a key step to understanding the image processing necessary to obtain the amplitude of the THz beam. In addition, transfer function f_3, presented by the Beer-Lambert law with heat transfer, will be showed in section 4 through the numerical modeling of the measurement chain.

1.1 Principle of thermoconversion

The thermoconverter (*TTC*) represents a thin homogeneous carbon-based paper with a thickness between 15 μm and 30 μm and a thermal diffusivity of 4.16 10^{-7} $m^2.s^{-1}$ [80]. The *TTC* is assumed to be a blackbody in the *IR* domain (Figure 3-3-a) with an absorbance equal to 1 in the spectral range of the *IR* camera. Moreover (Figure 3-3-b), the *TTC* is semitransparent in the *THz* range with an absorbance equal to 0.6 in the wavelength range of the Gunn diode used in this study (1 *mm to 3 mm*).

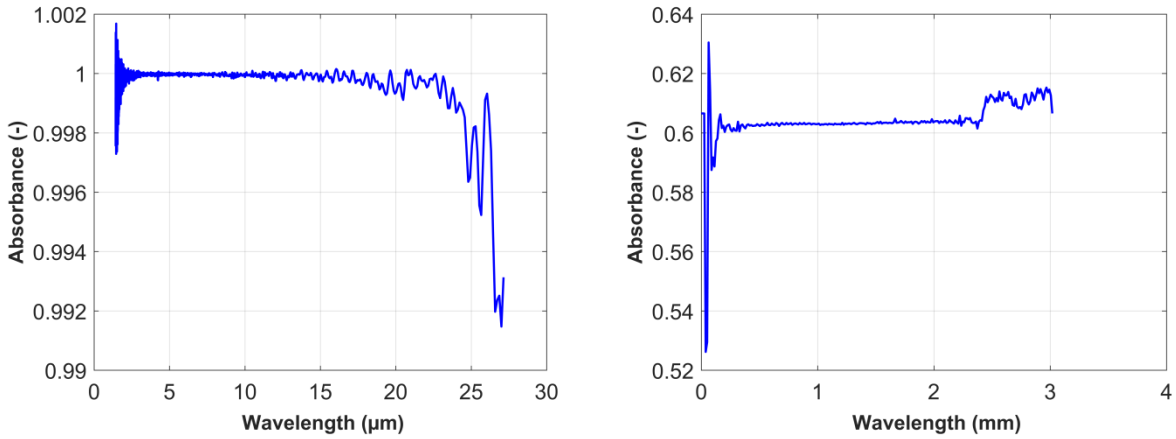

(a) (b)

Figure 3-3: Photothermal converter absorbance spectra: (a) from the near- to far-infrared (1 μm to 25 μm) and (b) in the millimeter range (0.1 *mm* to 3 *mm*).

As illustrated in Figure 3-3, from a thermal point of view, when the *TTC* is illuminated with a *THz* source, it creates a volumetric thermal source that generates heat diffusion in the converter. This indirect measurement of the true optical shape of the incident beam is based on the inversion of the complete thermal problem to retrieve a kind of initial condition. Nevertheless, by using Dirac excitation or lock-in modulation, it is possible to assume that the true optical shape corresponds to the volume source for short times.

Figure 3-4 presents a schema of the thermal conversion. Some well-established assumptions of a lumped body can be proposed to simplify the thermal modelization of the complete problem. First, due to the large ratio between the diameter (d = 5 *cm*) and the thickness of the *TTC* (e = 15 μm), the temperature through the thickness is considered constant (i.e., only a *2D* and transient thermal problem can be considered). The second assumption is that, as the absorption of the incident beam is a function of thickness (Beer-Lambert law), the heat-source power is considered constant along the thickness due to the large ratio between the wavelength (~2.7 *mm*) and the carbon-paper thickness (~15 μm). Moreover, we assume that convective and radiative heat losses occur where the incident *THz* radiation becomes an internal source for the *TTC*.

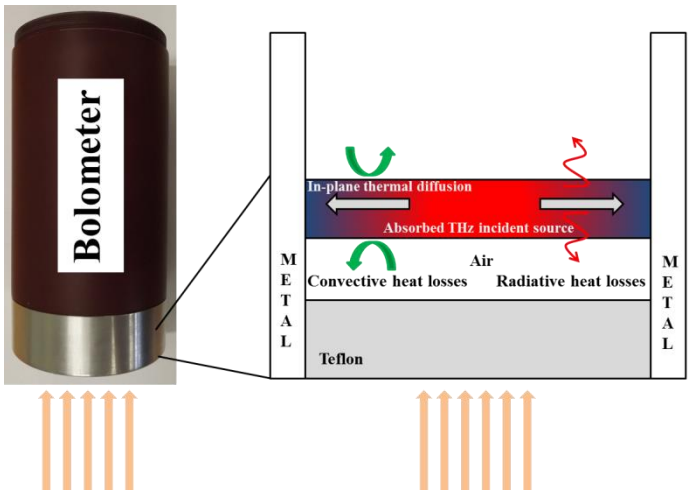

Figure 3-4: Scheme of the *heat diffusion problem* in the *TTC*.

1.2 Modelization of thermal conversion

As mentioned in the previous paragraph, the thickness of the carbon sheet is much smaller than the wavelength, and the source is homogeneous along *z*. As a consequence, the thermal response of the *TTC* to an excitation is the *2D* transient solution of the heat transfer equation with convective and radiative losses. The numerical finite-volume equation modeling the heat transfer with the heat source and heat losses is given by equation (3-1).

$$Fo_{i,j}\Delta T_{i,j}^{k} + \Phi_{i,j}^{k} - Bi_{i,j}\left(T_{i,j}^{k} - T_0\right) = \delta T_{i,j}^{k} \tag{3-1}$$

where F_o is the Fourier number given by $\frac{a_{i,j}\Delta t}{\Delta x^2}$, with $a_{i,j}$ as the thermal diffusivity of the *TTC* in ($m^2.s^{-1}$) and Δt (s) and Δx (m) as the time and space discretization steps; Φ (K) is the equivalent heat source given by $\frac{Q_0\Delta t}{\rho C_p V}$ (with Q_0 (W) as the incident *THz* beam power, ρ C_p as the volume specific heat ($J.m^{-3}.K^{-3}$) and V as the volume (m^3)); B_i is the Biot number given by $Bi = \frac{2h_{i,j}\Delta t}{\rho C_p e}$, with $h_{i,j}$ as the equivalent convection coefficient given by $h_{i,j} = h + 4\varepsilon\sigma T_0^3$ (where h is the natural convection in ($W.m^{-2}.K^{-1}$), σ is the Boltzmann constant equal to 5.67 10^{-8} $W.m^{-2}.K^{-4}$, ε is the emissivity coefficient of the *TTC*, T is the temperature (K), and T_0 is the ambient temperature (K)), e as the thickness (m), and the indices i and j representing the position in the discretization grid; and the exponent k represents the time step. Moreover, the thermophysical properties are the diffusivity (α = 4 10^{-7} $m^2.s^{-1}$), specific heat (ρC_p = 10^6 $J.m^{-3}.K^{-1}$) and conductivity (λ = 0.5 $W.m^{-1}.K^{-1}$). The convective coefficient is supposed to be h = 8 $W.m^{-2}.K^{-1}$, the pixel size is $\Delta x = \Delta y$ = 250 μm and the time step is 200 *ms*.

By numerically solving this equation with the previous parameters and the following acquisition rate of 5 *Hz* and image pixel size of 256 x 256 *pixels*, the obtained results are presented in Figure 3-5.

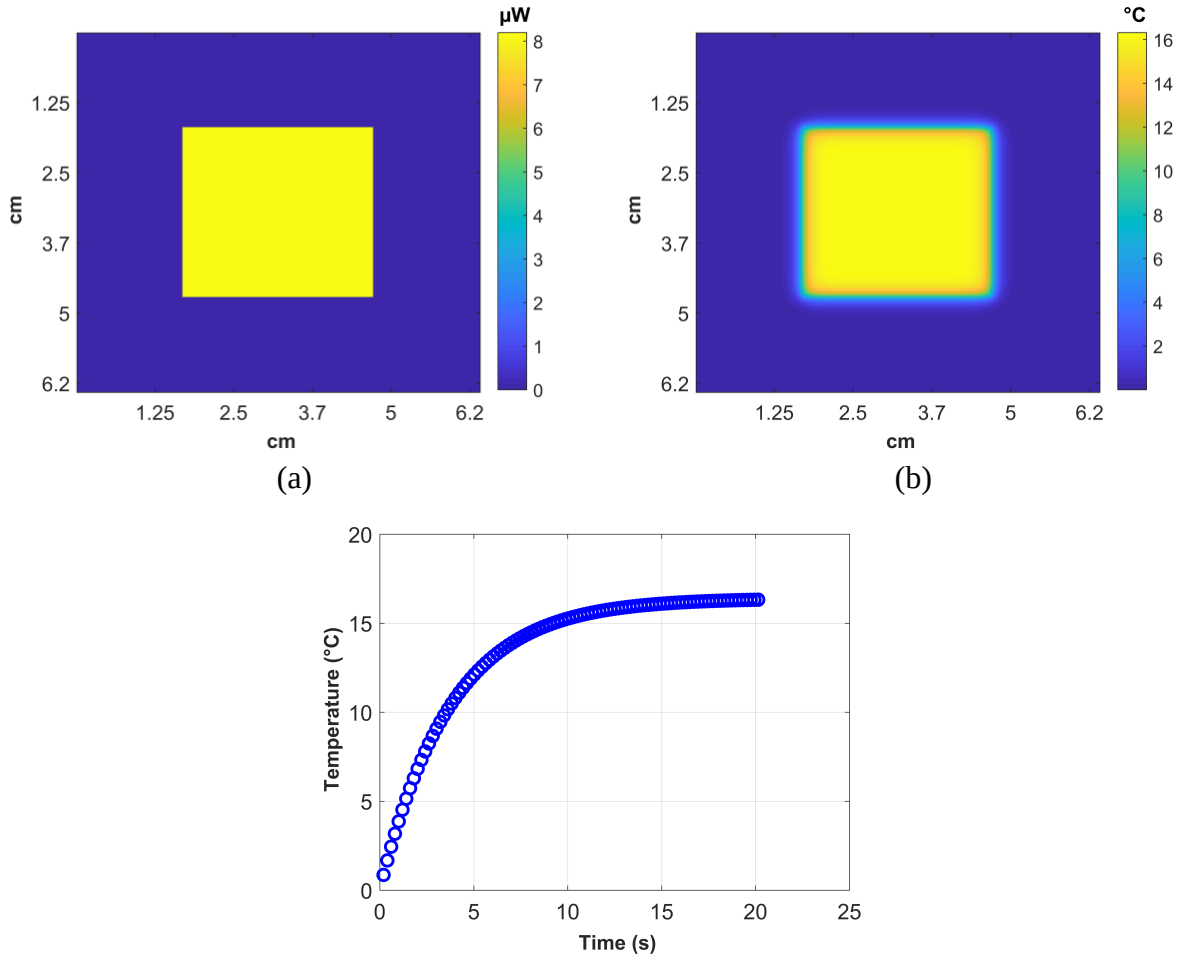

Figure 3-5: Thermal modeling of the converter: (a) the incident *THz* beam power Q_0 in (μW), (b) the temperature distribution at steady state and (c) the temperature evolution as a function of time.

Figure 3-5-a shows the incident *THz* beam calculated with the power of our source and the absorbance of the *TTC*. Here, we assume that the incident source is homogeneous. Figure 3-5-b shows the temperature response of the *TTC* at steady state (i.e., after 20 *s* of diffusion). Figure 3-5-c shows the temperature response of the pixel in the center of the images as a function of time. Note that the steady-state regime is reached after 20 *s* with the thermophysical properties of the *TTC* and a convective coefficient value of $h = 8\ W.m^{-2}.K^{-1}$.

This first calculation points out the effect of thermal diffusion (Figure 3-5-b) on the sharpness of the calculated images and the long time (20 *s*) required to reach complete steady state. For this reason, we are going to demonstrate that some strategies can be used to bypass such drawbacks to improve the quality and the time of image acquisition. One way to control this effect is to work in lock-in mode, consisting of the modulation of the incident source with a signal generator (see section 3-4 in chapter 2).

The performance of the *TTC* can be evaluated through an estimation of the conversion rate. The conversion rate is the ratio between the thermal flux measured by the *IR* camera (Φ) and the imposed heat flux. The radiative heat flux released by the *TTC* and measured by the *IR* camera is given by equation (3-2).

$$\Phi_{i,j}^{k} = \varepsilon\sigma S\left(T_{i,j}^{k\,4} - T_0^4\right) \tag{3-2}$$

The temperature $(T_{i,j}^{k})^4$ in ($°C$) can be calculated through a comparison of the *DL* to the $°C$ calibration curve given by the camera manufacturer and is indicated in equation (3-3).

$$T(°C) = IT\left(\mu s\right)\left[-7.27\times10^{-12}\times T_{DL}^4 + 328.3\times10^{-9}\times T_{DL}^9 - 5.8\times10^{-3}\times T_{DL}^2 + 52.77\times T_{DL} - 164.76\times10^3\right] \tag{3-3}$$

T_{DL} is the pixel-based signal in the digital level (*DL*), and *IT* (s) is the integration time of the *IR* camera. Therefore, the conversion rate is given by the ratio in equation (3-4).

$$\tau_{i,j}^{k} = \frac{\varepsilon\sigma S\left(T_{i,j}^{k\,4} - T_0^4\right)}{Q_{0i,j}^{k}} \tag{3-4}$$

where $\varepsilon\sigma S\left(T_{i,j}^{k\,4} - T_0^4\right)$ represents the measured thermal flux by the *IR* camera and $Q_{0i,j}^{k}$ is the imposed heat flux in (μW). Figure 3-6 shows the conversion rate at the central image pixel as a function of time.

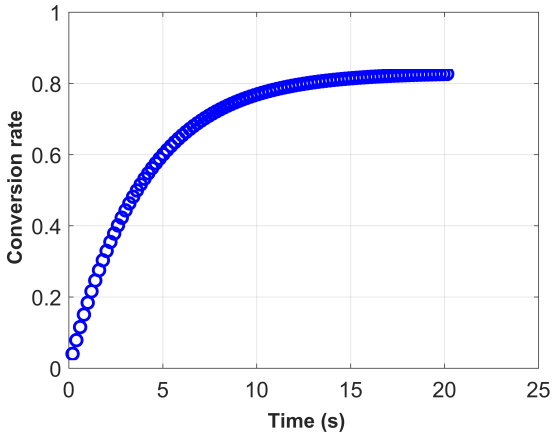

Figure 3-6: Maximum conversion rate as a function of time.

Figure 3-6 represents the conversion rate as a function of time obtained with the homogeneous shape of a square beam possessing the assumed parameters of incident power and beam size. The plot shows that the conversion reaches 80 % at steady state (20 *s*) but is approximately 10 % for short times ($t < 1$ *s*). In this time range, the diffusion length is less than 2 *pixels* [73]. Since the conversion is calculated as a function of parameters such as the incident power and the surface of the beam, a parametric study of the temperature and conversion rate is proposed in the next paragraph.

1.3 Sensitivity of the *TTC*

As shown in equation (3-4), the conversion rate is the ratio between the flux measured by the *IR* camera (ϕ) and the incident power (Q_0). Since the incident power is independent of source the, the flux (ϕ) depends on the temperature increase of the *TTC* (equation 3-4) and on the surface of the excitation beam. However, the temperature of the *TTC* detected by the *IR* camera also depends on the in-plane diffusion of heat within the *TTC*. Therefore, the conversion rate would depend mainly on the incident power (Q_0), in-plane diffusion and the shape of the beam (source for the *TTC*).

1.3.1 Diffusion control

As explained previously, the *THz* beam represents a source for the thin carbon sheet, and following this excitation, the temperature of the *TTC* increases, as shown in Figure 3-5. However, in order to detect the *TTC* response, the *IR camera acquisition* frequency (ranging from 1 *Hz* to 1 *kHz* with an integration time between 1 μs to 1 *ms)* and the *THz* modulation frequency (ranging from 0.1 *Hz* to 1000 *Hz)* should be synchronized. This means that the *THz* source frequency is modulated with the onset of the acquisition, which allows the camera to record movies during the source period. The modulation aims to avoid the in-plane diffusion, and thereby, improve the detection of the *THz* beam by the *IR* camera (Figure 2-14). The characteristic time of diffusion can be determined using the diffusivity of the carbon paper and the paper thickness, as given by equation (3-5).

$$e = \sqrt{\frac{a}{\pi . f}} \tag{3-5}$$

$$t_c = \frac{\pi . e^2}{a} \tag{3-6}$$

where e is the *TTC* thickness (m) and a is the thermal diffusivity ($m^2.s^{-1}$). Since the *1D* transfer along the thickness of the *TTC* is assumed to be instantaneous, the diffusion is mainly in the *TTC* plane. According to equation (3-5), the diffusion depth corresponding to a characteristic time of 1 s is 350 μm (~1.5 px). Thus, in order to limit the thermal diffusion depth at 1.5 px, the *THz* integration time should not be longer than the characteristic time (~1 s). It should be indicated that due to the difference in wavelengths (λ) of the *IR* and *THz* ranges, a pixel in the *THz* image that has an order of magnitude of ~1 *mm* x 1 *mm* is the equivalent of 4 pixels in the *IR* image, where the pixel size is 250 μm. Therefore, the in-plane diffusion (350 μm) can be considered to be submillimetric (< 1 *mm*).

Decreasing the modulation frequency enables, on the one hand, reaching the steady-state regime of the *TTC* response (long time), which increases the conversion rate to (80 %) (see Figure 3-6). On the other hand, the in-plane diffusion within the *TTC* becomes important and blurs the images. In addition, a high modulation frequency allows, on the one hand, for a decrease in the in-plane diffusion; however, on the other hand, the amplitude is reduced, leading to a decrease in the signal-to-noise ratio (*SNR*) and to noise in the image. For that, a

compromise in the choice of modulation frequency should be taken to limit the in-plane diffusion within the *TTC* and to maintain a high *SNR*.

1.3.2 Effect of beam size

The influence of the incident beam size is checked to reveal the shape that provides a high conversion rate. A power of 20 μW per pixel was applied with different uniform beam shapes: a point heat source, a small square heat source (16 *px* x 16 *px*) and an extended square heat source. Figure 3-7 shows the *TTC* thermal response at a given instant for the different heat-source shapes.

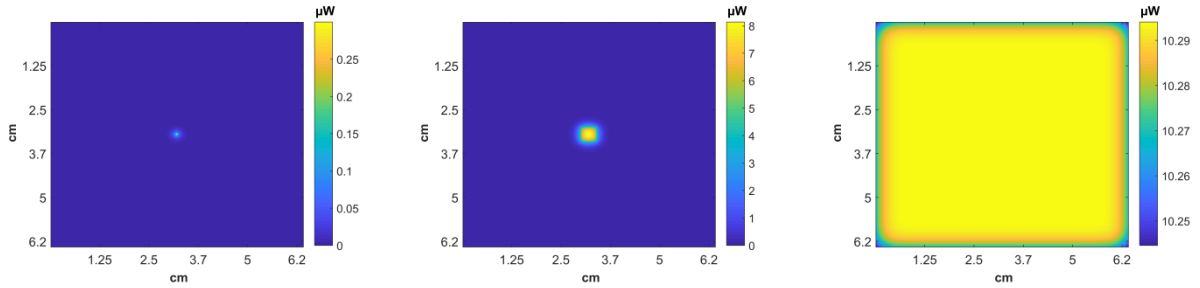

(a) (b) (c)

Figure 3-7: Heat-source geometry (steady-state case): (a) a point source, (b) a small square source and (c) an extended uniform heat source.

The thermal responses and the maximum conversion rates are presented as functions of time in the Figure 3-8.

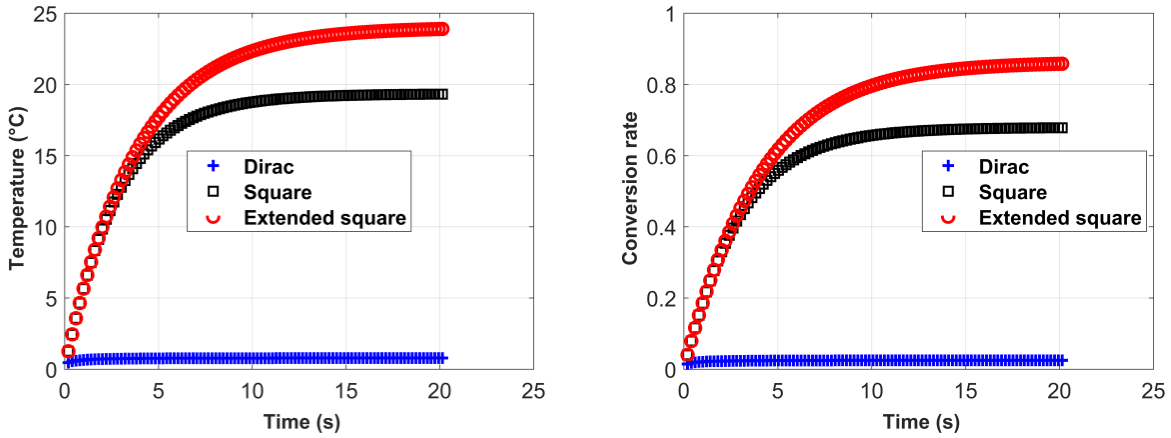

(a) (b)

Figure 3-8: Influence of the incident beam shape on (a) maximum thermal response for each case, (b) conversion rate as function of time.

Figure 3-8-a, shows that the thermal response of the *TTC* corresponds to the thermal response of a lumped body with heat losses. Moreover, Figure 3-8-b shows the conversion rate calculated using equation (3-4). The uniform extended heat source provides a high conversion rate. However, in the case of the point heat source, the influence of in-plane diffusion (the *2D* effect of heat transfer) is clear, and the transient phase duration is 2 *s;* however, the conversion rate is 0.02. The square beam reaches the steady-state regime earlier,

but the rate conversion is lower than that of the extended square. Therefore, the size of the beam seems to be proportional to the conversion rate. At time $t = 1\ s$ (integration time), the conversion rates are 2 % and 20 % for the presented case. Therefore, the conversion rate can be presented as a function of beam size (pixels number) in the transient (1 *s*) and steady-state cases. Figure 3-9 shows the effect of beam size for two different cases.

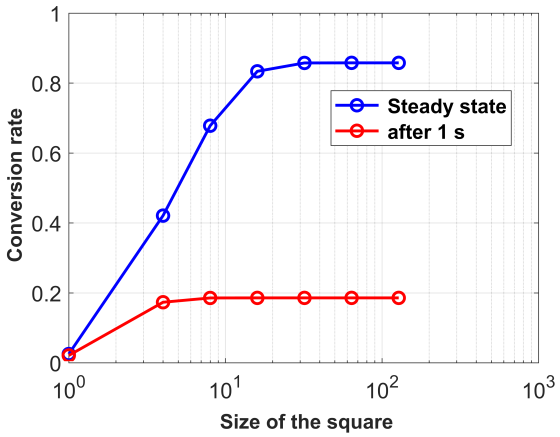

Figure 3-9: Conversion rate as a function of beam size (semilog scale) for the transient and steady-state cases.

Figure 3-9 shows that in the transient case ($t = 1\ s$), the maximum obtained conversion rate is 20 %. However, the conversion is almost the same when the beam-size area is bigger than 16 *px*. For the steady-state case ($t = 20\ s$), the conversion is maximum and reaches 80 % with a 16 *px* beam area. However, this time is long with respect to the characteristic time of in-place diffusion, and thereby, the integration time.

As the modulation is carried out at 1 *s*, the *THz* beam has to be expanded as much as possible to increase the conversion rate, as shown in Figure 3-8. However, working with small modulation frequencies leads to not only higher conversion rates but also higher in-plane diffusion, and thereby, a blurred image. Therefore, a compromise between increasing the conversion rate and decreasing the in-plane diffusion should be considered with respect to modulation.

1.3.3 Influence of incident power

According to equation (3-4), the flux is linked to the temperature via Boltzmann's law. The conversion rate can be presented as a function of the incident power. According to equation (3-4), the relationship between the incident power and the conversion rate is nonlinear. Figure 3-10 shows the effect of incident power on the conversion rate of a beam having a Gaussian shape in the steady-state case.

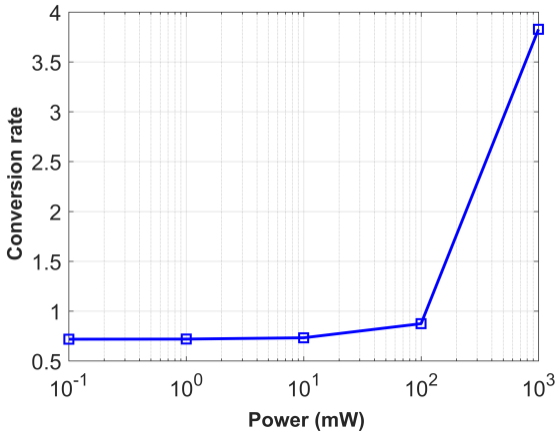

Figure 3-10: Conversion rate as a function of the incident source power.

In the simulations, the maximum imposed power is 1 *W*, corresponding to a temperature of 200 °*C*. For an incident power between 0.1 *mW* and 10 *mW*, the conversion rate is 70 %, which increases to 0.87 at a power equal to 100 *mW*. Then, the rate increases drastically to 4 at an incident power of 1 *W*.

1.3.4 Synthesis

Finally, the parametric study reveals the effect of the beam shape, incident power and modulation frequency on the conversion rate. It is proven that a beam with an extended uniform shape provides a higher photothermal efficiency, which justifies experimental expanding of the beam. Moreover, the incident power has to be approximately 100 *mW* to totally convert the incident *THz* beam. In addition, when choosing the modulation frequency, a compromise has to be made between maximizing the conversion rate and limiting the in-plane diffusion. To summarize, an expanded incident beam with a power of 100 *mW* and a modulation frequency of 1 *Hz* allows for a conversion rate of 10 % and an in-plane *TTC* diffusion limited to 360 μm. However, the modulation requires image processing to extract the amplitude for each period (film). The next section details a comparison between the different image processing methods aiming to extract workable information from the raw signal detected by the camera.

1.4 Detectability

The *NEP* of a detector is the optical power incident to the detector that results in an *SNR* of 1 [81]. It represents the threshold above which a signal can be detected. The minimum detectable power (P_{min}) can be calculated as follows:

$$P_{\min} = NEP(\lambda) \times \sqrt{IT} \tag{3-7}$$

where *NEP* is the noise equivalent power and *IT* is the measurement bandwidth (integration time). For an IT of 800 μs at room temperature, the minimum temperature variation corresponding to 1 *DL* signal of the *IR* camera is approximately 3 *mK*. In this case, the

detectivity of a single pixel (size of 250 μm) is found to be equal to 160 $pW.Hz^{-0.5}$ per pixel when only 0.2 of the total flux is converted.

The sensitivities of detectors employing bolometric or other detection approaches based on the developed infrared imager adjusted to *THz* frequencies are compared. In the literature, the *NEP* values of *THz* detectors for the *IRXCAM*-160 and *IRXCAM*-384 cameras at 70.4 μm (4.25 *THz*) were reported to be 79 and 24.7 $pW\ Hz^{-0.5}$, respectively [82]. In addition, *NEP* values that can vary from 26 $pW\ Hz^{-0.5}$ [83] to 260 $pW\ Hz^{-0.5}$ [84] have been reported for *FPA*s based on antenna-coupled FETs for *THz* detection (*TeraFET*s), which have been implemented in standard *CMOS* technology. The difference in the average *NEP* value can be explained by differences in pixel size, detector bandwidth and pixel responsivity.

2 Lock-in method to improve the acquisition

2.1 Principle of thermal lock-in

The lock-in method was proposed in 1979 by Gerhard Busse [85], who, for the first time, experimented with this technique in the field of nondestructive testing of aluminum samples containing localized defects at different depths. The experimental setup (Figure 3-11) consists of two halogen lamps to thermally excite the front face of the sample to be studied. These lamps are connected to a low-frequency generator creating a sinusoidal periodic modulation. This modulated thermal excitation then consists of an average component (offset) and a sinusoidal component. The infrared camera is connected to a synchronous detection system (lock-in amplifier), which is synchronized with the low-frequency generator.

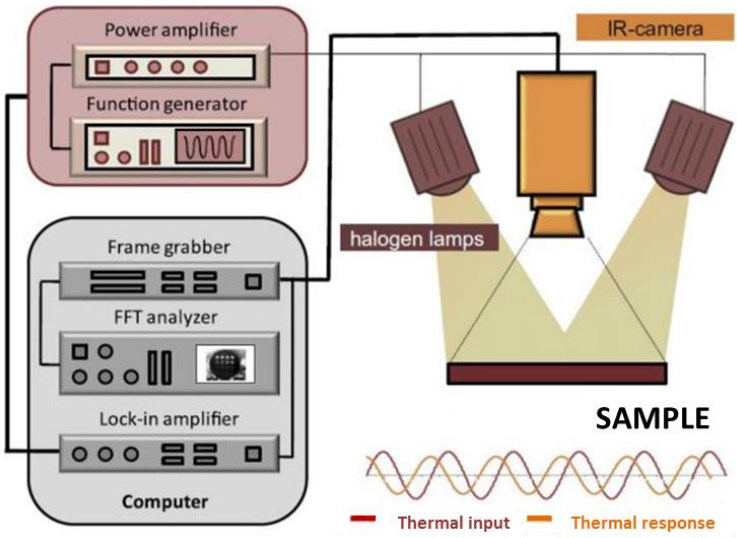

Figure 3-11: Lock-in thermography measurement principle [86].

From the contrast of the recorded infrared images, two types of signals can be distinguished: signals incoming from nondefective zones and those incoming from zones presenting defects. A study of the phase and amplitude of the differences between these two types of signals allows for revealing the presence of the defect. The "4-images method" [87] is applied to calculate the phase and amplitude. The technique recovers 4 values every quarter of the signal period, thereby reconstructing the signal (see equation 3-8 and Figure 3-12).

$$A(x_i) = \sqrt{(S_1(x_i) - S_3(x_i))^2 + (S_2(x_i) - S_4(x_i))^2}$$
$$\phi(x_i) = arctg\left(\frac{S_1(x_i) - S_3(x_i)}{S_2(x_i) - S_4(x_i)}\right) \quad (3\text{-}8)$$

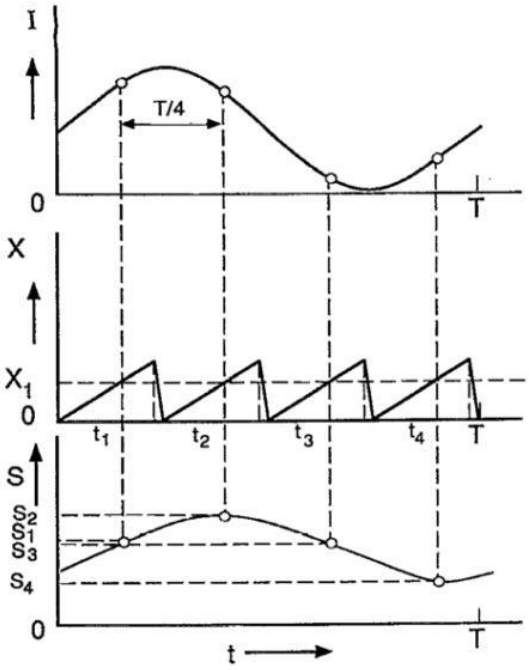

Figure 3-12: Principle of the four-images method. On top: the excitation wave as a function of time, in the middle: the scanning radiometer signal allowing retrieval of the 4 values of all period quarters, and at the bottom: a reconstruction of the signal from the previous acquisition. [88].

The depth of the defect can be calculated from the following expression:

$$\mu_d = cst\sqrt{\frac{a}{\pi f_{exc}}} \tag{3.9}$$

where *Cst* is a constant, which is 1 for amplitude or 1.8 for phase [89]; a is the thermal diffusivity ($m^2.s^{-1}$); and f_{exc} is the frequency of the incident sinusoidal wave in (*Hz*).

The lock-in method increases the spatial resolution by decreasing thermal effects, such as convection. In addition, the approach is very insensitive to measurement noise because the estimations of amplitude and phase are carried out using a large amount of data due to the periodic nature of the problem. In contrast, the length of thermal penetration depends directly on the frequency of the modulation of the halogen lamps. Hence, defects present in the material can be found at different depths that are unknown beforehand. Thus, it is necessary to proceed by "sweeping" at different modulation frequencies (starting from the characteristic frequency) of thermal excitation to target the exact depth of the defect to be revealed, which can be tedious in the case of a thick sample.

2.2 Influence of environment during lock-in measurements

The previously presented thermal lock-in method is used only in a periodic established state. As the objective of the study is to increase the camera acquisition frequency, we need to work as function of time without waiting in this regime. Moreover, especially for wetting or drying processes, the characteristic time of the experiment could reach a few days. For these reasons, we have to optimize the lock-in detection to avoid the *TTC* time response and environment drift and fluctuation. To point out this periodic drift, a wood sample, without any physical process (i.e., a steady heat and hydric state), is scanned during 2 d with the following procedure: a movie of 50 images (1 s duration) is recorded every 15 *min* in the near-field configuration, as shown Figure 3-13. Preprocessing is carried out with the software controlling the camera (Altair®) by applying the nonuniformity compensation (*NUC*), which allows for cleaning of the noise by deleting the background noise of a blackbody. Figure 3-13 shows the effect of the environment temperature on the *TTC* response during the measurement using the *TTC* near-field setup at stationary state (no heat and mass transfers occur) over 50 hours.

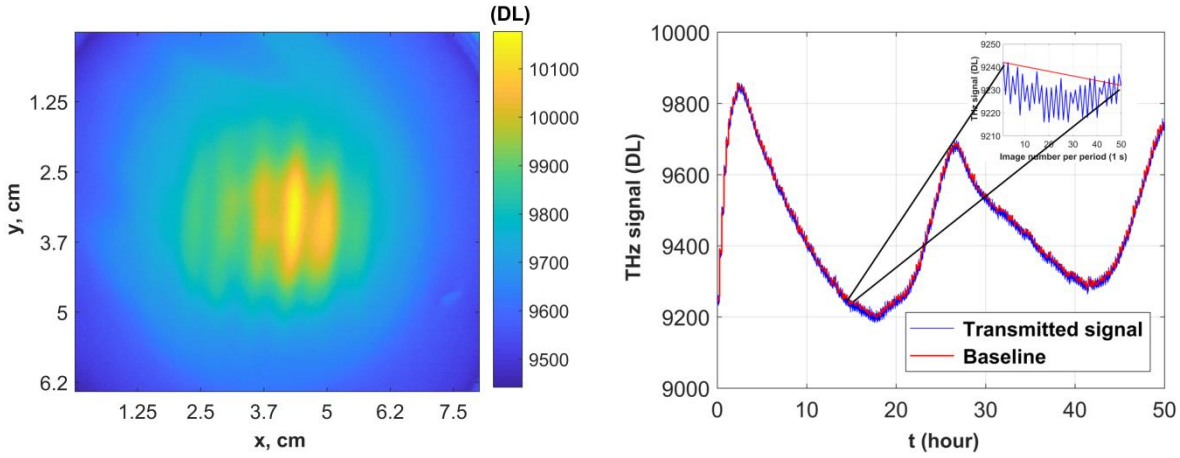

(a) (b)

Figure 3-13: (a) Raw image of the wood sample in the near-field configuration and (b) the influence of the environment temperature on the measurement during 50 hours.

Figure 3-13-a represents an image of the transmitted signal in the near-field configuration for the wood sample. Figure 3-13-b shows the *THz* signal taken at pixel (175, 135) of the image presented in Figure 3-13-a. It shows that the environment temperature variation influences the signal baseline, which changes periodically during night and day.

The obtained images are highly covered by the continuous component (response of the *TTC*). Moreover, environment noise such as light or temperature fluctuations in the room affects the *TTC* and *IR* camera during the experiment, mainly for experiments lasting tens of hours (mass diffusion experiment, for example).

The objective of this part is to find the best methodology to process the raw images (see Figure 2-16 of chapter 2) obtained by modulation of the source and synchronization between the source and camera (lock-in mode). In fact, in this study, there are main points that are crucial and need to be optimized to retrieve the best images with the complete TTC chain.

These points are as follows: ***(i) increase the SNR ratio and acquisition frequency****, (ii) remove the effect of the* ***"short time" periodic established state of the TTC*** *(variation due to the transient initial condition) and* ***longtime deviations*** *(air conditioner, night and day cycle, etc.) of the complete measurement chain (especially during the drying or wetting process) and (iii)* ***find the best method to numerically calculate the signal amplitude****. The two first points have been introduced and studied in the previous section, and the third one will be studied here.*

By combining all these points, the challenge is important, with the main problem based on the "true" calculation of the amplitude of the modulated signal when the baseline is a function of time. Therefore, the objective is to estimate the amplitude at short times in order to overcome the *TTC* characteristic time as well as natural environment deviations. As explained in the previous section, the thermal response of the *TTC* reaches steady state after 20 *s*. However, the modulation (source on/off) is carried out at 1 *Hz*, which means that the transient thermal response occurs every modulation period (every 1 *s*). Therefore, the processing method should overcome the transient effect and estimate the amplitude.

2.3 Presentation of the different lock-in methods

To extract the amplitude, several methods are benchmarked. The lock-in amplification method (*LA*), the four images algorithm method (*FIA*), signal Fourier analysis (*SFA*), and the ordinary least square method (*OLS*). These methods are applied on a numerical signal and then compared to choose the best method for estimation. For that, a numerical signal has been created with and without noise and with a continuous part. First, the principle of each method is depicted, and the results obtained with the generated function are presented and commented on. Finally, a comparison of the methods based on different parameters, such as noise, number of points per period and number of periods is carried out. Once the accurate method is chosen, it is applied in chapter 4.

2.3.1 Lock-in amplification method (synchronous detection)

The lock-in amplifier is a signal measurement and analysis method. It was developed as an electrical instrument capable of extracting the amplitudes and phases of a signal buried in a noisy environment (low signal/noise ratio, *SNR*) [90]. The principle of the lock-in amplifier is shown in Figure 3-14.

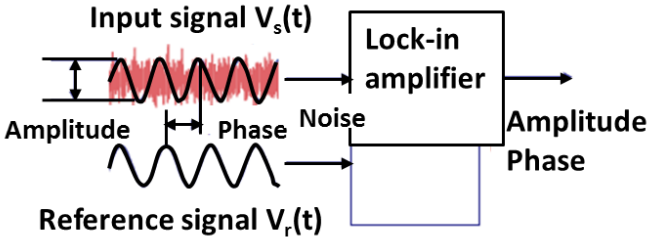

Figure 3-14: Lock-in amplifier for measuring the amplitude and the phase of a signal entirely buried in noise [91].

It is based on the homodyne detection scheme and low-pass filtering relative to a periodic reference signal. The lock-in measurement allows for extracting the amplitude by rejecting all other frequency components. It requires a signal with a similar or even different frequency than the sought signal frequency. This method is applied in several domains, including the measurement of low tension blurred by noise (such as in the sensing or transmission of modulated signals, infrared thermography and the measurement of the diffusivity of materials. Therefore, the lock-in amplifiers are versatile and aim to increase the signal/noise ratio through signal modulation.

In general, during measurement, noise is multifarious and can be caused by radiation, noise related to the measuring apparatus, etc. This noise influences the output data, because it covers the measured signal. The noise can be external, such as light falling on the infrared camera, the room temperature, day/night (if experiment lasts several hours), or internal, e.g., coming from the apparatus. Soft-computing detectors, such as infrared cameras, integrate methods to diminish the effects of background noise, reduce the number of dead pixels and maintain good image quality. For example, in FLIR infrared cameras, a calibrated thermal imaging camera generates nonuniformity compensation (*NUC*) coefficients that are applied in real time to obtain high-quality images.

The coefficients comprise an *NUC* table and are typically valid for a specific subset of the total operating temperature range. Consequently, there are multiple *NUC* tables to span the full operating temperature range, and the camera automatically selects the optimum table based on its temperature. Often, the obtained images (raw data) need to be processed in order to extract the amplitudes of useful signals. Experimentally, the modulation of signals also allows improving the *SNR* that is harmed by the low-frequency noise often related to the apparatus. However, several methods of signal and image processing can be applied to diminish the noise in space and/or time, such as the singular value decomposition of extracted amplitudes.

The lock-in amplification of a signal is based on the following stages: the amplification of its input with a reference signal, also called downmixing or homodyne/heterodyne detection, and then the adjustable low-pass filtering of a variable cut-off frequency is applied to the results [91-93]. This method is called demodulation and allows the isolation of a signal at a frequency of interest from the other frequencies. Demodulation can be performed with a reference signal (sine or square wave).

As shown in Figure 3-15, the experimental signal (Y) (or input signal) is split and separately multiplied with the reference signal (Y_{ref}) and its 90° phase-shifted signal. Then, the outputs pass through a low-pass filter, resulting in Y_1 and Y_2. The amplitude (A) and phase (φ) can be derived from Y_1 and Y_2 by a transformation from Cartesian to polar coordinates.

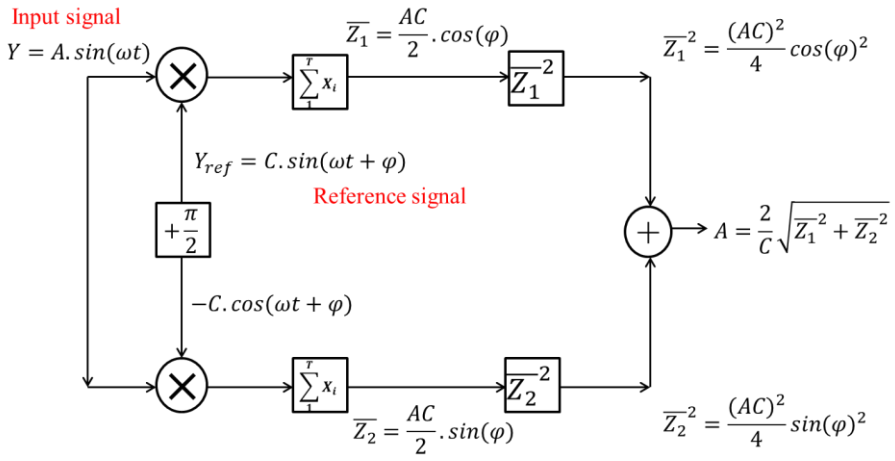

Figure 3-15: Diagram of the lock-in amplification principle.

Mathematically, the signal is supposedly blurred in low-frequency noise. The noise is thought to be Gaussian with a mean of zero and an amplitude of 10 % of the signal that has been chosen. The signal can be then defined as follows:

$$Y = A\sin(2\pi ft) + N \tag{3-10}$$

Y is the signal blurred in noise N, f is the excitation frequency, A is the amplitude of the excitation to estimate, and N is given as follows:

$$N = N + \varepsilon \tag{3-11}$$

$\overline{N}$ and n are respectively the mean value and size of the signal with $\overline{N} = 0$. The reference signal has a known amplitude and frequency that can be equal to the excitation signal, and it is given as follows:

$$Y_{ref} = C\sin(2\pi ft + \varphi) \tag{3-12}$$

φ is the phase of the signal sent to the synchronous detection. Therefore, the signal of detection is given as follows:

$$Y_{de} = AC\sin(2\pi ft)\sin(2\pi ft + \varphi) + NC\sin(2\pi ft + \varphi) \tag{3-13}$$

The lock-in amplification represents the time-weighted mean of the amplifications of the signal in time for each instant. Thus, the quantities Z_1 and Z_2 can be calculated as follows:

$$Z_1 = \frac{1}{t}\int_0^t A.C.\sin(2\pi fu).\sin(2\pi fu + \varphi)du \tag{3-14}$$

$$Z_2 = \frac{1}{t}\int_0^t N.C.\sin(2\pi fu + \varphi)du \tag{3-15}$$

As the noise (N) does not depend on frequency, which represents a constant at each instant, then:

$$Z_2 = \frac{NC}{2\pi fT}\left[\cos\left(2\pi fu + \varphi\right)\right]_0^t \tag{3-16}$$

$$Z_2 = \frac{NC}{2\pi fT}\left[\cos\left(2\pi fT + \varphi\right) - \cos\left(\varphi\right)\right]_0^t \tag{3-17}$$

Therefore, the integral of Z_2 along the period T is equal to zero. By the other hand, the quantity Z_1 is given as follows:

$$Z_1 = \frac{1}{t} A.C \int_0^t \sin\left(2\pi fu + \varphi\right).\sin\left(2\pi fu\right)du \tag{3-18}$$

Equation (3-18) can be integrated by using the following trigonometric formula:

$$\sin(a)\sin(b) = \frac{1}{2}\left(\cos(a-b) - \cos(a+b)\right) \tag{3-19}$$

Therefore, equation (3-18) can be written as follows:

$$Z_1 = \frac{AC}{2t}\left[\underbrace{\int_0^t \cos(\varphi)du}_{Y_1} - \underbrace{\int_0^t \cos\left(2\pi fu + \varphi\right)du}_{Y_2}\right] \tag{3-20}$$

As Y_1 is independent of t, when t tends to T, $Y_1 \rightarrow 0$, and then:

$$Z_1 = \frac{A.C}{2T}\cos(\varphi).T = \frac{A.C}{2}\cos(\varphi) \tag{3-21}$$

Moreover, the obtained equation for the amplification of the noised signal with a (π/2)-phased reference signal is carried out as follows:

$$Y_{de}^{'} = -AC\sin\left(2\pi ft\right)\cos\left(2\pi ft + \varphi\right) - NC\cos\left(2\pi ft + \varphi\right) \tag{3-22}$$

The amplification of equation (3-22) can be calculated as follows:

$$Z'_1 = \frac{1}{t} A.C \int_0^t \cos\left(2\pi fu + \varphi\right).\sin\left(2\pi fu\right)du \tag{3-23}$$

The following trigonometric relationship is used to calculate the integral along a period:

$$\sin(a)\cos(b) = \frac{1}{2}\left(\sin(a-b) + \sin(a+b)\right) \tag{3-24}$$

Thus, equation (3-24) can be written as follows:

$$Z'_1 = \frac{AC}{2t}\left[\underbrace{\int_0^t \sin(\varphi)du}_{Y'_1} + \underbrace{\int_0^t \sin(2\pi fu + \varphi)du}_{Y'_2}\right] \tag{3-25}$$

When *t* tends to *T*, equation (3-25) becomes:

$$Z'_1 = \frac{A.C}{2}\sin(\varphi) \tag{3-26}$$

Therefore, the modulus can be calculated as shown in Figure 3-15. Hence:

$$Z_1^2 + Z'^2_1 = \left(\frac{A.C}{2}\right)^2 \tag{3-27}$$

As the amplitude of the amplifier (*C)* is a known data (reference signal), the amplitude (*A*) can be estimated for each period as follows:

$$A = \frac{2\sqrt{Z_1^2 + Z'^2_1}}{C} \tag{3-28}$$

The amplification of the signal with two phased reference signals allows the increase of the signal-to-noise ratio (*SNR*). Then, the demodulation of the signal allows for the estimating of the amplitude. During a period, a significant estimation of the amplitude is obtained when the time integration tends to a period. Therefore, the minimum number of periods allowing a significant estimation has to be calculated. To find the necessary number of periods for a given error, the integral along time *t* of the sinusoidal function should be equal to the error. Thus:

$$\frac{1}{t}\int_0^t \sin(2\pi ft)dt \le 0.01 \tag{3-29}$$

Or:

$$\frac{1-\cos(2\pi ft)}{2\pi ft} = 0.01 \tag{3-30}$$

This function is equal to zero if $\frac{2\pi t}{T} = \pi + 2k\pi$, and then, the minimum number of used periods to obtain 1 % of error is:

$$t = \frac{1}{2}T(1+2k) \tag{3-31}$$

Therefore, the minimum number of periods (k) is given by:

$$\frac{1-\cos\left(\pi\left(1+2k\right)\right)}{\pi\left(1+2k\right)}=0.01 \tag{3-32}$$

Thus, the minimum number of periods to estimate with less than 1 % of error is 30, as shown in Figure 3-16.

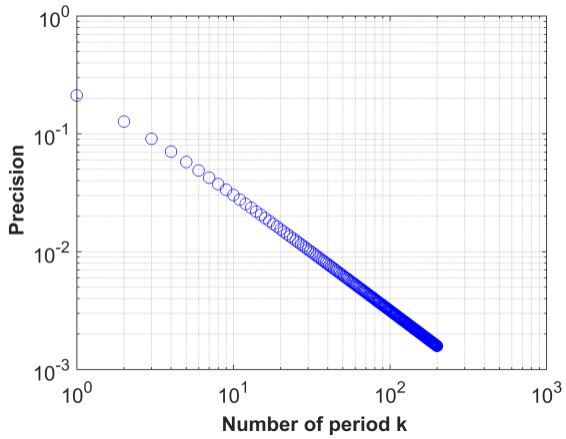

Figure 3-16: Calculated error as a function of the number of periods.

2.3.2 Four-images method

The four images technique is a method of image processing used to extract the amplitude of a modulated signal blurred in noise [73, 87]. The four-images method consists of calculating the sum of a signal (S_i) for each quarter of a period (T/4). Figure 3-17 shows the amount calculated during the four quarter periods used in an amplitude estimation.

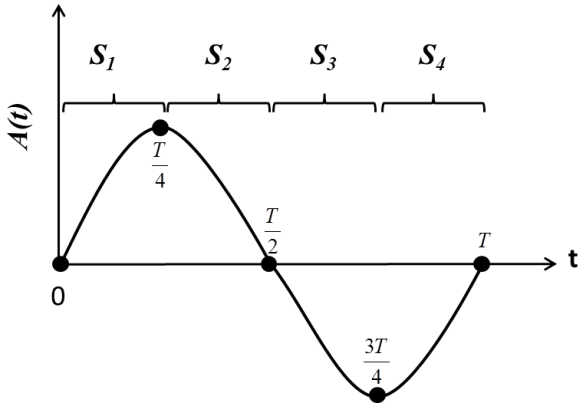

Figure 3-17: Calculated magnitudes of S_1, S_2, S_3 and S_4 for each quarter period.

The four images algorithm consists of calculating the sum of the signals at each quarter of a period, as shown in Figure 3-17. The calculated signals correspond to the following integrals given by equation (3-33).

$$s_1 = \int_0^{\frac{T}{4}} I(x,y,t)\,dt \qquad s_2 = \int_{\frac{T}{4}}^{\frac{T}{2}} I(x,y,t)\,dt$$
$$s_3 = \int_{\frac{T}{2}}^{\frac{3T}{4}} I(x,y,t)\,dt \qquad s_4 = \int_{\frac{3T}{4}}^{T} I(x,y,t)\,dt \tag{3-33}$$

where S_1, S_2, S_3, and S_4 are the signals integrated at each quarter of a period, and I represents the signal of each pixel recorded on the camera at instant t. These magnitudes are used to estimate the amplitude and phase as follows:

$$A(x,y) = \frac{1}{N_{ppp}/n}\sqrt{(S_1 - S_3)^2 + (S_2 - S_4)^2} \tag{3-34}$$

$$\varphi(x,y) = \arctan\left(\frac{S_1 + S_2 - S_3 - S_4}{S_1 - S_2 - S_3 + S_4}\right) \tag{3-35}$$

where A is the estimated amplitude, N_{ppp} is the number of points per period, n is the sampling number, and φ is the estimated phase. This method is based on the calculation of integrals, which allows taking into account all the points of a period.

2.3.3 Fourier spectral analysis

The Fourier transform of a function in time is a complex-value function of frequency. The absolute part represents the amount of a frequency present in the function, and the complex component is the phase offset of the basic sinusoid of that frequency [94]. Fourier transform refers to a frequency-domain representation of the original signal. Linear operations performed in one domain (time or frequency) have corresponding operations in the other domain, which are sometimes easier to perform. For example, the operation of differentiation in the time domain corresponds to a multiplication by the frequency, and convolution in the time domain corresponds to an ordinary multiplication in the frequency domain [95]. This means that linear time-invariant systems, such as a filter applied to a signal, can be expressed simply as an operation on frequencies. Once the desired operations are performed, the transformation of the result can be converted back to the time domain through the inverse transform [96].

The continuous Fourier transform is defined as:

$$f(\nu) = \int_{-\infty}^{\infty} f(t) e^{-2\pi i \nu t}\,dt \tag{3-36}$$

where $f(t)$ represents the signal in time domain defined under suitable conditions by:

$$f(t) = \int_{-\infty}^{\infty} f(\nu) e^{2\pi i \nu t} d\nu \tag{3-37}$$

Periodic functions are written as the sum of simple waves mathematically represented by sines and cosines. Due to the properties of sine and cosine, it is possible to recover the amplitude of each wave in a Fourier series using an integral. Fourier transform has some basic properties such as linearity, time shifting, frequency shifting and time scaling. The Fourier transform is applied in several fields, such as differential equation analysis, signal processing and spectroscopy analysis (Fourier transform infrared spectroscopy).

One of the important uses of Fourier transform is to solve the partial differential equations, such as heat transfer equation. First, the equation has to be written in Fourier space, and then the boundary conditions have to be expressed using the properties of the Fourier transform of the derivative. Once the solutions are calculated in Fourier space, they can be expressed in real space by applying a Fourier inversion.

Moreover, in signal processing, Fourier transform is used for the spectral analysis of a time-series. It serves to dissociate the different harmonics composing to the time-domain signal. If the input functions are equally spaced in their input variables (for example time), then the Fourier transform is known as a discrete Fourier transform (*DFT*). The generalization in the case of a discrete function, $f(t) \rightarrow f(t_k)$, is done by letting $f_k \cong f(t_k)$, where $t_k \equiv k\Delta t$, with *k = 1, ... , N-1*. Writing this out gives the discrete Fourier transform:

$$F_n = \sum_{k=0}^{N-1} f_k e^{\frac{-2\pi i}{N} kn} \tag{3-38}$$

where f_k represents the inverse transform $f_k = F_n^{-1}$ given as follows:

$$f_k = \frac{1}{N} \sum_{n=0}^{N-1} F_n e^{\frac{2\pi i}{N} kn} \tag{3-39}$$

$$F_{N-n} = \overline{F_n} \tag{3-40}$$

for *n* = 0, 1, ... , *N-1*, where $\overline{F}$ denotes the complex conjugate.

As a result of the above relation, a periodic function will contain transformed peaks, not in one place but in two. This happens because the periods of the input data become split into "positive" and "negative" complex frequency components. The fast Fourier transform (*FFT*) is an algorithm for computing the discrete Fourier transform (*DFT*). It is a particularly efficient algorithm for performing discrete Fourier transforms of samples containing a certain numbers of points.

2.3.4 Minimization method by ordinary least squares (*OLS*)

The fit-by-minimization method is a method based on ordinary least squares (*OLS*), which is a method used to estimate some parameters of experimental data that have a theoretical function shape. The estimation of parameters consists of the minimization of the objective function. The objective function represents the Euclidian norm of the difference between the theoretical function with the initial parameter values and the experimental data. The estimator represents the value verifying the fixed error between the theoretical values of the model and the experimental data. Once the error reaches the determined value, the values of the parameters are considered to be closest to the exact parameter vectors of the experimental data. Supposing a linear model of n input values with Y_n for all values of input X_n, then the model can be written as follows:

$$Y = S.X \tag{3-41}$$

where Y and X are (n,1) matrices (columns vectors), and S is a square (n,n) matrix called the sensitivity matrix. In the direct problem, the input X is known, and the output of model Y is calculated. Conversely, if Y is known, the solution of equation (3-41) can be given by the inversion of matrix S as follows:

$$X = S^{-1}Y \tag{3-42}$$

The inverse problem is then solved using the exact solution of X. If the output data (Y) are corrupted by noise (ε), it can be written:

$$Y_n = Y + \varepsilon \tag{3-43}$$

Y_n is the noised measurements. Then, retrieving an approximate solution to the inverse problem is accomplished by replacing the exact model (Y) with the noised output (Y_n).

$$X = S^{-1}Y \tag{3-44}$$

$\hat{X}$ is the estimated value of the input using the noised output. Then, $\hat{X}$ represents an ordinary least squares solution of model (3-43) with noisy data Y_n. It can be written as a function of the exact solution (X) as follows:

$$\hat{X} = X + e_x \tag{3-45}$$

where e_x represents the error in the $\hat{X}$ estimate. However, the passage from Y space to X space (the inverse problem) needs the inverse sensitivity matrix (S^{-1}) to be associated with a high amplification of the error (e_x). The amplification can achieve up to 90 %, and this problem is ill-conditioned. The coefficients of amplification [97] can be given as follows:

$$k_a(\varepsilon) = \frac{\left\| S^{-1}\varepsilon \right\|}{\left\| \varepsilon \right\|} = \frac{\left\| e_x \right\|}{\left\| \varepsilon \right\|} \tag{3-46}$$

and

$$k_a(\varepsilon) = \frac{\|S^{-1}\varepsilon\| / \|S^{-1}Y\|}{\|\varepsilon\| / \|Y\|} = \frac{\|e_x\| / \|X\|}{\|\varepsilon\| / \|Y\|} \tag{3-47}$$

where k_a and k_r represent the amplification coefficients of absolute and relative errors, where $\|u\|$ represent the Euclidian norm (L_2) and is defined by $\left(\sum_{i=1}^{m} u_i^2\right)^{1/2}$. These coefficients allow measurement of the effect of the amplification of noise ε on the stability of the solution. However, the estimation of these criteria requires a prior knowledge of the exact solution X. The coefficient k_r shows the transformation of the *SNR* ($\|\varepsilon\| / \|Y\|$) into a relative error estimation ($\|e_x\| / \|X\|$).

Supposing that the we have measurements $Y_i = Y(t_i)$ for a monodetector, then the measurements Y_i are (n x *1*) or (n x p) for a p-multidetector. The associated error matrix for the measurements (ε_n) should satisfy some conditions [98]:

- Additive errors: $Y = Y_{perfect} + \varepsilon$
- Unbiased model: $Y_{perfect} = Y_{mo}\left(X^{exact}\right)$
- Zero mean error: $E[\varepsilon] = 0$
- Constant covariance: $\mathrm{var}[\varepsilon] = \sigma_\varepsilon^2$
- Uncorrelated errors: $\mathrm{cov}\left[\varepsilon_i, \varepsilon_j\right] = 0$ for $i \neq j$
- Normal probability distribution

These conditions mean that the measurements represent the errorless measurements obtained by the perfect model with noise. The noise is supposed to be unbiased and has a zero mean. Moreover, the error covariance matrix (m x m) of the measurement errors contains the variance (σ_ε^2) believed to be constant for each time t_i, and it is defined as follows:

$$cov(\varepsilon) = E\left(\left(\varepsilon - E(\varepsilon)\right)\left(\varepsilon - E(\varepsilon)\right)^T\right) = E\left(\varepsilon\varepsilon^T\right) \tag{3-48}$$

If the error is supposed as uncorrelated, the errors at different instants are independent, which means $E\left(\varepsilon_i\varepsilon_j\right) = 0\big|_{i\neq j}$, and hence, the covariance can be given as follows:

$$cov(\varepsilon) = diag\left(\sigma_{\varepsilon_i}^2\right) \tag{3-49}$$

The model giving output $Y_{i=1:m}$ is a function of independent variables $X_{j:n}$ of n parameters. The classic linear model allowing the simultaneous estimation of the slope and origin

represent linearity with respect to parameters and no variables. In this case, the sensitivity matrix (*S*) shown in equation (3-41) can be given as follows:

$$S_k(t,x) = \left.\frac{\partial y_{mo}(t,x)}{\partial X_k}\right|_{t, X_j \text{ for } \quad i \neq k} \qquad k = 1,...,n \tag{3-50}$$

The linearity of the model makes the sensitivity matrix independent of parameter vector *X*. Moreover, the sensitivity can be calculated for any model (linear or nonlinear) as follows:

$$S(X) = \left(\nabla_X Y_{\text{mod}el}(X)\right)^T \tag{3-51}$$

Assuming that the model is right (by verifying the equation $Y_{mo}(X_{exact}) = Y_{perfect}$) with ($Y_1$, … , Y_m) are noised measurements, and the problem consists of determining the *n* unknown parameters using *m* measurements or observable data (*Y)*. In the case where the observables are bigger than unknowns ($m > n$), the problem to solve is a minimization problem.

A residual vector (r_m) represents the difference between the measurements *Y* (noised data) and the obtained output using the model $Y_{mo}(X)$, and $r(X)$ is given as follows:

$$r(X) = \left(Y_1 - Y_{mo,1} + ... + Y_i - Y_{mo,i} + ... + Y_m - Y_{mo,m}\right)^T \tag{3-52}$$

Moreover, the ordinary least squares objective function represents the square of the Euclidian norm of the residual vector as follows:

$$J_{OLS}(X) = \left\| r(X) \right\|^2 = \left\| Y - Y_{mo}(X) \right\|^2 \tag{3-53}$$

The objective function is then minimized to estimate the unknown parameters (*X*), and in the case where the model is linear, the objective function is given by:

$$J_{OLS}(X) = \sum_{i=1}^{m} \left(Y_i - \sum_{j=1}^{n} S_j(t_i) X_j \right)^2 \tag{3-54}$$

Or in matrix writing, is given by:

$$J_{OLS}(X) = \left[Y - Y_{mo}(X) \right]^T \left[Y - Y_{mo}(X) \right] \tag{3-55}$$

The solution to the minimization of function J_{OLS} corresponds to an estimator of the random vector (noise, ε). If the model is linear, the ordinary least squares estimator does not require the use of an iteration algorithm, and it is formulated as follows:

$$X_{OLS} = arg\left(min\left(J_{OLS}(X) \right) \right) \tag{3-56}$$

In this case, the parameters present in $\hat{X}_{OLS}$ represent numerical approximations that enable the model to be the closest to the set of measurements. Then, it can be written:

$$\nabla_X J_{OLS}\left(\hat{X}_{OLS}\right) = 0 \tag{3-57}$$

On the other hand:

$$\nabla_X J_{OLS}\left(X\right) = 2\left(\nabla_X \left(Y - Y_{mo}\left(X\right)\right)\right)^T \left(Y - Y_{mo}\left(X\right)\right) \tag{3-58}$$

Then:

$$\nabla_X J_{OLS}\left(X\right) = 2S^T\left(Y - SX\right) \tag{3-59}$$

By equalizing equation (3-59) to zero, we find:

$$\left(S^T S\right)\hat{X}_{OLS} = S^T Y \tag{3-60}$$

Therefore, if the matrix S^TS is not singular (the sensitivity coefficients are independent and have non zero norms), the inverse of this matrix allows for obtaining an approximate solution as follows:

$$\hat{X}_{OLS} = \left(S^T S\right)^{-1} S^T Y \tag{3-61}$$

The matrix $\left(S^T S\right)^{-1} S^T$ is the Moore-Penrose matrix (also called the pseudoinverse of matrix *S*). Equation (3-61) represents the ordinary least squares estimator of *X* for any linear model presented by equation (3-41). Moreover, the correlation matrix indicates the accuracy range of the model through the calculation of covariance matrix *C*. The covariance is given as follows:

$$C = \begin{bmatrix} \sigma_1^2 & cov\left(e_1, e_2\right) & \ldots & cov\left(e_1, e_n\right) \\ \vdots & \sigma_2^2 & \ldots & cov\left(e_1, e_2\right) \\ sym & \vdots & \ddots & \vdots \\ \vdots & \vdots & \cdots & \sigma_n^2 \end{bmatrix} \tag{3-62}$$

The diagonal elements are composed of the individual variances of error associated with each component of estimator $\hat{X}_{OLS}$, and the nondiagonal coefficients represent the covariance of crossed errors. In the case when cov(e_i,e_j)≠0, the error at each instant is correlated, and the correlation level between estimations can be quantified by:

$$\rho_{ij} = \frac{\mathrm{cov}\left(e_i, e_j\right)}{\sigma_i \sigma_j} = \frac{C_{ij}}{\sqrt{C_{ii} C_{jj}}} \tag{3-63}$$

The correlation coefficient is a coefficient situated between -1 and +1, representing an independent measurement of errors, and it only quantifies the collinearity of the sensitivity coefficients. This means that no information about error can be obtained from this coefficient. A high correlation is generally represented by $\left|\rho_{ij}\right| \geq 0.9$ [98].

2.4 Study of the best numerical lock-in method

As the goal is to develop a method able to cancel the effect of the baseline fluctuations during the measurements, this study will be performed with a mathematical function with the following general form:

$$Y = \underbrace{A\sin\left(2\pi.f.t+\phi\right)}_{oscillating\ \ part} + N + \underbrace{B - Ce^{-\frac{t}{D}}}_{continue\ \ part} \tag{3-64}$$

where A is the sine amplitude, N is the noise, B the amplitude shift, C is the constant of the carrier function, and D is the exponential coefficient.

- In case (a) of a signal without noise, N, B, C and D are equal to zero.
- In case (b) of a noised signal, B, C and D are equal to zero.
- In case (c) of a noised signal held by a carrier function, A, N, B, C and D are not equal to zero.

Figure 3-18 represents 50 periods of a numerical signal without noise (a), with noise (b) and carried by an exponential function (c), with $A = 0.1$, $f = 1$ *Hz*, $\varphi = \pi/6$, period number = 50 and $N = 0.01$ (10 %).

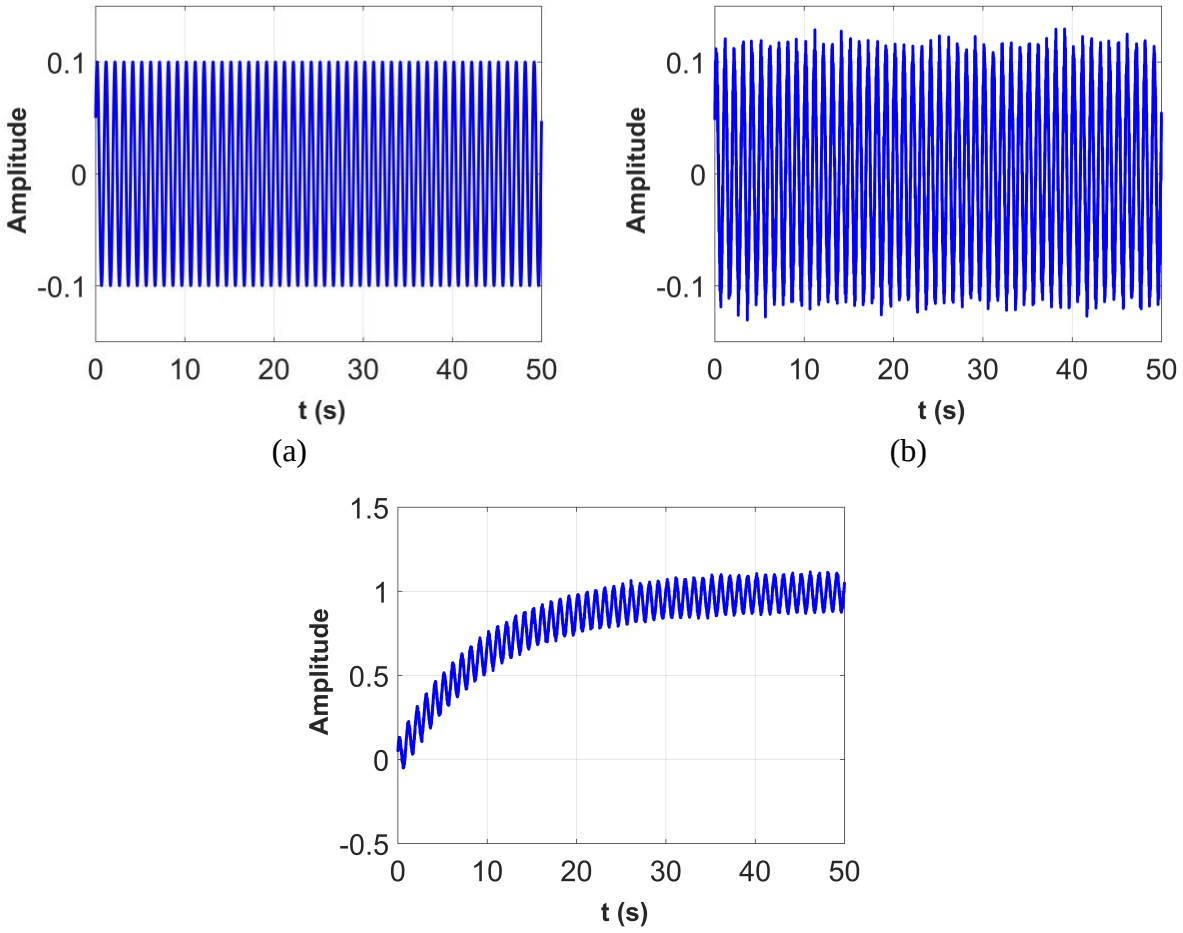

Figure 3-18: Sinusoidal signal in an established state: (a) without noise, (b) a noised signal with an *SNR* of 10 % and (c) a noised signal carried by a continuous exponential component.

For case (c), the continuous component or baseline is an exponential function corresponding to the time response of the *TTC* (see section 1). The correction of the continuous component is carried out by the subtraction of the baseline of each period (film). The baseline represents the curve linking the first and last points of each period. First, an assumption considering a linear baseline for each period is taken into account. This assumption is more accurate when the frequency increases. Therefore, the baseline can be subtracted by a linear fit between the beginning and the end of each period. Figure 3-19 shows the behavior of the baseline in two different cases depending on the frequency modulation.

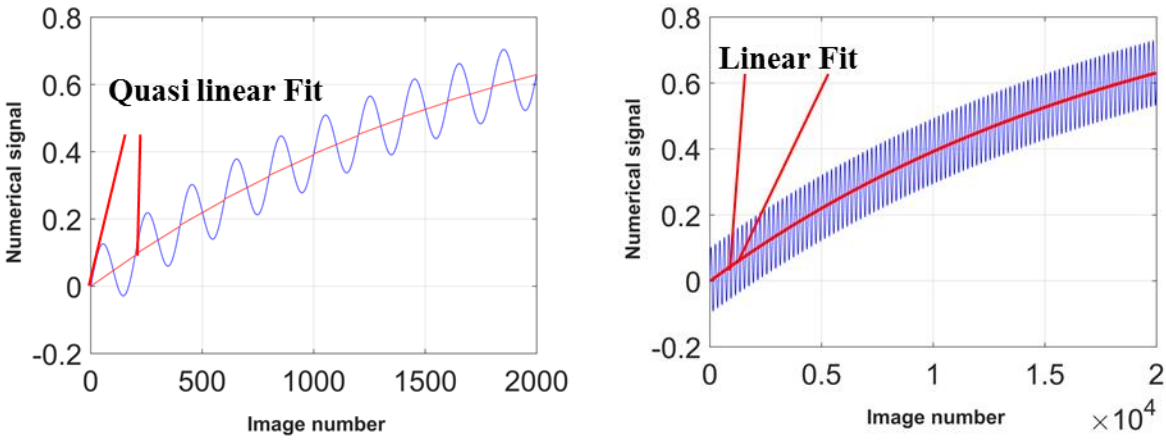

(a) (b)

Figure 3-19: Baselines obtained by linear fits of two modulation frequencies, (a) $f = 1$ *Hz* and (b) $f = 10$ *Hz*.

The increase in frequency allows obtaining a correct linear approximation for each period. However, according to the response of the *TTC* (see Figure 2-14 in chapter 2), the high frequency leads to a signal cut off, which decreases the amplitude and thereby decreases the sensitivity (to temperature or water content). A compromise should be taken in order to maintain good *THz* sensitivity and fast acquisition as well as a high incident source power or amplitude.

In the following sections, the lock-in amplification method, the four images algorithm, Fourier analysis and the ordinary least square method are applied to the three created signals. The objective is to compare the methods when the system is in an established state with and without noise, cases (a) and (b), as well as to determine the noise influence and the robustness of the method when the continuous component is a function of time (case c).

2.4.1 Influence of the continuous component

To determine the influence of the continuous component, numerical simulations corresponding the three cases (see section 2-4) are studied. The estimation of the amplitude is carried out using the four methods proposed in the previous section for each case; four images (*FI*), synchronous detection (*SD*), Fourier analysis (*FA*) and ordinary least square minimization (*OLS*). ***The comparison among the estimations from the different methods allows us to (i) show the influence of a continuous component, regardless of the method; (ii) determine the best method in terms of amplitude, standard deviation and calculation time; and (iii) determine the effect of different parameters such as SNR, number of points per period (Nppp) and number of periods (Np).***

For the first part of the simulations, concerning the influence of a continuous component, a signal presented by equation (3-64) is generated with the parameters: $A = 0.1$, $B = 1$, $C = 1$, $D = 10$, $SNR = 100$ and $f = 1$ *Hz*. The number of periods (*Np*) is fixed to 1. This means that the signal duration is $1\ s$ (which is the equivalent of duration of the *THz* movie in one

experiment). Figure 3-20 represents the results of the amplitude estimations for the different cases using the four processing methods.

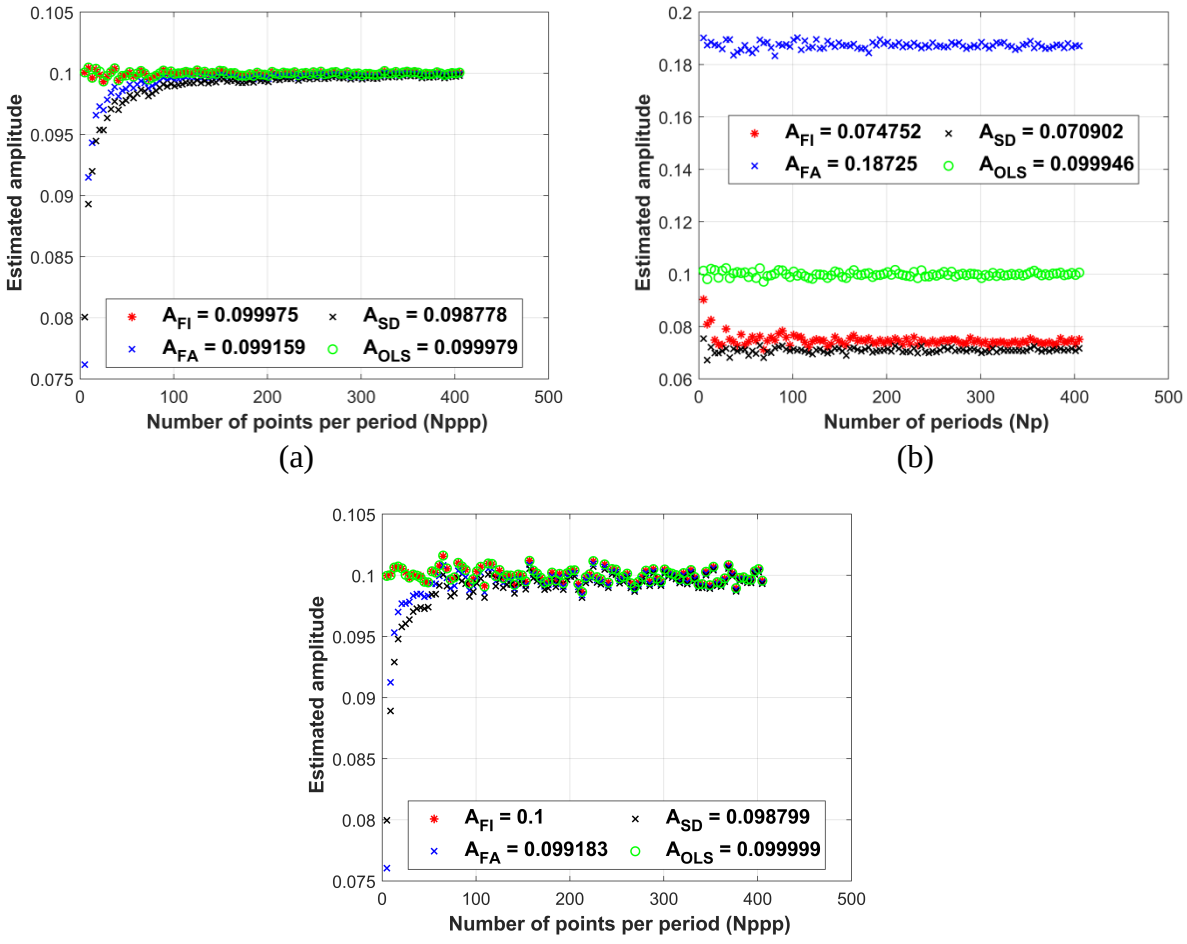

Figure 3-20: Estimated amplitude for one period as a function of different number of points per period using the four methods (*FI*, *FA*, *SD* and *OLS*): (a) the case of a noised signal (*SNR* = 100) without a continuous component, (b) the noised signal (*SNR* =100) with a continuous component and (c) the noised signal (*SNR* =100) with a continuous component but with a subtracted linear-fit baseline.

Figure 3-20-a represents the estimated amplitude for each period, and the overall mean values of the curves are reported in the legend. We remark that at a high number of points per period (*Nppp* > 200), mostly all methods succeed in estimating the amplitude that is close to 0.1 but with dispersed values because of noise (with an error of 2 %). However, for a small number of points per period, the four images and *OLS* methods give the best estimated amplitudes compared to the imposed one. However, for the Fourier analysis and synchronous detection methods, the estimated amplitude values are dispersed with a relative error of 15 %.

Moreover, Figure 3-20-b shows that the ordinary least squares method is able to estimate the amplitude of the noised signal carried by continuous part. The ordinary least squares shows the best estimation. On the other hand, the four images and synchronous detection methods are highly affected (error of 20 %) by the continuous component. Moreover, the

amplitude estimated using the first harmonic in Fourier space does not allow for estimating the amplitude since the first harmonic depends on the continuous part. Therefore, deleting this component is necessary. As mentioned in the previous section, the continuous component can be estimated to be linear (Figure 3-19). Therefore, the continuous part of the signal presented in Figure 3-19 is fitted linearly and then deleted.

Thereafter, the same methods are applied to estimate the amplitude function of a number of points per period with an *SNR* of 100. Figure 3-20-c shows the estimated amplitudes and evidence that the four images and ordinary least square methods show efficiency in estimating the amplitude regardless of the number of points per period. However, the estimation using the Fourier analysis and synchronous detection methods are influenced by the low points per period and tend to the right value with an increase in the number of points. It is shown that the latter methods reach a correct estimation at 200 points per period.

This result is very interesting since one of the advantages of the four-images method is the capability to estimate the amplitude at low *Nppp*. Experimentally, in some applications, such as infrared spectroscopy in microfluidic systems, the number of points per period should be low.

Despite the advantage of the *OLS* minimization over other methods in terms of error, the four-images method presents a lower calculation time. This method presents an estimation time 10-times lower than the calculation time of Fourier and synchronous detection methods and 1000-times that of ordinary least squares. This factor is very important, mainly in the case of image processing where an estimation is done for every pixel. To give an order of magnitude, the amplitude estimation time for one pixel using four images is shown to be $10^{-5}\ s$, while it is $10^{-2}\ s$ for ordinary least squares. This means that the time for measuring an image of $256\ px$ x $320\ px$ takes $0.8\ s$ using four images and $820\ s$ using the *OLS* minimization.

Moreover, similar numerical simulations aiming to reveal the influence of the number of periods on the estimation using the different methods are conducted. For that, the same signal presented by (equation 3-64) and created with the same parameters (*A*, *B*, *C* and *D*) is used, and the number of points per parameter, *Nppp*, and *SNR* are chosen to be 200 *Hz* and 100, respectively. As previously mentioned, the continuous component is deleted using a linear regression for each period. The results of the estimation are shown in Figure 3-21.

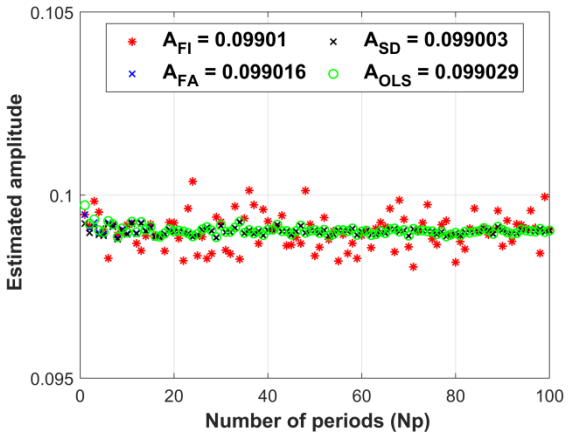

Figure 3-21: Estimated amplitude as a function of different period numbers using the four methods (*FI*, *FA*, *SD* and *OLS*).

Figure 3-21 shows that the number of periods (movies) has no influence on the estimation of the amplitude using the different methods. Experimentally, this result means that instead of recording successive movies by the *IR* camera during the monitoring of a phenomenon, it would be better to take intervals between films (for example, recording movies of 1 *s* each 5 *min* during 10 h), which allows decreasing the amount of data and processing needs.

Moreover, in order to check the noise effect on the estimation, estimations using the four methods at different *SNRs* and a number of periods (*Np*) equal to 1 and a number of points per period (*Nppp*) equal to 100. The results are shown in Figure 3-22.

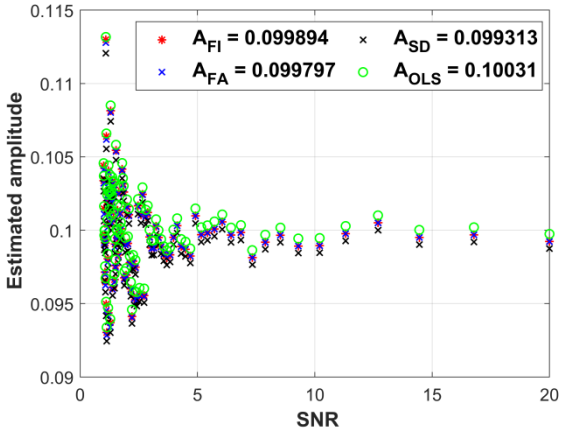

Figure 3-22: Estimation of the amplitude after deleting the continuous part by linear fit using the processing methods (*FI*, *FA*, *SD* and *OLS)* for different *SNRs*.

Figure 3-22 shows that the *SNR* influences the estimation of amplitude for all used methods. As expected, the estimation tends to the right value (0.1) with the increase in *SNR*. Moreover, the methods are influenced in the same way. Therefore, it is justified to work experimentally at an *SNR* higher than 20 with the given parameters *Np* and *Nppp*.

2.4.2 Synthesis and choice of best method

The comparison of the different processing methods allows us to list the following points:

- In the case of a noised signal, the used methods showed efficiency to estimate the amplitude with dispersion. However, the signal-to-noise ratio (*SNR*) influences the estimation (Figure 3-20-a).
- In the case of a noised signal carried by a function representing a continuous component, the ordinary least squares method showed efficiency in estimating the amplitude. However, the minimization of the experimental data needs knowledge of the theoretical shape of the continuous part (supposed as exponential in the numerical simulation). Moreover, the *OLS* minimization method presents a longer time of calculation relative to that of the other methods (Figure 3-20-b).
- Deleting the continuous component represents an important preprocessing step, allowing for removal of the influence of transient response (Figure 3-20-c).
- The four images and *OLS* methods showed an advantage over the other methods in estimating the amplitude after deleting the continuous component. Moreover, the four-images method presents a short time of calculation, which is the main drawback of the *OLS* method.

Due to the advantage of the four-images method in terms of accuracy over the synchronous detection and Fourier analysis and in terms of the time of calculation compared to that of the *OLS*, the four-images method is chosen to process the obtained *THz* images. Moreover, additional image processing methods, such as singular value decomposition (*SVD*), can be used. The *SVD* method allows for reconstructing the images of amplitude through deleting the high-frequency noise (singular modes), which will be detailed in the next section.

2.5 Image filtering using the *SVD*

To reduce the effect of the noise at the end of the lock-in processing, a filter based on singular value decomposition can be applied. This filter allows for improving the image quality through deleting the noise modes (singular high-frequency values) in image data.

Singular value decomposition is the factorization of any *m* x *n* normal matrix (*M*) to a product of matrices as follows:

$$M = U.S.V^T \tag{3-65}$$

where *U* is the orthogonal unitary m x m matrix, V' is the transposed unitary orthogonal n x n matrix, and *S* is a rectangular diagonal m x n matrix. The columns of matrices *U* and *V* represent the left and right singular vectors of *M*. The diagonal values of matrix *S* are decreasing positives values representing the singular values of matrix. Mathematically, the matrices *U* and *V* are rotation matrices, while *S* is a scaling matrix. It should be indicated that the columns of *U* represents the eigenvectors of matrix MM^*, the columns of *V* represent the eigenvectors of matrix M^*M, and the singular values of *S* represent the square root of the eigenvalues of matrix MM^* and M^*M. The *SVD* method is shown in Figure 3-23.

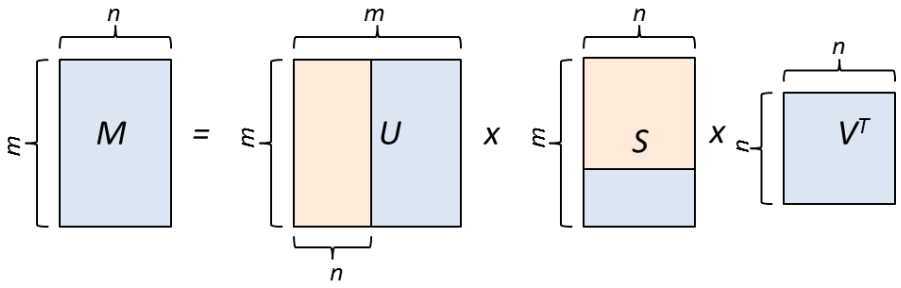

Figure 3-23: Singular value decomposition method.

The *SVD* using only the *n* columns of *U* corresponding to the dimension of *V* is called the "thin *SVD*" [99-101]. The thin *SVD* is quicker in terms of operations and economical in terms of storage, as $n << m$ when *U*, *S* and *V* have the same size (*n* x *n*). In this case, it can be written as:

$$M = \sum_{k=1}^{n} U_k S_k V_k^T \tag{3-66}$$

Moreover, the *SVD* can be a "truncated *SVD*" when the used singular value *k* is less than the dimension *n* of matrix *V*. Therefore, the truncated *SVD* is more economical and quicker than the thin *SVD* since $k << n$. However, the truncated *SVD* is not the exact decomposition of matrix *M* but represents an approximation of *M* of *k* range. The truncated *SVD* is shown in Figure 3-24.

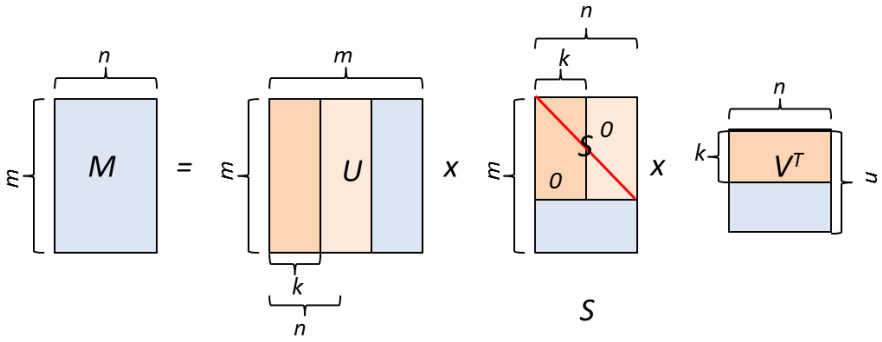

Figure 3-24: Truncated singular value decomposition method.

It can be simplified to:

$$M \approx \sum_{k=1}^{k} U_k S_k V_k^T \tag{3-67}$$

Equation (3-65) shows that the *SVD* method can be used for economical storage by keeping less information (*n* columns of *U* and *n* rows of *S*). Moreover, a good approximation to matrix *M* can be obtained using equation (3-66), allowing less information to be kept and the noise in *M* to be deleted. The *SVD* method allows the separation of combined information in *M* into two orthogonal bases containing decorrelated information in *U* and in *V*. On the

other hand, the higher singular values of matrix *S* contain signal information, whereas the smaller values represent the noise existing in the images.

In image processing, the *SVD* is used to separate the space and time bases and then to denoise the images. Thus, the matrix *U* represents the information in space within *M*, and matrix *V* represents the information in time within *M*. In the *SVD* processing method, deleting most singular values (or modes) drastically reduces the noise but also changes the shape of the signal (image), while deleting only few modes would not sufficiently reduce the noise. Thus, a compromise should be made to efficiently reduce the noise while keeping enough information within images. To determine the number of modes that must be kept nonequal to zero, plotting the modes on a logarithmic scale is suggested. Thus, the number of modes corresponding to the breakpoint represents the number of modes used to reconstruct cleaned-up images. An example of numerical images without and with noise is shown in Figure 3-25.

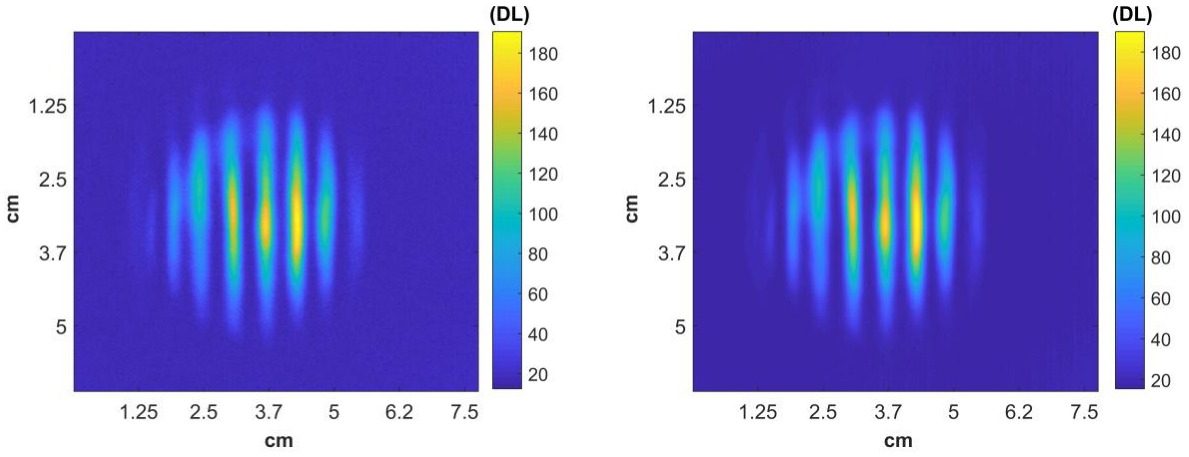

Figure 3-25: (a) Image of a wood sample in the near-field configuration processed with the four-images method. (b) The reconstructed image with the 4-images method and the *SVD* with 4 singular values.

The *SVD* method allows for denoising images, reducing data through truncating the singular values along with their corresponding columns and lines in matrices *U* and *V*. A compromise must be taken to denoise images without losing information and relies on choosing the right number of truncated singular values.

In this chapter, the used methods of processing are presented briefly. The main advantage of the four-images method is that it is based on the integral of a quarter of a period, which avoids losing information. Moreover, it allows reducing the data through estimation of the amplitude. In addition, the singular value decomposition method is used to denoise the image through the separation of space and time information and then to reconstruct the matrix with few truncated modes. Four images and singular value decomposition will be used in chapter 4, where the first measurements with *THz* are presented.

3 Examples of *THz* measurement imaging

After showing the sensitivity of the *TTC* to different parameters such as power and beam shape, a *THz* source of power of 110 GHz is used in experiments where the beam is expanded as much as possible to obtain a homogeneous large beam. The number of points per period (acquisition rate) and the modulation frequency are chosen to be 200 *Hz* and 1 *Hz*. Different images of the beam are shown in Figure 3-26.

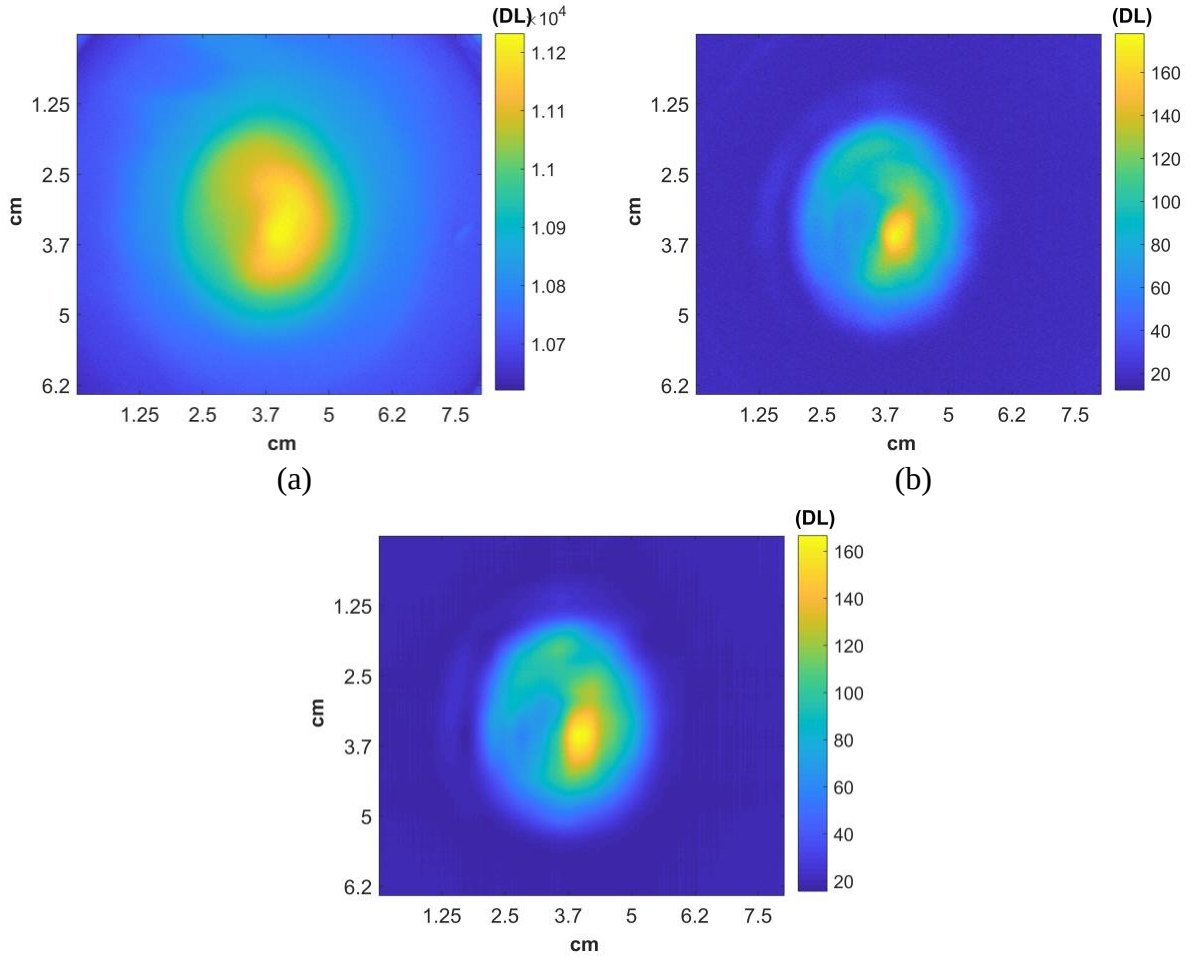

Figure 3-26: Images of a *THz* beam: (a) the raw image, (b) the image processed with the four-images method and (c) the image processed with the four-images method and *SVD* in Digital Level (*DL*).

Figure 3-26 shows different images of the incident beam (without sample). In fact, a slight displacement or misalignment of lenses results in a change in beam shape and homogeneity, which justifies the different images obtained. Hence, the optical deviations mentioned in section 1 can be a major limitation to obtaining homogeneous images. However, deleting the baseline and applying the four-images method to the image shown in Figure 3-26-a produces Figure 3-26-b, where the continuous part is removed (see the signal intensity shown in the color bar).

- **Near-field configuration**

The near-field configuration is a configuration where the sample is placed close to the *TTC* (focal plane of camera). The advantage of this configuration is that the heterogeneity of the sample can be distinguished. To improve the quality of images, processing methods such as the four-images method, the *SVD* method and thresholding of images are proposed. Figure 3-27 and Figure 3-28 show the raw and processed *THz* images of metallic and wood samples taken in the near-field configuration.

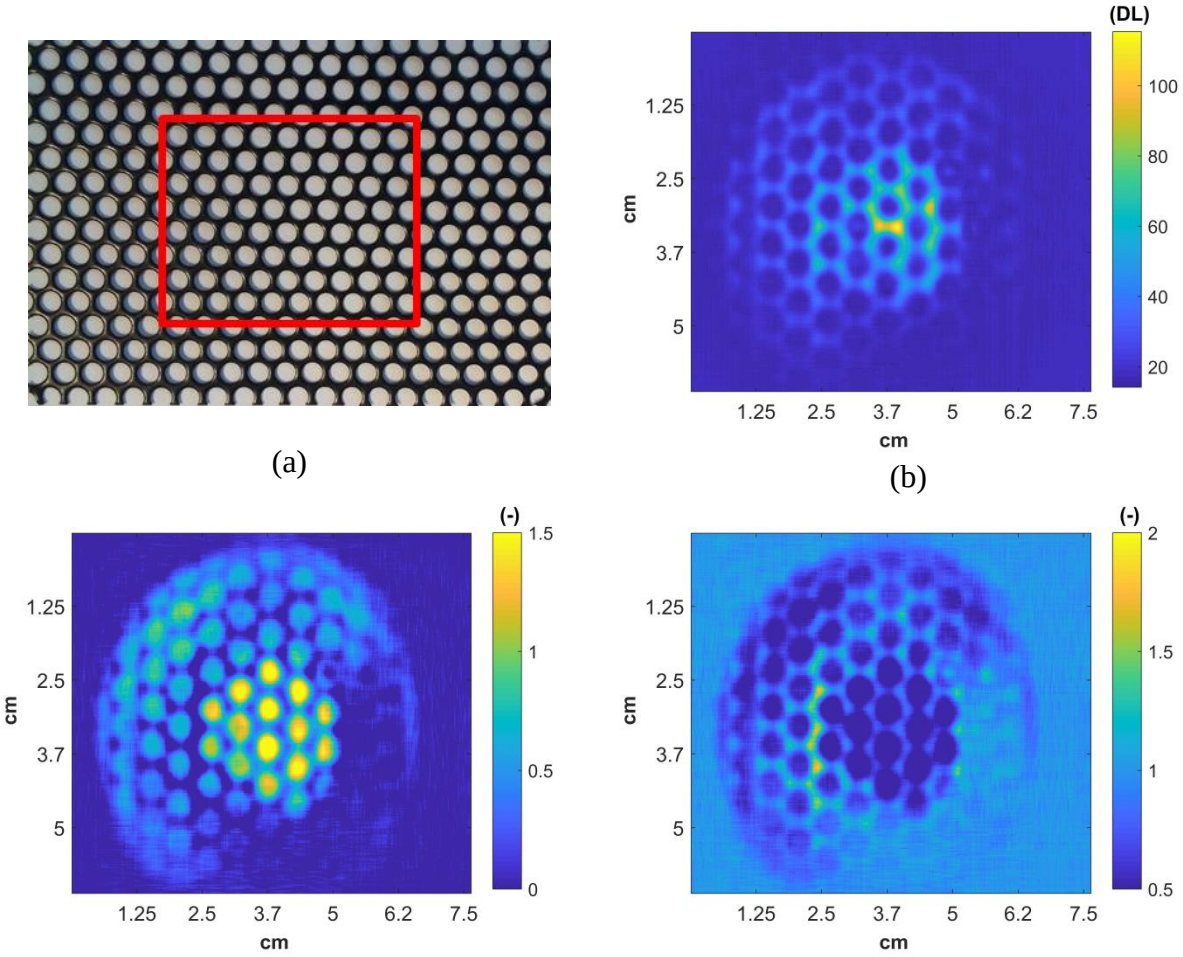

Figure 3-27: Images of a metallic grid: (a) a photo of the grid, (b) the image processed by the four-images method and *SVD*, (c) the transmittance image and (d) the absorbance image.

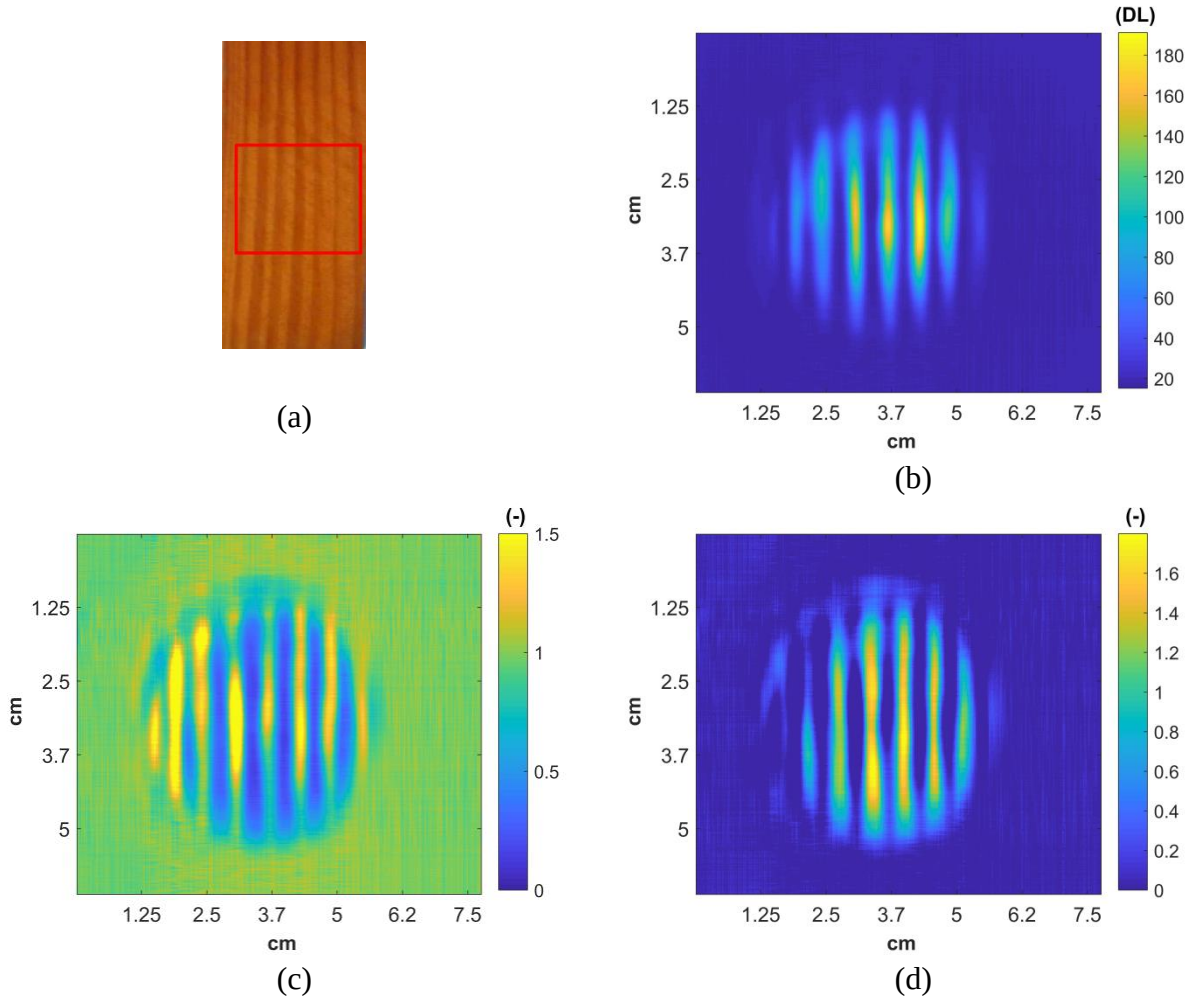

Figure 3-28: Images of a wood sample: (a) a photo of the sample, (b) the image processed by the four-images method and *SVD*, (c) the transmittance image and (d) the absorbance image.

Figure 3-27 and Figure 3-28 represent *THz* images obtained with measurements on a metallic sample (grid) and on a semitransparent sample (wood) in the near-field situation. Figure 3-27-b and Figure 3-28-b represent the results of the raw images processed by using the four-images method with deleted baseline. Thereafter, the *SVD* method is used to denoise the images. The signal-to-noise ratio in the processed images is approximately 100. The processing allows for better visualization of the sample structure, where the holes and ring alternation are distinguished. The images of transmittance and absorbance for the metallic grid and wood samples are presented in Figure 3-27- c, Figure 3-27-d, Figure 3-28-c and Figure 3-28-d.

- **Far-field configuration**

The far-field configuration presented in Figure 3-1 is a configuration where an objective separates the sample and the *TTC*. The images in far-field are more blurred due to the optical deviations, which prevent thin heterogeneous structure visualization within samples (such as the growth rings of wood and grids). However, improving the quality of images of samples such as the sample presented in Figure 3-29-a can be carried out using the sample processing method (four image and *SVD*). Figure 3-29 shows the processed image, transmittance image

and absorbance image of a metallic fixation element in the far-field configuration. In fact, working in the far-field mainly during heat transfer within a sample prevents excitation of the *TTC* by the hot sample.

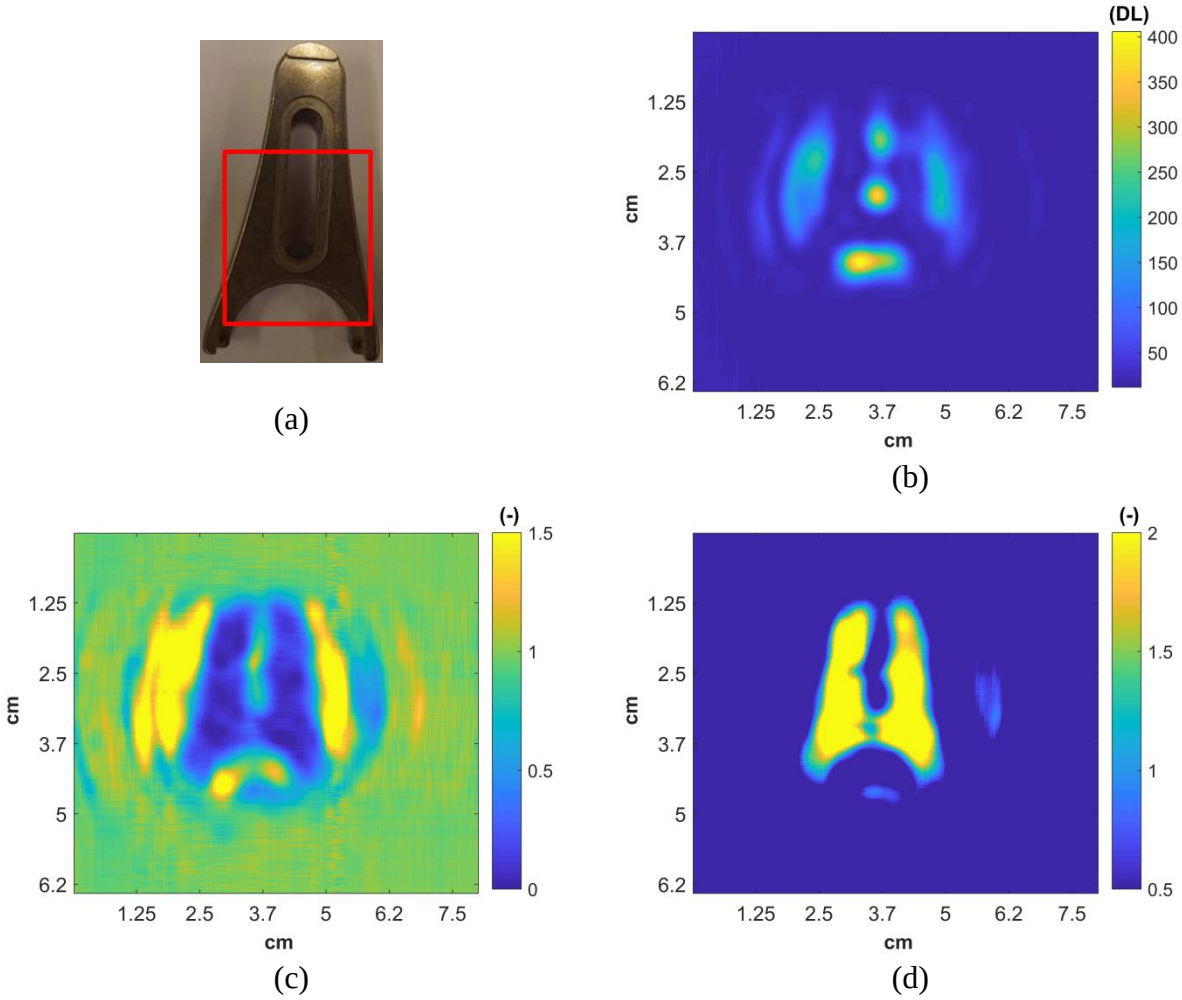

Figure 3-29: Images of a metallic fixation element: (a) a photo of the sample, (b) the image processed by the four-images method and *SVD*, (c) the transmittance image and (d) the absorbance image.

Figure 3-29 shows that the metallic sample structure, including holes, an aperture and cavities of dimensions larger than the wavelength through which the *THz* radiation is transmitted, can be distinguished. Moreover, the image processing shows efficiency in extracting the object from a blurred image (Figure 3-29-b). On the other hand, samples such as wood presenting rings with a width smaller than the wavelength cannot be detected in the far-field. However, despite the inability to visualize the structure of the sample, the sensitivity of the *THz* signal to temperature or water content may be obtained, which will be shown in section 2 and 3 in chapter 4.

4 Complete numerical modeling of the measurement chain

With the study performed on the lock-in method and before chapter 4, with experimental results relative to heat and mass transfer, it is important in this part to theoretically demonstrate the ability of our system to realize *THz* tomography and thermotransmittance measurements, for example. The idea is to first simulate the behavior of a sample as a function of the physical phenomenon in order to understand the signal obtained by the camera. For that, a complete numerical modeling of the global setup is presented here. The main idea is to theoretically show the capability of the *TTC* and camera to realize the tomography of an object (in transmission mode with the Beer-Lambert law) and a temperature measurement by thermotransmission (coupling the Beer-Lambert law and heat transfer in the sample). Two cases are simulated: tomography (without an increase in sample temperature) and a thermal gradient increase in the sample (thermal effect). We propose to first study the scanning of the sample at different angles and at constant temperature. For both cases, the first problem is solved inside the sample: the simple Beer-Lambert law for tomography and thermal diffusion for thermotransmittance. Then, the resulting solution is transposed to the *TTC* thermal problem.

4.1 Case of tomography imaging in the steady-state regime

The tomographic case illustrated in Figure 3-30 is based on the Radon projection of the incident *THz* beam passing through the sample as a function of the angle position. In this case, we have selected a homogeneous incident beam and a homogeneous cuboid semitransparent medium, with an absorbance of $\mu_0 = 1\ m^{-1}$ and the following dimensions: height 3.4 *cm*, width 9.1 *mm* and length 1.16 *cm*.

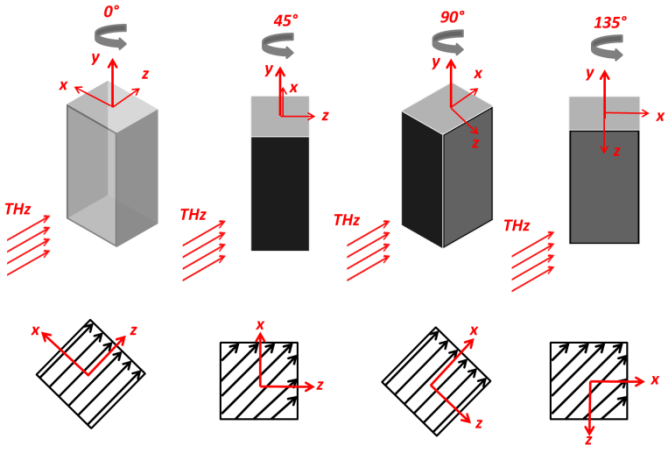

Figure 3-30: Four different sections of tomography.

The tomography of the sample shown in Figure 3-30 is numerically modeled within MATLAB® with a continuous part to show the capability to perform the tomography of objects taking into account the response of the *TTC*. The heat source resulting from taking the Beer-Lambert law through the sample and corresponding to the transmitted signal is given by equation (3-68).

$$\Phi = I_0\left(a + A\sin\left(2\pi f_{exc}t\right)\right)exp\left(-\int_0^e B(z,\theta).dz\right) \tag{3-68}$$

where I_0 is the incident signal, a is the continuous part, A is the amplitude, f_{exc} is the modulation frequency, z is the thickness direction, θ is the rotation angle, and B is the source function representing the integration of signal through the crossed section at different angles. The source function (B) is given by equation (3-69).

$$B(z) = \int_0^{\vartheta} b(z).d\theta \tag{3-69}$$

where b represents the signal at given depth of z. The parameters I_0, a, A and f_{exc} are given respectively by 10^{-3}, 1, 0.95 and 1 *Hz*. dz is given by equation (3-70).

$$dz = dL * Nz \tag{3-70}$$

where dL is the discretization element, and Nz is the node number along z. The numerical calculation represents an iterative calculation of the different projections of each angle (72 angles). The obtained source matrix represents a matrix of summed intensities resulting from the Beer-Lambert law (equation 3-67) on different sections of sample $\sum_0^{360} B(j,:,:,)$, as shown in Figure 3-31.

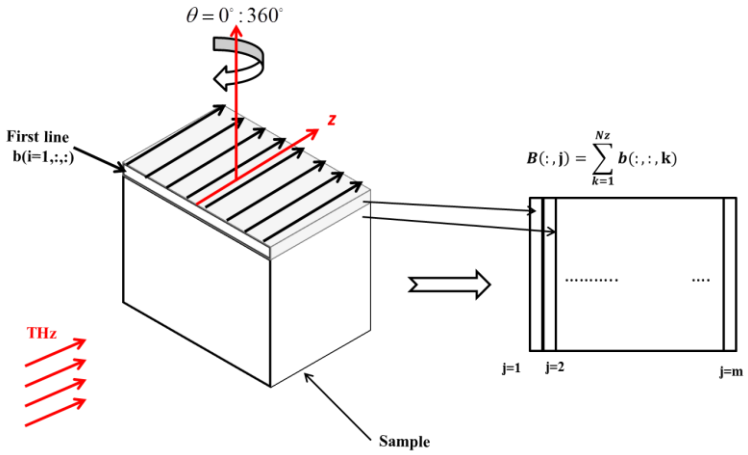

Figure 3-31: The integration along z as a function of the angle.

For each angular position, the intensity resulting from the Beer-Lambert law associated with the incident source modulation (equation 3-68) is projected as a thermal source on the *TTC* by taking into account the absorbance of the *TTC* equal to 0.6 (see Figure 3-32-a). From this modulated projection, the temperature resulting from the problem of thermal diffusion in the *TTC*, solved with a numerical finite volume, is calculated with equation (3-69). From this modulated temperature, the amplitude of the modulation is calculated with the 4-images lock-in technique presented in section 2. Here, 72 angular positions between 0 and 360° are selected; the incident source is modulated with a frequency of 1 *Hz* and a power of 100 *mW*. It

is a sinusoidal wave with a duty cycle of 50 % and an offset of half the power. The thermal response of the *TTC* (i.e., the temperature) is calculated with a time step of 0.25 *s* corresponding to 4 points per period of the source.

To illustrate such results as a function of angular position: (i) the initial incident sources are represented in Figure 3-32, then (ii) the resulting temperatures are illustrated in Figure 3-33, then (iii) the complete transient temperature evolution of the *TTC* located at one pixel in the center of the images is illustrated in Figure 3-34, and (iv) the estimated amplitude obtained with the four-images method is presented in Figure 3-35.

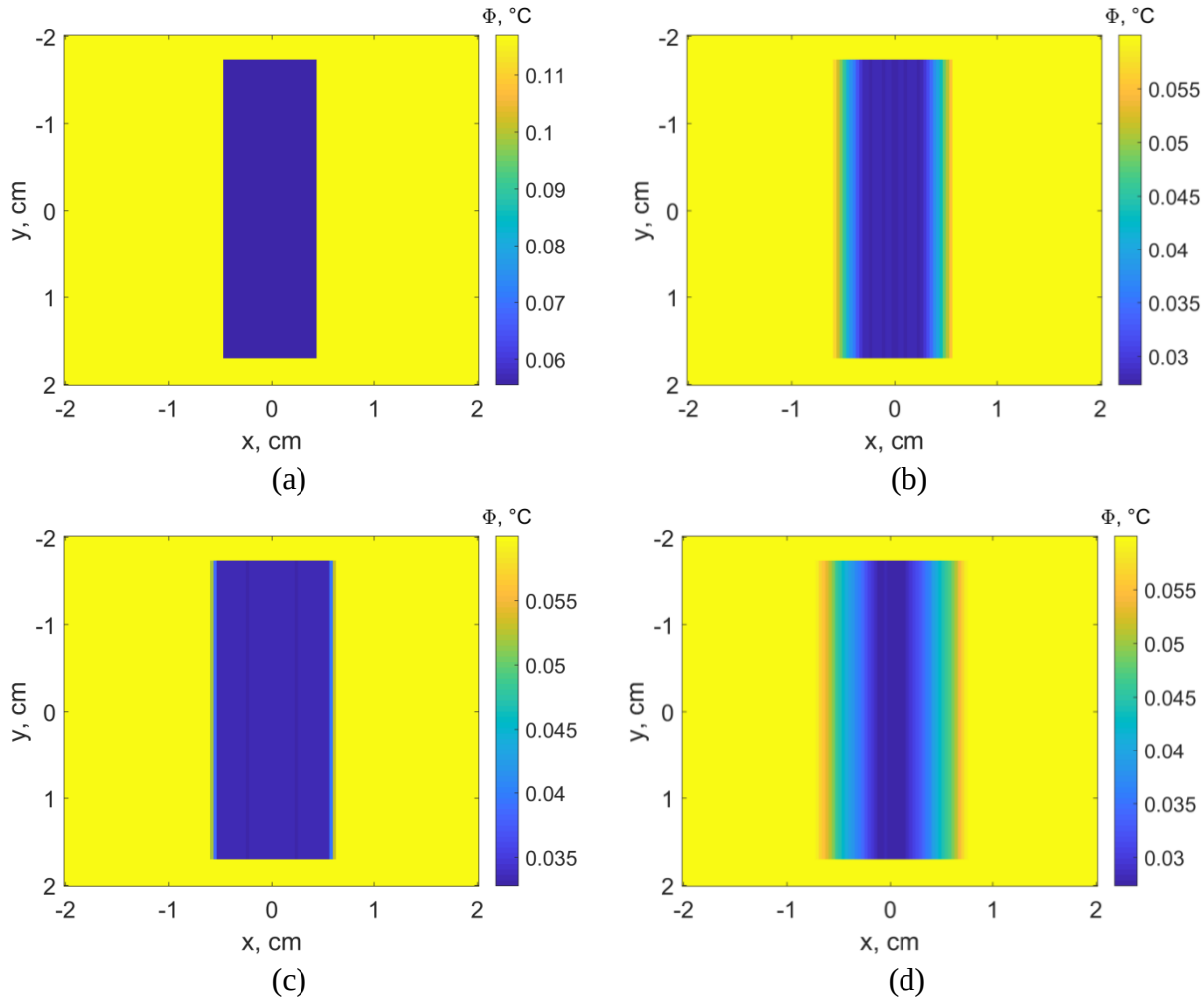

Figure 3-32: Incident source term (Φ) resulting from the Beer-Lambert law trough the sample as a function of the angular position: (a) $\theta = 0°$, (b) $\theta = 15°$, (c) $\theta = 45°$ and (d) $\theta = 90°$.

As predicted, it is interesting to note that the incident source term (i.e., the incident *THz* source passing through the sample) is affected by the angular rotation due to the differences in sample thickness, as shown Figure 3-30. For each angular position, the code calculates the resulting temperature, as shown in Figure 3-33. In this figure, the reader can clearly see the effect of the thermal diffusion of the *TTC* on the incident signal. In fact, the very sharp and homogeneous incident source of Figure 3-32-a remains homogeneous but starts to be blurred near the interface. This corresponds to the diffusion along 3 pixels. The size of the pixel is equal to 312.5 μm for this calculation. The same remark is true for the other angular positions.

Moreover, Figure 3-34 shows the temperature evolution of 2 pixels of the images represented as a function of time. This important illustration demonstrates the effect of the continuous component in the raw measurements (*TTC* behavior). In fact, the behavior of the pixel located at the corner corresponds to the response of the *TTC* to the incident beam alone. The observed time to reach steady state is shown to be 10 *s*. However, for the pixel located at the center, depending on the angular position of the sample, the incident beam (as a function of the attenuation coefficient and the crossed thickness) changes. Therefore, a new initial condition is imposed for the *TTC* creating a transient state. This point is very important and reinforces the conclusion of the previous section, evidencing the requirement of deleting the baseline that is a function of time.

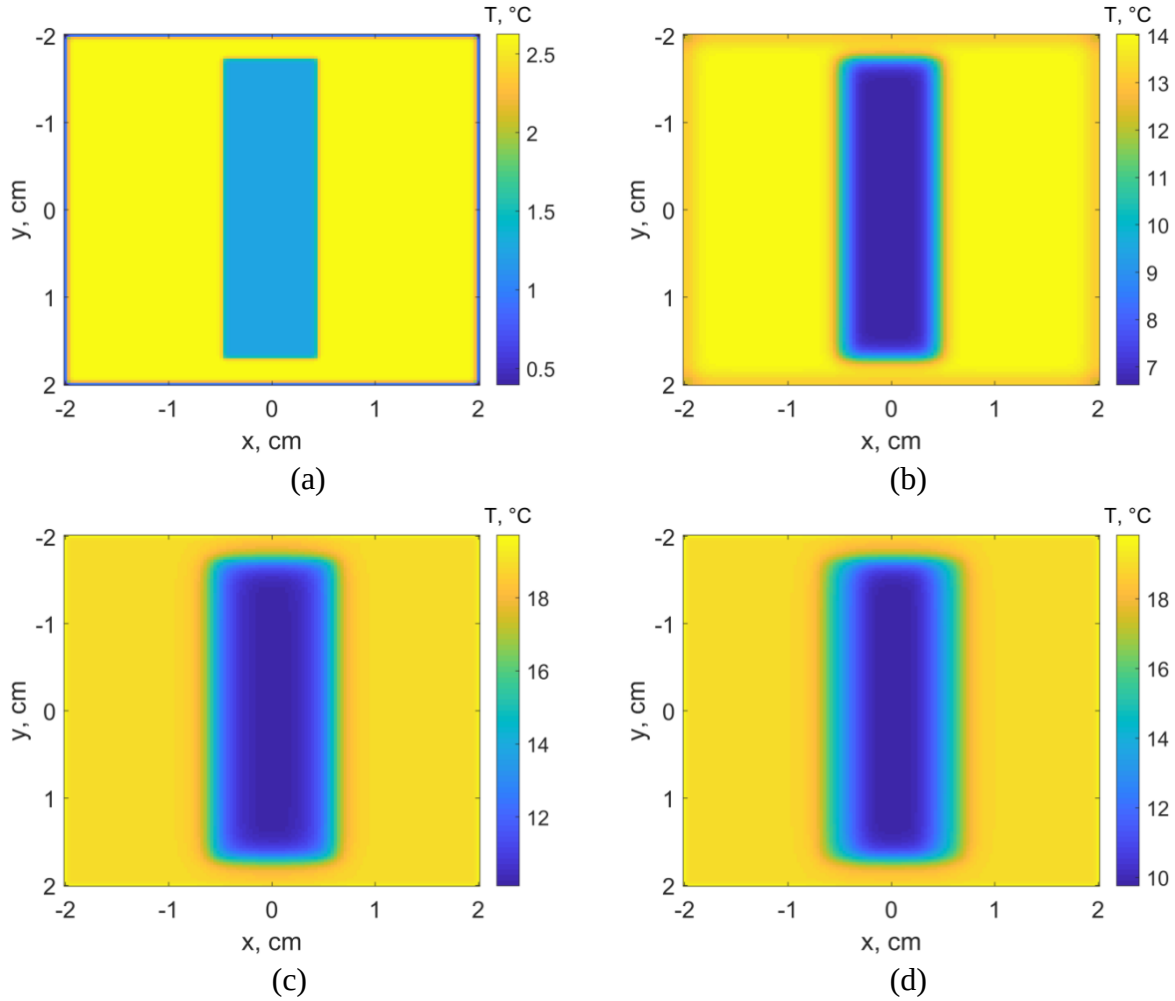

Figure 3-33: Raw calculated temperature at the end of each period as a function of the angular position: (a) $\theta = 0°$, (b) $\theta = 15°$, (c) $\theta = 45°$ and (d) $\theta = 90°$.

Then, from the transient temperature fields of Figure 3-33, the 4-images algorithm with baseline substation is applied to calculate the corresponding amplitude, as illustrated in Figure 3-34.

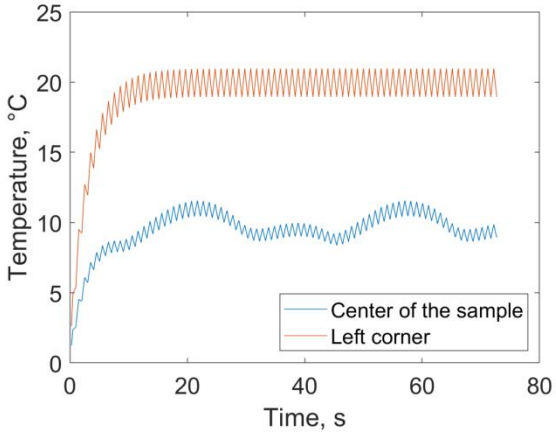

Figure 3-34: The complete transient temperature evolution of the *TTC* located at one pixel in the center of the images.

In Figure 3-35, we can observe that the amplitude is well estimated with a homogeneous value inside the sample. Moreover, the effect of the diffusion already exists. The only way to improve the diffusion problem is to increase the modulation frequency.

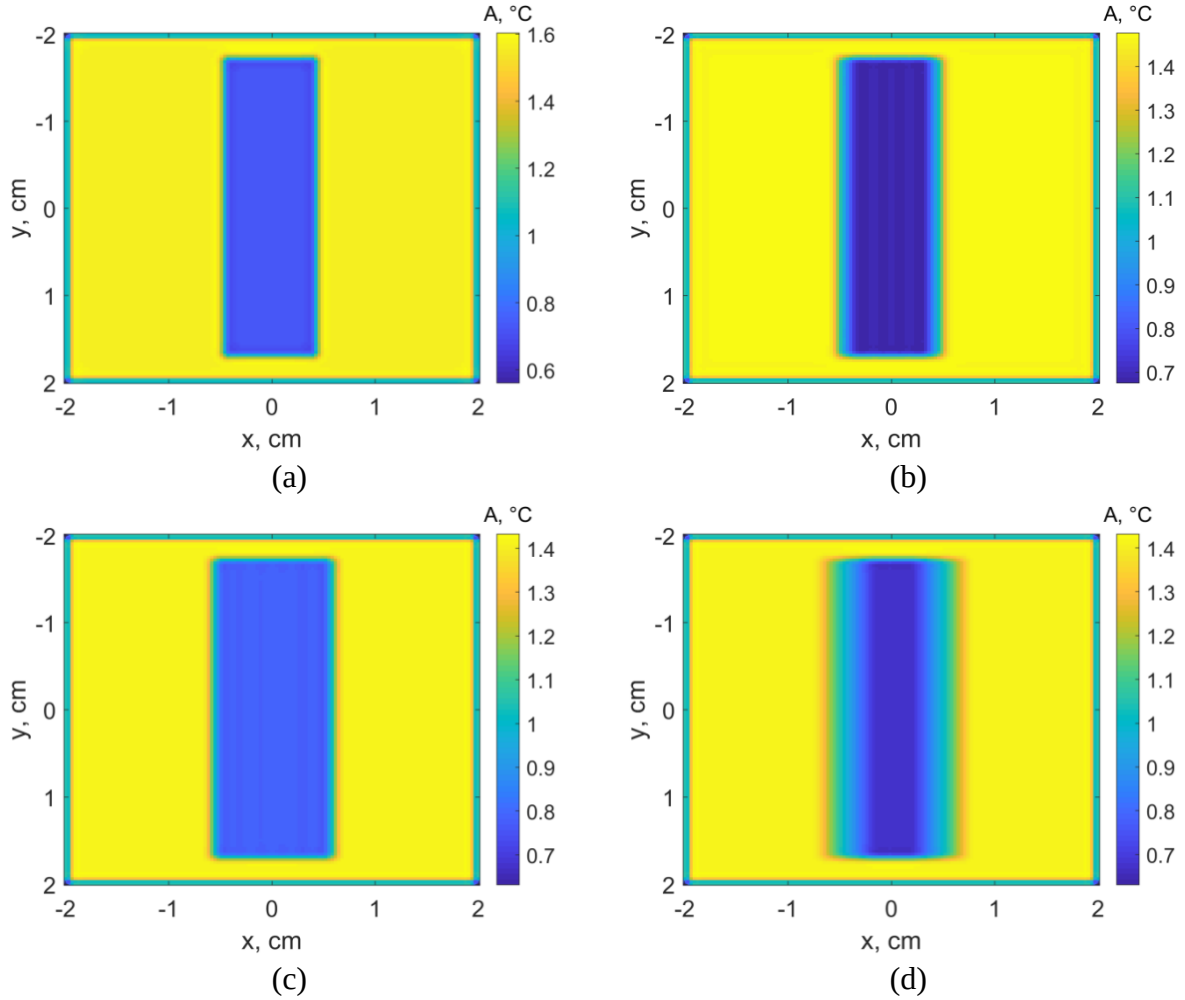

Figure 3-35: Calculated amplitude from the temperature with the four-images algorithm as a function of the angular position: (a) $\theta = 0°$, (b) $\theta = 15°$, (c) $\theta = 45°$ and (d) $\theta = 90°$.

Finally, from the calculated amplitude fields, the *3D* reconstruction of a sample can be obtained using an inverse Radon back projection in MATLAB®. The initial object and the reconstructed one are represented in Figure 3-36. It is important to note that the reconstruction shows a good result in terms of the value of the attenuation coefficient. However, the diffusion effect creates an object less sharp than the original. Again, to improve this drawback, the frequency of the source should be increased according to equation 3-68.

To conclude this section, we can assume that there is no obstacle to realize fast and accurate *THz* tomography with the quantum bolometric camera developed in this thesis.

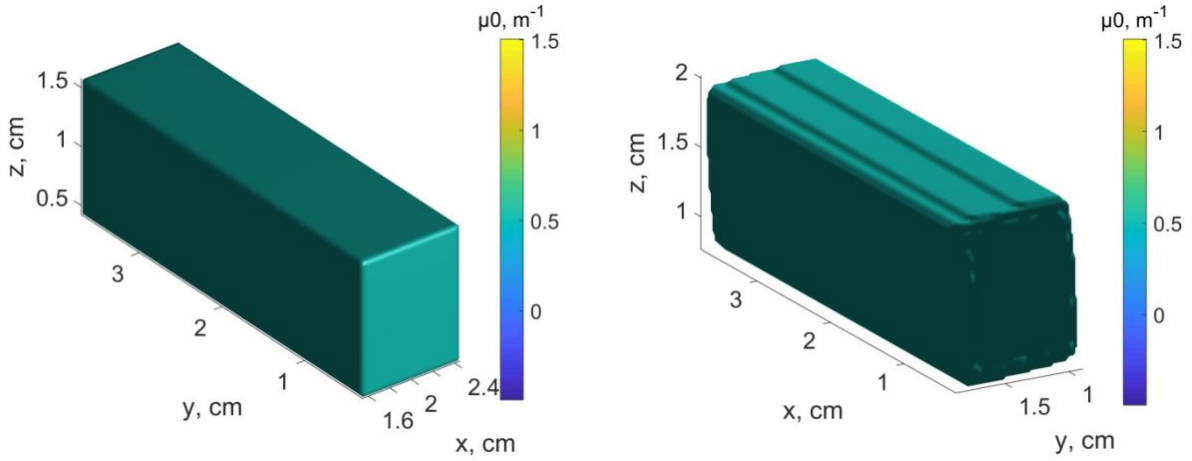

(a) (b)

Figure 3-36: (a) Initial sample and (b) reconstructed sample using an inverse Radon back projection.

4.2 Case of transient heat transfer in a homogeneous sample

To go deeper into the difficulty and to explore the ability of our *THz* camera, the problem of the thermotransmittance will be simulated here. As illustrated in Figure 3-37, in the true measurements, the thermal problems are always *3D*, with a temperature gradient in the depth. To simplify the real problem we have developed a 2D and transient modelization of the impulse response of a thin homogeneous sample ($e = 1\ mm$), where we assumed that the temperature profile is homogeneous in the depth. In this case, the temperature response can be analytically calculated with the function given by equation (3-71).

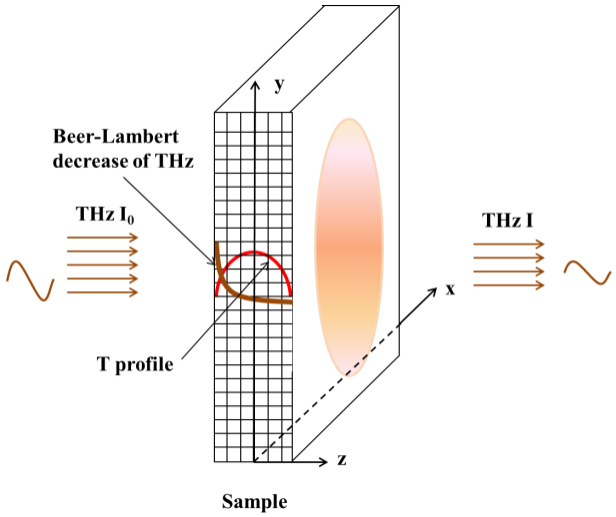

Figure 3-37: Parabolic temperature profile within a sample.

In the simulated case, the following parameters were taken into account: the thermal diffusivity equal to 4.10^{-7} $m^2.s$, the energy Q equal to 1 μJ, the sample size equal to *128* x *64* x 64 *pixels*, and the final time equal to 28 *s* with a time step of *200 ms*.

$$T(x,y) = \frac{Q}{\sqrt{\pi at}}\left(exp\left(-x^2/4at\right) + exp\left(-y^2/4at\right)\right) \tag{3-71}$$

From the temperature expression of equation (3-71), the Beer-lambert law is applied by considering a constant temperature along the thickness of the sample with a linear attenuation function, as shown in equation (3-72):

$$I\left(x,y,t\right) = I_0 exp\left(\left(\mu_0 + \kappa T\left(x,y,t\right)\right)dz\right) \tag{3-72}$$

where I is the transmitted signal in (W); I_0 is the incident signal in (W); μ_0 is the absorption coefficient at ambient temperature (assumed to be 10 = m^{-1}); κ is the thermotransmittance coefficient equal to 5.10^{-3} $m^{-1}.K^{-1}$; T is the temperature in (K); x, y, z represent the space dimensions in (m); and t is time in (s).

Then, from the Beer-Lambert formulation linked with the internal temperature of the sample by a linear attenuation function, the corresponding incident source (i.e., the *THz* beam passing through the sample in the measurement) can be calculated with equation (3-73):

$$\Phi\left(x,y,t\right) = I_0\left(a + A.\sin\left(2\pi.f_{exc}.t\right)\right)\ \exp\left(\left(\mu_0 + \kappa T\left(x,y,t\right)\right)dz\right) \tag{3-73}$$

where A is the amplitude (assumed to be equal to 0.5), a is the continuous part equal to 1, and f_{exc} is the frequency modulation (1 *Hz*).

Then, as for the tomographic case, this heat source is imposed, and the resulting temperature taking into account the heat transfer inside the *TTC* is calculated by the finite volume method.

To illustrate such results as a function of time: (i) Figure 3-38 presents the temperature evolution inside the sample, (ii) Figure 3-39 presents the initial incident sources, (iii) Figure 3-40 illustrates the resulting temperatures, (iv) Figure 3-41 presents the complete transient temperature evolution of the *TTC* located at one pixel in the center of the images, and finally (v), Figure 3-42 presents the estimated amplitude with the four images technique.

From the analytical solution of equation (3-71), the temperature of the Dirac impulse response is represented in Figure 3-41. We can observe that the temperature in Figure 3-42-a is high at the location of the spot, and then, the temperature exponentially decreases and diffuses as a function of time (Figure 3-42-b to Figure 3-42-d).

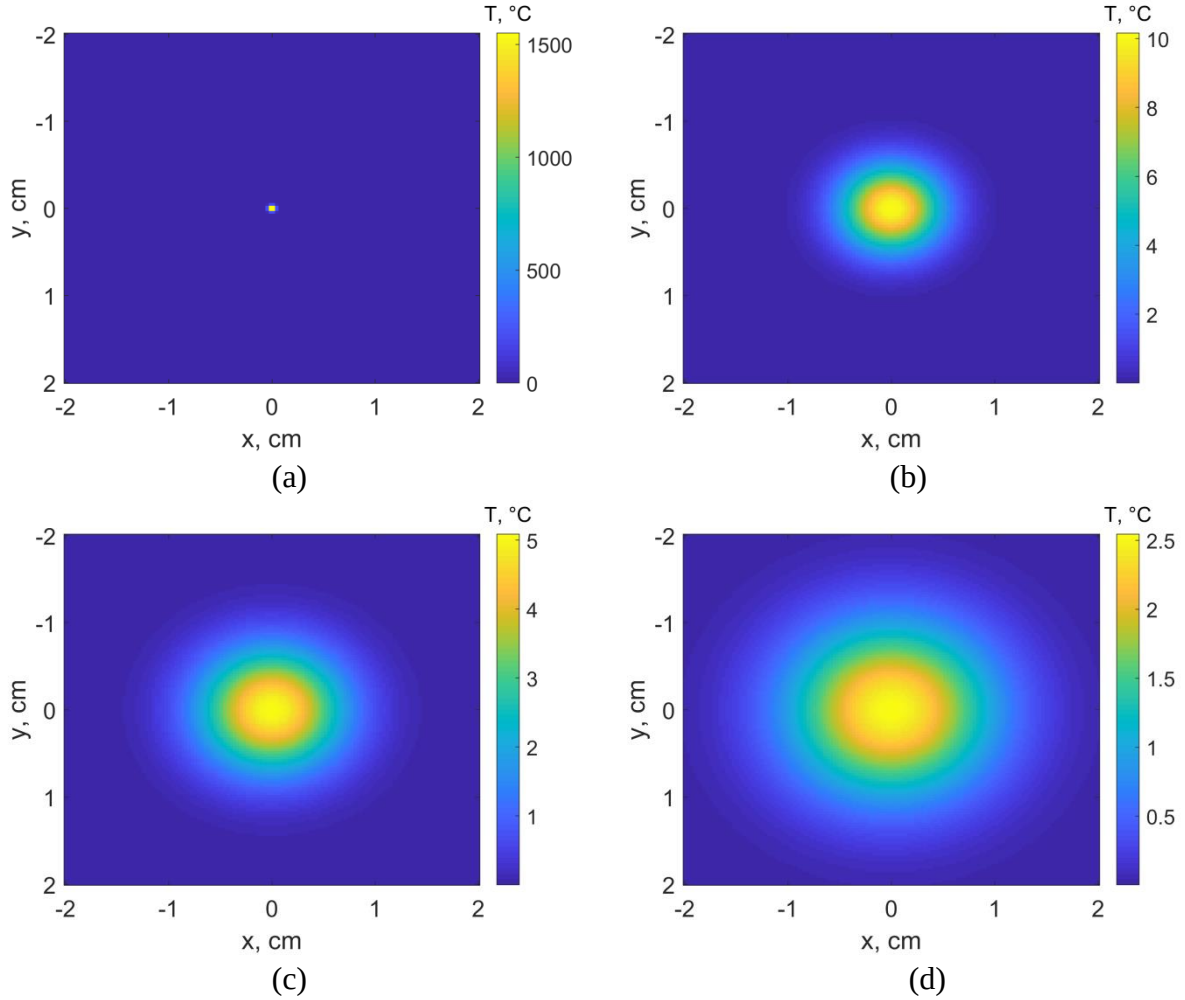

Figure 3-38: Calculated temperatures inside the sample with the analytical solution (equation 3-71) as a function of time: (a) t = 0 *s*, (b) t = 63 *s*, (c) t = 126 *s* and (d) t = 252 *s*.

In Figure 3-39, it is interesting to note that the incident source term (i.e., the incident *THz* source passing through the sample) is affected by the temperature variation inside the simulated sample. This variation is due to thermal diffusion in the plane. Due to the Beer-Lambert law (equation (3-72)) and the modulation (equation (3-73)), the amplitude of the imposed heat source is lower in the part of the image corresponding to the higher temperature of the sample. In fact, in Figure 3-38-a, the temperature is positive and high, and in Figure 3-39-a, the corresponding heat source is positive but low. Moreover, in Figure 3-38, due to the

exponential formulation of the heat source, the thermal gradient well visible in Figure 3-39-b is less present in Figure 3-38-b.

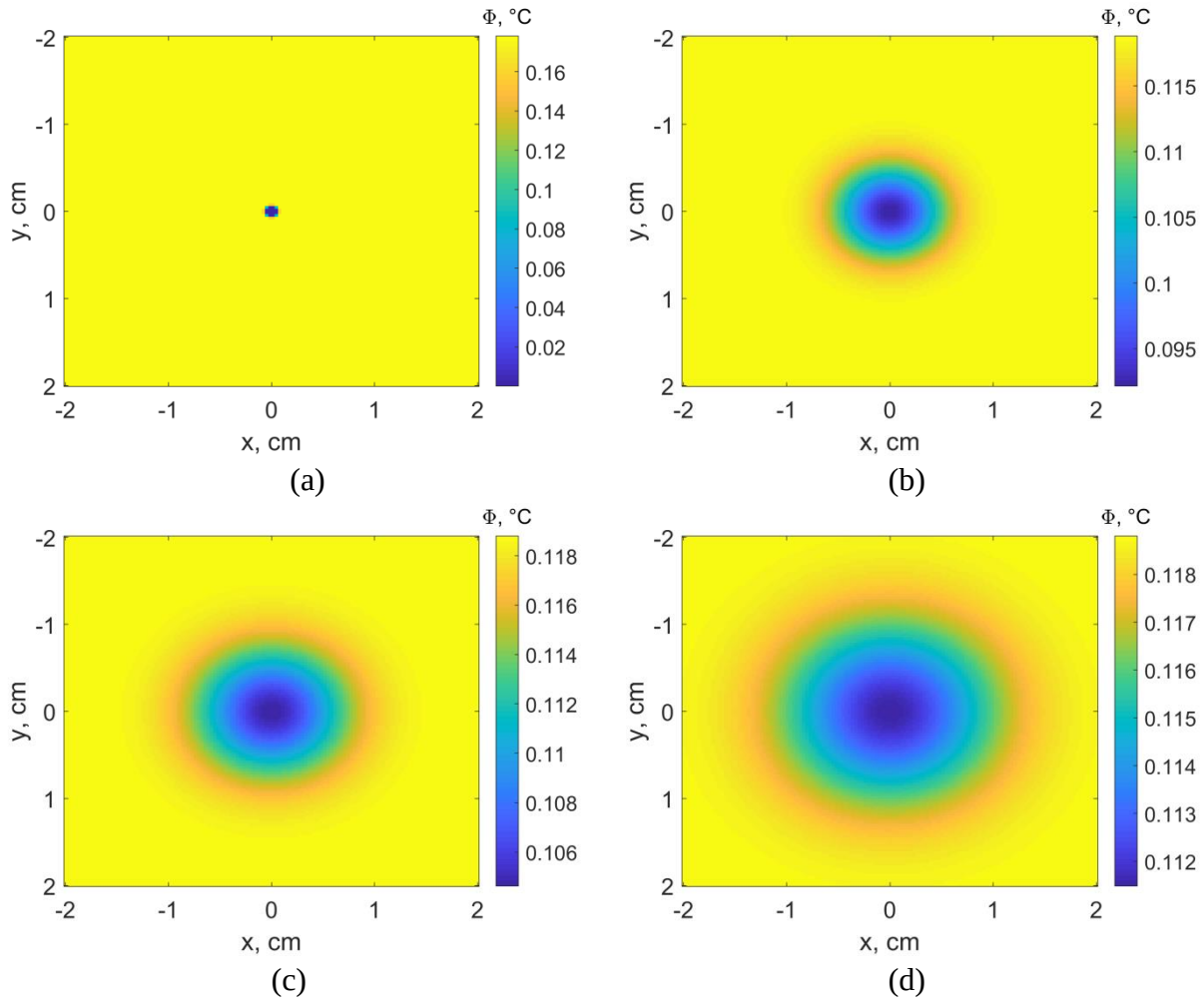

Figure 3-39: Incident source term (Φ) resulting from the Beer-Lambert law through the sample as a function of time: (a) t = 0 *s*, (b) t = 63 *s*, (c) t = 126 *s* and (d) t = 252 *s*.

For each time step, we calculate the temperature of the *TTC* when the heat source resulting from the temperature variation inside the sample is applied, as shown Figure 3-42. In this figure, the reader can clearly see the effect of the thermal diffusion in the *TTC* on the incident signal. As before, the thermal gradient is not visible, and the temperature of the *TTC* seems to be more homogeneous than the true temperature of the sample. It is important to understand that such "raw" images of the *TTC* cannot be used to represent the real problem or measurement.

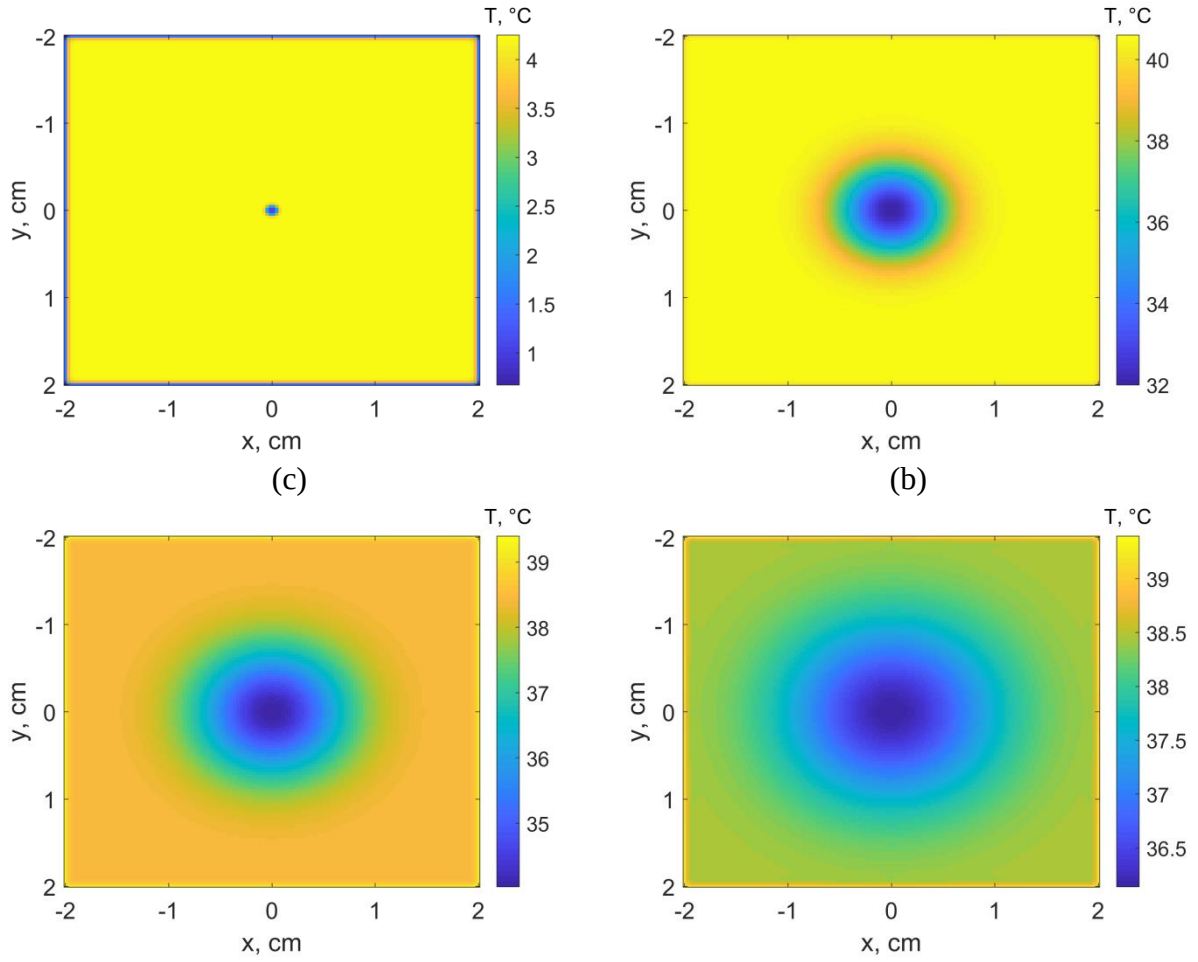

Figure 3-40: Raw calculated temperature at the end of each period as a function of time: (a) t = 0 s, (b) t = 63 s, (c) t = 126 s and (d) t = 252 s.

Figure 3-41 presents the temperature evolution of 2 pixels of the image as a function of time. This very important plot demonstrates the effect of the continuous component on the raw measurements or the *TTC* behavior. In fact, in the pixel located at the corner, which corresponds to the response of the *TTC* to the incident beam alone, we can observe the time in x s to reach steady state. For the pixel located at the center, we can observe that for each time step or when the incident signal (as a function of the attenuation coefficient and the sample temperature and diffusion) changes, a new initial condition is imposed, creating a transient state. This very important point reinforces the conclusion of the previous section and provides evidence of the requirement to subtract the baseline as a function of each period.

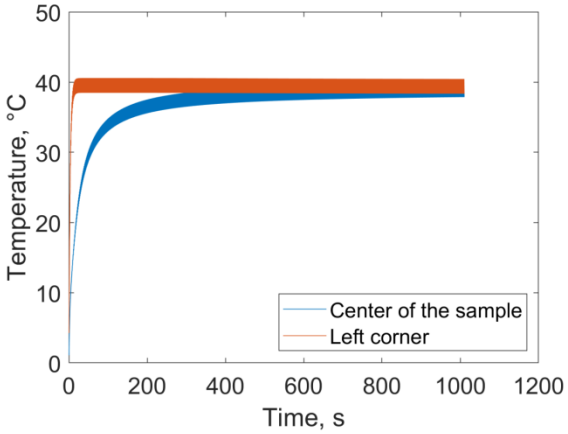

Figure 3-41: Temperature of the complete thermal response of the *TTC* as a function of the acquisition time.

Then, from the transient temperature fields of Figure 3-42, the four-images algorithm with baseline subtraction is applied to calculate the corresponding amplitude, as illustrated in Figure 3-40. We can observe that the amplitude is well estimated with a homogeneous value inside the sample. Moreover, the effect of the diffusion already exists. The only way to improve the diffusion problem is to increase the modulation frequency.

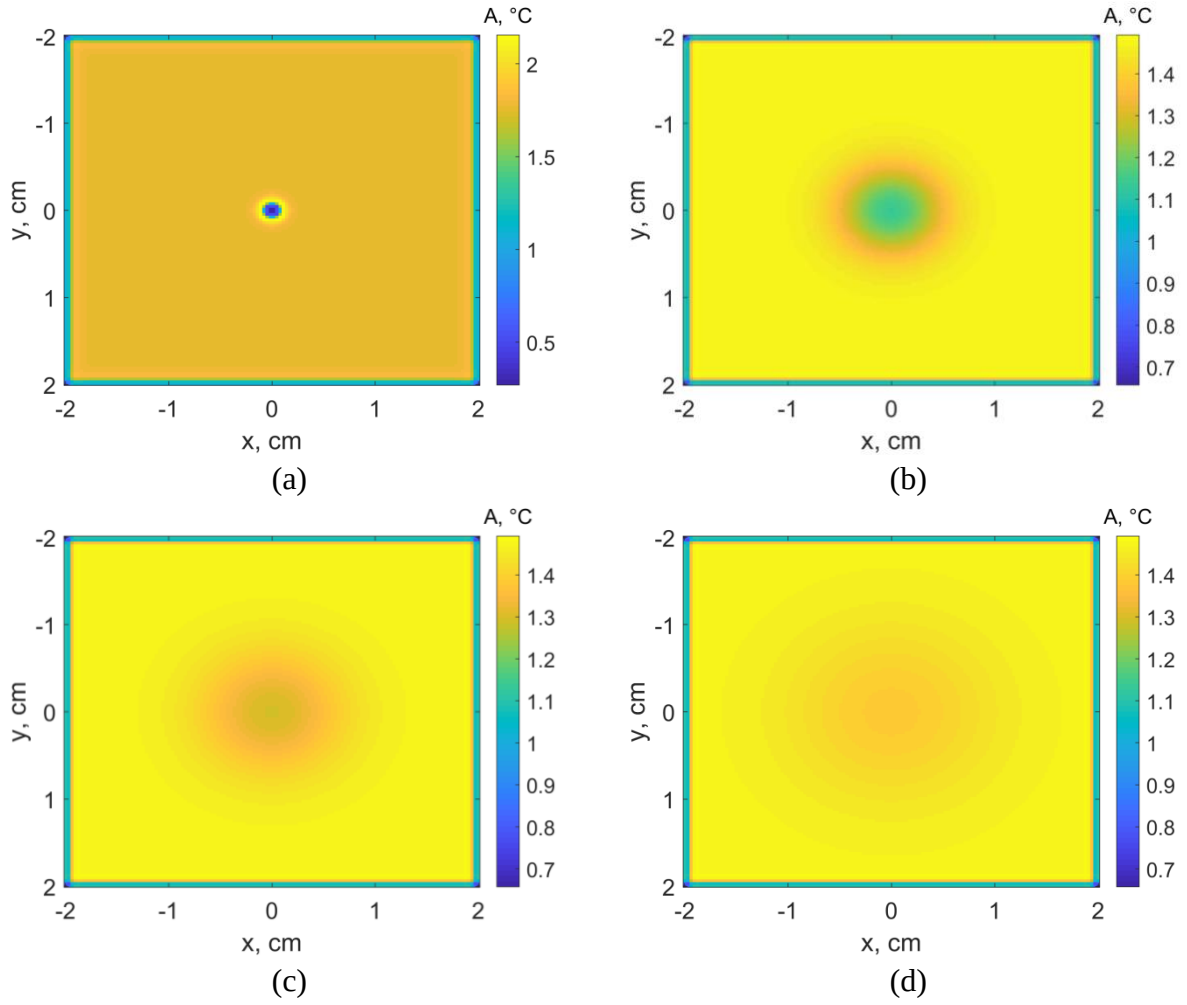

Figure 3-42: Calculated amplitude from the temperature with the four-images algorithm as a function of time: (a) t = 0 s, (b) t = 63 s, (c) t = 126 s and (d) t = 252 s.

Finally, from the calculated amplitude field, the temperature can be calculated with the following formulation:

$$T_{calc}(x,y,t) = \frac{-log\ \left(A(x,y,t)\right)}{\kappa.e} \tag{3-74}$$

From this temperature (extracted from the complete simulation of the camera chain), the temperature at the center of the sample is plotted in Figure 3-43 as a function of T_{calc}. In Figure 3-43-a, we can observe that, at short times, the generated and reconstructed temperatures are not linear. For the moment, we did not have any explanation or reason for why we retrieved such a problem. Nevertheless, if we plot after the fourth time step, we obtain perfect linear behavior between both temperatures (see Figure 3-43-b). By making a linear fit, we obtain a slope of $4.9.10^{-3}\ m^{-1}.K^{-1}$, corresponding to the value of $\kappa = 5.10^{-3}\ m^{-1}.K^{-1}$ that we initially used to generate the problem. To conclude, this good result shows that there is no obstacle to contactless measurements of temperature variation by transmission in semitransparent-to-*THz* media by using our quantum bolometric *THz* camera.

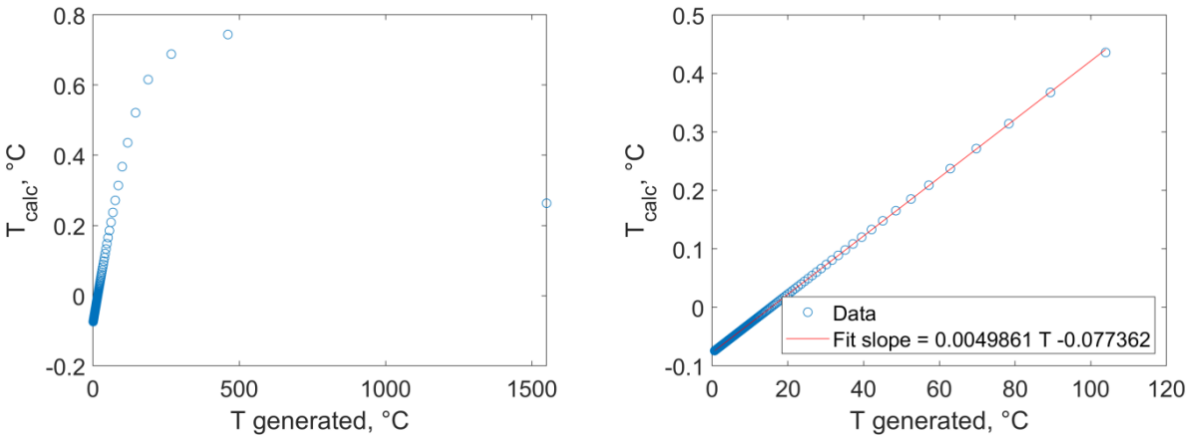

(a) (b)

Figure 3-43: Calculated temperature as a function of the generated temperature: (a) at the center and (b) at the corner.

Finally, from the linear fit, the temperature of the sample can be estimated by retrieving T_{calc}. The obtained results are illustrated in Figure 3-44. In Figure 3-44-a, the illustrated temperature represents the exact temperature of the sample after 10 s, and Figure 3-44-b represents the retrieved temperature. Moreover, Figure 3-44-c represents the residual given by $\varepsilon = 100\left(1 - \frac{T_{calc}}{T_{generated}}\right)$. In Figure 3-44-c, we can remark that, in the exact diffusion zone, the retrieved temperature has a homogenous error of lower than 1 %.

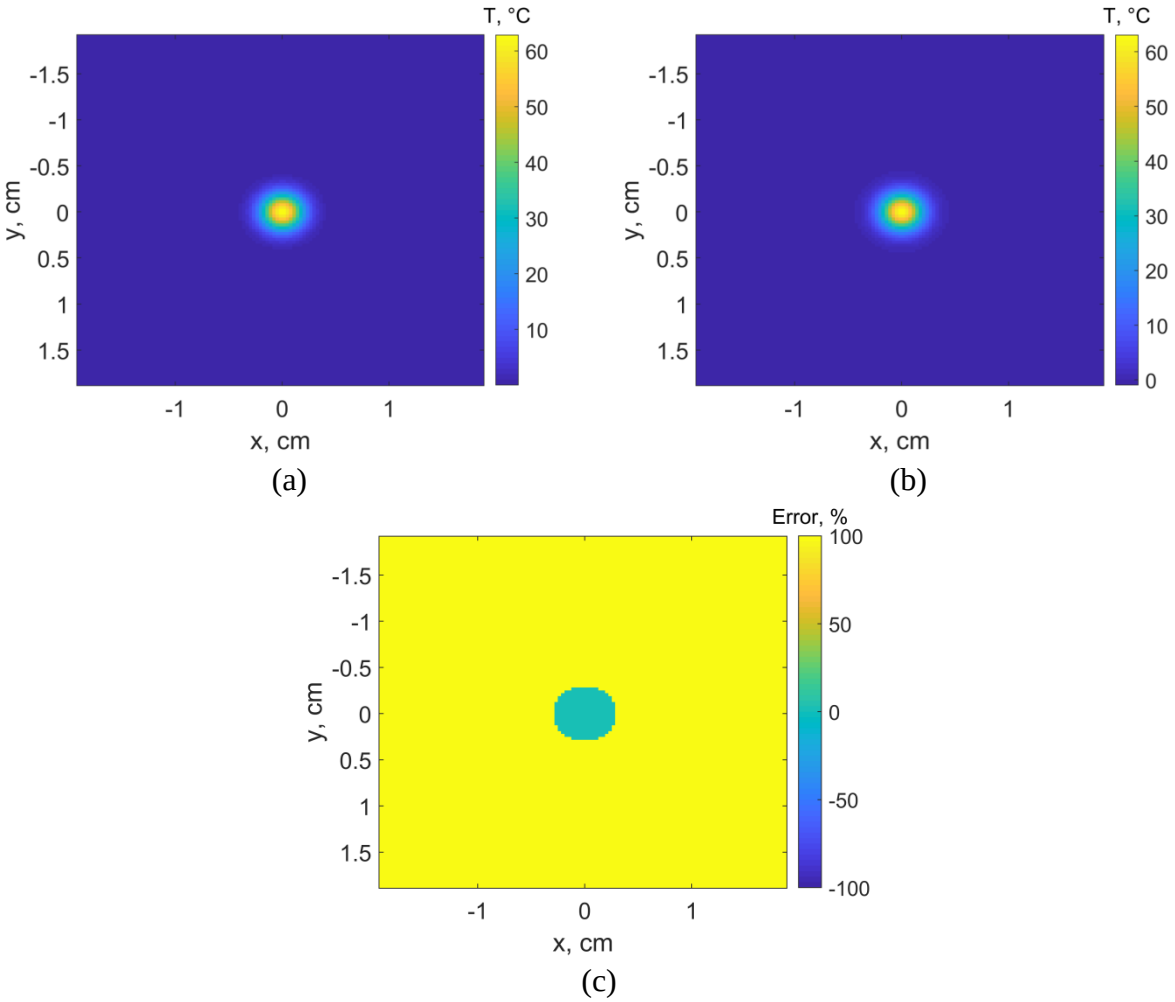

Figure 3-44: Temperature of the sample at t = 10 s: (a) the exact temperature, (b) the calculated temperature and (c) the relative error between the temperature fields presented in (a) and (b).

5 Conclusion

In conclusion to this chapter, the method that has been developed makes it possible to realize good-quality *THz* imaging with the developed *THz* camera.

The complete numerical modelization of the *TTC* heat transfer problem has shown that, even if the conversion rate is low, the convertor associated with the very high-sensitivity *IR* camera allows for obtaining a *THz* camera with a detectivity of 160 $pW.Hz^{-0.5}$ per pixel when only 0.2 of the total flux is converted. Moreover, the fact that the *TTC* is not pixelized is much more advantageous because it allows having a real wide-band sensor not limited by the diffraction linked to the pitch size. The drawback of this nonpixelized sensor is linked to the thermal diffusion that blurs the images. We have demonstrated that, by using the lock-in technique at an appropriate frequency (close to 1 *Hz* or more), the obtained images are sharp enough because the effect of the diffusion length is lower than the size of the pixel. Moreover, as the conversion rate is nonlinear with the Gunn diode power, we can expect to drastically improve the measurements and the acquisition frequency in the future.

The other very important conclusion is the use of a good lock-in method to calculate the amplitude of the measured signal. The benchmark tests of all the methods, has revealed that the four-images algorithm is the best compromise in term of accuracy, calculation time and robustness. However, the influences of parameters such as the frequency, the number of points per period and the period number may affect the estimation of the studied signals. In fact, the method makes it possible to quickly exploit all the pixels of the image by means of a direct linear estimation (weighted least squares) to obtain the amplitude field as a function of time. It is important to note that one of the major points is the introduction of the baseline subtraction to improve the real-time and fast amplitude calculation. To summarize the complete procedure: (i) the Gunn diode is synchronized with the camera acquisition to realize a movie at a high frequency (200 *Hz*) of one period of the modulated diode (1 *s*), (ii) from this movie and in real time, the software can extract the amplitude of the signal measured by the *IR* camera on the *TTC*. The amplitude is calculated for each pixel by subtracting the baseline from a linear fit and then applying the 4-images algorithm and *SVD* filtering method. All these calculations are performed in less than t = 0.2 *s*.

Then, this new lock-in processing has been validated experimentally on three kinds of sample from plastic to wood and a metallic grid in both near-field and the imaging mode of the setup.

Finally, a complete theoretical modelization of the measurement chain for the cases of *THz* tomography and thermal heat transfer inside a sample was realized. The major conclusion is that there is no obstacle to performing such measurements with the *THz* camera developed in this study.

Chapter IV: Results of heat and mass transfer measurements with *THz* waves

A possible advantage of using the *THz* as a contactless tool for water content measurement or *NDT* was underlined in chapter 1. Then, the materials used for *THz* imaging of heat and mass transfers were presented in chapter 2. Thereafter, the measurement chain using the developed thermoconverter (*TTC*) and the appropriate image processing methods were detailed in chapter 3. In this chapter, first, the application of *THz* imaging of heat and mass transfers in semitransparent materials is carried out. Since the *THz* sensitivity to water content is higher than the sensitivity to temperature, the effect of temperature on the water content measurements under environmental conditions (a low variation in temperature) can be neglected. On the other hand, the influence of environmental water content during the heat transfer experiments is neglected because of the short duration of the experiments (minutes), where the *RH* is considered to be constant.

The first part of this chapter is devoted to ***THz calibration for monitoring water content*** within homogeneous and heterogeneous materials (blotting paper and wood). Second, the monitoring of transient mass transfer and the ***contactless estimation of diffusion coefficient by inverse methods*** are shown. The estimation of the diffusion coefficient using different *THz* sensor technologies (monodetector and *TTC*) for of drying and hydric excitation is carried out. Finally, the first use of *THz* imaging ***as a contactless measurement of temperature is presented***.

1 Calibration method for contactless imaging of water content with *THz*

This section is dedicated to check the feasibility of the ***terahertz imaging*** technique as a tool for the ***contactless*** measurement of water content within ***semitransparent porous materials***. In this part, the infrared monodetector described in II-1 and *2D* thermoconverter described in II-2 are used for the ***calibration phase*** aiming to determine the ***absorbance of the materials***. To check the ***Beer-Lambert law***, *THz* scanning of dry blotting paper samples, dry wood samples and liquid water is performed. Once the absorbance is determined, tests on samples of different water contents are conducted. Therefore, the blotting paper and wood samples are conditioned at different *RH* until equilibrium is reached. The equilibrium indicates the stabilization of exchanged mass between the sample and environment. This happens when the inner pressure equals the partial pressure of environment. Once the sample reaches equilibrium, the *THz* imaging is performed. This test aims to reveal ***the relationship between the absorbance and the relative humidity***. Moreover, thanks to the assessment of the sorption curves of the materials, a link between the water content and the *THz* absorbance of materials is established.

1.1 Studied materials

1.1.1 Homogeneous material (blotting paper)

First, tests have been conducted on a homogeneous mono-constituent material such as blotting paper. This material, often used to absorb by capillarity excess of liquid substances, is mainly composed of cellulose. It consists of a mixture of sulfite, without charge or glue and without a mechanical primer. As cellulose represents one of the main constituents of wood, the blotting paper is a good homogeneous sample to perform the standard test, calibration and method validation using *THz* imaging. Thereafter, a heterogeneous material will be tested (maritime pine wood).

1.1.2 Heterogeneous material (maritime pine)

Wood is a natural heterogeneous and anisotropic material with complex cellular structures. Wood is composed of many chemical compounds and cell types acting together. Its heterogeneous characteristics and structure serve three main functions: (i) in plants, the conduction of water from the roots to the leaves; (ii) the mechanical support of the plant body and (iii) the storage of biochemical species. Wood cells consist of a cell wall and lumen, filled with air, interconnected to perform these functions. The cells are formed during the growth seasons of the tree, resulting in a variation in dimensions, and therefore, in the physical properties of wood.

Wood is composed of reinforcement (resistant cellulose fibers) embedded in a less mechanically strong matrix (lignin) whereby hemicellulose is used to interface these materials. Wood consists of 41 % to 43 % of cellulose and between 20 % and 30 % of hemicellulose, mainly as five-carbon sugars, and lignin, approximately 27 % in softwoods and 23 % in hardwoods. Lignin is a hydrophobic macromolecule that fills the spaces between the cellulose and the hemicellulose in the cell wall.

At the macroscale, a wood sample can be extracted from a trunk's sapwood or heartwood area. The sapwood is the active "living" wood that is responsible for conducting the water (or sap) from the roots to the leaves. The heartwood is the nonconductive part of the trunk where the chemicals are set apart and is found as a core wood in the middle of most trees. On the other hand, the wood can be softwood or hardwood. The softwoods are come from gymnosperms (mostly conifers), and hardwoods come from angiosperms (flowering plants). The thermophysical, hygroscopic and mechanical properties can be different from one wood to another. In this study, the experiments are conducted on maritime pine wood (*Pinus pinaster*), i.e., a softwood.

1.2 Sample preparation and measurement protocol

The investigated samples are blotting sheets and maritime pine boards. The blotting papers have a size of 30 *mm* x 20 *mm* x 0.2 *mm*, and the maritime pine boards have dimensions of 100 *mm* x 40 *mm* x 3 *mm*. For the wood, samples are cut from the longitudinal-radial section (*L*-*R*). To scan samples at different thicknesses, the samples should be stacked. Figure 4-1 shows the samples of cellulose sheets and wood.

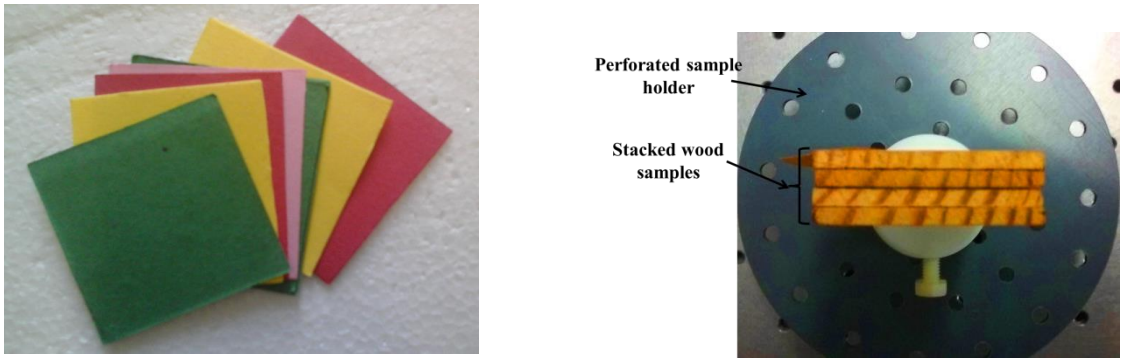

(a) (b)

Figure 4-1: Stacked samples of (a) blotting paper and (b) wood tested by *THz* to estimate attenuation coefficients in the dry case.

The samples are dried for 48 *h* in an oven at 105 °*C* until the stabilization of their mass. Then, they are scanned at the different thicknesses obtained by stacking. However, during the experiment, the blotting paper samples are put between two semitransparent plates, and the wood boards are scanned inside the semitransparent conditioning containers (see chapter 2, section 3.1), as shown in Figure 4-2.

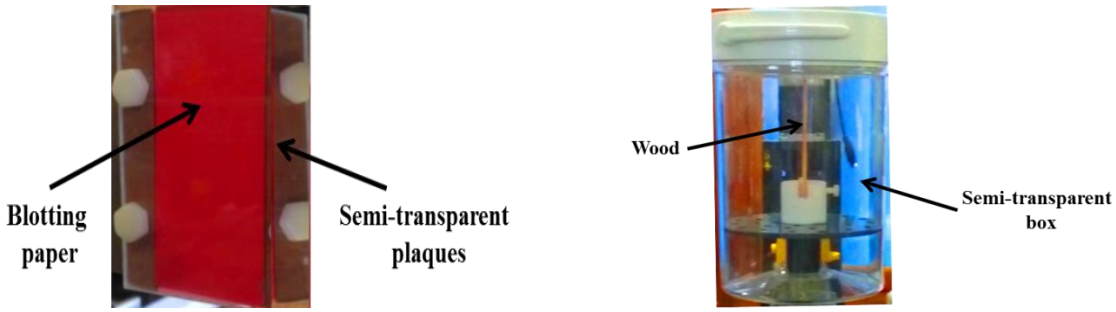

(a) (b)

Figure 4-2: Insulation of samples during scanning.

In the second step devoted to checking the capability of the *THz* for the contactless measurement of water content, the sample preparation is carried out as follows:

The samples are oven-dried for 48 h at 105 °C and then weighed using an electronic balance. This mass value is then called m_s, i.e., the mass of the solid phase (dry wood).

The hydric conditioning of the samples is performed via saline solutions (see chapter 2, section 3.1). The resulting relative humidity and temperature are measured by a contactless sensor (Tinytag plus 2) that is placed inside the container, as shown in the Figure 4-3.

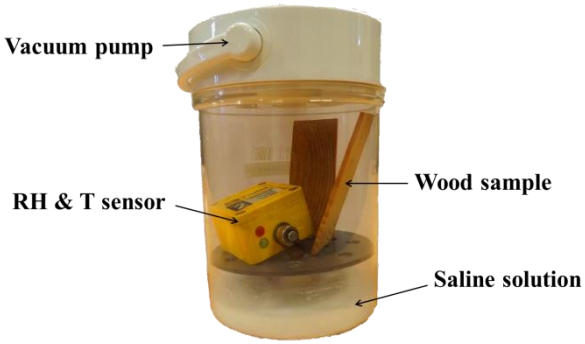

Figure 4-3: Hydric loading of blotting paper and wood samples in a vacuum pump container.

Once the dry samples are put in the containers, the evacuation of the containers is performed. A manual pump allows the generation of a pressure gradient inside the container, promoting mass transfer (vapor movement) from the internal container environment towards the sample. Each sample is periodically weighed until the stabilization of its mass, which allows the identification of equilibrium. The equilibrium represents the equality of incoming and outgoing mass fluxes between the sample and the inside environment of the container. The equilibrium is attained when the variation between two successive weighings is less than 0.1 % ($\Delta m \leq 0.1$ %). This corresponds to the order of magnitude of the balance accuracy, which is 0.001 g.

First, the dry wood sample is conditioned in a container at *RH* 11 %. Once the mass of the sample is stabilized, the sample is scanned by *THz*. Then, the sample is moved to a higher *RH* container, where the mass stability is controlled by periodic weighing. The procedure is repeated until reaching an *RH* of 97 %. The sample is weighed before and after the scanning

to estimate the mass loss during the experiment. Figure 4-4 shows the water content of one wood sample during the whole process.

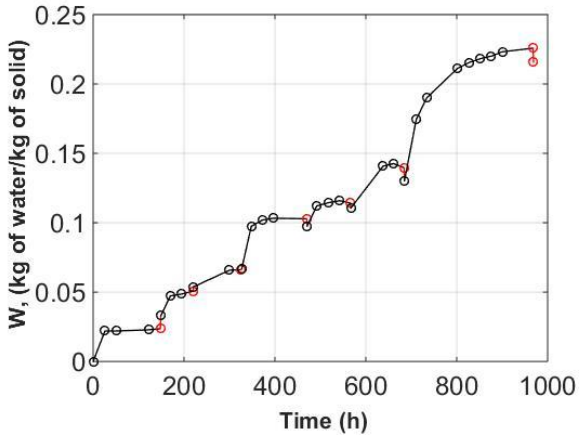

Figure 4-4: Water content of a wood sample during conditioning (black circles), and before and after the experiment (red circles).

Figure 4-4 shows that the water content is controlled until equilibrium, which represents the equilibrium water content (*EWC*). At this water content, the sample is scanned inside the enclosure to avoid contact with air. The red points represent the weighing of the sample before and after *THz* scanning (~40 *min*). We remark that when the sample is conditioned at an *RH* less than the environment *RH*, the sample slightly increases in mass. However, when it is conditioned at an *RH* higher than the environment *RH*, the sample losses mass during scanning.

The scan of the sample inside the container allows limiting the mass exchange with the environment of experiment room, which keeps the sample at a constant water content during the scan. For that, a preliminary *THz* calibration of the empty containers is carried out in order to take into account the signal attenuation due to the container. The scan is performed using a sample holder controlled by a homemade LabVIEW program. The movement of the scanned object (container + sample) is carried out by parameters in the program such as reference point, image size, pixel size, and the stability criterion of measurement in each pixel. Since the samples are scanned in a raster pattern (point by point), the scanning of the whole sample would take a long time (approximately 3 *h*). For that reason, only the region of interest (*ROI*, 30 *mm* x 20 *mm*) situated in the center of sample is scanned, which only lasts approximately 40 *min*.

In our study, we assume that the water content field in the *ROI* is homogenous. This assumption allows for mapping the water content within the *ROI* based on this calibration. However, this assumption is not totally correct due to the heterogeneity of wood in terms of structure. Indeed, the growth rings of wood have a different porosity and permeability to vapor. The alternation of early wood and latewood rings should affect the water content field.

The conditioning of samples also allows for obtaining the isothermal sorption curve, which is the empirical relation between the *RH* and the water content of the sample. Figure 4-5

presents the experimental sorption curves of three wood samples and the fitted model. In the literature, there are many models expressing water content as a function of *RH*, such as the GAB model, the Harkins model and the Henderson model [12]. The Henderson model shows a better fit of the experimental data and is given by equation (4-1):

$$RH = 1 - e^{-A(T+B)W^C} \tag{4-1}$$

where *A*, *B* and *C* are empirical coefficients and *T* is the temperature (*K*). These coefficients are given in Figure 4-5 for the blotting paper and three samples of maritime pine. A Levenberg–Marquardt minimization between the experimental data and equation (4-1) allows for estimating the coefficients *A*, *B* and *C*.

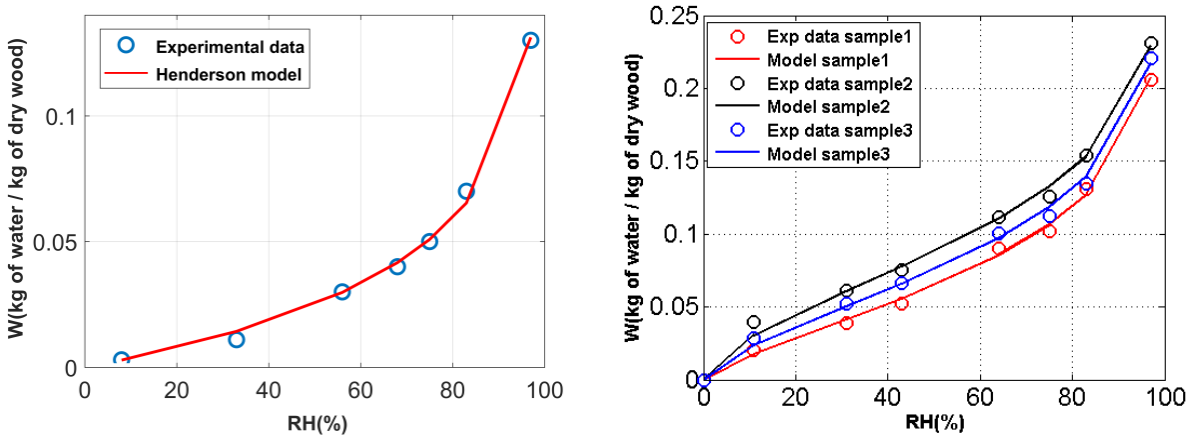

(a) (b)

Figure 4-5: Sorption curves of (a) blotting paper and (b) three samples of wood. Circles: experimental water content; continuous lines: fitted points using the Henderson model. The values of the constants are: A_b = 0.0843, B_b = 0.9981, C_b = 0.9793 for blotting paper and A_{wood1} = 0.1034, B_{wood1} = 0.9981, C_{wood1} = 1.3928, A_{wood2} = 0.1403, B_{wood2} = 0.9969, C_{wood2} = 1.6951, A_{wood3} = 0.1195, B_{wood3} = 0.9978, and C_{wood3} = 1.5316 for wood.

1.3 Analytical model for absorption in a multiphase material

A hypothesis about the water in the studied materials is tested. Regardless of the material, the samples are considered to be composed of two effective layers: i) a dry porous layer and ii) a fictive water layer. The fictive water layer is considered to be the resultant content of distributed water existing in the sample. The relation linking the incident and transmitted signals through a material exposed to *THz* radiation can be found using the Beer-Lambert law presented in equation (4-2).

$$I(x, y, \lambda) = I_0(x, y, \lambda) exp(-A) \tag{4-2}$$

where $I(x, y, \lambda)$ is the transmitted signal through a cell filled with water in (*V*), $I_0(\lambda)$ is the incident signal (*V*), λ is the wavelength (m), *A* is the *THz* absorbance without unit, and *x* and *y* are the spatial dimensions (*m*).

The global absorbance (A) in a multiphase material composed of a dry solid phase (blotting paper or wood) and a fluid (water) can be linearized to a sum of the water and solid absorption coefficients weighted by the thickness of each layer. It is given by equation (4-3).

$$A = -log\left(\frac{I(x,y,\lambda)}{I_0(x,y,\lambda)}\right) = \mu_s.e_s + \mu_w.e_w \tag{4-3}$$

where μ_s and μ_w are the absorption coefficients of solid and water (m^{-1}), and e_s and e_w are the thicknesses of the solid and water (m). Substituting equation (4-3) into (4-2) and dividing by the solid thickness (e_s) leads to equation (4-4).

$$Y = \frac{-log\left(\frac{I(\lambda)}{I_0(\lambda)}\right)}{e_s} = \mu_s + \mu_w \frac{e_w}{e_s} \tag{4-4}$$

where Y is called the absorption coefficient of the multiphase material (m^{-1}). Additionally, the water content (W) in a multiphase material is defined by equation (4-5).

$$W = \frac{m - m_s}{m_s} \tag{4-5}$$

where W is the water content in (kg of water / kg of dry material), m is the global mass of the multiphase material (kg), m_s is the mass of the solid phase (wood) in (kg), and m_w is the mass of the water (kg). By assuming a unit surface of the material, the water content can also be written according to equation (4-6).

$$W = \frac{\rho_w.e_w}{\rho_s.e_s} \tag{4-6}$$

where ρ_s is the density of the solid phase and ρ_w is the density of the water (1000 $kg.m^{-3}$). Combining equations (4-4) and (4-6), we obtain equation (4-7)

$$Y = \frac{-log\left(\frac{I(\lambda)}{I_0(\lambda)}\right)}{e_s} = \underset{b}{\mu_s} + \underset{a}{\rho_s \frac{\mu_w}{\rho_w}} W \tag{4-7}$$

Equation (4-7) allows for the linear linking of the global water content of the material to the absorption coefficient.

A calibration is done to ***validate an analytical model*** based on the Beer-Lambert law, linking ***the absorption coefficient***, ***the density of the solid*** and its ***water content***. In equation (4-7), W is controlled and measured by a gravimetric method (isothermal sorption curve); μ_s and ρ_s are the absorption coefficient and the density of the solid phase (wood), respectively,

and they are coefficients used to estimate by an inverse method. In the case of a material with known solid parameters (μ_s and ρ_s), it is enough to perform the *THz* scan to measure ***the water content without contact***. However, the absorption coefficient of water (μ_w) must first be first.

A calibration on pure thin water layers and dry samples using the *THz* technique allows for the estimation of the absorption coefficients of the water and dry samples and for checking the capability of the setup for contactless measurement through a comparison with values in the literature. Moreover, this calibration permits determination of the depth of water crossed by the *THz* at this wavelength. Once the water content coefficient is found, the tests are carried out on blotting paper and wood samples after the humidification process. The *THz* measurements allow for assessing the parameters of the model (4-7), i.e., the dry density of the material and its absorption coefficient.

1.4 Measurement of the *THz* material absorbance (Beer-Lambert)

1.4.1 Calibration of water

Since the experiments aim to estimate the water content by contactless measurement, the determination of water optical properties by the *THz* is crucial (absorption coefficient). The absorption coefficients of liquid water and water vapor at the millimetric wavelength range are shown to be quite close. In the literature, this coefficient is found to be equal to $10^4\ m^{-1}$ [102]. To check the absorption coefficient of liquid water, *THz* scans of water at different thicknesses have been carried out. The Omni-cell with spacer device (Figure 2-18) allows for setting the water to different layers from 50 μm to 300 μm. Due to the small size of the Omni-cell, small image of six pixels are taken for liquid water. Figure 4-6 presents the images of the transmitted signal for different thicknesses of water.

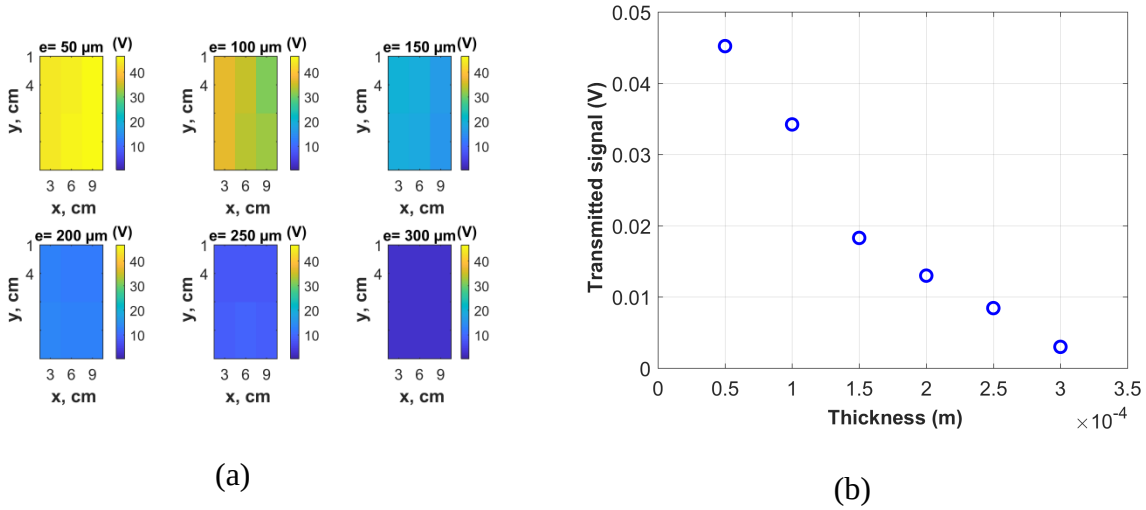

Figure 4-6: (a) Images of transmitted signal *I* for different water thicknesses in (*V*) and (b) the mean transmitted signal as a function of the water layer thickness.

Figure 4-6-a shows the transmitted signal decreasing with the increase in water layer thickness, which confirms the inverse proportionality between the *THz* signal and water

thickness. The curve in Figure 4-6-b presents Beer-Lambert behavior, as given by equation (4-2). For the case of a semitransparent enclosure (Omni-cell) filled with water, the absorbance can be linearized, as shown in equation (4-3), to the water absorbance and solid absorbance. Therefore, the scanning of an empty enclosure allows for obtaining the absorbance of the solid that is used to obtain the absorption coefficient of liquid water (equation 4-3).

Equation (4-3) shows a direct linear relationship between the absorbance of liquid water and its thickness. The slope is the absorption coefficient of water at this wavelength. To validate this equation, the mean absorbance of Figure 4-6-b is presented as a function of thickness and then fitted with a linear function. Figure 4-7-a presents the evolution of the liquid water absorbance with water thickness.

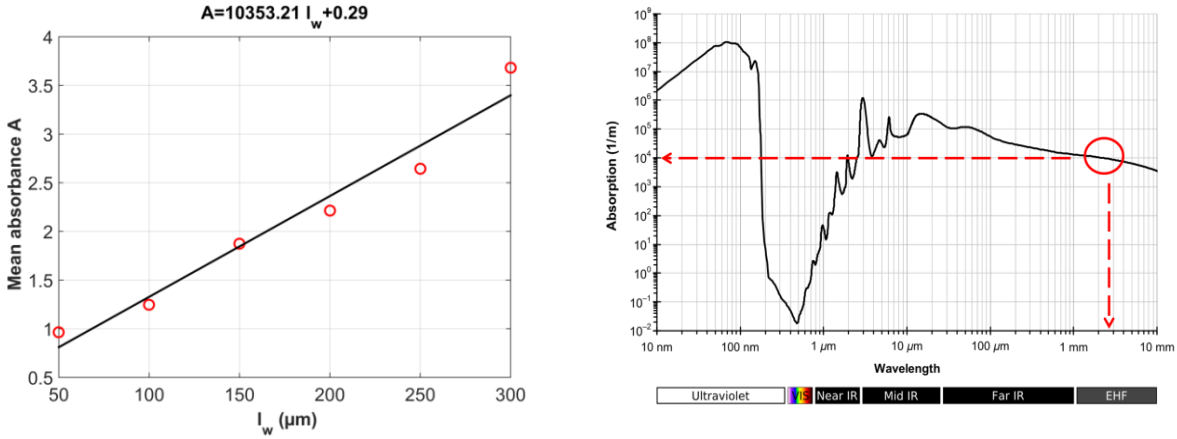

(a) (b)

Figure 4-7: (a) Mean absorbance of the liquid water as a function of its thickness. (b) The absorption coefficient of water as a function of wavelength, according to [98].

As expected, the water absorbance-thickness curve shows a linear behavior. According to equation (4-7), the slope of this curve is the absorption coefficient of liquid water. Here, the estimated value is $\mu_w = 10353\ m^{-1}$, which is in agreement with the literature (Figure 4-7-b), i.e., approximately $10^4\ m^{-1}$ for a wavelength of 2.7 *mm*.

1.4.2 Calibration of blotting paper

Similar to the previous section, the Beer-Lambert law given by equation (4-2) can be rewritten for a dry solid material (only dry solid phase). To validate equation (4-2) for blotting paper, a region of interest of 10 *px* x 10 *px* is scanned by the *THz* with a resolution of 1 *mm / px*. The thickness ranges from 0.2 *mm* to 9 *mm* (see section 1-2). Figure 4-8-a shows images of the transmitted intensity (*I*) measured through different thicknesses of the blotting paper.

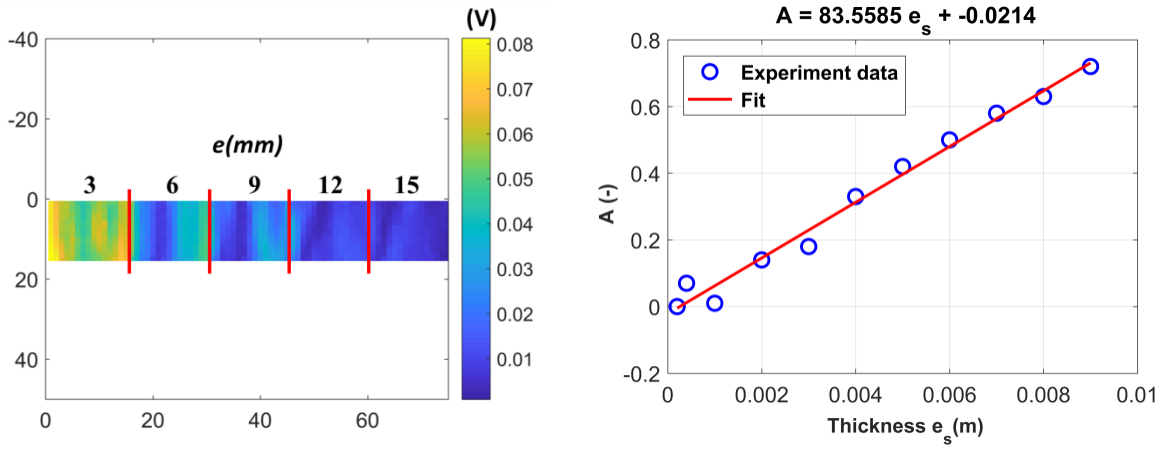

(a) (b)

Figure 4-8: (a) Images of the *THz* signal transmitted through different thicknesses of blotting paper (in V) and (b) the mean absorbance of blotting paper in terms of the thickness.

As expected, the signal decreases as the thickness increases. However, the stacking of samples shows a heterogeneity due to fiber compaction. As the sample is considered homogeneous, an average signal of the *ROI* is calculated. The absorbance behavior is linear, and the linear fit allows for obtaining an absorption coefficient of 83.56 m^{-1} for the blotting paper. Thus, the dependency of the Beer-Lambert type is verified. Figure 4-8-b shows that at thickness higher than 2 *mm*, the measurement of the *THz* is close to the fit. Therefore, to maintain a good measurement sensitivity to the water content, the cellulose sheet thickness is chosen to be 2 *mm* in the next tests.

1.4.3 Calibration of wood

In this section, the same experiment is conducted on wood boards with an *ROI* of 15 *mm* x 15 *mm* for a thickness ranging from 3 *mm* to 15 *mm*. Figure 4-9-a shows the images of the transmitted intensity (*I*) obtained through the wood for different thicknesses.

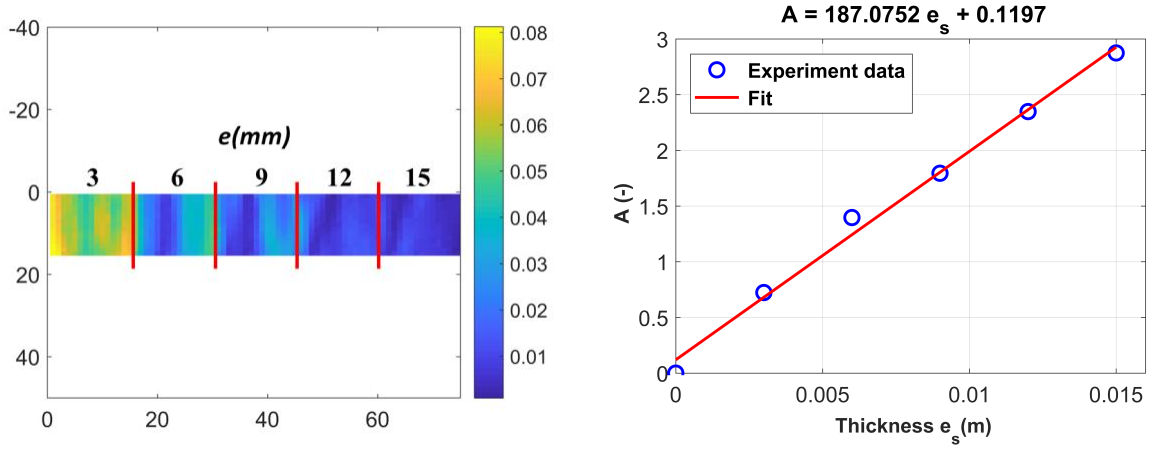

(a) (b)

Figure 4-9: (a) Images of the transmission signal of the *THz* beamline through different thicknesses of wood (in *V*) and (b) the mean absorbance of wood in terms of the thickness.

The signal seems to be heterogeneous, which is logical because of the heterogeneous structure of wood. However, at a wavelength of 2.7 *mm*, the rings are not distinguished due to the spot size covering several rings. To visualize the heterogeneity, it should be possible, for example, to work at other wavelengths using a multispectral source. Therefore, the mean absorbance is used to estimate the average absorption coefficient of wood (Figure 4-9-b). For a heterogeneous material, the absorbance shows a linear function with the thickness, which confirms the Beer-Lambert behavior. The estimated absorption coefficient of wood is 187 m^{-1}. Moreover, the studied materials are shown to be semitransparent where the signal is more or less attenuated, depending on the absorption coefficient of the material.

Theoretically, the maximum penetrated depth is the depth corresponding to a transmitted signal that has an order of magnitude of noise level. The noise signal-to-noise ratio (*SNR*) is defined as the ratio of the mean signal to its standard deviation. Therefore, the maximum crossed depth can be calculated by equation (4-8).

$$e_{max} = \frac{log\left(SNR\right)}{\mu_{est}} \tag{4-8}$$

where e_{max} represents the penetrated depth by the *THz* at this wavelength (m) and μ_{est} is the estimated absorption coefficient of the used material (m^{-1}). If we suppose that the *SNR* is 1 %, the maximum crossed depths for liquid water, dry blotting paper and dry maritime pine are respectively 445 μm, 55.1 *mm* and 24.6 *mm*.

For wet samples, the maximum crossed depth by the *THz* radiation depends on two parameters, the thickness of the solid and thickness of the fictive water layer (water content). The equation representing the crossed solid thickness as a function of water thickness is given by equation (4-9).

$$e_s = \frac{A}{\mu_s} - \frac{\mu_w}{\mu_s} e_w \tag{4-9}$$

However, the absorbance at noise level corresponds to the maximum crossed depth in the wet sample. Therefore, the maximum crossed thickness of a solid can be given as a function of water thickness (water content), as shown in equation (4-10).

$$\left(e_s\right)_{max} = \frac{log\left(SNR\right)}{\mu_s} - \frac{\mu_w}{\mu_s}\left(e_w\right)_{max} \tag{4-10}$$

Therefore, the crossed thickness of the sample is inversely proportional to the water depth, i.e., the thicker the water layer, the thinner the maximum cross thickness. The maximum cross thickness of a solid is shown as a function of water layer in Figure 4-10.

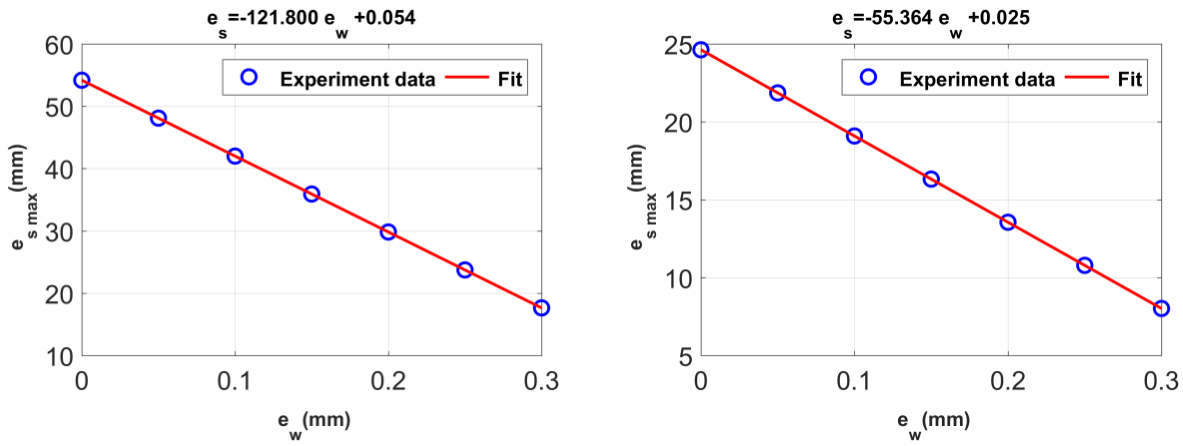

(a) (b)

Figure 4-10: Maximum crossed thickness of the solid as a function of the water layer (a) for blotting paper and (b) for maritime pine.

1.5 Contactless terahertz measurement of the water content distribution

1.5.1 Blotting paper

As shown in section 1-2, once the sample of blotting paper (2 *mm*) is equilibrated (via a saline solution), it is scanned inside the container to prevent mass exchange with the environment. Figure 4-11 presents the *THz* absorbance images obtained for a blotting paper sample with a thickness of 2 mm at different relative humidity values. The increase in water content leads to an increase in the *THz* absorbance of the material.

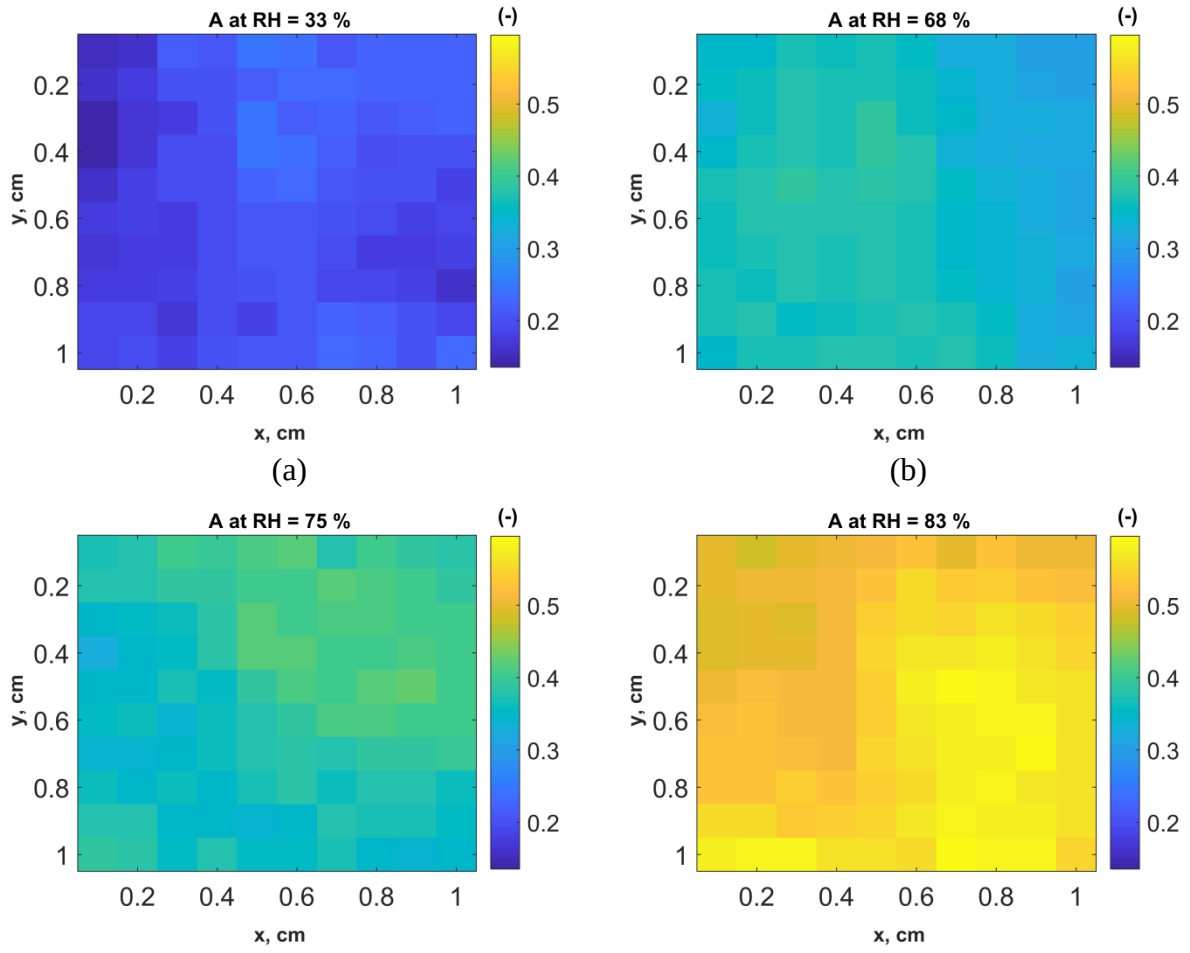

Figure 4-11: *THz* absorbance images (without unit) of a blotting paper sample for different *RH:* (a) at *RH* = 33 %, (b) at *RH* = 68 %, (c) at *RH* = 75 % and (d) at *RH* = 83 %.

The global water content at equilibrium and the mean *THz* signal are measured (Figure 4-12-a). The transmitted *THz* signal decreases with increasing water content (water thickness), which is confirmed by equation (4-7). The calibration between the *THz* absorbance and water content allows for obtaining Figure 4-12-b. It is convenient to emphasize the linear relationship that connects the water content and the *THz* absorbance. This relationship allows for the validation of the new imaging technique presented in this study, which opens new perspectives in the study of monitoring the water content of semitransparent heterogeneous materials at the local scale.

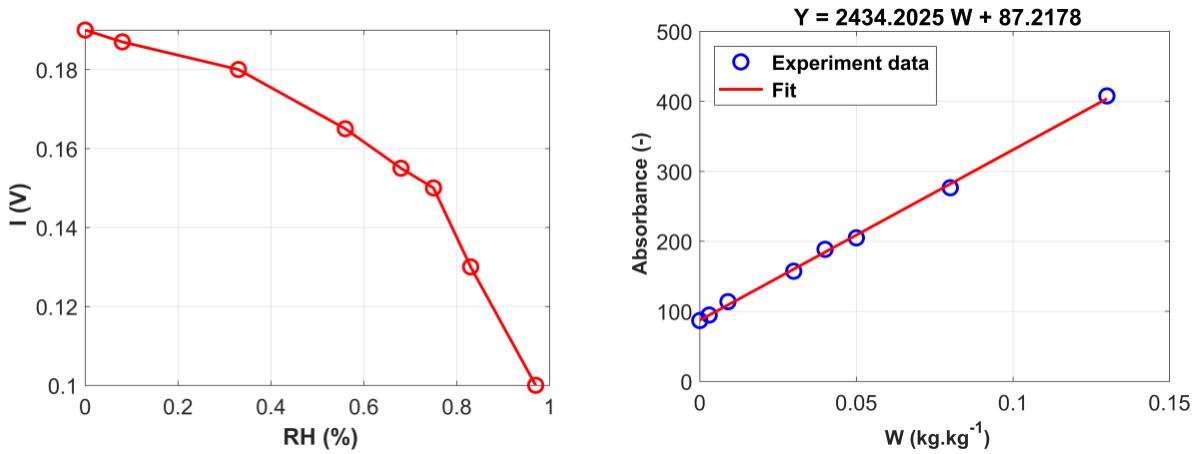

(a) (b)

Figure 4-12: (a) The *THz* signal transmitted through blotting paper (thickness 2 *mm*) as a function of the relative humidity within the sample and (b) the average *THz* absorbance imaging in terms of the water content.

The ordinary least squares based-regression (*OLS*) allows for revealing the empirical relationship between the absorption coefficient of a multiphase material and its global water content. This relation gives information about the solid matrix, such as its density or absorption coefficient. By comparing the fitted equation with equation (4-7), the absorption coefficient and density of a solid can be estimated. According to equation (4-7), the slope of the regression shown in Figure 4-12-b is proportional to the density, and the origin point represents the absorption coefficient of the solid matrix. For blotting paper, $\rho_s \frac{\mu_w}{\rho_w} = 2434.2$, with $\rho_w = 10^3\ kg.m^{-3}$ and $\mu_s = 10^4\ m^{-1}$ (as checked in 1-4-1). Thus, the density of the solid blotting paper is $\rho_s = 243.4\ kg.m^{-3}$, and its absorption coefficient is 87.2 m^{-1}. This coefficient is in agreement with the value found in the calibration of dry blotting paper (see section 1-4-2). These two values will allow the mapping of water content through *THz* images.

Using the coefficients (absorption coefficient and density) estimated for each pixel, the water content can be mapped, as shown in Figure 4-13.

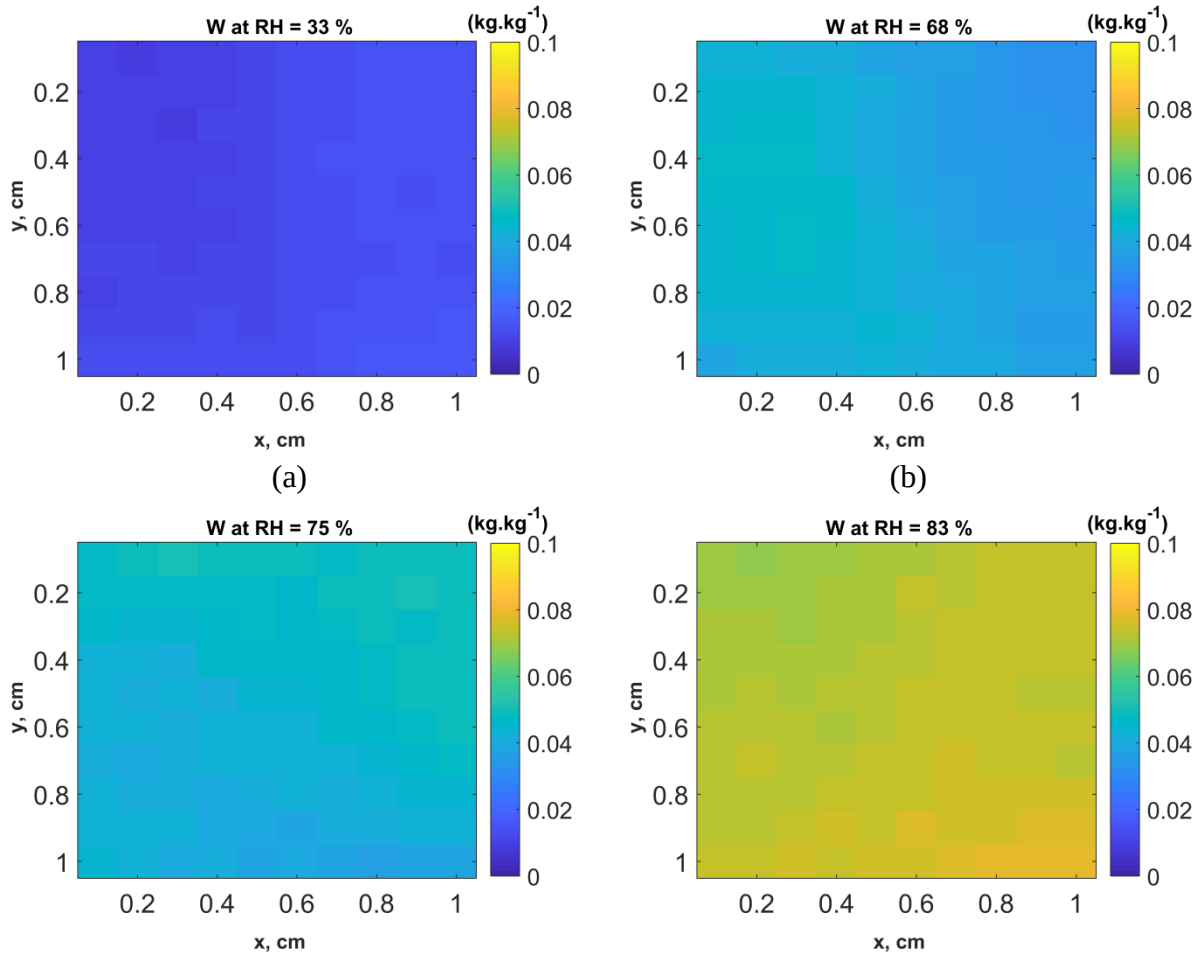

Figure 4-13: Contactless measurement of water content in a blotting paper sample after conditioning at different *RH* and at equilibrium (10 *mm x* 10 *mm*): (a) at *RH* = 33 %, (b) at *RH* = 68 %, (c) at *RH* = 75 % and (d) at *RH* = 83 %.

1.5.2 Maritime pine

Figure 4-14 presents the *THz* absorbance images obtained on a wood sample at different relative humidity values. The influence of the water content of wood on the *THz* absorbance of the material is clearly shown: the higher the water content (or the *RH*) is, the higher is the absorbance of the material.

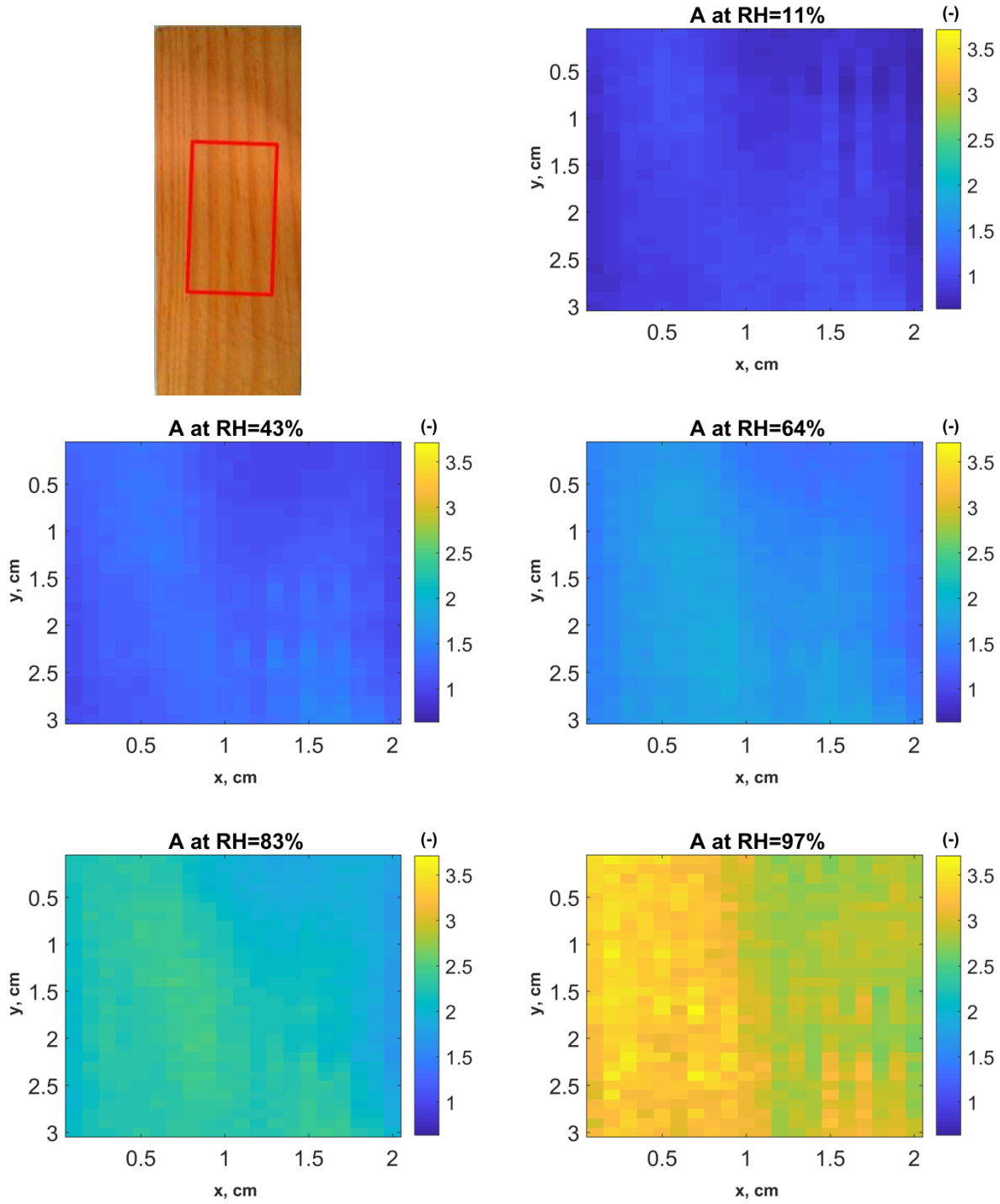

Figure 4-14: *THz* absorbance images (without unit) of a wood sample for different *RH*.

By using neutron radiography [36], it is found that the spatial distribution of moisture in softwood is not uniform and depends on the position of the wood rings, i.e., the alternation of early and late wood. In Figure 4-14, as mentioned before, at this wavelength, the influence of the wood rings is not clearly seen, and consequently, the absorbance field of the samples is quite uniform. This can also be due to the structure of the wood sample, where the rings are inclined in the third dimension (Figure 4-15). Indeed, as the wavelength is millimeteric, the spot size covers several rings, and thereby, distinguishing the rings is not possible.

Consequently, the measured signal is representative of the water content contained in both early and late wood.

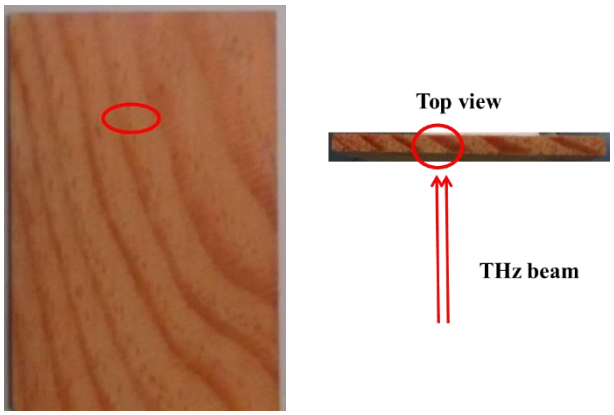

Figure 4-15: The effect of the inclined rings on the *THz* beam attenuation.

A first improvement to the *THz* signal measurement using an infrared camera is made, which will allow for a better understanding of the effect of the wood structure on the water content distribution. Figure 4-16 presents the experimental relationship between the global absorption coefficient of each sample and its water content. The global absorption coefficient is the mean value of that of the image pixels.

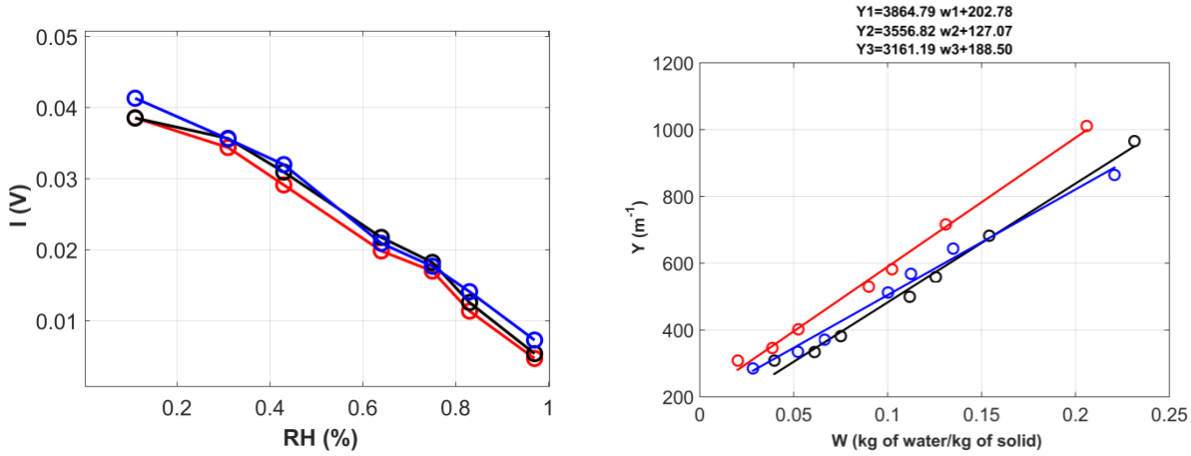

(a) (b)

Figure 4-16: (a) The *THz* signal transmitted through three pine samples (thickness 3 *mm*) as a function of the relative humidity within the sample. (b) The mean absorption coefficient of each sample as a function of its relative humidity. Circles: experimental values, continuous lines: model fit using equation (4-7). Header: Fitting equations for each sample.

The measurements of the three wood samples show a linear relationship between the absorption coefficient of the material and the sample's water content. It is then possible to fit the experimental values by using the analytical model developed previously and by using equation (4-7). With a linear regression, it is then possible to assess the missing parameters of equation (4-7) (i.e., μ_s and ρ_s, which are respectively the absorption coefficient and the density of the solid phase (wood)). The obtained values and the mean values for each sample are presented in Table 4-1.

	Density (kg/m^3)	Absorption coefficient (m^{-1})	Coefficient of determination, R^2
Sample 1	386.5	202.8	0.9977
Sample 2	355.7	127.1	0.9953
Sample 3	316.1	188.5	0.9936
Mean value	**353.1**	**171.4**	
Standard deviation	35.3	40.2	

Table 4-1: Density, absorption coefficient and mean value of wood for each sample. The coefficient of determination (R^2) of the linear regression of equation (4-7) is also given to indicate the reliability of the fitting.

Table 4-1 shows that the density of the solid matrix of maritime pine is 353 $kg.m^{-3}$, which is in agreement with values found in [103, 104]. Moreover, the absorption coefficient of the solid at this wavelength is 171 m^{-1}. This coefficient is in agreement with the value found for the calibration of dry wood (see section 1-4-3). These two values will allow mapping the water content through *THz* absorbance images.

Using a linear ordinary least squares based-inverse method, the absorption coefficient and density can be estimated for each pixel, which allows mapping of the water content field of samples, as shown in Figure 4-17.

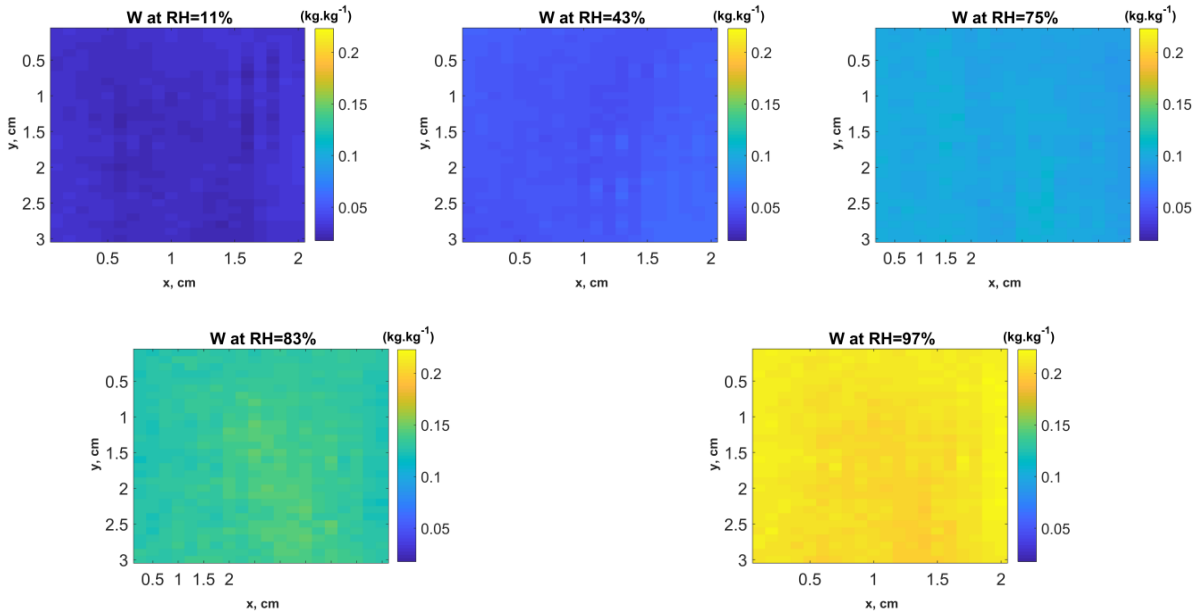

Figure 4-17: Contactless measurement of water content of a wood sample after conditioning at different *RH* and at equilibrium (30 *mm x* 20 *mm*).

1.6 Conclusion on the *THz* measurement of water content

The aim of this first section was to demonstrate the possibility of using a *THz* imaging technique for quantitative contactless measurements at the local scale. An infrared monodetector has been used to calibrate the relation between the *THz* absorbance and the water content of the material.

First, a linear relationship between the thickness and absorbance is shown for three different materials: liquid water, dry blotting paper and dry maritime pine. As shown by equation (4-3), the absorbance of a material decreases with increasing thickness. Moreover, the setup showed the capability to cross different thicknesses depending on the absorption coefficient of the scanned material. In addition, at different relative humidity levels, a linear behavior between the water content and the absorbance was demonstrated. As expected, the absorption of the material decreases as the global water content increases.

The absorption coefficient of blotting paper was found to be 87.2 m^{-1}, and the wood absorption coefficient was found to be 171.4 m^{-1}.

The *THz* wave sensitivity to water content allows for validating the use of the *THz* technique as an efficient, low-cost tool for contactless measurements of water content. This paves the way to use the developed model for studying the transient diffusion of vapor within homogeneous and heterogeneous materials and for estimating the hydric diffusion coefficient. The next section will be devoted to the *THz* imaging of transient vapor diffusion during drying or hydric excitation.

2 Contactless *THz* monitoring of transient water content and diffusion coefficient estimation

In the previous section, it was shown that it is possible to obtain the water content field from the *THz* image through a preliminary calibration of the absorption coefficient of a material in a steady-state hydric state. In this section, the ***monitoring of transient water content in blotting paper and wood samples is presented.*** For both materials, preliminary tests are performed during the drying of small samples in such a way that ***the diffusion can be considered unidimensional.*** Then, ***2D images*** of planar samples during ***hydric excitation*** are carried out. For both materials, ***inverse methods are used*** in order ***to estimate the water diffusion coefficient.***

2.1 Study on homogeneous material (blotting paper)

2.1.1 Water content measurement under a *1D* drying condition

In this section, the experimental water content profiles evolution in time is measured and then compared with a diffusion model. For that, a wet blotting paper sample is scanned inside a rectangular semitransparent enclosure open at the top and bottom (Figure 4-18). The sample is being dried by the environment through natural convection (boundary conditions). Then, an inverse method based on the Levenberg–Marquardt minimization algorithm between the experimental image and the theoretical solution of Fick's equation is used to estimate the diffusion coefficient.

Twenty samples of blotting paper are cut with dimensions of 120 *mm* x 5 *mm* x 0.2 *mm*. These samples are stacked to obtain a total thickness of 4 *mm*. The sample is first conditioned at a relative humidity of 83 % (*KCl* solution) and a temperature of 30 °*C*. Once equilibrium is established, the sample is placed in the drying enclosure and then scanned. The monitoring of drying is carried out by scanning three vertical lines with dimensions of 100 *mm* x 3 *mm* in the middle of the sample with a resolution of 1 *mm / px*. The scanned lines are situated along the area shown in Figure 4-18.

Since the mass gradient along the width of the sample is small with respect to the diffusion occurring along direction *z* ($\partial W/\partial z >> \partial W/\partial x$), the diffusion can be considered one dimensional. Therefore, the vertical scanned lines are averaged to obtain a mean vertical line representing the diffusion at a given instant. The scan is performed every 26 *min* with 5 *s / px*. The obtained image is then a column of 100 points recorded every 26 *min* during 17 *h*. The results showing the space-time monitoring of water diffusion are presented in Figure 4-18.

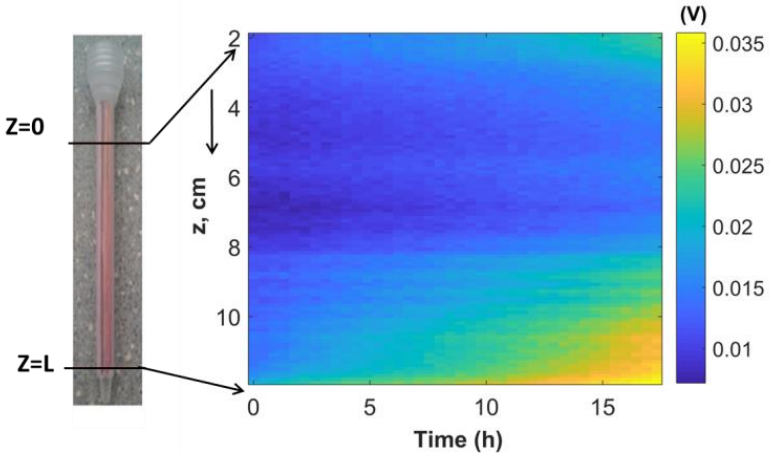

Figure 4-18: The analyzed sample and the region of interest (100 points of 1 *mm*) and (b) monitoring of the *THz* transmitted intensity during drying.

As shown in Figure 4-18, the initial transmitted signal is quite low due to the high water content of the material. It is worth noting that the water distribution at $t = 0$ is nonhomogeneous. The lower part of the sample (lower than $z = 80$ *mm*) shows a smaller *THz* signal, which corresponds to a higher initial water content. This can be due to an imperfection in the equilibration of the blotting paper. In addition, the space-time image of the water content can be obtained using the developed model given by equation (4-7). The signal increases with time at both sides of the enclosure, due to the drying of the blotting paper sample.

Thereafter, a theoretical solution of the Fick equation with symmetric boundary conditions in Fourier space is proposed. An inverse method based on the minimization of the experimental image and the theoretical solution can then be used to estimate the water diffusion coefficient.

The equation for a *1D* transient mass diffusion within a homogeneous material, i.e., where the diffusion coefficient is independent of space, can be given by the Fick equation. (4-11)

$$\frac{\partial W(z,t)}{\partial t} = D\frac{\partial^2 W(z,t)}{\partial z^2} \tag{4-11}$$

where W is the water content in (*kg* of water by *kg* of dry solid), z is the diffusion direction in (*m*), t is the time in (*s*), and D is the mass diffusion coefficient in ($m^2.s^{-1}$). The boundary conditions of the diffusion problem mentioned in Figure 4-18 are symmetric at $z = 0$ and $z = L$. The initial and boundary conditions can be given by equation (4-12).

$$\begin{cases} W\left(t=0,z\right) = W_0 \\ W\left(t,z=0\right) = W(t,z=L) = W_1 \end{cases} \tag{4-12}$$

where W_0 is the initial water content in (*kg* of water / *kg* of solid) and W_1 is the water content at the extremities $z = 0$ and $z = L$. The normalization of equation (4-13) and conditions (4-12) by the initial water content is given by equation (4-13).

$$\begin{cases} \dfrac{\partial X(z,t)}{\partial t} = D\dfrac{\partial^2 X(z,t)}{\partial z^2} \\ X(t=0,z) = X_0 \\ X(t,z=0) = X(t,z=L) = X_1 \end{cases} \tag{4-13}$$

where X is the dimensionless water content, X_0 is the initial water content and X_1 is the ambient water content. This system is resolved using a Fourier transform among z, where the general solution is given by equation (4-14).

$$X(z,t) = X_0 + F^{-1}\left[(X_0 - X_1)\left(\frac{1-\cos(\alpha_n)}{\alpha_n}\right) exp\left(-D\alpha_n^2 t\right)\right] \tag{4-14}$$

A Levenberg-Marquardt-based ordinary least squares minimization method between the analytical solution (equation 4-14) and the measured space-time image (Figure 4-18) is performed. The minimization aims to find the best value of the diffusion coefficient, allowing for the model to fit the experimental data with a low error. Moreover, the ambient atmosphere water content (X_1) can be estimated. Thus, the normalized measured water content by the initial value (X) and the estimated normalized field is shown in Figure 4-19.

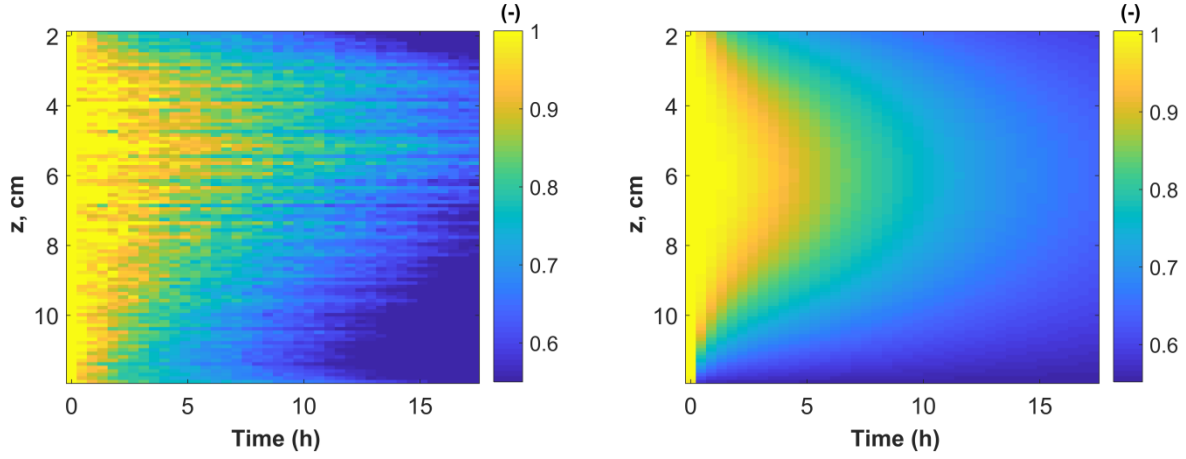

(a) (b)

Figure 4-19: (a) Normalized experimental water content, (b) the space-time field calculated by minimization using the estimated parameters (D_{est} = 4.07.10^{-8} $m^2.s^{-1}$ and X_{1est} = 0.55).

The result of the mass diffusion minimization presented in Figure 4-19-b is in agreement with the obtained experimental data in Figure 4-19-a. The estimated mass diffusion coefficient is D_{est} = 4.07 10^{-8} $m^2.s^{-1}$. This value shows a gap of 2 % with the found value in the literature (D = 4.10^{-8} $m^2.s^{-1}$) [105]. The relative error between the experimental and calculated water content fields is presented in Figure 4-20.

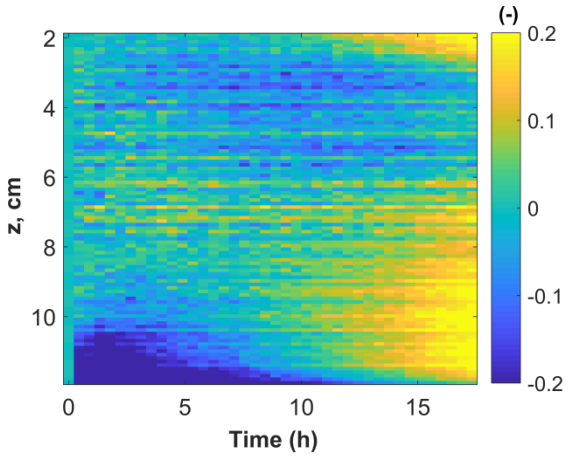

Figure 4-20: Relative error between the experimental and the theoretical model.

Figure 4-20 shows the relative error between the experimental and numerical fields of water contents. This error shows a heterogeneity ranging from -0.2 to 0.2. However, in the region between 0 *h* and 10 *h*, nonhomogeneity of the water content is observed due to the difference between the boundary conditions situated at $z = 0$ and $z = L$. In the experiment, the diameters of the openings are 2 *cm* at $z = 0$ (on top) and 2 *mm* at $z = L$. Since the top diameter is 10 times wider than that at the bottom, the drying will be faster in the superior part of tube, which is shown in Figure 4-20 ($z > 0.09$ *m*). Therefore, the water content is asymmetric.

Despite this weakness, this section proves that the use of the *THz* imaging method associated with the inverse methods allows for the local estimation of mass diffusivity in drying problems. However, it should be indicated that, generally, the diffusion coefficient is not constant and depends on the water content of the material. For example, [14] showed that the diffusion coefficient decreases exponentially with increasing water content. As an initial approach, in this study, the diffusion coefficient is considered to be independent of the water content.

2.1.2 Water content imaging under hydric excitation

Since the scan of a sample region of 100 *mm* x 3 *mm* takes 26 *min* (5 *s* / *px*), a larger region of interest needs a longer time. This will not allow for the monitoring of transient diffusion within samples. Therefore, the use of a *2D* detector (developed in chapter 2) would allow the monitoring of water content within homogeneous and heterogeneous samples in transient diffusion due to the instrument's high acquisition rate. Thus, the monitoring of diffusion at transient regime is now conducted by using the *TTC* in the situation of a hydric excitation. The experimental setup is presented in chapter 2, section 2. It is also summarized in Figure 4-21.

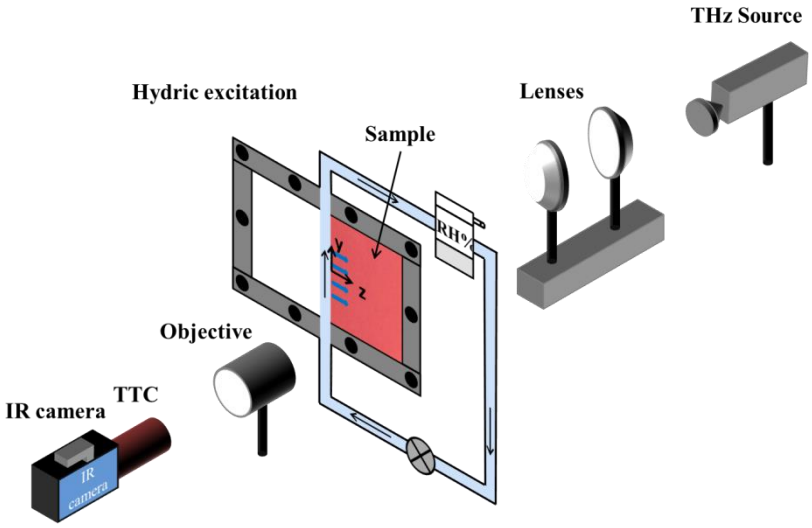

Figure 4-21: Setup of the *THz* experiment for the situation of hydric excitation.

The measurement of the full field of the *THz* transmittance by the *2D* detector provides more data about the diffusion due to the high acquisition rate (200 images / *s*). As a reminder of chapter 2, in the experiments performed with hydric excitation, the sample is insulated on three sides by rubber and excited on one side by a wet-air flux with a flow rate of 100 *L / h* continuously pumped from a conditioning container at *RH* 97 %. The sample is then imaged during 16 *h* (films of 1 *s* every 5 *min*). Once the films are recorded, image processing using the four images method and *SVD* decomposition is carried out, aiming to obtain the amplitude (chapter 3).

The boundary conditions in this experiment can be given by equation (4-15).

$$\begin{cases} D_y \left.\dfrac{\partial W(y,z,t)}{\partial y}\right|_{y=\pm l} = 0 \\ D_z \left.\dfrac{\partial W(y,z,t)}{\partial z}\right|_{z=L} = 0 \\ W(y=0,z,t=0) = W_0 \end{cases} \tag{4-15}$$

Thereafter, since the material is considered to be homogeneous and the sample is insulated at $y = -l$ and $y = +l$, the diffusion is supposed to be monodimensional along the z direction. Thereafter, the images are averaged along y to obtain one average line along z as a function of time. The obtained image represents the mean absorbance as a function time. The image of the water content is calculated through the images of absorbance using equation (4-7), which is presented in Figure 4-22.

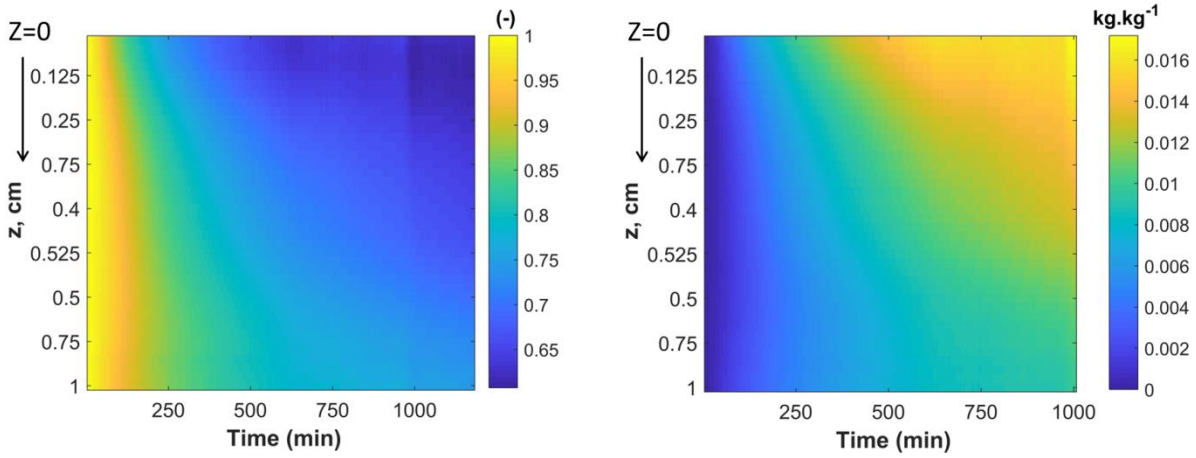

(a) (b)

Figure 4-22: Averaged image of amplitude along *z* within the blotting paper as a function of time: (a) transmittance and (b) water content.

The boundary conditions can be rewritten as follows:

$$\begin{cases} \overline{W}(z,t=0) = W_0(z) \\ D_z \left. \dfrac{\partial \overline{W}(z,t)}{\partial z} \right|_{z=L} = 0 \end{cases} \tag{4-16}$$

The water content is initially low and then increases with time due to the diffusion of vapor with time. Figure 4-23 shows the time evolution of the water content at different points along *z*, showing the diffusion process into the material.

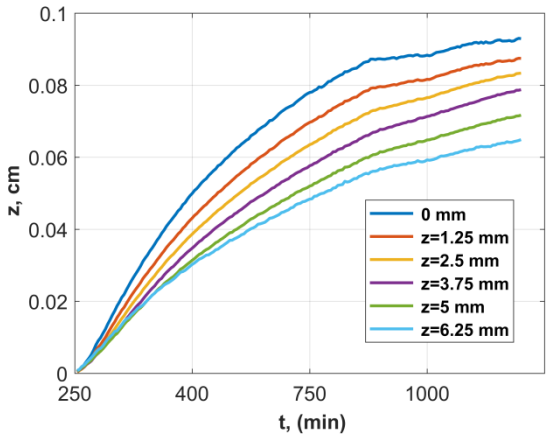

Figure 4-23: Profiles of the water content at different positions along the z direction as a function of time.

Since the mean diffusion is along *z*, the problem can be modeled with the *1D* diffusion given by equation (4-13). Therefore, the *1D* modeling solution to the diffusion problem is used for the minimization, aiming to estimate the diffusion coefficient of the blotting paper. A numerical simulation of diffusion using finite difference (central scheme) with the experimental and initial boundary conditions is performed. The obtained water content image is shown in Figure 4-24.

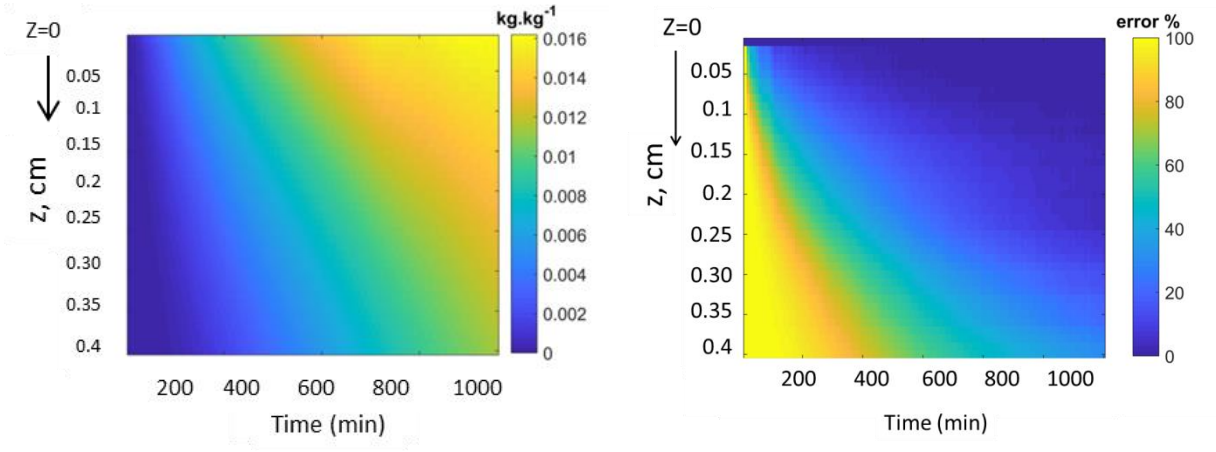

(a) (b)

Figure 4-24: (a) Numerical image of the water content using boundary conditions mentioned in Figure 4-22-b. (b) The relative error between the experimental and numerical water content, with 1 *px* = 0.25 *mm*.

The Levenberg–Marquardt minimization of the experimental and numerical data allows for the estimation of the hydric coefficient D_{est} = 4.1 10^{-8} $m^2.s^{-1}$. However, Figure 4-24-b allows for determining the dynamic part where the minimization is done. This value is in agreement with the found value in the previous section (D = 4.07 10^{-8} $m^2.s^{-1}$) using the *THz* monodetector for the drying situation with different boundary conditions. The error between the two values is only 3 %, which proves the capability of the *TTC*-based *THz* setup for contactless measurements of hydric diffusion.

2.2 Study on heterogeneous material (maritime pine)

2.2.1 Preliminary study at a local scale under drying

As for the blotting paper, a first type of test has been carried out on wood, consisting of the *1D* drying problem and studied by the point-by-point method. A wood sample (same dimensions as previously, 100 *mm* x 40 *mm* x 3 *mm*) was preconditioned at *RH* = 97 %, resulting in an initial water content of approximately 23 % (initial mass = 7.454 *g*, and dry mass = 6.064 *g*). After stabilization of the mass, the sample was placed on a balance in the ambient laboratory atmosphere. Then, the natural convection at the sample faces are involved in its drying until the stabilization of its mass. The final mass of the sample is 6.692 *g*, i.e., a water content of 10.4 %. The measurement of relative humidity in the laboratory is performed by a contactless sensor (Tinytag plus 2). During the drying of the sample, the *RH* varied between 47.3 % and 51.5 %, with a mean of 48.88 % and a standard deviation of 0.95 %. The temperature ranged from 294.4 *K* to 297 *K*, with a mean temperature of 295.3 *K* and a standard deviation of 0.67 *K*.

The sample holder is kept still to avoid the perturbation of the balance measurement. Thus, the *THz* measurement is only focused on the center point of the sample (3 *mm* x 3 *mm*), as shown in Figure 4-25.

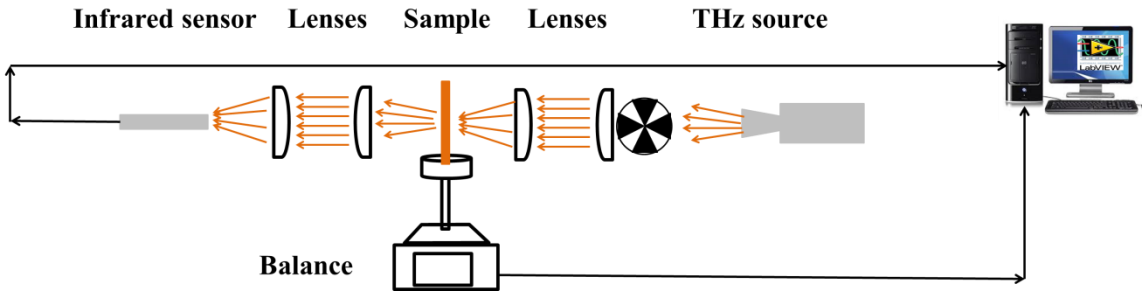

Figure 4-25: *THz* global schemes of the monodetector based-setup with controlled balance weighting of the sample every 6 *s*.

The total duration of the test is 20 *h*. The sample mass and the *THz* signal are measured every 6 *s* through LabVIEW program recording the weight and the transmitted signal through the wood sample. Figure 4-26 shows the evolution of the global water content and the absorption coefficient of the studied point (center of the sample) as a function of time. As expected, the *THz* absorption decreases with the water content of the sample.

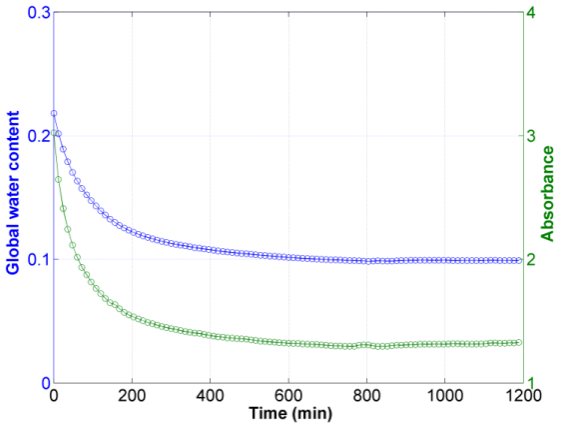

Figure 4-26: Left axis: the evolution of the global water content of the sample (measured by weighing). right axis: the evolution of the absorbance at the center of the sample.

By considering the known μ_s and ρ_s values (Table 4-1), the local water content of the center of the sample can be calculated by equation (4-7).

Figure 4-27 represents the evolution of the local water content in the center of the sample, which was assessed by the interpretation of the *THz* measurement. For comparison, the evolution of the global water content, which was assessed by weighing the sample, is also plotted in this figure.

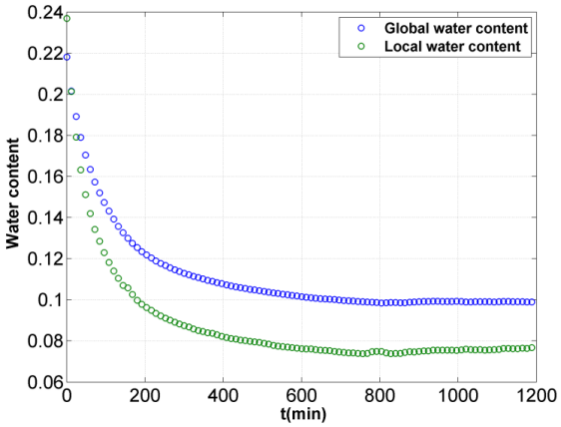

Figure 4-27: Evolution of the local water content in the center of the sample and the global water content.

The evolution of the local water content is similar to the global one. At the local scale, the initial water content is approximately 24 %, and the final water content (at the end of drying) is approximately 8 %. On a global scale, the initial and postdrying water content values are 23 % and 10 %, respectively. The magnitude of the local water content acquired by the *THz* measurement is therefore reliable, and the capacity of the *THz* technique to measure water content is demonstrated. The difference between global and local water contents can be explained by a drying gradient, especially along the vertical direction of the sample. The sample is placed on a balance, and then, the convective exchange at the lower part of the sample is probably less important.

2.2.2 Water content imaging under hydric excitation

In this part, the same experiment performed with blotting paper (see section 2.1.2) is conducted on a maritime pine sample in the tangential longitudinal section (*T-L*), as shown in Figure 4- 28.

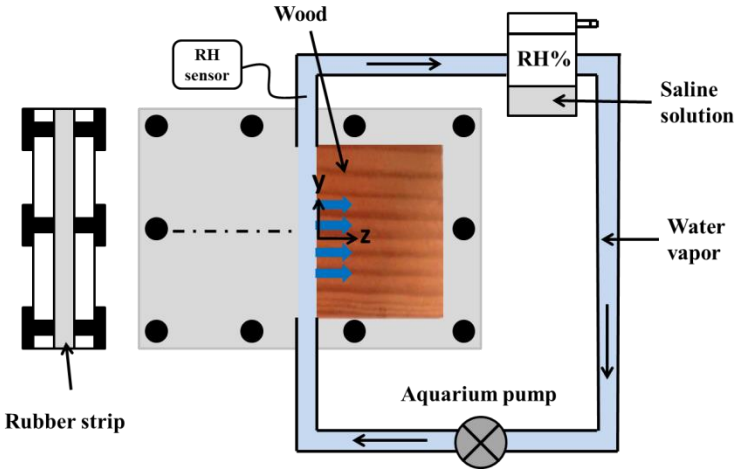

Figure 4- 28: Hydric excitation of a maritime pine sample along the longitudinal direction (along the ring direction, *z*)

Since the wood is anisotropic, the diffusion is a function of *y*. However, since the excitation is constant along *y* at $z = 0$ and since the sample is insulated by rubber at $z = L$, $y = 0$ and $y = l$, we assume that the diffusion mainly occurs along the *z* direction. Moreover, it is worth noting that along the *z* direction the diffusion coefficient may not be constant due to growth ring alternation. In addition, at this wavelength, the earlywood and latewood cannot be distinguished. This leads us to suppose that we are estimating an apparent diffusion coefficient along the *z* direction. This simplification leads us to simplify the *2D* transient model to a *1D* transient model, which joins the case of a homogeneous material (blotting paper).

The Levenberg–Marquardt minimization between the experimental and numerical water contents obtained by a finite difference scheme is carried out. Figure 4-29 shows the experimental numerical water content obtained with the same boundary conditions.

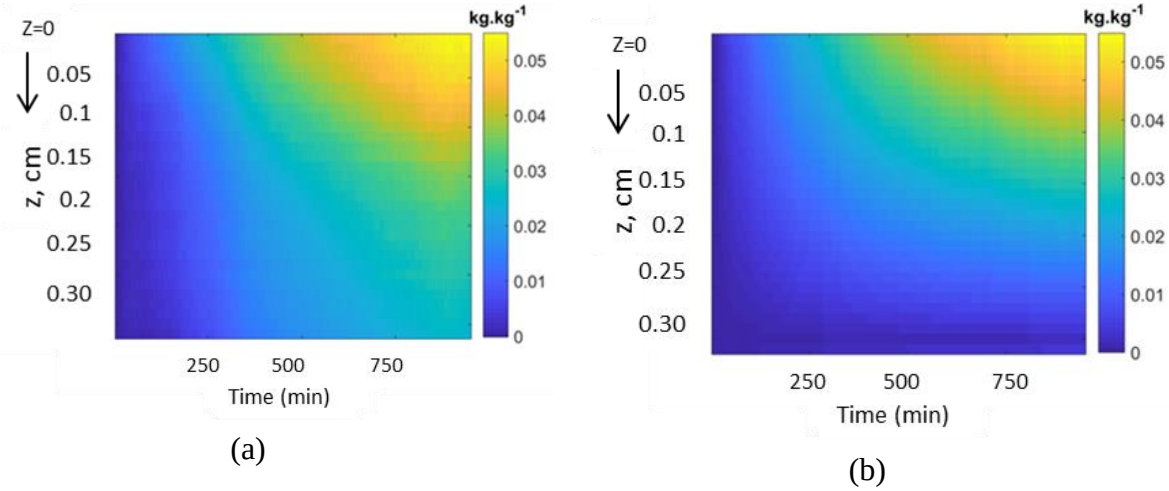

Figure 4-29: (a) Space-time image using the *TTC* during the hydric excitation of wood. (b) The numerical image of the water content using the boundary conditions with 1 pixel = 0.25 *mm*.

As shown in Figure 4-29, the diffusion within wood is slower than in blotting paper. The diffusion depth (dynamic part of *z*) is lower than 3 *mm*. However, the diffusion coefficient in such a case represents the apparent value since the growth rings are not distinguished. The first estimation shows a value for the diffusion coefficient as 4. 10^{-7} $m^2.s^{-1}$ However, in the literature, the value ranges between 10^{-7} $m^2.s^{-1}$ and 10^{-12} $m^2.s^{-1}$, depending on the wood and the diffusion direction (tangential-longitudinal, radial-tangential or radial-tangential direction).

2.3 Conclusion on *THz* monitoring of transient drying and excitation

The aim of this first section was to demonstrate the possibility of using *THz* imaging for contactless monitoring of transient water content. The *TTC* based-setup has been used to measure water content during mass transfer and to estimate the diffusion coefficient within homogeneous and heterogeneous materials.

First, the scanning is conducted on blotting paper in the drying situation. The minimization with the theoretical solution of the Fick equation allows the estimation of the diffusion coefficient with an accuracy of 3 % with respect to found value in the literature. Thereafter,

the experiment using the *TTC* in the hydric excitation situation with blotting paper and maritime pine samples has been conducted. However, the main drawback of this part is that the heterogeneity of the structure is not distinguished due to the dimension of the growth rings being smaller than the wavelength. The excitation device allowing for a continuous excitation is used.

Once, the image representing the mean diffusion along z is obtained, the numerical water content is calculated using the finite difference scheme with the experimental boundary conditions. The minimization between the experimental and numerical results allowed for the estimation of the mean diffusion coefficient along the diffusion direction of the blotting paper and maritime pine.

The next section will be devoted to the use of *THz* imaging for the contactless measurement of transient temperature within insulating materials.

3 Contactless transient *THz* temperature imaging of semitransparent materials by the thermotransmittance technique

Among the potential applications of *THz* radiation, the contactless measurement of insulating materials' temperature deserves further interest. This type of measurement involves verifying ***the relationship between the THz transmittance of a material and its temperature***. The *THz* wave ***optical properties of materials*** show a ***sensitivity to temperature variations***. This part aims to highlight the use of the ***2D THz detector*** based on ***an infrared camera coupled with the TTC*** (see section 3 in chapter 2) in transmission mode for the ***contactless measurement of transient temperature in insulating materials***. The used materials represent ***materials opaque in the visible or IR range*** (*PVC*, *PTFE*, *PMMA* and wood).

The measurement protocol and theoretical modeling are presented. Thereafter, ***calibration tests*** will be carried out for ***the THz transmittance and measured temperature*** using the samples and then discussed. ***The thermotransmittance coefficient of materials will be estimated*** through ***an inverse method***. Finally, ***the temperature field will be mapped*** using the estimated coefficient map, which allows for ***the validation of the THz imaging technique*** as ***a contactless method for transient temperature measurement***.

Moreover, ***3D simulations of the transient heat diffusion*** in a sample that has the same dimensions and the same initial and boundary conditions as those of the experiments have been carried out. The simulations allow justifying ***the lumped body assumption*** and ***the homogeneity of the temperature field in the region of interest*** *(ROI)*.

3.1 Measurement protocol

The experimental setup is represented by the setup shown in Figure 2-10. The samples are placed between the two systems. The sizes of the samples are as follows: *PVC* (100 *mm* x 40 *mm* x 4 *mm*), *PTFE* (100 *mm* x 40 *mm* x 4 *mm*), *PMMA* (100 *mm* x 40 *mm* x 5 *mm*) and wood (100 *mm* x 40 *mm* x 3 *mm*). For each experiment, the sample is preheated in an oven at 100 °*C*. After homogenization of the sample's temperature, it is placed on a holder situated on the focal plane between the focus and the second lenses. A thermocouple (type *K*) is fixed onto the sample surface (on the side in front of the *THz* source) to record its temperature during the experiments. The sample is then cooled by natural convection until it reaches the ambient temperature (approximately 20 °*C*). The transient evolution of each sample's temperature affects the capacity of the material to transmit *THz* waves. A two-channel wave-form generator (Agilent 33500B Series) is used to synchronize the *THz* source ignition and the *CCD* acquisition [73]. The synchronization method is detailed in section 3-4 in chapter 2.

As shown in Figure 2-10, the setup is based on the transmittance configuration, as the source and the detector are situated on opposite sides of the sample. Therefore, the transmitted signal would be affected along the third dimension (*z*-axis). The transmitted signal is the integration of the absorption coefficient along the sample *z*-axis in the Beer-Lambert equation. The hypothesis is justified by calculation of the Biot number and by numerical simulations using Finite Volume Toolbox, MATLAB FVT®.

The setup allows obtaining a series of films representing the *THz* signal transmitted as the temperature decreases in each sample. Once the raw films are recorded, they are processed to enhance the image quality. The four-images algorithm [87] is used to obtain the amplitude images. Once the amplitude images are obtained, the singular value decomposition (*SVD*) method is applied to denoise the images and reduce the data. The four images algorithm and *SVD* processing method are detailed in section 2 in chapter 3.

The assumption of a lumped body supposes that conduction is faster than convection, which makes the temperature field inside the sample uniform. In general, the Biot number (*Bi*), which represents the ratio between the conductive and convective resistances, should be less than 1 to validate the thermal thin-body hypothesis. The Biot numbers for the different materials tested in this study are presented in Table 4-2.

	ρ (kg / m^3)	C_p (J / $K.kg$)	k (W / $K.m$)	e (m)	t_c (s)	H (W / $m^2.K$)	Bi
Wood	400	2400	0.13	3.10^{-3}	**144**	20	**0.462**
PVC	1380	1050	0.2	4.10^{-3}	**290**	20	**0.500**
PMMA	1190	1470	0.19	5.10^{-3}	**437**	20	**0.421**
PTFE	2150	1000	0.24	6.10^{-3}	**645**	20	**0.333**

Table 4-2: Thermophysical properties of semitransparent materials.

As the Biot number is less than 1, the temperature along z can be considered constant (independent of z), and the integral in equation (4-19) can be reduced to the temperature measured on the surface multiplied by the thickness of the sample, as shown in equation (4-20). This hypothesis simplifies the model used and can be verified by the *3D* simulation of the temperature diffusion in a sample that has the proprieties of *PVC* with similar initial and boundary conditions. The convection coefficient and initial and final temperatures are H = 20 $W.m^2.K^{-1}$, ΔT_{init} = 44 $°C$, and ΔT_{fin} = 0 $°C$, respectively. The dimensions are 40 mm x 100 mm x 5 mm, with spatial discretization Δx = 1 mm, Δy = 1 mm, and Δz = 1 mm and time discretization Δt = 3 s. The simulation results are shown in Figure 4-30.

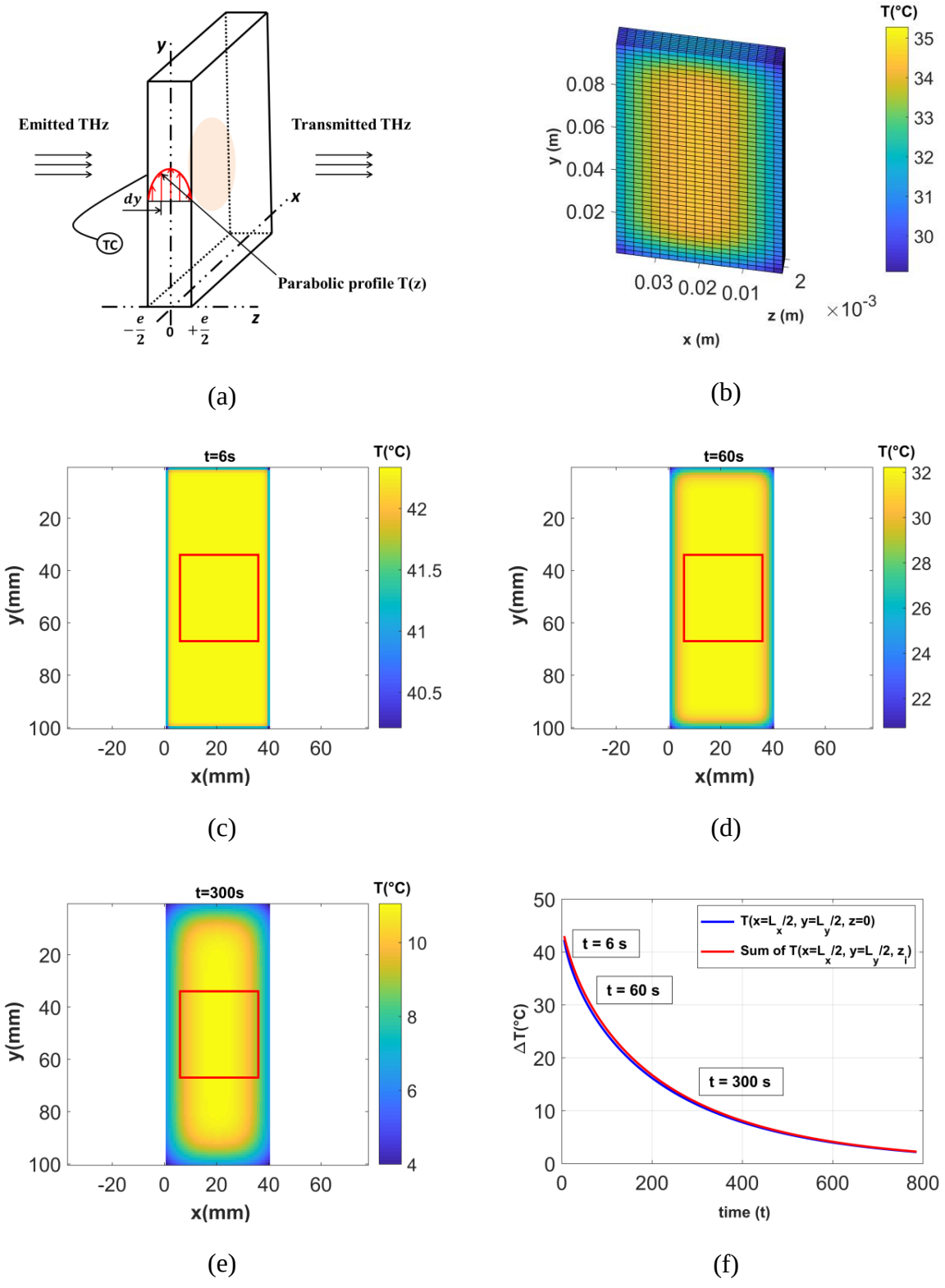

Figure 4-30: Simulation of the 3D transient case using the Finite Volume Toolbox MATLAB FVT® [106] under similar boundary and initial conditions. (a) The parabolic profile of the temperature within the sample along the thickness, (b) the 3D visualization of the sample temperature at t = 60 s, (c) the temperature field of the surface (z = 0) at t = 6 s, (d) the temperature field of the surface at t = 60 s, (e) the temperature field of the surface at t = 300 s, and (f) the evolution of the measured surface temperature and of the z-integrated temperature of the central pixel. Red rectangle: equivalent *ROI* in experiments.

Figure 4-30-c, Figure 4-30-d and Figure 4-30-e represent the temperature field of the sample surface (x, y, $z = 0$) at 6 *s*, 60 *s* and 300 *s*, respectively. The temperature field is quite uniform in the region of interest *(ROI)* and decreases with time, and the uniformity of the temperature field is justified. Moreover, Figure 4-30-f shows that the difference between the temperature measured at the surface and the average temperature (weighted average along the thickness) at early stages is only approximately 1 °*C* to 2 °*C*. This difference progressively decreases during the simulation. These results confirm that the temperature can be considered independent of *z* and homogeneous in the *ROI*. Therefore, the assumption of a lumped body is validated in this study, which allows for simplifying the model. Thereby, the punctual measurement taken by a thermocouple in the *ROI* can be linked to the thermotransmittance of all pixels within the ROI. Finally, the simulation has been validated for other materials (*PTFE*, *PMMA* and wood).

As previously mentioned, this setup allows obtaining a series of films representing the transmitted *THz* signal as the temperature decreases in each sample. Once the raw films are recorded, they are processed to enhance the image quality. Different processing methods (lock-in amplification, four images algorithm, Fourier spectral analysis and least squares minimization) have been tested and then compared (See section 2 in chapter 3). The four images algorithm has shown the best processing results and has yielded the clearest amplitude images.

As the source is modulated to 1 *Hz*, with an acquisition frequency of 200 *Hz*, the obtained film consists of 300 films of 1 *s* for each experiment. The image size is 256 *px* x 320 *px*, resulting in an enormous amount of data. Therefore, the obtained data are preliminarily processed. First, an *ROI* is chosen (approximately 120 *px* x 120 *px*) and processed. The obtained hypercubes (120 *px* x 120 *px* x 200 *px* x 300 *px*) are transformed into *2D* matrices (space-time) of ((120 *px* x 120 *px*) x (200 *px* x 300 *px*)). Then, these images are processed.

This method is applied to each pixel of each film to extract the amplitude of the modulated excitation, which increases the quality of the images. The amplitude images of each film are obtained using equation (3-34).

The obtained image (*I)* represents the image of the amplitude (image per film). The four images method increases the quality of the images, but noise is present in terms of the signal as a function of time (each pixel). The noise sources include the infrared camera and temperature fluctuations, among others. Hence, to diminish the noise in each pixel as a function of time, the singular value decomposition (*SVD*) is applied [101].

Thereafter, the amplitude images are reshaped to an image (120 *px* x 120 *px* x 300 *px*) to obtain images containing the space-time information. A projection on separate bases of space and time is carried out. The equation representing the *SVD* decomposition is given in equation (3-67).

3.2 Analytical formulation of thermotransmittance

The solution to equation (4-17) for each pixel is given as follows:

$$I\left(x,y,\lambda,T\right)=I_0\left(x,y,\lambda\right).e^{-\int_{-\frac{e}{2}}^{\frac{e}{2}}\mu\left(x,y,\lambda,T\right).dz} \tag{4-17}$$

where I_0 is the incident signal in (*DL*), I is the transmitted signal in (*DL*), μ is the absorption coefficient of the material in (m^{-1}), z is the thickness direction, λ is the wavelength in (*m*), T is temperature in (*K*), and e is the thickness of the sample in (*m*).

Equation (4-17) represents the Beer-Lambert equation that links the incident and transmitted signals. At different temperatures, the thermotransmittance represents the logarithm of the ratio of the transmittance at a given temperature and the transmittance at a reference temperature, and it is given as follows:

$$\Gamma\left(x,y,\lambda,T\right)=-log\left(\frac{I\left(x,y,\lambda,T\right)}{I_0\left(x,y,\lambda,T_0\right)}\right) \tag{4-18}$$

$\Gamma(x,y,\lambda,T)$ is the thermotransmittance of sample as a function of temperature, thus:

$$\Gamma\left(x,y,\lambda,T\right)=\int_{-\frac{e}{2}}^{\frac{e}{2}}\left(\mu\left(x,y,\lambda,T\right)-\mu\left(x,y,\lambda,T_0\right)\right)dz \tag{4-19}$$

On the other hand, the absorption coefficient (μ) can be given as a linear function of the temperature as follows:

$$\mu\left(x,y,\lambda,T\right)=\kappa.T \tag{4-20}$$

where κ is the thermotransmittance coefficient in ($m^{-1}.K^{-1}$). Thus, for monochromatic waves, equation (4-19) can be written as follows:

$$\Gamma\left(x,y,T\right)=\kappa\int_{-\frac{e}{2}}^{+\frac{e}{2}}\left(T\left(x,y,z\right)-T_0\right)dz \tag{4-21}$$

As the lumped-body assumption allows for supposing a temperature-independent space and depends only of the time, equation (4-21) can be rewritten as follows:

$$\Gamma\left(T\right)=\kappa e\left(T-T_0\right) \tag{4-22}$$

The estimation of the thermotransmittance coefficient (κ) is then possible by the inverse method. The matrix form of equation (4-21) can be given as follows:

$$\underbrace{\begin{bmatrix} \Gamma_1(T_1) \\ \vdots \\ \Gamma_n(T_0) \end{bmatrix}}_{Y} = \underbrace{\begin{bmatrix} T_1 - T_0 \\ \vdots \\ T_0 - T_0 \end{bmatrix}}_{X(T)} e[\kappa] \tag{4-23}$$

Y is the thermotransmittance vector (for each pixel) at a given temperature, and X is a matrix representing the relative temperature decrease. The thermotransmittance coefficient (κ) can be estimated using the Moore-Penrose pseudoinverse matrix of X as follows:

$$\kappa = e^{-1}\left(X^T X\right)^{-1} X^T Y(T) \tag{4-24}$$

Once the thermotransmittance coefficient is estimated, the temperature signal can be reconstructed as follows:

$$X^{est} = e^{-1} Y(T) \kappa^T \left(\kappa \kappa^T\right)^{-1} \tag{4-25}$$

The matrix (X^{est}) represents the reconstructed temperature field using the estimated thermotransmittance coefficient (κ).

3.3 Results and discussion

The technique presented in chapter 2 allows for the obtaining of *THz* transmittance images as a function of time for several samples. The transmitted imaging fields at t = 120 s for *PVC*, *PTFE*, *PMMA* and wood are presented in Figure 4-31Figure 4-31.

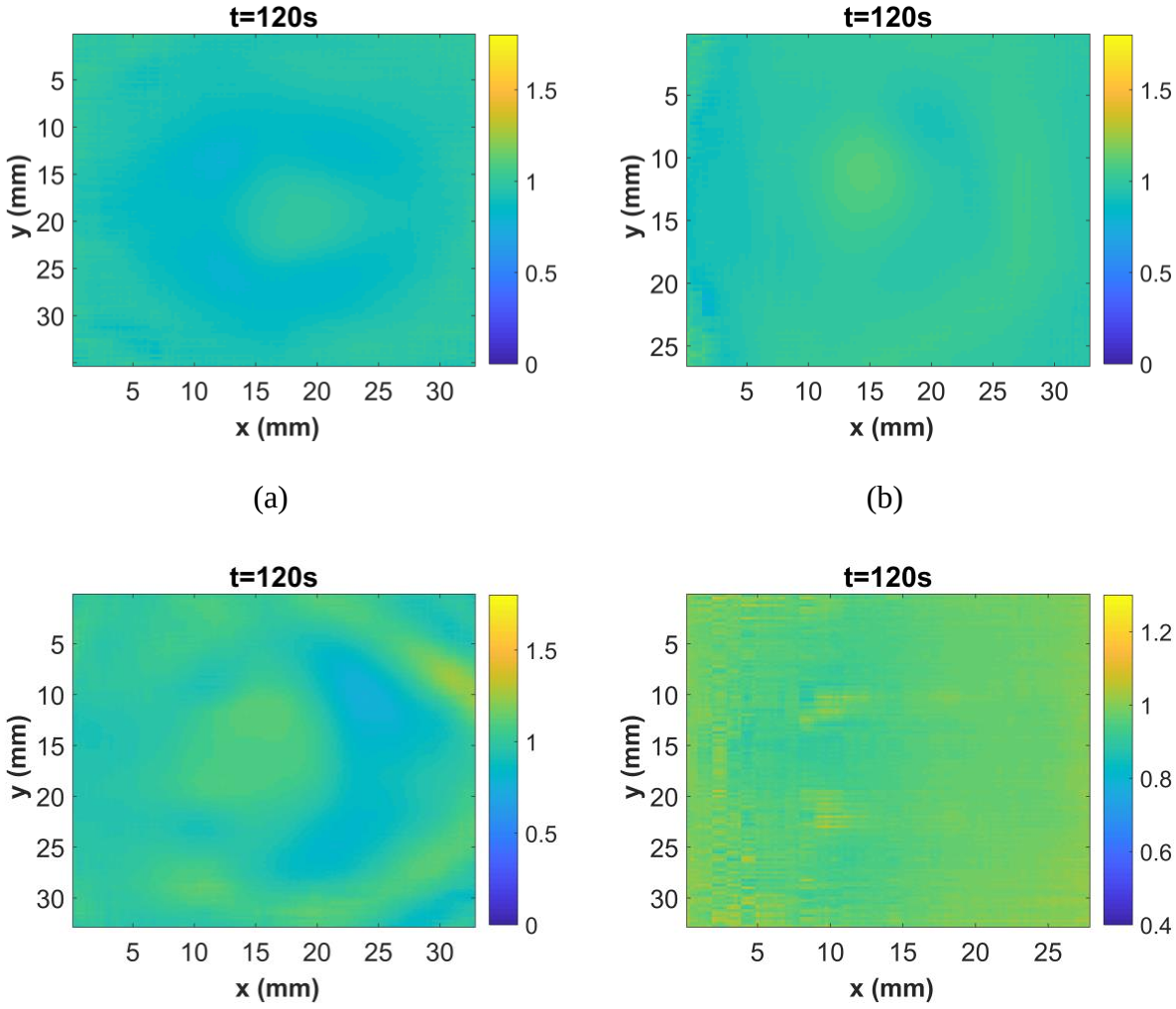

Figure 4-31: *THz* transmittance images of (a) *PVC*, (b) *PTFE*, (c) *PMMA*, and (d) wood at t=120 s.

The transmittance maps appear to vary among the materials at the same instant. The wood sample attains a high transmittance at $t = 120\ s$, indicating that the transmittance is more sensitive to temperature in wood. The transmittance appears to be heterogeneous, possibly due to optical misalignment, sample surface states, heterogeneity or the incident beam.

The temperature measurements obtained by the thermocouple and the thermotransmittance signal of the chosen pixel in homogeneous semitransparent materials (*PVC*, *PTFE* and *PMMA*) and a heterogeneous material (maritime pine wood) are presented in Figure 4-32. The pixel was chosen in a region where there was a contrast in thermotransmittance between the initial and final temperatures (a region where the signal was neither low nor saturated).

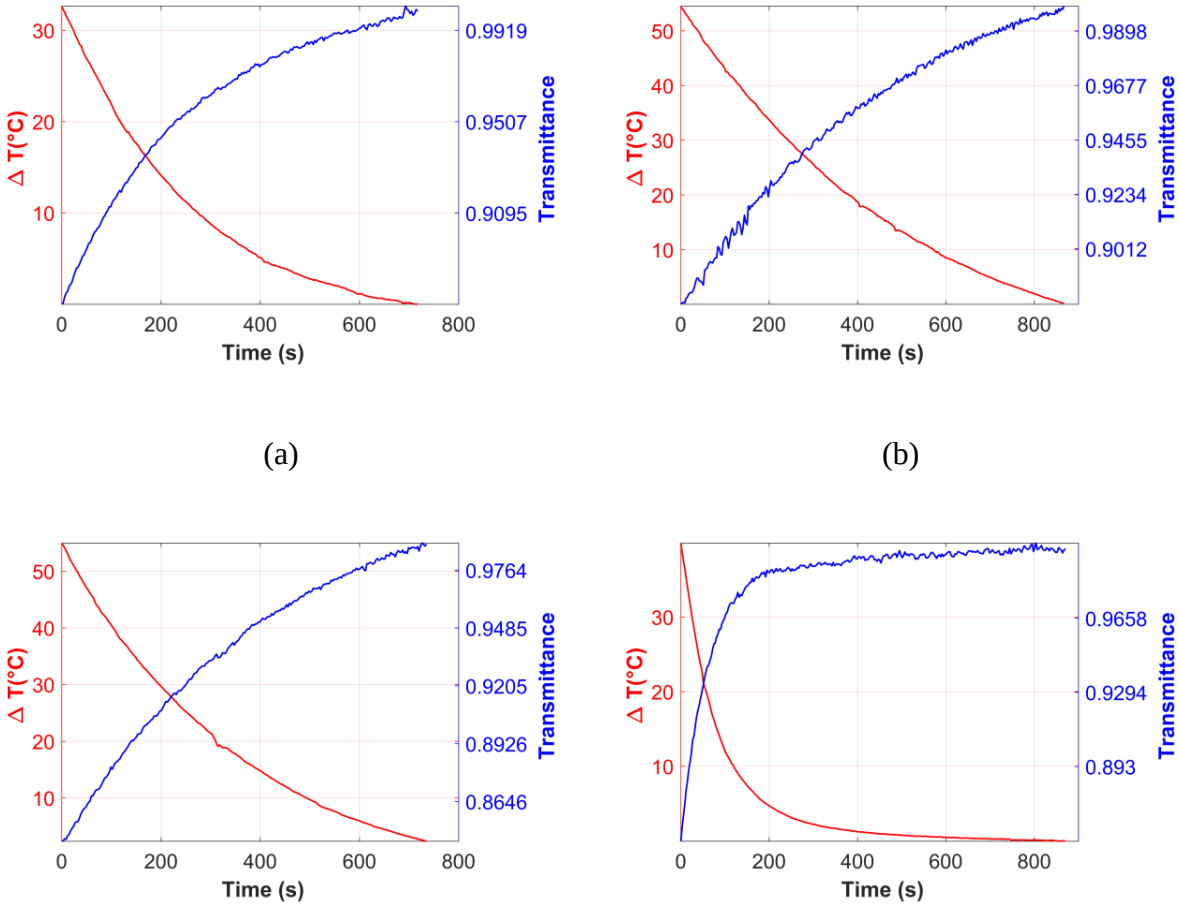

Figure 4-32: Curves of transmittance ($I(T)/I(T_0)$) and temperature measurement as a function of time for (a) *PVC*, (b) *PTFE*, (c) *PMMA* and (d) wood.

The results show that the transmittance increases with decreasing temperature and stabilizes when the sample temperature reaches the ambient temperature. The figures show that the transmittance variation to temperature is low and approximately 0.12 by 30 °*C* for *PCV*, 0.11 by 50 °*C* for *PTFE*, 0.14 by 50 °*C* for *PMMA* and 0.11 by 30 °*C* for wood. Therefore, the sensitivity of the *THz* transmittance to temperature is low and between 0.2 10^{-2} $°C^{-1}$ and 0.4 10^{-2} $°C^{-1}$, which shows the capacity of setup to detect such a small sensitivity.

Moreover, the duration of the transient case is different from sample to sample depending on the characteristic times appearing in the solution of the equation of a lumped body with ($t_c = \rho C_p e/H$). The wood sample attains steady state earlier than do the other samples due to its lowest characteristic time, as shown in Table 4-2.

The temperature measurements show behavior similar to that of the *3D* simulation shown in Figure 4-30-f. The decrease in transient temperature represents the dynamic part, which must be compared with the transient transmittance increase. The calibration curves

representing the relationship between the thermotransmittance and temperature according to equation (3-25) for the four samples are presented in Figure 4-33.

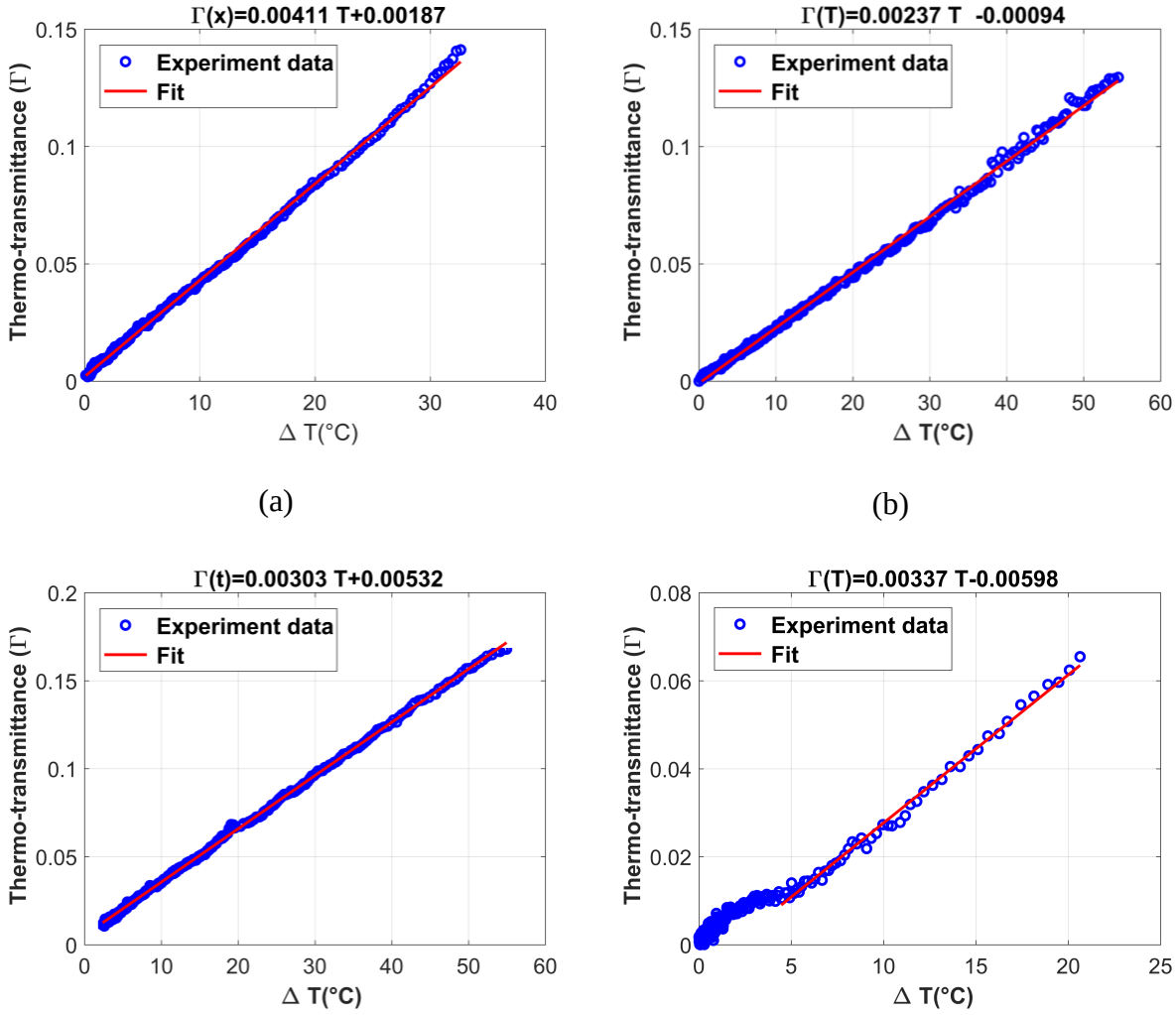

Figure 4-33: Calibration curves of thermotransmittance vs. temperature for (a) *PVC*, (b) *PTFE*, (c) *PMMA* and (d) wood. Circles: experimental values. Continuous lines: fitting model obtained using equation (3-25). Header: fitting equation for each sample.

The lumped-body hypothesis, supposing that the punctual temperature measurement taken by the thermocouple is the same over the *ROI*, is proven by calculating the Biot number and by the *3D* transient finite volume numerical simulation. This hypothesis justifies the calibration between the thermotransmittance and the punctual temperature measured in the *ROI*. Figure 4-33 shows that the behavior of the thermotransmittance is linear with respect to the temperature decrease for all materials. The linearity is more distinct for homogeneous materials such as *PVC*, *PTFE* and *PMMA* (Figure 4-33-a, Figure 4-33-b and Figure 4-33-c, respectively). For wood (Figure 4-33-d), the linearity during the transient phase is shorter due to the physical properties of wood (ρ, C_p, e and H). Moreover, the measurements seem to be noisy, probably because of the heterogeneous structure. Therefore, the thermotransmittance coefficient (κ) can be obtained by dividing the slope of the fitting equation by the

corresponding thickness of each material (equation 3-25). The obtained values are presented in Table 4-3.

	Slope (K^{-1})	Thickness (m)	Thermotransmittance coefficient, κ ($K^{-1}\ m^{-1}$)	R^2
Wood	$3.37\ 10^{-3}$	$3\ 10^{-3}$	**1.177**	0.9914
PVC	$4.11\ 10^{-3}$	$4\ 10^{-3}$	**0.805**	0.9994
PMMA	$3.20\ 10^{-3}$	$5\ 10^{-3}$	**0.64**	0.9992
PTFE	$2.37\ 10^{-3}$	$6\ 10^{-3}$	**0.395**	0.9988

Table 4-3: Thermotransmittance coefficients of the materials: *PVC*, *PTFE*, *PMMA* and wood.

The thermotransmittance coefficient values presented in Table 4-3 are comparable with other values reported for similar insulating materials. In [70], the thermotransmittance of *POM* was reported to be approximately 2 $K^{-1}m^{-1}$, which is of the same order of magnitude as the values obtained in this study. The gap between these values and the value found in [70] may be due to the nature of material (density and heat capacity) and the thickness, which makes their behavior in terms of transmittance during temperature release different.

This can be noticed in Table 4-2, where the characteristic time of a material is inversely proportional to the estimated thermotransmittance coefficient. The factor t_c represents the denominator of the exponential term in the heat-equation solution of the lumped body. The decrease in this factor leads to a drastic decrease in the temperature (short transient case), which can be shown in Figure 4-32-d, and thereby, increases the thermotransmittance coefficient.

In this study, the temperature is considered constant along the thickness, whereas the temperature has a parabolic profile. Moreover, the temperature field of the *ROI* is supposed as homogeneous (Figure 4-30-c, Figure 4-30-d and Figure 4-30-e) and independent of space, which allows for calibration between the temperature of one pixel measured by the thermocouple and the thermotransmittance of all pixels. Nevertheless, a numerical check of the temperature difference between the center and end of the *ROI* shows that it is low and approximately 2 °*C*. On the other hand, the difference between the temperature on the surface and the z-weighted temperature is shown to be low (Figure 4-30-f), which allows for validating this hypothesis and the calibration with transmittance.

At this stage, once the thermotransmittance coefficient is estimated, the reconstruction of the temperature signal according to equation (3-25) is possible. The obtained results are shown in Figure 4-34.

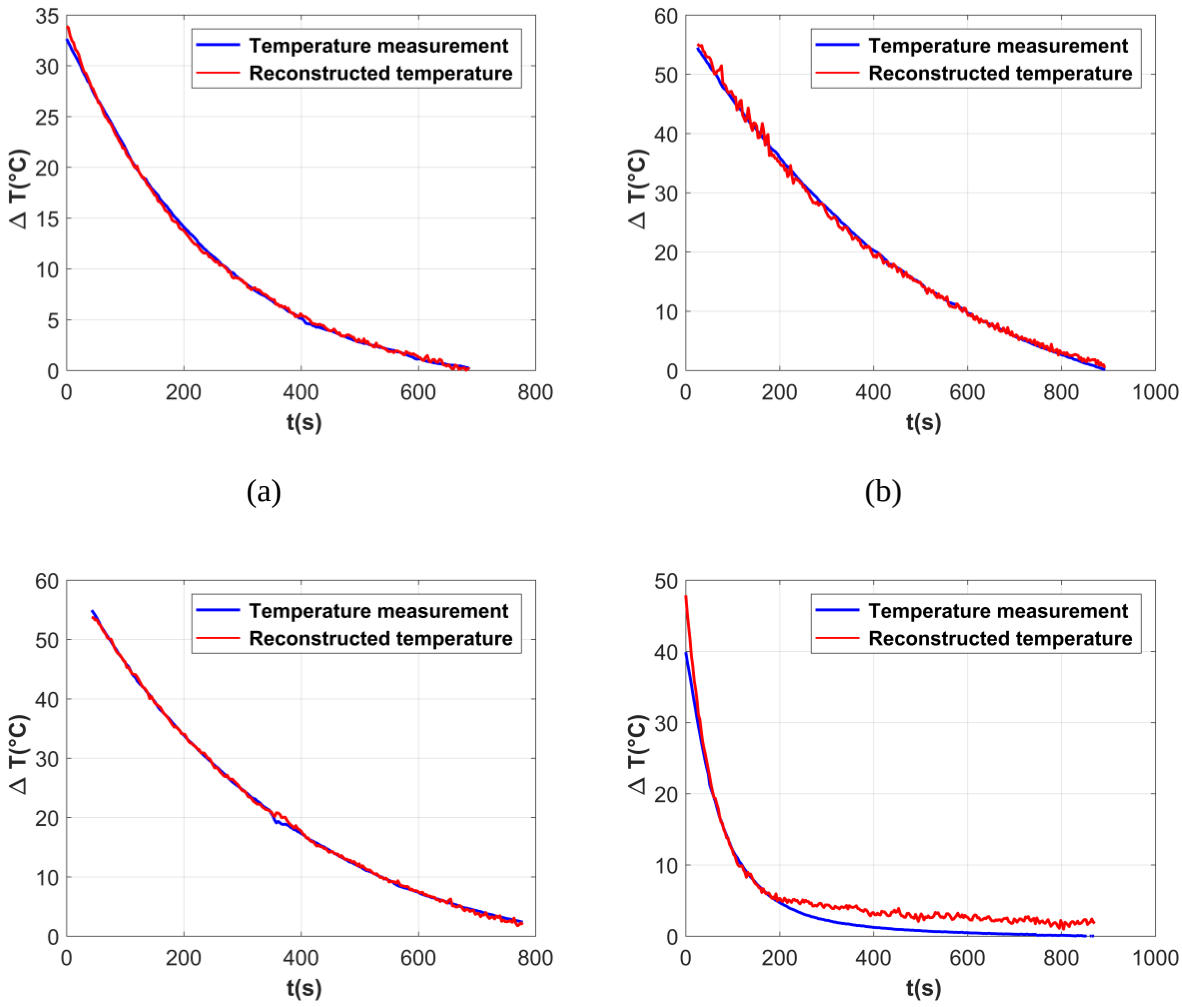

Figure 4-34: Contactless temperature measurement by the *THz* method of (a) *PVC*, (b) *PTFE*, (c) *PMMA* and (d) wood. Blue line: reconstructed temperature; red line: temperature measurement.

The relative error of the transient temperature estimation is approximately 0.5 % for the homogeneous materials and approximately 1 to 3 % for the heterogeneous material (wood). This result shows that the *THz* imaging technique is efficient for the contactless measurement of the transient temperature of semitransparent materials. A gap in the estimation is observed in the steady-state regime for wood, which is justified, as the estimation was carried out only on the dynamic part (the steady-state part represents the region of noise).

The temperature images of *PVC* and wood, as examples of homogeneous and heterogeneous semitransparent materials, respectively, can be mapped using the estimated thermotransmittance coefficient of each pixel. This calibration is validated numerically in section 4 in chapter 3, which allows for the temperature field to be considered uniform. The estimated temperature field is shown in Figure 4-35.

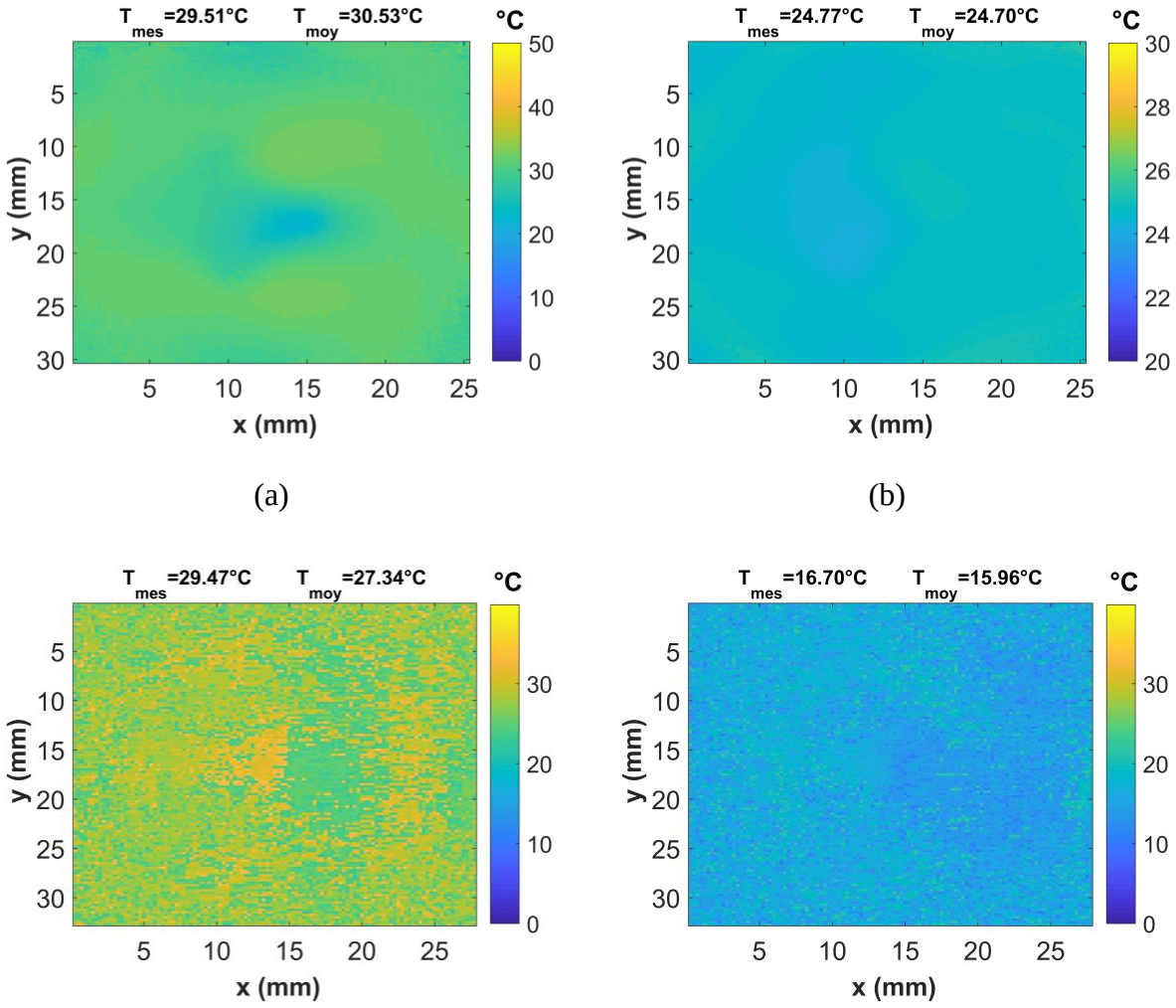

Figure 4-35: Temperature field of (a) *PVC* at t = 30 s, (b) *PVC* at t = 75 s, (c) wood at t = 30 s and (d) wood at t =75 s. T_{mes} is the temperature measurement given by the thermocouple, and T_{moy} is the mean of the temperature field.

Figure 4-35-a and Figure 4-35-b represent the estimated temperature field for *PVC* at $t = 30\ s$ and $t = 75\ s$, respectively. It can be observed that the field is not as homogeneous in the early transient case ($t = 30\ s$) as it is at $t = 75\ s$. The estimated temperature at the center is approximately 4 °*C* lower than the mean temperature (the region where the beam is dense in Figure 4-35-a). This can be explained by saturation of the beam and optical misalignment. The distribution of estimation residual is situated between -1 % and 10 %, with a mean of 5 %. At $t = 75\ s$, the temperature is quite homogeneous (approximately 24 °*C*). The estimation error is situated between -1 % and 1 %, with a mean of 0.2 %. This indicates that the estimation is better at $t = 75\ s$ and confirms that for the early transient case, the displacement of the sample perturbs the temperature field at $t = 30\ s$. On the other hand, the relative error between the mean of the temperature field and the measured temperature is approximately 3.5 % at $t = 30\ s$, whereas it is less than 1 % at $t = 75\ s$.

Figure 4-35-c and Figure 4-35-d represent the estimated temperature field for wood at $t = 30\ s$ and $t = 75\ s$, respectively. The images are noised, and the optical effects are clear, which are likely due to beam diffraction within the wood through alternating rings. At $t = 30\ s$, the estimation of the temperature field is affected by the heterogeneous structure (the residual of the estimation is between -15 % and 5 %, with a mean of -3 %). However, at $t = 75\ s$, the estimation appears to be better. with an estimation error between -15 % and 5 % and a mean of -3 %. These values are shown in Figure 4-34-d.

The estimation at $t = 75\ s$ shows to be more efficient than at $t = 30\ s$, which can be seen in Figure 4-34-a for *PVC* and Figure 4-34-d for wood. Moreover, the inhomogeneity of the *THz* beam and optical misalignment (beam refraction) lead to a map of thermotransmittance coefficients, where its distribution is based on the sole value determined by the calibration.

These results prove that a *THz* imaging system employing the appropriate optics and image processing methods allows for the contactless estimation of a semitransparent material's temperature.

3.4 Conclusion on *THz* transient measurement on temperature

The aim of this study was to demonstrate the capability of using transmission *THz* imaging as a contactless tool for measuring the transient temperature of semitransparent materials. For the reported set of materials, a strong correlation between the temperature and *THz* transmittance was observed.

The measurements were performed by a lock-in technique (chapter 2) in conjunction with the four images algorithm (chapter 3) to obtain images of the transmitted amplitude. The *SVD* method was applied to the amplitude images to clear the noise and to enhance the image quality. Moreover, a *3D* simulation of the transient release of temperature for a thin insulating sample allowed for the validation of the lumped-body hypothesis, which simplified the Beer-Lambert law-based model. Then, a linear model linking the thermotransmittance to the transient release of temperature was established. The thermotransmittance coefficients of the *PVC*, *PFTE*, *PMMA* and wood materials were estimated. This study shows that the *THz* technique is able to estimate the thermotransmittance coefficient at transient temperatures.

Finally, the temperature fields of *PVC* and wood at two instants in the transient case were mapped. The efficiency with which the temperature of semitransparent materials can be estimated was demonstrated. Therefore, the *THz* technique coupled with the appropriate image processing methods appears to be a promising imaging technique for the contactless measurement of transient temperatures. Such a result paves the way to more sophisticated *THz* applications, such as *THz* tomography [71, 72 and 107], aiming to create *3D* reconstructions of transient temperature fields, which is the goal of ongoing studies.

4 Conclusion

In this chapter, we first showed results about the capability of *THz* waves in heat and mass transfer applications. This wave range seems to be efficient mainly with materials opaque in the visible and infrared domains. The *THz* radiation was shown to be transmitted by most of the insulating materials, reflected by metals and absorbed by water. This wavelength range shows a different sensitivity scales for the temperature and water content. This property allows for the contactless measurement of the temperature of semitransparent materials and the water content within hygroscopic materials.

The first part focused on the efficiency of the *THz* as a tool for the contactless monitoring of water content. It is worth noting that since the wavelength is millimeteric, the submillimeteric details cannot be revealed, which prevents the distinguishing of growth rings within wood. However, the setup based on a monodetector showed a capability for the contactless estimation of water content within a material conditioned at a given hydric state. A model explaining the relationship between the absorbance and water content was built. This model also allows for estimating the absorption coefficient and dry density of samples.

Moreover, the *THz* showed a capability to monitor the transient mass transfer and to estimate the diffusion coefficient of materials. Indeed, the model previously shown allows for the contactless estimation of water content images, and thereby, the diffusion coefficient of a material. The diffusion coefficients of blotting paper and softwood were estimated using the *TTC*-based setup. The Levenberg-Marquardt minimization between the experimental and numerical fields obtained using the finite difference scheme with the same boundary conditions allows for the estimation of the hydric diffusion coefficient with an error of 3 %.

In addition, the first contactless measurements of the transient temperature of semitransparent materials using the *TTC* were performed. The sensitivity of the *THz* to a transient temperature gradient allows for estimating the thermotransmittance coefficient, which has an order of magnitude of 10^{-3} $m^{-1}.K^{-1}/°C$. This means that our measurement system is capable of detecting 1 $°C$ of sample transient temperature variation, corresponding to 0.1 % of the signal variation, which proves its efficiency in such application. Therefore, using the estimated thermotransmittance coefficient, the transient temperature field can be mapped.

CONCLUSIONS & PERSPECTIVES

This work, motivated by the industrial ***problematic of drying*** and in which the objective was to study heat and mass transfers during drying, allowed us to address the capability of using ***THz radiation as a contactless, cheap and safe tool for the measurement of water content and temperature within insulating materials at the local scale***.

One of the main points of this study was ***to develop a tool capable of realizing THz imaging in transmission mode based on a THz-to-IR camera imaging system***. The aim was to focus on the development of a versatile experimental tool for characterizing heat and mass transfer. This tool consists of combining an IR camera and a terahertz-to-thermal converter to transform a simple IR camera to a broadband *GHz* to *THz* one. A lock-in technique was developed by the synchronization of the incident *THz* beam and the acquisition of the camera to avoid external artifacts and deviations. However, the acquisition frequency is currently limited by the power density of the *THz* Gunn diode.

In addition, the scanner with which the *THz* camera is associated provides an extreme flexibility (in terms of geometry) and corresponds to a high speed of movement. Due to the possibilities offered by the system, one of the major stakes of the rest of this work lies in the development of robust acquisition and characterization methods.

From the point of view acquisition, one of the most important points of this work is that the modelization of the convertor *TTC* showed a high sensitivity, even at a low conversion rate (0.2). However, the drawback of this sensor is linked to the thermal diffusion that blurred the images. To overcome this effect, a lock-in technique at an appropriate frequency to limit the diffusion is proposed. In addition, since the conversion rate is nonlinear with the Gunn diode power, a better measurement quality can be obtained by using a *THz* source of higher power.

From the point of view processing, a study of several processing methods aiming to extract the measured amplitude revealed that the four images algorithm is the best method in term of accuracy, calculation time and robustness. Moreover, preprocessing consists of subtracting the linear-fitted baseline for each period and allows for improving the amplitude calculation in real time and for overcoming the diffusion problem of the transient response of the *TTC*. An additional filter such as the *SVD* method can be applied to denoise the amplitude images.

Thereafter, the first results showed that the ***THz sensitivity to temperature is 100 times less that the sensitivity to water content***. A model linking the *THz* absorbance and global water content of a sample, allowing for the estimation of the water content distribution, is developed. On the other hand, this model allows for estimating the absorption coefficient and the density of samples by knowing its water content. However, the main drawback of the far-field configuration is that the millimeteric or the submillimeteric details cannot be revealed.

Moreover, a ***fluidic excitation device*** allowing for the exciting of samples by vapor is designed. This device also-called a ‘fluidic laser” represents the equivalent of a laser in mass transfer, where its power is a function of the concentration and speed of the flux stream. The

excitation can also take different forms such as continuous excitation, Dirac excitation, or periodic excitation.

The *TTC* coupled with the fluidic laser allowed for the monitoring of the diffusion of vapor within a sample. An inverse method based on the Levenberg-Marquardt minimization between experimental and numerical fields allowed for the estimation of the hydric diffusion coefficient with an error of 3 % for blotting paper.

On the other hand, the *THz* experiments conducted on samples presenting heat transfer allowed for estimating the optical properties of semitransparent materials. The estimation of the thermotransmittance coefficient has an order of magnitude of 10^{-3} $m^{-1}.K^{-1}/°C$. This means that our measurement system is capable of detecting 1 $°C$ of sample transient temperature variation corresponding to 0.1 % of the signal variation, which proves the technique's efficiency in such an application. Therefore, using the estimated thermotransmittance coefficient, the transient temperature field can be mapped.

The perspectives are numerous, from which we can underline that *THz* scanners represent an optimal tool for the in-line monitoring of wood drying or nondestructive testing, and thereby, deploying *THz* systems in industry is interesting. Since the power of the source is low, the system would be limited to thin samples, as the crossed depth for a dry sample was 25 *mm*; for wet samples, the crossed depth is thinner (paper or packaging industry). The *THz* technique seems to be adaptable for measurements on dry and less-dense products, which pave the way to applications in the food industry (biscuit, malt, etc.), which does not often have reliable online measurements.

From the point of view research, the first perspective is to transpose the developed analytical estimation methods for heat transfer to mass transfer through exciting samples by vapor in different forms. ***The second perspective*** boils down to the developed *TTC* based-setup being a promising imaging technique for thicker materials, which paves the way to more sophisticated *THz* applications, such as *THz* tomography, aiming to create *3D* reconstructions of transient temperature fields

APPENDICES

1 Appendix I

The compared models are summarized in the Table I-1.

Model	Expression	Parameters
Guggenheim Anderson Boer (GAB)	$W = \frac{A.B.C.RH}{(1-B.RH)(1-B.RH+B.C.RH)}$	$C = C_0 \exp\left(\frac{H_1 - H_m}{RT}\right)$ $B = K_0 \exp\left(\frac{H_1 - H_q}{RT}\right)$ A
Harkings	$RH = \exp\left(k - \frac{n}{W^2}\right)$	k, n
Smith	$RH = 1 - \exp\left(\frac{k-W}{n}\right)$	k, n
Henderson	$RH = 1 - \exp\left(-A(T+B).W^C\right)$	A, B, C

Table I-1: Sorption curve models used in the literature.

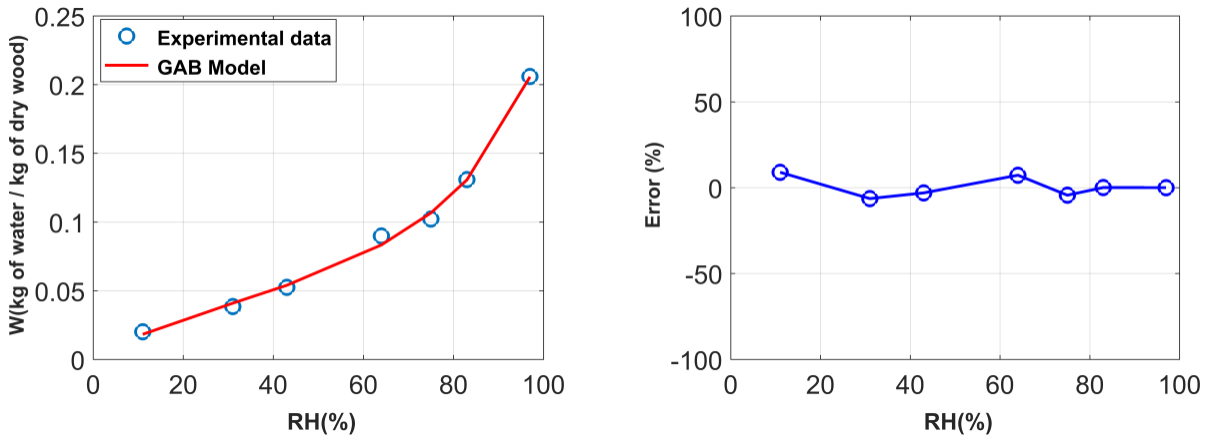

(a) (b)

Figure I-1: (a) Experimental data fitted with the GAB model, A = 0.047, B = 0.8064 and C = 5.6821. (b) The fit precision obtained with the GAB model.

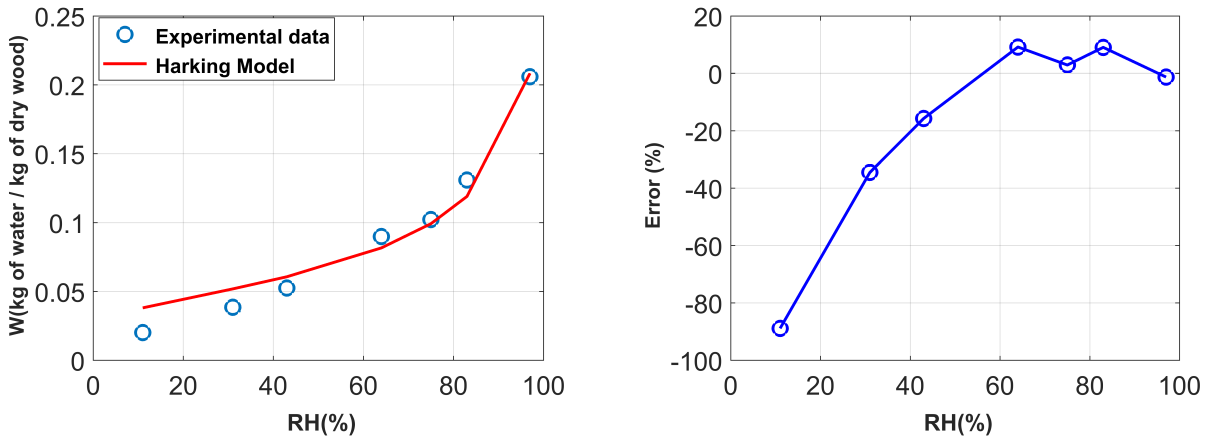

(a) (b)

Figure I-2: (a) Experimental data Fitted with the Harking model, n = 0.0033 and k = 0.0449. (b) The fit precision obtained with the Harking model.

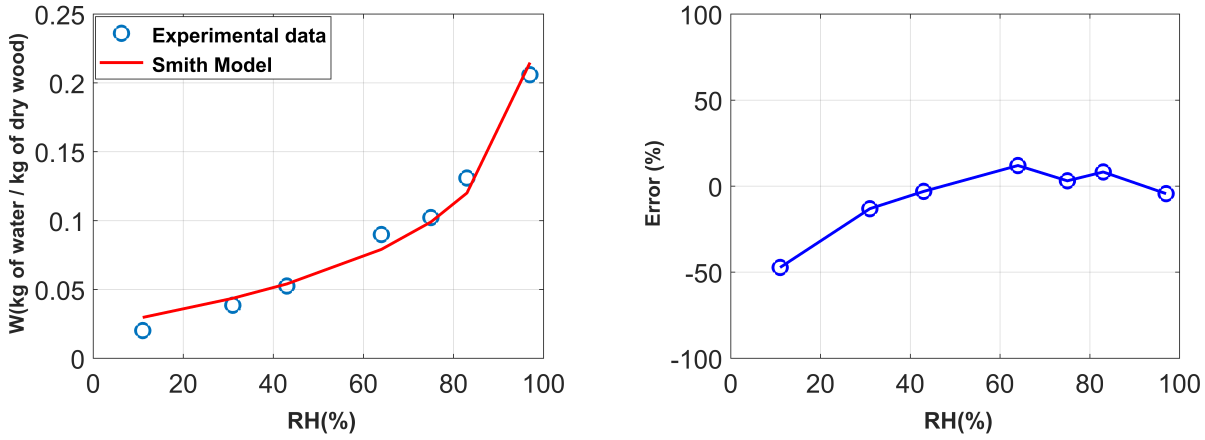

(a) (b)

Figure I-3: (a) Experimental data fitted with the Smith model, n = 0.0546 and k = 0.0234. (b) The fit precision with Smith model.

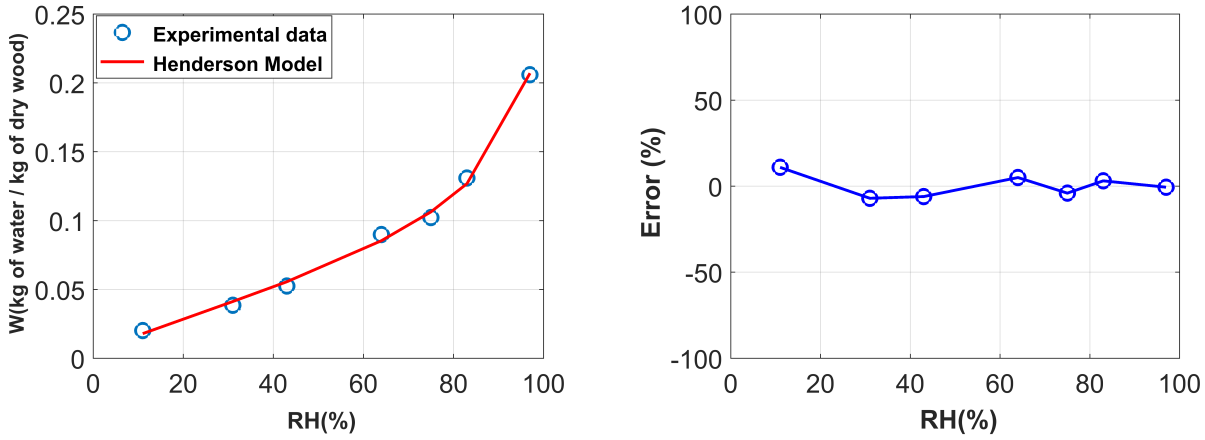

(a) (b)

Figure I-4: (a) Fitted experimental data with Henderson model, A = 0.1034, B = 0.9981 and C = 1.3928. (b) The fit precision obtained with the Henderson model.

2 Appendix II

Signal Channel	
Current Input	10^6 to 10^8 *V/A*
Gain Accuracy	±1 % from 20 °*C* to 30 °*C* (notch filters off)
Input Noise	6 $nV/\sqrt{Hz}$ at 1 *kHz* (typical)
Full-scale Sensitivity	2 *nV* to 1 *V* in 1-2-5-10 sequence ‘expand off’
Reference Channel	
Phase Resolution	0.01°
Phase Drift	< 0.01° / °*C* below 10 *kHz* < 0.1° / °*C* to 100 *kHz*
Frequency Range	1 *mHz* to 102 *kHz*
Acquisition Time	2 cycles + 5 *ms* or 40 *ms*, whichever is greater
Demodulator	
Demodulator Time Constant	10 μs to 30 *s* (reference > 200 *Hz*)
Internal Oscillator	
Frequency Range	1 *mHz* to 102 *kHz*
Frequency Accuracy	25 *ppm* +30 μHz
Amplitude Accuracy	1 %

Table II-1: SR830 DSP and lock-in amplifier specifications.

PTFE lenses THORLABS	Characteristics
Design Frequency	500 *GHz*
Surface Irregularity for Ø50 mm Lenses	10 μm, corresponding to $\lambda/20$ at 1.5 *THz*
Diameter Tolerance	+0.0/-0.2 *mm*
Center Thickenss Tolerance	±0.20 *mm*

Spherical Surface Power	0.0025 λ
Clear Aperture	> 85 % of diameter

Table II-2: Characteristics of *PTFE* lenses (THORLABS).

Zaber T-LST0500B rail	
Travel range	500 *mm*
Accuracy	126 μm
Speed range	0.0047 *mm/s* – 100 *mm/s*
T operating range	0 °*C*– 40 °*C*
weight	4.7 *kg*
Repeatability	< 2 μm

Table II-3: Characteristics of the motorized sample holder.

Camera model	SC7000 InSb
Cooling type	Integral Stirling cooler
Integration time	3 μs to 2 *s* (programmable), 1 μs Step
Overall dimension (mm)	253 x 130 x 168 (w/o lens)
Weight (W/O lens)	4.950 *kg*
Operational temperature range	-20 °*C* to +55 °*C*
Detector material	Indium Antimonide (InSb)
Number of pixels	320 X 256
Spectral response	3.5 μm – 5.15 μm
Frame rate	Up to 250 *Hz* Full Frame
Image capture	Snapshot
Pitch	25 μm x 25 μm
NETD	< 25 *mK* at 25 °*C*

Aperture	F/2

Table II-4: Infrared SC7000 camera characteristics.

Contactless *RH* sensor Tinytag plus 2 TGP-4500	
Sensor type	10 K NTC Thermistor for *T* / Capacitive for *RH*
Reading capacity and logging interval	32000 readings (actual, *min*, *max* from 1 *s* to 10 *d*)
RH operating range	0 % – 100 %
T operating range	-25 °*C*– 85 °*C*
RH response time	25 mins to 90 % *FSD* in moving air 40 *s* to 90 *FSD*
Reading resolution accuracy	0.01 °*C*/ ±3 % *RH* at 25 °*C*

Table II-5: Characteristics of the *RH* sensor used within conditioning containers (Tinytag plus 2).

RH sensor Sensirion SHT3x (*RH*/T)	
Size	2.5 x 2.5 x 0.9 (*mm*)
Supply voltage range	2.4 – 5.5
RH operating range	0 % – 100 %
T operating range	-40 °*C*– 125 °*C*
RH response time	8 *s* (tau 63 %)
Energy consumption	4.8 μW at 2.4 *V*

Table II-6: Characteristics of sensor used for *RH*.

EHEIM air pump 100	Characteristics
Frequency	50 *Hz*
Pump power per hour at 50 Hz	100 *l*
Pumping head at 50 Hz	2 *m*

Power at 50 Hz	3.5 *Watts*
Dimension	152 *mm* x 89 *mm* x 71 *mm*
Hose pressure side	4 *mm*

Table II-7: Air pump used for the hydric excitation device.

3 Appendix III

3.1 Monodetector improvement

As mentioned in section 1 of chapter 2, the infrared pyrometer scans in a raster pattern, which means that scanning must be carried out pixel by pixel. This behavior means the scanning takes a time long. As is known, the notions of response time, integration time and intermeasurement time are important in electronic and optical devices. In our case, the response time is defined by the time necessary for heating up the pyrometer (needed time to reach a stabilized value) and is on the order of milliseconds. The integration time is the time during which the signal is held, as it maximizes and stabilizes, so it can be measured. The output (measured by detector) value can be the value reached after verifying a fixed criterion of the minimum between two successive values (stabilization) or the average of a given number of last-stabilized measurement points. In other words, the integration time is the "time window" during which a given pulse is measured.

The intermeasurement time represents the movement time of the scanned sample between two measurements. The conducted experiments in this part consist of fixing the detector and source and moving the sample in a raster pattern. As the intermeasurement time representing the displacement time of sample is constant, the main improvement will be found with the response time. The early detection of a stable signal (the signal during integration time) allows for economizing the response time and integration time. Figure III-1 presents a simulated example of a detected signal with the previously described times.

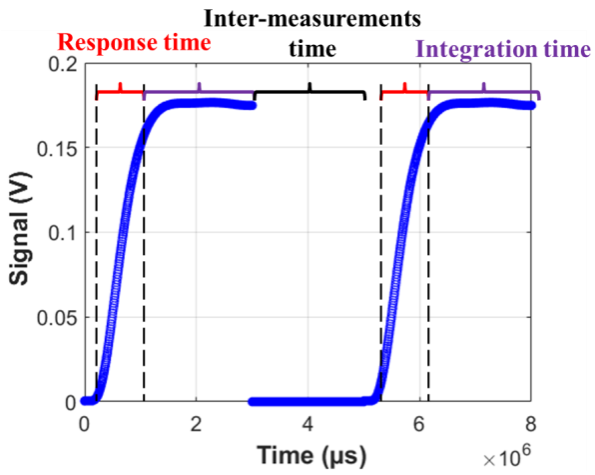

Figure III-1: Signal detecting with different characteristic times.

The idea aims to estimate the stabilized value at an early transient time (mostly at 10 % of the response time). For that, a modeling of the detector response time consists of finding the best fit response of an excitation of the detector and then estimating the parameters that represent the characteristic constant response of the device. This work has been performed in [80] to model the transient voltage of the Peltier element. An exponential model allowed for estimating a calibration coefficient in a short time.

To estimate the coefficient of the monodetector response used in this study, a hyperbolic model has been proposed, and then, a short-time approximation has been considered. Thereafter, the estimated coefficient allows for the measurement of a value stabilized at 10 % (linear part in the approximation) of the response time of the detector. The model is given as follows:

$$f = A\,\mathrm{t}\,ahn\left(\frac{t}{\tau}\right) \qquad \text{(III-1)}$$

Where: A represents the maximum value of the measurements (output value), and τ is the characteristic time. At short times, equation (III-1) can be written as follows:

$$f = log\left(\frac{A}{\tau}\right) + log\left(t\right) \qquad \text{(III-2)}$$

The minimization of the objective function (g) that represents the difference between the theoretical model and the experimental data, in the sense of the Marquart-Levenberg algorithm (see chapter III), allows for the estimation of the parameters A and τ. Five hundred measurement points of the infrared pyrometer response can be obtained without a sample using the LabVIEW program to fix a measurement step of 35 µs. Figure III-2 shows the experimental data with the curve fitted with the estimated parameters.

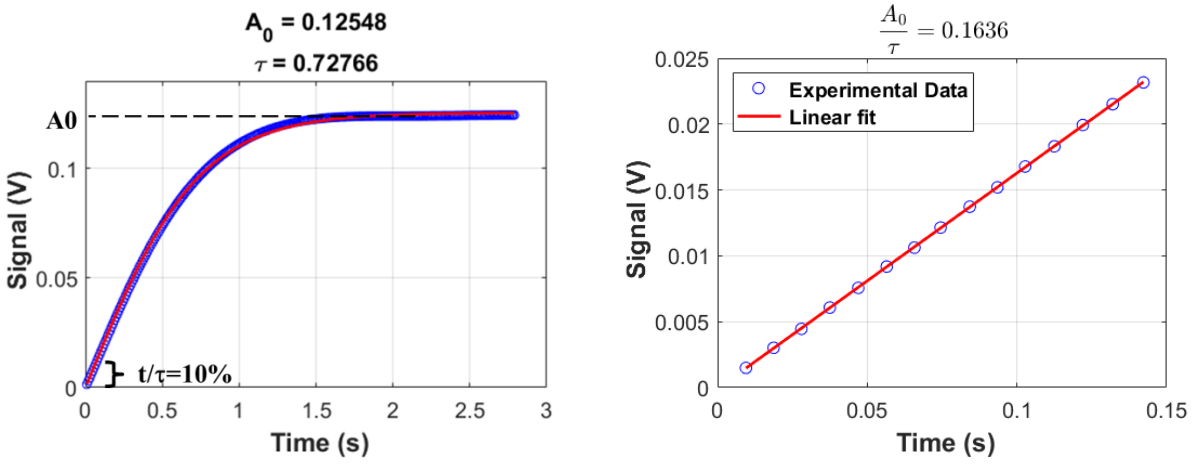

(a) (b)

Figure III-2: (a) Monodetector response of the infrared pyrometer. (b) The linear behavior at the early stage of the response time ($t/\tau = 10$ %). Circle: experimental data; continuous line: model fitted using equations (III-1) and (III-2). Header: the estimated coefficients.

The values found for the full fitting of the curve are $A_0 = 0.126\ V$ and $\tau = 0.7276$ s, thus, the ratio $A_0/\tau = 0.17\ V.s^{-1}$. On the other hand, the linear approximation at the early stage of the response time ($t/\tau = 0.1$) is capable of detecting the same value. Therefore, if $(t/\tau < 0.1)$, the approximation is linear, and A can be determined by knowing the time response coefficient (τ). We can then write:

$$A_{est} = \tau \frac{f_{10\%}}{t_{10\%}} \quad \text{(III-3)}$$

Equation (III-3) allows for detecting the maximum value of the signal that will be displayed by the monodetector (output value). This means that the determination of the signal value will be found 90 % earlier than the response time. Thus, if the response time is approximately 1 s and the scanned area is 20 *px* x 20 *px*, the scanning will be performed 360 *s* earlier.

3.2 Spatial resolution

Although in this work, the spatial resolution of the monodetector *THz* imaging has not been studied, a tentative extraction of the beam form by deconvolving the obtained signal with a spatial-scanned form is performed. Theoretically, each detector has its own function transfer or intensity distribution (f). If the object has a form represented by function h, the obtained transmitted signal can be expressed by g and is given as follows:

$$f \otimes h = g \quad \text{(III-4)}$$

Taking the function h as a Heaviside function, the obtained signal is shown in Figure III-3-a.

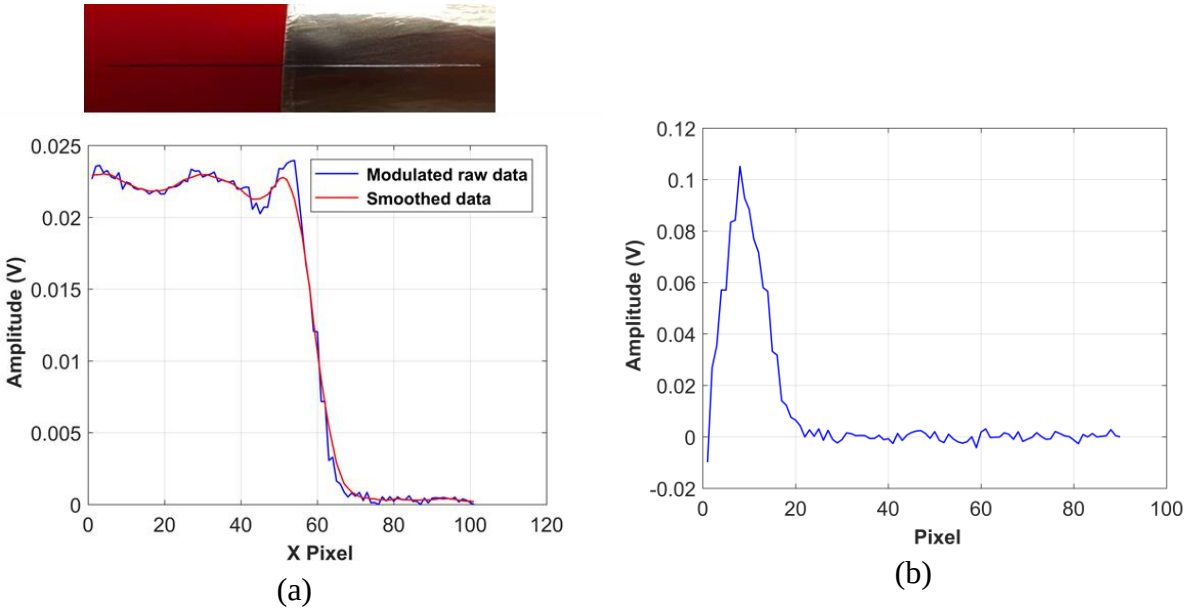

(a) (b)

Figure III-3: (a) Blotting paper half taped with aluminum tape with the transmitted modulated and smoothed signal of the *1D* scanning (line in (a)) using the monodetector (b) The obtained function representing the response as a function of the detector.

Figure III-3-a represents a line scanning of blotting paper half taped with aluminum, which turns the transmitted signal off. Since the deconvolution operator uses matrix Moore-Penrose inversion operator, an additional moving average filter is necessary to smooth the obtained noised signal. The noise in this inverse method can highly amplify the estimation of *f*. Therefore, moving smooth function, for example, consisting of averaging each 10 values,

allows for the obtaining of the red curve represented by *g'*, as shown in Figure III-3-a. Thereafter, the deconvolution between the noised signal (*g'*) and the theoretical signal (*h*), according to equation (III-5), allows for the obtaining of the intensity distribution of the *THz* beam, as shown in Figure III-3-b.

$$\left(g' \otimes h\right)^{-1} = f' \tag{III-5}$$

However, the smoothed experimental signal (*g'*) is often affected by environmental noise and system bias, and the estimation of the transfer function can also be affected. Therefore, a signal processing (image processing in the *2D* case) is recalled aiming to minimize the effect of noise in order to obtain a better transfer function of the detector. This result is extremely important, especially for the *2D* detector, and allows for obtaining the response by convolving the transfer function and the theoretical shape of the scanned object.

REFERENCES

[1] G. Scalari, C. Walther, J. Faist, H. Beere and D. Ritchie. “Electrically swithable two-color quantum cascade laser emitting at 1.39 and 2.3 *THz*”. Appl. Phys. Lett. **88**, 141102. (2006).

[2] F. Blanchard, L. Razzari, H. C. Bandulet, G. Sharma, R. Morandotti, J. C. Kieffer, T. Ozaki, M. Reid, H. F. Tiedje, H. K. Haugen and F. A. Hegmann. “Generation of 1.5 uJ single-cycle terahertz pulses by optical rectification from a large aperture ZnTe crystal”. Opt. Express **15**, 13212-13220. (2007).

[3] H. Ito, F. Nakajima, T. Furuta, and T. Ishibashi. “Continuous *THz*-wave generation using antenna-integrated uni-travelling-carrier photodiodes”. Semicond. Sci. Technol. **20**, S191-S198. (2005).

[4] M. K. Chen. “Terahertz generaion and its applications”. *Ph.D* thesis, Pennsylvania State University. (2010).

[5] L. Gaverina. “Caractérisation thermique de milieux hétérogènes par excitation laser mobile et thermographie infrarouge”. *Ph.D* thesis, University of Bordeaux. (2017).

[6] J. Gril. ‘‘Modelling mechano-sorption in wood through hygro-locks and other approaches’’. International Symposium on Wood Science and Technology. (IAWPS), Tokyo, 15-17.03.15, Isogai A, Iwata. (2015).

[7] B. Clouet. “Comportement hydromécanique d’assemblages bois collés à l’état vert - approches expérimentale et numérique”. *Ph.D* thesis, University of Bordeaux. (2014).

[8] C. Gauvin, D. Jullien, P. Doumalin, J. C. Dupre, J. Gril. ‘‘Image correlation to evaluate the influence of hygrothermal loading on wood’’. Strain 50(5):428-435. DOI:10.1111/str. 12090. (2014).

[9] B. Clouet, R. Pommier and M. Danis. “New composite timbers, full field analysis of adhesive behavior”. Part of the series Conference Proceedings of the Society for Experimental Mechanics Series pp 51-58. (2013).

[10] E. Serrano, J. Oscarsson, B. Enquist, M. Sterley, H. Petersoon and B. Källsner. “Green-glued laminated beams-high performance and added value”. World conference on timber engineering. Riva des Garda, Italy, p. 829-830. (2010).

[11] S. Ormarsson, O. Dahlblom and H. Petersson. “A numerical study of the shape stability of sawn timber subjected to moisture variation-Part 3: influence of annual ring orientation”. Wood Science and Technology 34-207-219© Springer-Verlag. (2000).

[12] T. A. N’Guyen, N. Angellier, S. Caré, L. Ulmet, and F. Dubois. "Approaches to the moisture content monitoring in timber elements: Development of a resistive method". Advanced Materials Research Vol. 778, pp 335-341. Doi: 10.4028/ Trans Tech Publications, Switzerland. (2013).

[13] W. Zillig. “Moisture transport in wood using a multiscale approach”. *Ph.D* thesis, Catholic University of Louvain. (2009).

[14] Y. Jannot. “Isothermes de sorption: modèles et détermination, transferts thermiques, métrologie et séchage”. http://www.thermique55.com/principal/sorption.pdf. (2008).

[15] A. C. Kouchade. “Mass diffusivity of wood determined by inverse method from electrical resistance measurement in unsteady state”. *Ph.D* thesis, Ecole Nationale du Génie Rural, des Eaux et des Forets. (2004).

[16] D. C. Mannes. “Non-destructive testing of wood by means of neutron imaging in comparison with similar methods”. *Ph.D* thesis, Albert-Ludwigs-Universität Freiburg i. Br. (2009).

[17] J. Crank. “The Mathematics of diffusion”. Second edition. Brunel University Uxbridge. Clarendon press. Oxford. (1975).

[18] D. Maillet, S. André, J. C. Batsale, A. Degiovanni, and C. Moyne. “Thermal quadrupoles, solving the heat equation trough integral transforms”. John Wiley & Sons, Ltd. (2000).

[19] V. C. Tidwell, L. C. Meigs, C. F. Tracy and B. Craig. “Effects of spatially heterogeneous porosity on matrix-diffusion as investigated by X ray absorption imaging”. Journal of Contaminant Hydrology. Doi: 10.1016/S0169-7722(99)00087-X. (2000).

[20] S. Roels and J. Carmeliet. “Analysis of moisture flow in porous materials using microfocus X-ray radiography”. International Journal of Heat and Mass Transfer 49 4762–4772. (2006).

[21] X. He and D. Qi. “Density and moisture content forecasting based on X-ray computed tomography”. Eur. J. Wood Prod. Doi 10.1007/S00107-013-0722-3. (2013).

[22] D. Derome, S. Roels and J. Carmeliet. “Qualitative work to study water movement in wood”. Source: Div. of Building Technology, Department of Civil and Architectural Engineering, Royal Institute of Technology, Brinellvägen 34, SE-100 44, Stockholm, Sweden.

[23] K. Sandberg. “Modelling water sorption gradients in spruce wood using CT scanned data”. New Zealand Journal of Forestry Science 36(2/3): 347–364. (2006).

[24] S. V. Dvinskikh, M. Henriksson, A. L. Mendicino, S. Fortino and T. Toratti. “NMR imaging study and multi-Fickian numerical simulation of moisture transfer in Norway spruce samples”. Engineering Structures. Doi:10.1016/j.engstruct.2011.04.011. (2011).

[25] R. J. Gummerson, C. Hall, W. D. Hoff, R. Hawkes, G. N. Holland and W. S. Moore. “Unsaturated water flow within porous materials observed by NMR imaging”. Nature Vol. 281. 0028-0836/79/360056-02. (1979).

[26] L. Pel, K. Kopinga and H. J. P Brocken. “Moisture transport in porous building materials”. Heron, 41(2), 95-105. (1996).

[27] S. Hameury and M. Sterley. “Magnetic resonance imaging of moisture distribution in pinus sylvestris L exposed to daily indoor relative humidity fluctuations”. Wood Material Science and Engineering. Doi: 10.1080/17480270601150578. (2006).

[28] M. B. MacMillan, M. H. Schneider, A. R. Sharp and B. J. Balcom. “Magnetic resonance imaging of water concentration in low moisture content wood”. Wood and fiber science, 34(2), pp. 276-286. (2002).

[29] I. V. Mastikhin, H. Mullally, B. MacMillan and B. J. Balcom. “Water content profiles with a 1D centric sprite acquisition”. Journal of Magnetic Resonance. Doi: 10.1006/jmre.2002.2544. (2002).

[30] Q. Chen, M. K. Gingras and B. J. Balcom. “A magnetic resonance study of pore filling processes during spontaneous imbibition in Berea sandstone”. Journal of chemical physics, Volume 119. Doi:10.1063/1.1615757. (2003).

[31] A. F. Nielsen. “Gamma-ray-attenuation used for measuring the moisture content and homogeneity of porous concrete”. Build. Sci. Vol. 7, pp.257-263. Pergamon Press. Printed in Great Britain. (1972).

[32] M. K. Kumaran and M. T. Bomberg. “A Gamma-spectrometer for determination of density distribution and moisture distribution in building materials”. Proceedings of the International Symposium on Moisture and Humidity. Washington, D. C. P. 485-490. (1985).

[33] S. A. Srinilta. “Flow of water through columns of layered soil”. *Ph.D* thesis, IOWA State University. 3431. (1967).

[34] T. Olsson, M. Megnis, J. Varna and H. Lindlberg. “Study of the transverse liquid flow paths in pine and spruce using scanning electron microscopy”. Japan Wood Sciences 47,282-288. (2001).

[35] M. S. Gilani, M. Griffa, D. Mannes, E. Lehmann, J. Carmeliet and D. Derome. “Visualization and quantification of liquid water transport in softwood by means of neutron radiography”. International Journal of Heat and Mass Transfer, Volume 55, Pages 6211-6221. (2012).

[36] M. S. Gilani, S. Abbasion, E. Lehmann, J. Carmeliet and D. Derome. “Neutron imaging of moisture displacement due to steep temperature gradients in hardwood”. International Journal of Thermal Sciences 81 1-12. (2014).

[37] S. Abbasion, J. Carmeliet, M. S. Gilani, P. Vontobel and D. Derome. “A hygrothermo-mechanical model for wood: part A. Poroelastic formulation and validation with neutron imaging – COST Action FP0904. 2010 – 2014: thermo-hydro-mechanical wood behavior and processing”. Article in Holzforschung. Doi: 10.1515/hf20140189. (2015).

[38] M. S. Gilani, K. G. Wakili, M. Koebel, E. Hugi, S. Carl and E. Lehmann. “Visualizing moisture release and migration in gypsum plaster board during and beyond dehydration by

neutron radiography". International Journal of Heat and Mass Transfer, Doi: 10.1016/j.ijheatmasstransfer.2013.01.039. (2013).

[39] J. F. Federici. "Review of moisture and liquid detection and mapping using terahertz imaging". J Infrared Milli Terahz Waves. Doi 10.1007/s10762-011-9865-7. (2012).

[40] C. Jansen, S. Wietzke, O. Peters, M. Scheller, N. Vieweg, M. Salhi, N. Krumbholz, C. Jördens, T. Hochrein and M. Koch. "Terahertz imaging: application and perspectives". Optical Society of America. Applied Optics/ vol. 49, No, 19/1. (2010).

[41] J. P. Guillet, B. Recur, L. Frederique, B. Bousquet, L. Canioni, I. Manek-Hönninger, P. Desbarats and P. Mounaix. "Review of Terahertz tomography techniques". J. Infrared Milli Terahz. DOI: 10.1007/s10762-014-0057-0. (2014).

[42] J. F Federici, B. Schulkin, F. Huang, D. Gary, R. Barat, F. Oliveira and D. Zimdars. "*THz* imaging and sensing for security applications-explosives, weapons and drugs". Semicond. Sci. Technol. Doi:10.1088/0268-1242/20/7/018. (2005).

[43] J. White and D. Zimdars. "Time domain terahertz non-destructive evaluation of water intrusion in composites and corrosion under insulation". Conference on Lasers and Electro-Optics. (2007).

[44] F. Ospald, W. Zouaghi, R. Beigang, C. Matheis, J. Jonuscheit, B. Recur, J. P. Guillet, P. Mounaix, W. Vleugels, P. V. Bosom, L. V. González, I. López, R. M. Edo, Y. Sternberg and M. Vandewalj. "Aeronautics composite material inspection with a terahertz time-domain spectroscopy system". Society of Photo-Optical Instrumentation Engineers (SPIE). DOI: 10.1117/1.OE.53.3. (2014).

[45] J. Beckmann, He. Richter, U. Zscherpel, U. Ewert, J. Weinzierl, L. P. Schmidt, F. Rutz, M. Koch, H. Richter and H. W. Hübers. "Imaging capability of terahertz and millimeter-wave instrumentations for NDT of polymer materials". 9th European Conference on NDT. (2006).

[46] R. M. Woodward, B. E. Cole, V. P. Wallace, R. J. Pye, D. D. Arnone, E. H. Linfield and M. Pepper. "Terahertz pulse imaging in reflection geometry of human skin cancer and skin tissue". Physics in Medicine and Biology. 47(21): p. 3853–3863. (2002).

[47] E. Pickwell and V. P. Wallace. "Biomedical applications of terahertz technology". J. Phys. D: Applied Physics. Doi:10.1088/0022-3727/39/17/R01. (2006).

[48] D. Banerjee, W. V. Spiege, M. D. Thomson, S. Schabel and H. G. Roskos. "Diagnosing water content in paper by terahertz radiation". Optics Express 9060 Vol. 16, No. 12. (2008).

[49] C. Jördens, S. Wietzke, M. Scheller and M. Koch. "Investigation of the water absorption in polyamide and wood plastic composite by terahertz time-domain spectroscopy". Polymer Testing. doi:10.1016/j.polymertesting.2009.11.003. (2010).

[50] R. Piesiewicz, C. Jansen, S. Wietzke, D. Mittlemann, M. Koch and T. Kürner. "Properties of building and plastic materials in the *THz* range". Int J Infrared Milli Waves. Doi 10.1007/s10762-007-9217-9. (2007).

[51] C. Jördens, M. Scheller, B. Breitenstein, D. Selmar and M. Koch, "Evaluation of leaf water status by means of permittivity at Terahertz frequencies". J Biol Phys. Doi 10.1007/s10867-009-9161-0. (2009).

[52] S. Hadjiloucas, L. S. Karatzas and J. W. Bowen. "Measurement of leaf water content using Terahertz radiation". IEEE Transactions on Microwave Theory and Techniques. Doi:10.1109/22.744288. (1999).

[53] H. B. Zhang, K. Mitobe and N. Yoshimura. "Application of terahertz imaging to water content measurement". Japanese Journal of Applied Physics. Vol. 47, No. 10, pp. 8065-8070. (2008).

[54] I. Maestrojuan, A. Martinez, G and Crespo. "*THz* water content analysis in biomass material". Global Symposium on Millimeter Waves & ESA Workshop on Millimeter-Waves Technology and Applications. 978-1-5090-1348-7/16. (2016).

[55] R. Gente, N. Born, N. Voß, W. Sannemann, J. Léon, M. Koch and E. Castro-Camus. "Determination of leaf water content from terahertz time-domain spectroscopic data". J Infrared Milli Terahz Waves. Doi 10.1007/s10762-013-9972-8. (2013).

[56] R. Gente and M. Koch. "REVIEW: Monitoring leaf water content with *THz* and sub-*THz* waves". Gente and Koch Plant Methods 11:15. BioMed Central. Doi 10.1186/s13007-015-0057-7. (2015).

[57] A. J. Teti, D. E. Rodriguez, J. F. Federici and C. Brisson. "Non-destructive measurement of water diffusion in natural cork enclosures using terahertz spectroscopy and imaging". J Infrared Milli Terahz Waves. Doi 10.1007/s10762-011-9769-6. (2011).

[58] L. G. Santesteban, I. Palacios, C. Miranda, J. C. Iriarte, J. B. Royo and R. Gonzalo. "Terahertz time domain spectroscopy allows contactless monitoring of grapevine water status". Frontiers in Plant Science. Doi: 10.3389/fpls.2015.00404. (2015).

[59] P. Parasoglou, E. P. J. Parrott, J. A. Zeitler, J. Rasburn, H. Powell, L. F. Gladden and M. L. Johns. "Quantitative moisture content detection in food wafers". 34th International Conference on Infrared, Millimeter, and Terahertz Waves. Doi: 10.1109/ ICIMW.2009.532 4623. (2009).

[60] B. Li, W. Cao, S. Mathanker, W. Zhang and N. Wang. "Preliminary study on quality evaluation of pecans with terahertz time-domain spectroscopy". Infrared, Millimeter Wave, and Terahertz Technologies. Proc. SPIE 7854. Doi: 10.1117/12.882201. (2010).

[61] H. S. Chua, J. Obradovic, A. D. Haigh, P. C. Upadhya, O. Hirsch, D. Crawley, A. A. P. Gibson, L. F. Gladden and E. H. Linfield. "Terahertz time domain spectroscopy of crushed

wheat grain". International Microwave Symposium. Doi: 10.1109/MWSYM.2005.1517162. (2005).

[62] B. S. Y. Ung, B. M. Fischer, B. W. H. Ng and D. Abbott. "Towards quality control of food using terahertz". Proceedings of SPIE-The International Society for Optical Engineering. Doi: 10.1117/12.759825. (2007).

[63] T. Yasui, T. Yasuda, K. I. Sawanaka and T. Araki. "Terahertz paintmeter for noncontact monitoring of thickness and drying progress in paint film". Applied Optics. Vol. 44, No.32. Optical Society of America. (2005).

[64] K. Fukunaga, I. Hosako, I. N. Duling and M. Picollo. "Terahertz imaging systems: A non-invasive technique for the analysis of paintings". Proceedings of SPIE-The International Society for Optical Engineering. Doi: 10.1117/12.827452. (2009).

[65] A. S. Skry, J. B. Jackson, M. I. Bakunov, M. Menu and G. A. Mourou. "Terahertz time-domain imaging of hidden defects in wooden artworks: application to a Russian icon painting". Applied optics. Vol. 53, No. 6. Optical Society of America. (2014).

[66] M. Bensalem, A. Sommier, J. C. Mindeguia, J. C. Batsale and C. Pradere. "Terahertz measurement of the water content distribution in wood materials". J Infrared Milli Terahz Waves. Doi 10.1007/s10762-017-0441-7. (2017).

[67] M. Koch, S. Hunsche, P. Schumacher, M. C. Nuss, J. Feldmann and J. Fromm. "*THz*-imaging: a new method for density mapping of wood". Wood Science and Technology 32 421-427. Springer-Verlag. (1998).

[68] C. Pradere, M. Ryu, A. Sommier, M. Romano, A. Kusiak, J. L. Battaglia, J. C. Batsale and J. Morikawa. "Non-contact temperature field measurement of solids by infrared multispectral thermo-transmittance". Journal of Applied Physics. Doi: 10.1063/1.4976209. (2017).

[69] C. Pradere, J. P. Caumes, S. Benkhemis, G. Pernot, E. Palomo, S. Dilhaire and J. C. Batsale. "Thermo-reflectance temperature measurement with millimeter wave". Review of scientific instruments. Doi: 10.1063/1.4884639. (2014).

[70] C. Poulin, M. Triki, K. Bousmaki, A. Duhant, H. Louche and B. Wattrisse. "Terahertz thermometry system to measure temperature in the thickness of a solid polymer". Quantitative InfraRed Thermography Journal. QIRT-0032. (2016).

[71] E. Stübling, Y. Bauckhage, E. Jelli, B. Fischer, B. Globisch, M. Schell, A. Heinrich, J.C. Balzer and M. Koch. "A *THz* tomography system for arbitrarily shaped samples". J Infrared Milli Terahz Waves. Doi: 10.1007/s10762-017-0415-9. (2017).

[72] S. R. Tripathi, Y. Sugiyama, K. Murate, K. Imayama and K. Kawase. "Teraherz wave three-dimensional computed tomography based on injection-seeded terahertz wave parametric emitter". Optics Express. Doi: 10.1364/ OE.24.006433. (2016).

[73] M. Romano, A. Chulkov, A. Sommier, D. Balageas, V. Vavilov, J. C. Batsale and C. Pradere. “Broad-band sub-terahertz camera based on photo-thermal conversion and *IR* thermography”. Journal of Infrared Millimeter and Terahertz waves. Doi: 10.1007/s10762-015-0241-x. (2016).

[74] H. Pron and C. Bissieux. “Focal plane array infrared cameras as research tools”. Quantitative Infrared Thermography Journal, 1, 229–240. (2004).

[75] W. Isoz, T. Svensson and I. Renhorn. “Non-uniformity correction of infrared focal plane arrays”. Proceedings of SPIE - The International Society for Optical Engineering. Doi: 10.1117/12.606691. (2005).

[76] A. E. Mudau, C. J. Willers, D. Griffith and F. P. Le Roux. “Non-uniformity correction and bad pixel replacement on LWIR and MWIR images”. Saudi International Electronics, Communications and Photonics Conference, 1–5. (2011).

[77] H. Budzier and G. Gerlach. “Calibration of uncooled thermal infrared cameras”. J. Sensors and Sensor Systems. Doi:10.5194/jsss-4-187-2015. (2015).

[78] W. J. Parker, R. J. Jenkins, C. P. Butler and G. L. Abbott. “Flash method of determining thermal diffusivity, heat capacity, and thermal conductivity”. Journal of applied physics. Doi: 10.1063/1.1728417. (1961).

[79] A. Degiovanni. “Correction de longueur d’impulsion pour la mesure de la diffusivité thermique par méthode flash”. International journal of heat and mass transfer, 30, 2199–2200. (1987).

[80] C. Pradere, J. P. Caumes, J. Toutain, E. Abraham, B. Chassagne and J. C. Batsale. “Absolute self-calibrated room-temperature terahertz powermeter”. Applied optics. Doi: 10.1364/AO.52.002320, (2013).

[81] V. Mackowiak, J. Peupelmann, Y. Ma and A. Gorges. "Noise equivalent power NEP". Thorlabs, Inc. (web: https://www.thorlabs.com/images/TabImages/Noise_Equivalent_Power_White_Paper.pdf).

[82] D. Dufour, L. Marchese, M. Terroux, H. Oulachgar, F. Généreux, M. Doucet and A. Bergeron. “Review of terahertz technology development at *INO*”. J Infrared Milli Terahertz Waves. Doi: 10.1007/s10762-015-0181-5. (2015).

[83] J. Oden, J. Meilhan, J. Lalanne-Dera, J. F. Roux, F. Garet, J. L. Coutaz and F. Simoens. “Imaging of broadband terahertz beams using an array of antenna-coupled micro-bolometers operating at room temperature”. Optics Express. Doi: 10.1364/OE.21.004817. (2013).

[84] J. Zdanevičius, M. Bauer, S. Boppel, V. Palenskis, A. Lisauskas, V. Krozer, and H. G. Roskos. “Camera for high-speed *THz* imaging”. J Infrared Millim Terahertz Waves. Doi: 10.1007/s10762-015-0169-1 (2015).

[85] G. Busse. “Optoacoustic phase angle measurement for probing a metal”. Applied Physics Letters Doi: 10.1063/1.90960. (1979).

[86] R. Montanini. “Quantitative determination of subsurface defects in a reference specimen made of plexiglas by means of lock-in and pulse phase infrared thermography”. Infrared Physics & Technology. Doi: 10.1016/j.infrared.2010.07.002. (2010).

[87] J. M. Rampnoux, H. Michel, M. A. Salhi, S. Grauby, W. Claeys and S. Dilhaire. “Time gating imaging through thick silicon substrate: A new step towards backside characterization”. Microelectronics Reliability. Doi:10.1016/j.microrel.2006.07.029. (2006).

[88] G. Busse, D. Wu and W. Karpen. “Thermal wave imaging with phase sensitive modulated thermography”. Journal of Applied Physics. Doi: 10.1063/1.351366. (1992).

[89] C. I. Castanedo. “Quantitative subsurface defect evaluation by pulsed phase thermography: depth retrieval with the phase”. *Ph.D* thesis, University of Laval. (2005).

[90] Stanford Research Systems. “About lock-in amplifiers”. Application Note #3. Web: www.thinkSRS.com.

[91] Zurich Instruments White Paper. “Principles of lock-in detection and the state of the art”. Web: www.zhinst.com. Release date: (2016).

[92] G. Clybouw, É. Deray, F. Fradcourt, J. Levacher, M. Salenne and J. Yon. “Détection Synchrone : Mesures de signaux noyés dans le bruit de mesure”. projet de physique INSA Rouen. (2015).

[93] P. Bouchareine. “Extraction d’un signal noyé dans le bruit, filtrage, détection synchrone. autocorrélation”. Technique de l’ingénieur. (1978).

[94] B. Osgood. “Lecture notes for the Fourier transform and its applications”. Stanford University. (web: https://see.stanford.edu/materials/lsoftaee261/book-fall-07.pdf)

[95] A. L. Schoenstadt. “An introduction to Fourier analysis Fourier series, partial differential equations and Fourier transforms”. Department of Applied Mathematics Naval Postgraduate School. Code MA/Zh. Monterey, California. (2005).

[96] M. Müller. “Fundamentals of music processing. Chapter: the Fourier transform in a nutshell”. Springer International Publishing Switzerland. DOI 10.1007/978-3-319-21945-5_2. (2015).

[97] P. Le Masson, O. Fudym, J. L. Gardarein and D. Maillet. “Lecture 1: Getting started with problematic inversions with three basic examples”. Metti 6 Advanced School: Thermal Measurements and Inverse Techniques Biarritz. (2015).

[98] F. Rigollet, O. Fudym and D. Maillet. “Lecture 3: Basics for linear estimation, the white box case”. Metti 6 Advanced School: Thermal Measurements and Inverse Techniques Biarritz. (2015).

[99] C. Pradere, J. P. Caumes, E. Palomo and J. C. Batsale. “Use of *SVD* decomposition to increase signal and noise ratio on *THz* imaging measurements”. Conference paper. QIRT. Doi: 10.21611/198. (2014).

[100] M. Bamford. “Méthode flash et thermographie infrarouge pour la cartographie de propriétés thermo-physiques: application à la caractérisation en thermo-mécanique”. *Ph.D* thesis, University of Bordeaux. (2007).

[101] V. Ayvazyan. “Etude de champs de température séparables avec une double décomposition en valeurs singulières : quelques applications à la caractérisation des propriétés thermo-physiques des matériaux et au contrôle non destructif”. *Ph.D* thesis, University of Bordeaux. (2012).

[102] J. E. Bertie and Z. Lan. “Infrared intensities of liquids XX: The intensity of the OH stretching band of liquid water revisited, and the best current values of the optical constants of H_2O(l) at 25 °C between 15,000 and 1 cm^{-1}”. Applied Spectroscopy, Volume 50 Issue 8: 1047–1057 Bibcode: ApSpe. 50.1047B. (1996).

[103] Afnor. “EN 14080 - Structures en bois lamellé collé et bois massifs reconstitué – exigences”. (2013).

[104] F. F. P. Kollmann and W. A. Côté. “Principles of wood science and technology”. Solid Wood. Springer-Verlag. (1968).

[105] D. Desrosiers. “Modélisation du transfert de chaleur et d’humidité dans une membrane de cellulose”. Maîtrise thesis, University of Québec. Trois-Rivières, Montréal. (2009).

[106] A. A. Eftekhari. “MATLAB FVT®*: Copyright (c) 2012, 2013, 2014, 2015. All rights reserved.

[107] M. Romano, A. Sommier, J. C. Batsale and C. Pradere. “3D transient temperature measurement in homogeneous solid material with *THz* waves”. Photonics and Digital Technologies for Imaging Applications. Doi: 10.1117/12.2225444. (2016).